Laser-free trapped-ion quantum logic with a radiofrequency magnetic field gradient

by

R. Srinivas

B.Sc., National University of Singapore, 2013

M.S., University of Colorado, Boulder, 2016

A thesis submitted to the

Faculty of the Graduate School of the

University of Colorado in partial fulfillment

of the requirements for the degree of

Doctor of Philosophy

Department of Physics

2020

This thesis entitled:
Laser-free trapped-ion quantum logic with a radiofrequency magnetic field gradient
written by R. Srinivas
has been approved for the Department of Physics

_____

Dr. Andrew C. Wilson

_____

Dr. David J. Wineland

Date _____

The final copy of this thesis has been examined by the signatories, and we find that both the content and the form meet acceptable presentation standards of scholarly work in the above mentioned discipline.

Srinivas, R. (Ph.D., Physics)

Laser-free trapped-ion quantum logic with a radiofrequency magnetic field gradient

Thesis directed by Dr. Andrew C. Wilson and Dr. David J. Wineland

Coupling the internal (spin) states of trapped ions to their shared motion is essential for applications in metrology, quantum simulation, and quantum information processing. Spin-motion coupling requires a state-dependent force and is typically performed with laser-based interactions. However, laser-based interactions can be limited by photon scattering, which is the leading error in the highest fidelity two-qubit gates demonstrated thus far. Laser-free methods, which are not limited by photon scattering, have been proposed and demonstrated using either static magnetic field gradients, or magnetic field gradients close to the qubit frequency at gigahertz frequencies. We develop a new laser-free method of spin-motion coupling that instead uses a radiofrequency magnetic field gradient. We extend this technique to novel two-qubit entangling gates that are intrinsically insensitive to qubit frequency errors, achieving a symmetric Bell-state fidelity of 0.999(1), competitive with the highest-fidelity laser-based gates. The insensitivity to qubit frequency errors enables laser-free individual addressing which we employ to create anti-symmetric Bell states with fidelity 0.998(1). These techniques are demonstrated in a surface-electrode trap with integrated microwave and rf circuitry.

Dedication

To my sister, a constant inspiration.

Acknowledgements

It is somewhat strange to have only one author on this thesis when so many have contributed to the work.

First, I would like to thank my advisor Dave Wineland. Aside from being an inspiring physicist, he is one of the nicest people I have ever interacted with. I have always appreciated his open door to all the questions I have had over the years, profound or (mostly) not. His presence was greatly missed when he left.

I've had the privilege of having not one, but two advisors. Andrew Wilson has been a great source of advice throughout my PhD, for problems physics related and not. He has an incredibly calm approach to dealing with the trickiest problems, and always remained affable regardless of the situation. These are qualities I seek to emulate. He also owes me a cake which I mention here for posterity.

Dietrich "Didi" Leibfried has been the victim of my many physics questions over the years. He has a knack of distilling the most important physics from any problem and has inspired me to be more clear and precise in all that I do. I hope to convince him one day that Beach House is a good band.

Daniel Slichter and David Allcock have also been great mentors, and friends. They were postdocs at the start of my PhD and did much of the heavy lifting initially in setting up and planning the experiment. Everything I know (which isn't much) about rf and microwaves is from

them. David Allcock is a master ground-loop sniffer and great problem solver in the lab. I've learnt a lot of debugging skills from him, which is basically to put everything on the scope. Daniel Slichter has a great eye for detail and is a master of electronics. Much of the hardware on our experiment only works due to his careful designs. He has also been a great source of advice for both physics and non-physics related issues and I will miss being able to rely on him. Both David and Daniel have plied me with alcohol over the years which is hard to separate from Stockholm Syndrome.

Along with Shaun Burd, Daniel, David and I made up the original "μ-crew" on the "magtrap". Shaun is very much the laser guru on our experiment, and has been a great friend and companion, often there in the late hours when data was taken. He is a great person to bounce ideas off, and it's been great having him down in the trenches so to speak.

Hannah Knaack has been a breath of fresh air since she joined the experiment. Her enthusiasm has been a welcome change from the cynicism that Shaun and I had accumulated by then. Her sense of humour will be sorely missed. I wish we had had a longer overlap so she could pronounce words properly; we have worked on iodine but not aluminium.

Tyler Sutherland has been a great person for us to collaborate with; he's been the source of so many good ideas that we could implement in our setup. Hard to believe he is a professor now, y'all best pay attention to what he gets up to next!

Our experiment was embedded in the larger "Quantum 1" lab. I have fond memories of spending time, both in and out of the lab, with fellow graduate students Susanna Todaro and Katie McCormick, and postdocs Jonas Keller and Robert Jördens. Justin Niedermeyer, Felix Knollmann, and Laurent "Loz" Stephenson joined the lab more recently, it's been great working with them for the brief amount of time that it's been.

It's been my privilege to be part of the Ion Storage Group, where I've had the opportunity to interact not only with great physicists, but people as well. John Bollinger has done a great job of taking over as group leader and has always provided a listening ear. Ting Rei was a great person to bug with random questions and helped me get settled in the group. In no particular order, I've had enlightening discussions with Lin Yiheng, John Gaebler, Ryan Bowler, Yong Wan, Daniel Kienzler,

Dan Cole, Stephen Erickson, Hou Panyu, Jenny Wu, Aaron Hankin, Ethan Clements, Kevin Boyce, Cui Kaifeng, Dave Hume, Sam Brewer, Jwo-Sy Chen, May Kim, Jose Valencia, Dave Leibrandt, Jim Bergquist, James Chin-wen Chou, Alejandra Collopy, Julian Schmidt, Christoph Kurz, Shon Cook, Kevin Gilmore, Joe Britton, Elena Jordan, Matt Affolter, Justin Bohnet, Bryan Sawyer, Shlomi Kotler, Dustin Hite, Dave Pappas and Kyle McKay. Apologies to anyone I might have missed out on inadvertently. Amongst these group, Aaron Hankin, Elena Jordan, and Alejandra Collopy had a desk next to mine but subsequently abandoned me for greener pastures with more natural light.

Being at NIST, we benefited greatly from our theory collaborators Scott Glancy, Emanuel Knill, and Alex Kwiatkowski who have helped us navigate the murky waters of fidelity analysis.

Theodore "Ted" Stauffer provided the lifeblood of our experiment, liquid helium. He kept up with our increasing helium consumption and odd schedules, without which the experiments described in this thesis would not be possible.

I've been somewhat sheltered from administrative tasks throughout my studies. At NIST, I am grateful to Anne Reidy, Kelsey Light, Kelsey Rodriguez, Petrina Potts, Kerry Yannacito, Camille Mandarino, Shannon Kelly amongst others for all the work behind the scenes. At PREP, Tiffany Mason, JoAnne Stein, and Lisa Valencia have helped sort out all of my travel and helped to keep food on the table. Jeanne Nijhowne at CU has saved me multiple times from missing deadlines and making sure everything was in order.

Outside of work, I've been lucky to have a fantastic group of friends to keep me sane. In particular, I'd like to thank Kevin Gilmore and Gargi Datta, who aside from being a constant source of support, put me up for the last few months of my PhD and very generously allowed me to take their cat Koshka. In Boulder, I've had the pleasure of knowing (in no particular order) Caroline Whiteman, Nicole Simmons, Dan Hackett, Sven and Kat Dönges, Judith Olson, Trevor Doner, Abhinav Prem, Robert "Bob" Hueftle and Anita Wagner, Marion Boulet, Pete Siegfried, Ng Kia Boon, Zach Ulibarri, Tim Large, Nigel Arruda and Katy Wilkin, Bryan Changala, Joseph Isaac Samaniego, and Stijn DeSmet. Special thanks also to Alejandra Collopy and Andrew Spott for taking me in and letting me play with their wonderful pets Daphne, Apollo, and Artemis.

I've had the benefit of many great teachers and mentors throughout my life, Bjørn Hessmo and David DeMille in particular are to blame for setting me down the path of experimental atomic physics.

Leaving Boulder is a little easier with another project to look forward to. For that, I thank David Lucas and Chris Ballance for providing the next step. I've also had some great discussions with Tom Harty at Oxford over the years.

My parents and sister have been a never-ending source of support throughout all my life. My nephew and nieces have been a great source of entertainment and help keep things in perspective. In particular, my niece Mallika was born when I started, and is now a fully functional human being who can even play the piano. In the mean time we've messed around with some ions...

I would like to thank Hannah Knaack, Laurent Stephenson, Felix Knollman, Dave Wineland, Andrew Wilson, David Allcock, and Daniel Slichter for a close reading of the thesis. Future readers of the thesis should also be indebted to them, this document would have been much worse otherwise!

Contents

Tables

Table

Figures

Figure

You can try the best you can

The best you can is good enough

Radiohead

1

Introduction

Magnetic field gradients have a long history in atomic physics. The Stern-Gerlach experiment in 1922 using a 1000 T/m gradient[1] was one of the earliest demonstrations of quantum behaviour [Gerlach and Stern, 1922]. In this experiment, a beam of silver atoms was sent through an inhomogeneous magnetic field, and their resulting trajectories were recorded on a screen upon exiting the magnetic field. According to classical theory, the angular momentum of these atoms would have a random orientation with respect to the magnetic field gradient and there would be a broad central peak of undeflected atoms. Instead, two distinct peaks[2] were observed, corresponding to the internal spin states of the unpaired outermost electron. These spin states are quantized, and experienced a spin-dependent force due to the magnetic field gradient, resulting in two possible trajectories as shown in Fig. 1.1.

Other examples of magnetic field gradients in atomic physics include the continuous Stern-Gerlach effect [Dehmelt, 1986] for precision electron g-factor measurements [Van Dyck et al., 1987], and magnetic trapping of neutral atoms [Pritchard, 1983, Raab et al., 1987] which was an important

[1] In our experiment, we only generate gradients of about 100 T/m, about an order of magnitude lower. Progress!

[2] Somewhat serendipitously due to the reaction of cigar smoke with silver, producing silver sulphide. See Ref. [Friedrich and Herschbach, 2003] for an excellent overview of this experiment. No cigars were used for this thesis.

step towards the subsequent observation of Bose-Einstein condensates [Anderson et al., 1995, Davis et al., 1995]. The focus of this thesis is the use of magnetic field gradients with trapped ions to demonstrate another aspect of quantum behaviour, entanglement.

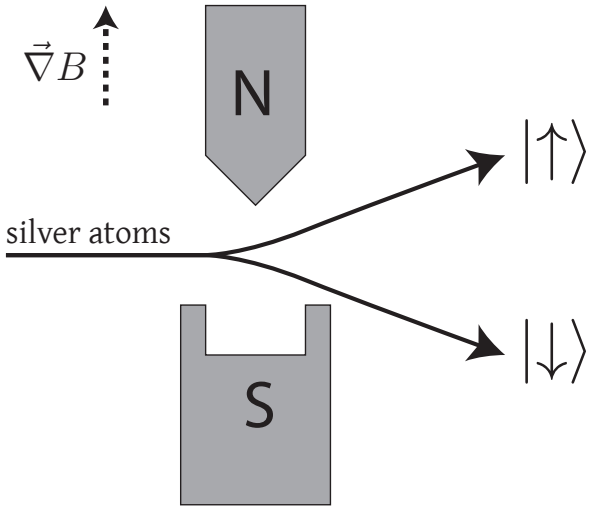

Figure 1.1: Schematic of Stern Gerlach experiment. A beam of silver atoms enters a region with a magnetic field gradient. The atoms experience a force that depends on their angular momentum. Only two deflected trajectories were observed; the angular momentum or spin of these atoms is quantized and can take one of two values, $|\uparrow\rangle$ or $|\downarrow\rangle$ corresponding to the $m_J = \pm 1/2$ states of the silver atom.

1.1 Quantum entanglement

Entangled states of matter exhibit behaviour that cannot be explained classically. An example of an entangled state is

$$|\psi\rangle = \frac{1}{\sqrt{2}}(|\downarrow\downarrow\rangle + |\uparrow\uparrow\rangle), \tag{1.1}$$

where $|\uparrow\rangle$ and $|\downarrow\rangle$ can correspond, for example, to the two spin states previously discussed. A striking feature of this state is that it cannot be decomposed into a product state of individual spins; a measurement on one of the spins will immediately determine the spin-state of the whole system,

regardless of how far each spin might be separated from the other. Einstein described this feature as a "spooky action at a distance" [Bell and Bell, 2004], and along with Podolsky and Rosen argued that the quantum description of nature was incomplete [Einstein et al., 1935]. In response, John Stewart Bell pointed out that local realism is inherently incompatible with quantum mechanics, and formulated inequalities that could be verified experimentally with entangled states [Bell, 1964]. These experiments, known as Bell tests, were soon carried out using entangled states of photons [Freedman and Clauser, 1972, Aspect et al., 1982] and subsequently loophole free tests were performed [Hensen et al., 2015, Shalm et al., 2015, Giustina et al., 2015].

1.2 Quantum computing with trapped ions

Aside from verifying fundamental aspects of quantum theory, the ability to make entangled states also enables quantum computing. Quantum computers hold the promise of solving many problems intractable to classical computers, with applications ranging from cryptography [Shor, 1994] to nitrogen fixation [Reiher et al., 2017]. Trapped ion systems are one of the leading candidates towards that goal; trapped ions have excellent coherence properties [Bollinger et al., 1991, Fisk et al., 1995, Wang et al., 2017] and have been used to demonstrate some of the highest-fidelity single [Harty et al., 2014] and two-qubit entangling operations [Gaebler et al., 2016, Ballance et al., 2016] across any platform. However, there are many challenges still in scaling these systems towards a practical device [Bruzewicz et al., 2019].

One such challenge is improving the fidelity of fundamental operations such as two-qubit gates that generate entanglemenet. These gates are typically performed with laser-based interactions, which have led to the highest two-qubit gate fidelities of 0.9992(4) and 0.999(1) in Ref. [Gaebler et al., 2016] and Ref. [Ballance et al., 2016] respectively. However, both of these gates were limited by photon scattering, intrinsic to the laser-based interaction used.

Alternative laser-free methods that eliminate photon scattering have been proposed and demonstrated using magnetic field gradients to perform these entangling operations. These laser-free methods can employ either static magnetic field gradients [Mintert and Wunderlich, 2001, Khromova

et al., 2012] or magnetic field gradients oscillating close to the qubit frequency at gigahertz frequencies [Wineland et al., 1998, Ospelkaus et al., 2008, Ospelkaus et al., 2011]. In addition to eliminating photon scattering, these methods enable simpler phase and amplitude control at microwave frequencies($\sim$GHz), as opposed to the $\sim 1000\,\mathrm{THz}$ radiation used in laser-based gates. While there are no fundamental limits to the fidelity of laser-free operations, technical challenges have limited the demonstrations thus far.

1.3 Thesis outline

In this thesis, we develop a new technique that addresses some of the challenges of previous laser-free methods. Instead of a static or gigahertz magnetic field gradient, we use a radiofrequency magnetic field gradient to generate a spin-dependent force. We give an overview of the trapped ion physics in Chapter 2, while Chapter 3 describes the apparatus we built, including the surface-electrode trap with integrated microwave and rf circuitry used to perform all the experiments in this thesis. Chapter 4 outlines the various calibrations we perform, as well as provides a description of the relevant atomic structure of our choice of trapped ion, $^{25}Mg^{+}$. We first use a radiofrequency gradient to couple the internal state of a single ion to its motion in Chapter 5. Chapter 6 describes how we extend this technique to two-qubit entangling gates, while Chapter 7 explains how we achieve laser-free single-ion addressing as well. Finally, we discuss how we perform the fidelity analysis for the entangled states we created in the preceding chapters in Chapter 8.

Seasons change and our love went cold

Feed the flame 'cause we can't let go

Run away, but we're running in circles

Post Malone

2

Trapped ion quantum logic

In this chapter, we discuss the basics of trapping ions, how to couple their internal states (here denoted as spin states to indicate they are states of different angular momentum) to their motion, and how to perform entangling gates. We also include some numerical simulations of different error mechanisms in entangling gates.

2.1 Linear rf Paul Traps

There are several trapping configurations that can be used for charged particles. We focus on the linear rf Paul trap, which is used in the experiments described in this thesis. We mainly follow Ref. [Wineland et al., 1998] and Ref. [Foot, 2007]. Earnshaw's theorem states that a charged particle cannot be in stable equilibrium when acted upon by only a static electric field. This theorem follows from Maxwell's equations where $\vec{\nabla} \cdot \vec{E} = 0$ for a region with no charge density, i.e., all the electric field lines do not point to one location. One way around this constraint is to use oscillating potentials instead.

We analyze the simple four-rod configuration in Fig. 2.1, where a potential $V_0 \cos \Omega_T t$ is applied to two diagonally opposite electrodes a distance R from the trapping location. The applied

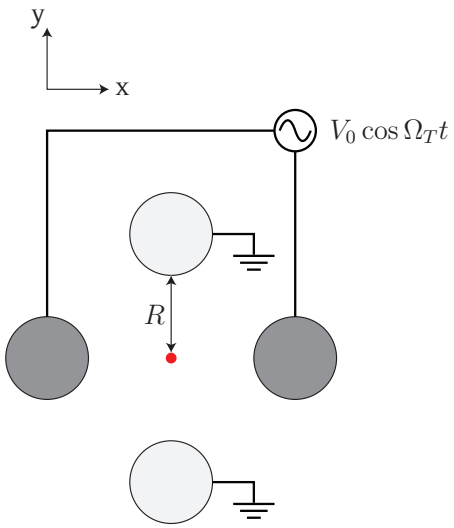

Figure 2.1: Paul trap. An oscillating potential $V_0 \cos \Omega_T t$ is applied to the two electrodes in dark grey, while the other two electrodes are grounded. The ion (red) is trapped at the center, a distance R from each of the electrodes.

potential is oscillating with frequency Ω_T and amplitude V_0. For the potential Φ in the (x-y) plane, the boundary conditions are

$$\begin{aligned} \Phi &= V_0 \cos \Omega_T t, & x &= \pm R, y = 0, \\ \Phi &= 0, & x &= 0, y = \pm R, \end{aligned} \tag{2.1}$$

which are satisfied by

$$\Phi = \Phi_0 + \frac{V_0 \cos(\Omega_T t)}{2} \left(1 + \frac{x^2 - y^2}{R^2}\right). \tag{2.2}$$

Here, we make the approximation that we have a quadratic dependence close to the axis. The electric field along the x direction is

$$E_x = -\frac{\partial \Phi}{\partial x} \tag{2.3}$$

$$= -\frac{V_0}{R^2} \cos(\Omega_T t) x, \tag{2.4}$$

which gives rise to the equation of motion

$$M\frac{\mathrm{d}^2x}{\mathrm{d}t^2} = -\frac{eV_0}{R^2}\cos(\Omega_T t)x, \tag{2.5}$$

where we assume the ion has a single elementary charge e and mass M. Here, a classical treatment is sufficient. We make a substitution $\tau = \Omega_T t/2$, which leads to

$$\frac{\mathrm{d}^2x}{\mathrm{d}\tau^2} = -\frac{4eV_0}{\Omega_T^2 MR^2}\cos(2\tau)x. \tag{2.6}$$

This equation is a form of the Mathieu equation

$$\frac{\mathrm{d}^2x}{\mathrm{d}\tau^2} + (a_x - 2q_x\cos 2\tau)x = 0. \tag{2.7}$$

In our simplified case, $a_x = 0$ and $q_x = (2eV_0)/(\Omega_T^2 MR^2) \ll 1$. In practice, a_x will be non-zero if an additional static quadrupole potential is applied to the electrodes (see Ref. [Wineland et al., 1998]). The solution is

$$x = x_0\cos\left(\frac{q_x\tau}{\sqrt{2}} + \theta_0\right)\left(1 + \frac{q_x}{2}\cos 2\tau\right) \tag{2.8}$$

$$= x_0\cos\left(\frac{q_x\Omega_T}{2\sqrt{2}}t + \theta_0\right)\left(1 + \frac{q_x}{2}\cos\Omega_T t\right) \tag{2.9}$$

where x_0 and θ_0 are determined by initial conditions. The term on the left is usually referred to as the "secular" motion with frequency

$$\omega_x = \frac{q_x\Omega_T}{2\sqrt{2}} = \frac{eV_0}{\sqrt{2}\Omega_T MR^2}. \tag{2.10}$$

The faster oscillating term at Ω_T is referred to as micromotion[1] . It has the effect of modulating the ion's wavepacket position at Ω_T, but with a small enough amplitude that we can ignore it for the

[1] Distinct from the "excess" micromotion we compensate for when a stray static electric field pushes the ion off the rf null [Berkeland et al., 1998].

key results described below. We get an identical frequency along the y-direction; this degeneracy is broken by a static potential. Additional end caps with static potentials can provide confinement along the z axis.

2.2 Trapped ion hyperfine qubits

The hyperfine states within a trapped ion are useful as qubits due to their long coherence times; up to tens of seconds [Langer et al., 2005, Harty et al., 2014] or even minutes [Bollinger et al., 1991, Fisk et al., 1995, Wang et al., 2017] have been demonstrated. The qubit can be described by the Hamiltonian

$$\hat{H}_{\text{qubit}} = \frac{\hbar\omega_0}{2}\hat{\sigma}_z, \tag{2.11}$$

where ω_0 is the qubit frequency. For trapped ion hyperfine qubits, $\omega_0/2\pi$ is typically in the GHz range. As these qubits are within the S manifold of the ion, electric dipole transitions are forbidden. Instead, single-qubit rotations can be performed using either two-photon stimulated Raman transitions via an intermediate electronic state, or magnetic dipole transitions using an oscillating magnetic field at ω_0 [Wineland et al., 1998]. Both of these methods have been used for high-fidelity single-qubit rotations using lasers [Ballance et al., 2016, Gaebler et al., 2016] and microwaves [Brown et al., 2011, Harty et al., 2014]. In particular, Ref. [Harty et al., 2014] demonstrated single-qubit-rotation gate errors at the 1×10^{-6} level. Ref. [Bruzewicz et al., 2019] contains an overview of other types of trapped-ion qubits that can be used such as optical frequency qubits.

2.3 Trapped ion spin-motion coupling

Aside from the internal spin states, the ions also have motional states. To a very good approximation [Wineland et al., 1998], the ions' modes of motion can be described by a quantum harmonic oscillator with Hamiltonian

$$\hat{H}_{\text{motion}} = \hbar\omega_r \hat{a}^\dagger \hat{a}, \tag{2.12}$$

where ω_r is the frequency of the motional mode. For a single ion, the position operator $\hat{r}$ for a single mode is

$$\hat{r} = r_0(\hat{a} + \hat{a}^\dagger), \tag{2.13}$$

with $r_0 = \sqrt{\hbar/(2m\omega_r)}$ describing the ion's ground state extent. The creation and annihilation operators are $\hat{a}^\dagger$ and $\hat{a}$ respectively. For the experiments in this thesis using $^{25}Mg^+$ and motional frequencies which are typically $\omega_r/2\pi \approx 6\,\text{MHz}$, $r_0 \approx 6\,\text{nm}$. The motional states are usually described in the Fock state basis $|n\rangle$.

Coupling the ions' internal states to their motion, or spin-motion coupling, is the workhorse for many applications in trapped ions, from elementary logic gates [Monroe et al., 1995] to quantum logic spectroscopy [Schmidt et al., 2005] that has enabled some of the world's most precise clocks, for example Ref. [Brewer et al., 2019]. These demonstrations all involved only sideband transitions (described below), using the motion as an information bus between ion spin states [Cirac and Zoller, 1995]. Here, we discuss how these sideband transitions are generated from a field gradient and how they can be implemented with and without laser beams.

2.3.1 Sideband transitions

First, let us look at the Hamiltonian that corresponds to the potential energy of an ion, given by

$$\hat{H} = \hat{V}(r), \tag{2.14}$$

where the potential is dependent on position. Expanding to first order,

$$\hat{H} \approx \hat{V}(r)\Big|_{r=r_{\text{average}}} + \frac{\partial V}{\partial r}\Big|_{r=r_{\text{average}}} r_0(\hat{a} + \hat{a}^\dagger), \tag{2.15}$$

where r_{average} is the average position of the ion. We see that if there is a gradient in the potential, we now have terms that couple to the motion. To see sideband transitions, let us analyze a Hamiltonian describing a field with frequency ω that can drive spin-flip transitions in an ion.

$$\hat{H} \approx 2\hbar\Omega_f \cos(\omega t)\hat{\sigma}_x + 2\hbar\Omega_g \cos(\omega t)\hat{\sigma}_x(\hat{a} + \hat{a}^\dagger), \tag{2.16}$$

where Ω_f corresponds to the coupling of the internal states of the ion to the field, while Ω_g is the coupling of the internal states and the ion motion to the gradient following Eq. 2.15. Transforming to the interaction picture with respect to $\hat{H}_0 = \frac{\hbar\omega_0}{2}\hat{\sigma}_z + \hbar\omega_r\hat{a}^\dagger\hat{a}$ (the ion qubit and motional energies), we obtain (following Appendix. A.1)

$$\hat{H}_I \approx \hbar\Omega_f(\hat{\sigma}_+ e^{-i\delta t} + \hat{\sigma}_- e^{i\delta t}) + \hbar\Omega_g(\hat{\sigma}_+ e^{-i\delta t} + \hat{\sigma}_- e^{i\delta t})(\hat{a}e^{-i\omega_r t} + \hat{a}^\dagger e^{i\omega_r t}), \tag{2.17}$$

where $\delta = \omega - \omega_0$. The spin-raising and lowering operators are $\hat{\sigma}_+ = |\uparrow\rangle\langle\downarrow|$ and $\hat{\sigma}_- = |\downarrow\rangle\langle\uparrow|$ respectively, where $|\uparrow\rangle$ and $|\downarrow\rangle$ are the internal spin states of the trapped ion. When $\delta = 0$, we implement $|\downarrow\rangle \leftrightarrow |\uparrow\rangle$ spin-flip transitions (ignoring fast-rotating terms). Similarly, when $\delta = \omega_r$, we implement the blue sideband transition with the interaction

$$\hat{H}_{\text{bsb}} = \hbar\Omega_g(\hat{\sigma}_+\hat{a}^\dagger + \hat{\sigma}_-\hat{a}). \tag{2.18}$$

This interaction drives the $|\downarrow\rangle|n\rangle \leftrightarrow |\uparrow\rangle|n+1\rangle$ transition with $\Delta n = 1$. If instead $\delta = -\omega_r$, we implement the red sideband transition

$$\hat{H}_{\text{rsb}} = \hbar\Omega_g(\hat{\sigma}_+\hat{a} + \hat{\sigma}_-\hat{a}^\dagger), \tag{2.19}$$

which drives the $|\downarrow\rangle|n\rangle \leftrightarrow |\uparrow\rangle|n-1\rangle$ transition with $\Delta n = -1$. These transitions are summarized in Fig. 2.2.

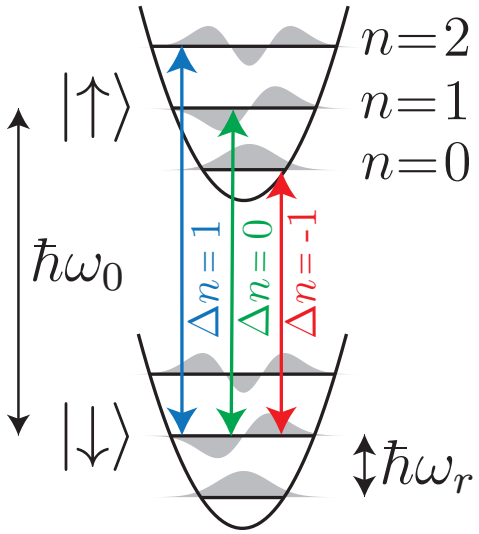

Figure 2.2: Schematic of sideband transitions. The ion has spin states denoted by $|\downarrow\rangle$ and $|\uparrow\rangle$ with energy $\hbar\omega_0$. The ion also has motional (Fock) states denoted by n with energies $\hbar\omega_r$. A carrier transition that flips the ion spin but leaves the motional state unchanged ($\Delta n = 0$) is denoted by the green arrow. A blue (red) sideband transition corresponds to adding (subtracting) a motional quantum when starting in $|\downarrow\rangle$, such that $\Delta n = 1$ ($\Delta n = -1$).

2.3.2 Position-dependent energy shifts

Not all spin-motion coupling results in sideband transitions. If instead we have an interaction that modulates the qubit frequency at frequency ω, the Hamiltonian becomes

$$\hat{H} \approx 2\hbar\Omega_f \cos(\omega t)\hat{\sigma}_z + 2\hbar\Omega_g \cos(\omega t)\hat{\sigma}_z(\hat{a} + \hat{a}^\dagger), \tag{2.20}$$

which is identical to Eq. 2.16, except that $\hat{\sigma}_x$ has been replaced by $\hat{\sigma}_z$. Again, going into the interaction picture with respect to $\hat{H}_0$,

$$\hat{H}_I \approx 2\hbar\Omega_f \cos\omega t\hat{\sigma}_z + 2\hbar\Omega_g \cos\omega t\hat{\sigma}_z(\hat{a}e^{-i\omega_r t} + \hat{a}^\dagger e^{i\omega_r t}). \tag{2.21}$$

The first term corresponds to an oscillation of the qubit frequency at frequency ω. The second term, while arising from the gradient, does not drive sideband transitions, but instead spin-dependent

displacements that are the basis for the entangling gates described in Sec. 2.4.3. However, an additional field can be used to drive sideband transitions as we discuss in Chapter 5.

2.3.3 Laser-based spin-motion coupling

Laser-based spin-motion coupling typically involves driving electric dipole transitions according to the Hamiltonian

$$\hat{H}_e = -\vec{\mu}_d \cdot \vec{E}. \tag{2.22}$$

The ion's electric dipole operator is $\vec{\mu}_d$ and $\vec{E}$ is the electric field. In this case, our qubit states will correspond to different electronic levels in the atom (for example S and P states). For an electric field $\vec{E} = E_x \hat{x} \cos(kr - \omega t + \phi)$, where k is the wavevector $2\pi/\lambda$ and ω its frequency,

$$\hat{H}_e = \hbar\Omega_e(\hat{\sigma}_+ + \hat{\sigma}_-)\left(e^{i(kr-\omega t+\phi)} + e^{-i(kr-\omega t+\phi)}\right). \tag{2.23}$$

The Rabi frequency is $\Omega_e = -\mu_{dx}E_x/4$. Expanding to first order following Eq. 2.15,

$$\begin{aligned}\hat{H}_e \approx & \hbar\Omega_e(\hat{\sigma}_+ + \hat{\sigma}_-)\left(e^{i(-\omega t+\phi')} + e^{-i(-\omega t+\phi')}\right) && \text{field} \\ & + \hbar\Omega_e kr_0(\hat{\sigma}_+ + \hat{\sigma}_-)(\hat{a} + \hat{a}^\dagger)\left(e^{i(-\omega t+\phi')} + e^{-i(-\omega t+\phi')}\right), && \text{gradient}\end{aligned} \tag{2.24}$$

where $\phi' = kr_{\text{average}} + \phi$. The gradient term has a Rabi frequency that is smalelr than the field term by a factor $\eta = kr_0$, where η is the Lamb-Dicke parameter that describes the ratio of the wavelength to the ion's ground-state wavefunction extent. Transforming into the interaction picture with respect to $\hat{H}_0$, we obtain

$$\begin{aligned}\hat{H}_I = & \hbar\Omega_e(\hat{\sigma}_+ e^{-i\delta t} + \hat{\sigma}_- e^{i\delta t}) && \text{field} \\ & + \hbar\Omega_e\eta(\hat{\sigma}_+ e^{-i\delta t} + \hat{\sigma}_- e^{i\delta t})(\hat{a}e^{-i\omega_r t} + \hat{a}^\dagger e^{i\omega_r t}), && \text{gradient}\end{aligned} \tag{2.25}$$

where for simplicity we have dropped the complex phase corresponding to $e^{i\phi'}$. We now have all the ingredients to drive spin-flip or sideband transitions by appropriate choice of δ as shown in Eq. 2.17. Note that here we assume the interaction of the dipole moment with just one field. A similar derivation follows for two-photon transitions except two fields would have to be considered, and instead of k we have Δk, the difference between the k-vectors of the two fields [Wineland et al., 1998].

2.3.4 Laser-free spin-motion coupling

Instead of using the ion's electric dipole moment, we can also use its state-dependent magnetic dipole moments coupled to a magnetic field gradient. Laser-free spin-motion coupling has been proposed and demonstrated using static magnetic field gradients [Mintert and Wunderlich, 2001, Johanning et al., 2009] and oscillating magnetic field gradients close to the qubit frequency [Ospelkaus et al., 2008, Ospelkaus et al., 2011]. We first look at how these gradients can be generated in the near-field relative to current-carrying electrodes, and give an overview of the different types of gradients that can be used.

2.3.4.1 Near-field magnetic field gradients

As we have seen in this chapter, we need field gradients to couple the ions' spin to their motion. For a plane wave, this gradient is proportional to $\partial/\partial r \exp(ikr) \propto 1/\lambda$. Thus, for laser-based methods, this gradient can be large as the wavelength is small, $\sim 300\,\mathrm{nm}$. For microwave or rf transitions, this gradient would be negligible as the wavelengths are now $\sim 100\,\mathrm{mm}$, 6 orders of magnitude higher. However, as pointed out in Ref. [Wineland et al., 1998][2], near-field gradients can also be used. The interaction describing an ion's magnetic moment in a magnetic field is

[2] One of the reasons we call ref. [Wineland et al., 1998] the "Bible". Every time you think you have a good idea you check the "Bible" and Dave thought about it 20 years ago.

$$\begin{aligned}\hat{H}_B &= -\vec{\mu}\cdot\vec{B} \\ &\approx -\vec{\mu}\cdot\vec{B}\Big|_{r=r_{\text{average}}} - \vec{\mu}\cdot\frac{\partial B}{\partial r}\Big|_{r=r_{\text{average}}}\hat{r},\end{aligned} \tag{2.26}$$

where $\vec{\mu}$ is the ion magnetic moment, and $\vec{B}$ is the magnetic field. We have expanded the magnetic potential following Eq. 2.15. In future chapters, the first term in the second line of Eq. 2.26 is what we will refer to as the **field** component, and the second the **gradient**.

For simplicity, we consider a magnetic field generated by an infinitely long current-carrying wire and its gradient in the radial direction

$$\begin{aligned}B &= \frac{\mu_0 I}{2\pi d}, \\ \frac{\partial B}{\partial d} &= -\frac{\mu_0 I}{2\pi d^2},\end{aligned} \tag{2.27}$$

where d is the distance from the wire and I can be time-dependent. The gradient is independent of the wavelength and dependent only on the ion-electrode distance (with the near-field approximation of $d \ll \lambda$). Thus, by placing the ion very close to a current-carrying electrode, we can generate a magnetic field gradient that is large enough to couple the ion's spin to its motion.

2.3.5 Near-qubit-frequency oscillating magnetic-field gradient

Following Eq. 2.26, for a magnetic field that couples the qubit states, $\vec{B} = B_x\hat{x}\cos\omega t$, the Hamiltonian is

$$\begin{aligned}\hat{H}_I &= -\vec{\mu}\cdot\vec{B} \\ &\approx \hbar\Omega_B(\hat{\sigma}_+ e^{-i\delta t} + \hat{\sigma}_- e^{i\delta t}) && \text{field} \\ &+ \hbar\Omega_g(\hat{\sigma}_+ e^{-i\delta t} + \hat{\sigma}_- e^{i\delta t})(\hat{a}e^{-i\omega_r t} + \hat{a}^\dagger e^{i\omega_r t}), && \text{gradient}\end{aligned} \tag{2.28}$$

where we have transformed into the interaction picture with respect to $\hat{H}_0$. The Rabi frequencies are

$$\Omega_B = \frac{B_x}{2\hbar}\mu_{\downarrow\uparrow}, \tag{2.29}$$

corresponding to spin-flip transitions[3] with $\delta = 0$, and $\mu_{\downarrow\uparrow} = \langle\downarrow| \mu_x |\uparrow\rangle$. The Rabi frequency of the gradient is

$$\Omega_g = \frac{\frac{\partial B}{\partial r} r_0}{2\hbar}\mu_{\downarrow\uparrow}, \tag{2.30}$$

which drives sideband transitions when $\delta = \pm\omega_r$. The matrix element $\mu_{\downarrow\uparrow}$ describes the coupling of the ion spin states via the magnetic moment and r_0 is the ground state extent[4] .

2.3.5.1 Static magnetic field gradients

Instead of an oscillating magnetic field gradient, a static magnetic field gradient can also be used. The magnetic field gradient can be from permanent magnets [Lake et al., 2015, Weidt et al., 2016, Khromova et al., 2012] or a wire with a dc current [Welzel et al., 2019]. This gradient is typically used in conjunction with additional oscillating fields close to the qubit frequency to drive sideband transitions as we discuss in Sec. 5.1.

2.3.5.2 Radiofrequency magnetic field gradient

Finally, we demonstrate a new laser-free method of spin-motion coupling that uses a radiofrequency magnetic field oscillating close to the ion motional frequency, in addition to oscillating fields close to the qubit frequency; this technique is discussed in more detail in Chapter 5.

2.4 Entangling gates

Trapped ion qubits have weak direct spin-spin interactions due to the Coloumb repulsion that keeps the ion-ion spacing large. However, as pointed out in Ref. [Cirac and Zoller, 1995], the

[3] This is equivalent to Ω^x in Ref.[Ospelkaus et al., 2008].
[4] This is equivalent to $\Omega^x_{j,n}$ in Ref.[Ospelkaus et al., 2008].

spin-motion coupling techniques discussed in the previous section enable strong spin-spin interactions via the shared motion of the ions. By using tightly focused beams on ions in their ground state of motion, entangled states can be created using only sideband interactions on each ion. Experimental demonstrations soon followed using a single ion entangled with its motional state [Monroe et al., 1995], and later with multiple ions [Schmidt-Kaler et al., 2003]. More recently, this technique has been used to entangle atomic and molecular ion qubits [Lin et al., 2020].

However, there are two big disadvantages to the Cirac-Zoller technique. First, it requires cooling to the ground state of motion. Any motional occupation outside of $n = 0$ would result in a gate error. Second, individual addressing of ions is necessary. Both of these problems are circumvented with geometric phase gates.

2.4.1 Geometric phase gates

Geometric phase gates use spin-dependent forces to drive closed spin-dependent trajectories in phase space. As the ions return to their original position in phase space, their motion is disentangled at the end of the sequence independent of the initial state of motion, eliminating the need for ground state cooling. Broadly, there are two classes of phase gates. First, are the $\hat{\sigma}_x\hat{\sigma}_x$ gates proposed in Ref. [Mølmer and Sørensen, 1999, Sørensen and Mølmer, 1999], which was first demonstrated in Ref. [Sackett et al., 2000]. Second, are the $\hat{\sigma}_z\hat{\sigma}_z$ gates which were proposed in Ref. [Milburn et al., 2000] and inspired the demonstration of a high fidelity phase gate[5] in Ref. [Leibfried et al., 2003]. While the two interactions broadly generate the same dynamics [Lee et al., 2005], the origins of spin-dependent forces are physically distinct. We discuss their specific implementations after a general overview of phase gates. The gate interaction for two ions is

$$\hat{H}_g = \hbar\Omega_g \left(\hat{\sigma}_{i1} \pm \hat{\sigma}_{i2}\right) \left(\hat{a}e^{i\Delta t} + \hat{a}^\dagger e^{-i\Delta t}\right), \tag{2.31}$$

where Ω_g is the Rabi frequency corresponding to the gradient producing the spin-dependent force and Δ is the gate detuning. The spin operators are $(\hat{\sigma}_{i1} + \hat{\sigma}_{i2})$ for the center-of-mass mode and

[5] Also known as the Didi gate.

$(\hat{\sigma}_{i1} - \hat{\sigma}_{i2})$ for the out-of-phase mode. The spin operator $\hat{\sigma}_i$ can have $i = x, y, z$ while 1 and 2 specify the ion index. Following Appendix D.2, the time evolution operator for this interaction is

$$\hat{U}_g = \hat{D}(\alpha(t))e^{-i\phi(t)}, \tag{2.32}$$

where $\hat{D}$ is the displacement operator. The displacement is

$$\alpha(t) = \frac{\Omega_g}{\Delta}\left(\hat{\sigma}_{i1} \pm \hat{\sigma}_{i2}\right)\left(e^{-i\Delta t} - 1\right), \tag{2.33}$$

and the phase is

$$\phi(t) = \frac{\Omega_g^2}{\Delta^2}\left(\hat{\sigma}_{i1} \pm \hat{\sigma}_{i2}\right)^2\left(\Delta t - \sin\left(\Delta t\right)\right). \tag{2.34}$$

This propagator describes a spin-dependent trajectory in phase space, with a spin-dependent geometric phase. To generate spin-spin entanglement while disentangling the spin states from the motion, we require that the displacement $\alpha = 0$ at the end of the gate sequence. We fulfill this requirement by choosing the gate duration and detuning such that $\Delta = 2K\pi/t_g$, where K is an integer corresponding to the number of loops in the phase-space trajectory. The phase space dynamics are shown in Fig. 2.3.

To generate the maximally entangled state, we need $\phi(t) = \pi/2$. As the eigenvalues of $(\hat{\sigma}_{i1} \pm \hat{\sigma}_{i2})$ are 2 and 0, solving for Δ and t_g we obtain

$$\Delta = \pm 4\sqrt{K}\Omega_g, \tag{2.35}$$

$$t_g = \frac{2\pi\sqrt{K}}{4\Omega_g}. \tag{2.36}$$

Note that the positive and negative values of Δ correspond to different maximally entangled states. For the specific case of the spin operators in Eq. 2.31 being $(\hat{\sigma}_{z1} - \hat{\sigma}_{z2})$, the acquired phases for each of the different spin states (Δ positive) are

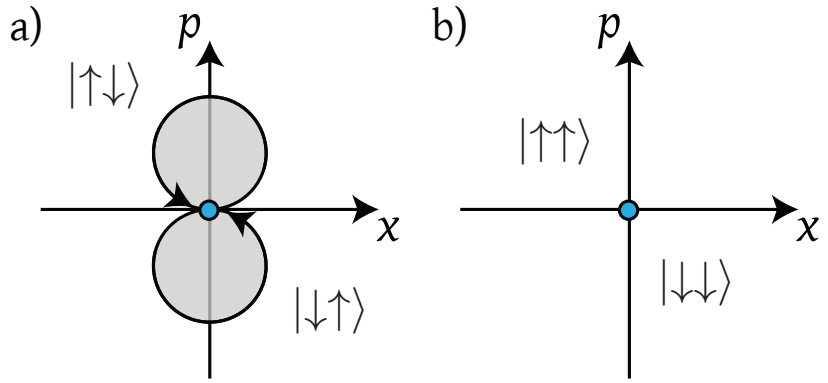

Figure 2.3: Geometric phase gates in phase space for $(\hat{\sigma}_{z1} - \hat{\sigma}_{z2})$ in Eq. 2.31. The center of the ions' motional wavefunction is indicated by the blue dot. a) Two of the four two-ion spin states undergo a circular trajectory in phase space. Returning to the origin, these spin states acquire a geometric phase proportional to the area enclosed in phase space and are disentangled from the ion motion. b) The other two spin states do not experience a spin-dependent force and stay at the origin. Setting the acquired geometric phase to $\pi/2$ enables the generation of entangled states. This example shows the initial position of the ion at the origin in phase space but, in principle the ion could be initialized anywhere.

$$\begin{aligned} |\downarrow\downarrow\rangle &\rightarrow |\downarrow\downarrow\rangle\,, \\ |\uparrow\uparrow\rangle &\rightarrow |\uparrow\uparrow\rangle\,, \\ |\downarrow\uparrow\rangle &\rightarrow -i\,|\downarrow\uparrow\rangle\,, \\ |\uparrow\downarrow\rangle &\rightarrow -i\,|\uparrow\downarrow\rangle\,. \end{aligned} \tag{2.37}$$

This spin-dependent phase, along with global $\pi/2\big|_x$ pulses before and after the phase-space displacement, produces a maximally entangled state,

$$|\downarrow\downarrow\rangle \rightarrow \frac{1}{\sqrt{2}}\left(|\downarrow\downarrow\rangle + i\,|\uparrow\uparrow\rangle\right). \tag{2.38}$$

2.4.2 Mølmer-Sørensen gates

Having gone through the general theory, we now discuss specific implementations of the geometric phase gates. For the Mølmer-Sørensen gate, the interaction is generated by simultaneous

application of red and blue sideband interactions that are symmetrically detuned from the qubit resonance. In other words, if the blue sideband is detuned by Δ, the red sideband is detuned by $-\Delta$. The Hamiltonian in the interaction picture is

$$\begin{aligned}
\hat{H}_{\text{ms}} &= \hat{H}_{\text{bsb}} + \hat{H}_{\text{rsb}} \\
&= \hbar\Omega_g\Big((\hat{\sigma}_{+1} + \hat{\sigma}_{+2})\hat{a}^\dagger e^{-i\Delta t} + (\hat{\sigma}_{-1} + \hat{\sigma}_{-2})\hat{a}e^{i\Delta t} && \text{BSB} \\
&+ (\hat{\sigma}_{+1} + \hat{\sigma}_{+2})\hat{a}e^{i\Delta t} + (\hat{\sigma}_{-1} + \hat{\sigma}_{-2})\hat{a}^\dagger e^{-i\Delta t}\Big) && \text{RSB} \\
&= \hbar\Omega_g\left(\hat{\sigma}_{x1} \pm \hat{\sigma}_{x2}\right)\left(\hat{a}e^{i\Delta t} + \hat{a}^\dagger e^{-i\Delta t}\right). && (2.39)
\end{aligned}$$

While our spin operators correspond to $\hat{\sigma}_x$ here, adjusting the phase of the BSB and RSB interactions can result in $\hat{\sigma}_\phi\hat{\sigma}_\phi$ interactions, where $\hat{\sigma}_\phi = \cos\phi\hat{\sigma}_x + \sin\phi\hat{\sigma}_y$. This technique has resulted in both high-fidelity laser-based gates [Gaebler et al., 2016] and laser-free gates [Harty et al., 2016, Weidt et al., 2016, Zarantonello et al., 2019].

2.4.3 $\hat{\sigma}_z\hat{\sigma}_z$ gates

The $\hat{\sigma}_z\hat{\sigma}_z$ interaction is

$$\hat{H}_g = \hbar\Omega_g\left(\hat{\sigma}_{z1} \pm \hat{\sigma}_{z2}\right)\left(\hat{a}e^{i\Delta t} + \hat{a}^\dagger e^{-i\Delta t}\right). \tag{2.40}$$

The physical basis of this force is the gradient of an oscillating energy shift at the ion, for laser-based gates from the gradient of a spin-dependent ac Stark shift [Leibfried et al., 2003]. This technique has been used to demonstrate high-fidelity gates such as Ref. [Ballance et al., 2016, Schäfer et al., 2018]. There has also been a laser-free demonstration of this interaction using static magnetic field gradients [Khromova et al., 2012]. This interaction is the basis for the entangling gates in Chapter 6.

One disadvantage of the $\hat{\sigma}_z\hat{\sigma}_z$ interaction is that states that have a spin-dependent oscillating ac Stark shift are typically static magnetic field-sensitive as well, in contrast with the MS gates that work with any qubit states. However, there has been a recent demonstration that used an auxiliary

state to generate this interaction on a field-insensitive qubit [Baldwin et al., 2020a]. In contrast to MS gates however, only two laser beams are required with a difference frequency close to the motion at MHz frequencies. For MS gates using Raman transitions, two pairs of laser beams are required, one for each sideband, each with a difference frequency close to the qubit at GHz frequencies. The use of ac Stark shifts also enables the generation of a spin-dependent force on qubits of a different species using the same pair of beams [Ballance et al., 2015, Hughes et al., 2020].

2.5 Phase gate errors and suppression

With an understanding of how phase gates work, we discuss the different error mechanisms in phase gates, with a focus on the motional errors as those cause the dominant errors in the gates we later demonstrate.

2.5.1 Motional errors

While the ions' spin is ideally disentangled from the motion at the end of the gate, the spins are entangled with the motion during their trajectories. Thus, any error due to the motion would affect the gate as well. We can broadly divide these errors into incoherent and coherent errors. Incoherent errors include heating or motional dephasing, while coherent errors include fixed detuning and gate duration errors. Following Ref. [Sepiol, 2016], we model incoherent errors using a Lindblad master equation

$$\dot{\rho} = -\frac{i}{\hbar}[\hat{H}, \rho] + \frac{1}{2}\sum_k \left(2\hat{C}_k\rho\hat{C}_k^\dagger - (\rho\hat{C}_k^\dagger\hat{C}_k + \hat{C}_k^\dagger\hat{C}_k\rho)\right), \tag{2.41}$$

where $\hat{C}_k = \sqrt{\gamma}_n\hat{A}_k$ is the collapse operator. The rate of decoherence is γ_k and $\hat{A}_k$ is the operator that governs the decoherence mechanism and is typically either Pauli spin, or creation and annihilation operators. Here, we have used the notation in QuTiP [Johansson et al., 2013], which we use later to model these errors. For our simulations, $\hat{H}$ will correspond to the gate interaction.

2.5.1.1 Heating

Heating refers to incoherent heating of the ion motion from for example, coupling to a thermal bath. This heating causes an increase in the ions' motional state occupation as a function of time [Brownnutt et al., 2015], characterized by $\dot{\bar{n}}$, where $\bar{n}$ is the average motional occupancy. Following Ref. [Harty et al., 2014], the master equation for this process is,

$$\dot{\rho} = -\frac{i}{\hbar}[\hat{H}, \rho] + \frac{\dot{\bar{n}}}{2}\left(2\hat{a}^\dagger\rho\hat{a} - (\rho\hat{a}\hat{a}^\dagger + \hat{a}\hat{a}^\dagger\rho) + 2\hat{a}\rho\hat{a}^\dagger - (\rho\hat{a}^\dagger\hat{a} + \hat{a}^\dagger\hat{a}\rho),\right) \tag{2.42}$$

which corresponds to Eq. 2.41 with two collapse operators: $\sqrt{\dot{\bar{n}}}\hat{a}^\dagger$ and $\sqrt{\dot{\bar{n}}}\hat{a}$.

2.5.1.2 Motional dephasing

Fast frequency fluctuations in the ion motion [Harty, 2013] can cause dephasing, but not necessarily heating. For the axial mode, this could result from fluctuations in the dc voltages that provide the axial confinement. Amplitude fluctuations in the trapping rf voltage will cause the same effect for the radial modes. This dephasing can be measured by a Ramsey experiment on the motional states. For a Fock state superposition $\frac{1}{\sqrt{2}}(|n\rangle + |n + \Delta n\rangle)$, the Ramsey contrast decays with time constant $(\Delta n)^2\tau_c$. Using this definition, the master equation is

$$\dot{\rho} = -\frac{i}{\hbar}[\hat{H}, \rho] + \frac{1}{\tau_c}\left(2\hat{a}^\dagger\hat{a}\rho\hat{a}^\dagger\hat{a} - (\rho(\hat{a}^\dagger\hat{a})^2 + (\hat{a}^\dagger\hat{a})^2\rho)\right), \tag{2.43}$$

which corresponds to Eq. 2.41 with a single collapse operator $\sqrt{(2/\tau_c)}\hat{a}^\dagger\hat{a}$ in Eq. 2.41.

2.5.1.3 Detuning errors

Detuning errors refer to miscalibrations or changes of the motional frequency which result in an error in the gate detuning Δ. This error will result in incomplete loop closure and residual spin-motion entanglement that will reduce the gate fidelity. We require all of the motional wave functions of the different spin states to overlap at the end of the gate sequence; if there is no overlap

there is no interference between the spin states that gives rise to entanglement. An example of a detuning error is shown in Fig. 2.4a).

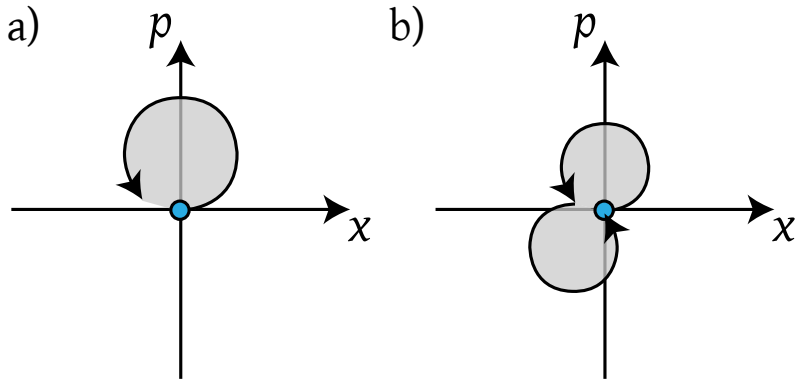

Figure 2.4: Detuning errors and Walsh sequences for the mode of motion used in the gate. a) A detuning error results in an incomplete loop closure for one or more of the spin states. b) This error can be mitigated by a two-loop sequence, flipping the sign of the spin-dependent force in between the loops. This results in a trajectory that ends closer to the starting point. This sequence corresponds to Walsh 1 modulation.

2.5.2 Reducing motional errors: multi-loop sequences

An effective method of reducing motional errors is to employ multi-loop sequences[6] . As pointed out in Ref. [Hayes et al., 2012], changing the sign of the spin-dependent force during a gate sequence, or Walsh modulation, reduces the effect of detuning errors as shown in Fig. 2.4b). A Walsh 1 sequence corresponds to one phase change, Walsh 3 to two, and Walsh 7 to five. Walsh 1, 3, and 7 sequences also have a minimum of 2, 4, and 8 loops respectively.

We perform a simulation in QuTiP to investigate the effect of Walsh modulation on static detuning errors as shown in Fig. 2.5. For static errors, using Walsh 1 modulation reduces the infidelity by about an order of magnitude. Higher Walsh sequences reduce this error further but less significantly. Note that higher Walsh sequences might help for time-varying detuning errors.

Multi-loop sequences can also reduce the effects of incoherent motional errors. We plot a simulation with both heating and dephasing in Fig. 2.6. We model both errors following Eq. 2.42 and

[6] Unlike humans on a roller coaster, ions have less motion sickness the more loops they do.

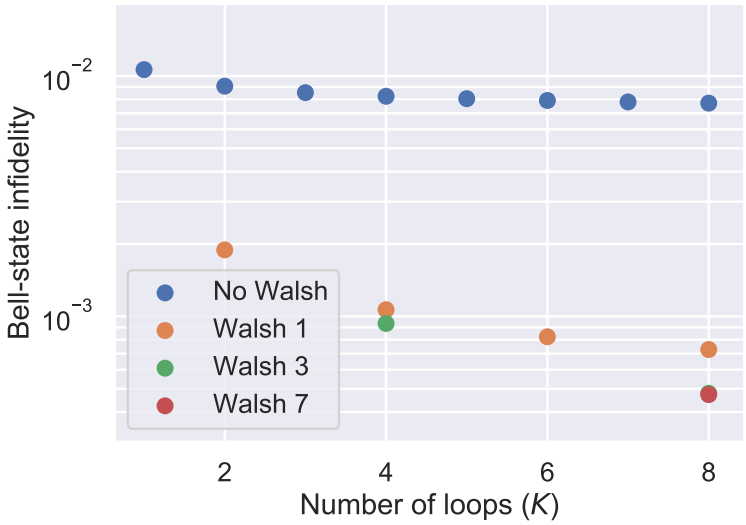

Figure 2.5: Simulation of detuning errors with Walsh modulation. Using a gate Rabi frequency of $\Omega_g/2\pi = 1.25\,\text{kHz}$, we simulate a detuning error of 200 Hz. We plot the Bell-state fidelity versus the number of loops for different Walsh sequences: no Walsh (1-8 loops), Walsh 1 (2, 4, 6, 8 loops), Walsh 3 (4, 8 loops), Walsh 7 (8 loops). Using Walsh 1 modulation as opposed to no Walsh modulation reduces the error by an order of magnitude. Using higher Walsh modulation and increasing the number of loops reduces the error further, but less significantly. For all simulations, we use $\Omega_g/2\pi = 1.25\,\text{kHz}$ and adjust the gate duration and detuning according to the number of loops (see equations 2.35 and 2.36).

Eq. 2.43 respectively. We find that increasing the number of loops reduces the infidelity, independent of the Walsh modulation. The reduction in this error also roughly follows $1/\sqrt{K}$ scaling. Purely geometrically, these errors would be larger the larger the ions' excursion in phase space. The phase space trajectory has a radius that is proportional to $1/\sqrt{K}$; the more loops there are, the smaller each loop has to be to acquire the same geometric phase.

2.5.2.1 Temperature dependence of motional errors

While geometric phase gates are nominally insensitive to the initial temperature of the mode, higher temperatures make the gate more sensitive to other errors. We only expand Eq. 2.25 to first order with respect to the Lamb-Dicke parameter η. Higher order terms in the gradient expansion (for example $\hat{a}^2$) will add error terms that scale more quickly with $\bar{n}$.

We plot the temperature dependence of the gate fidelity versus the average motional occupation

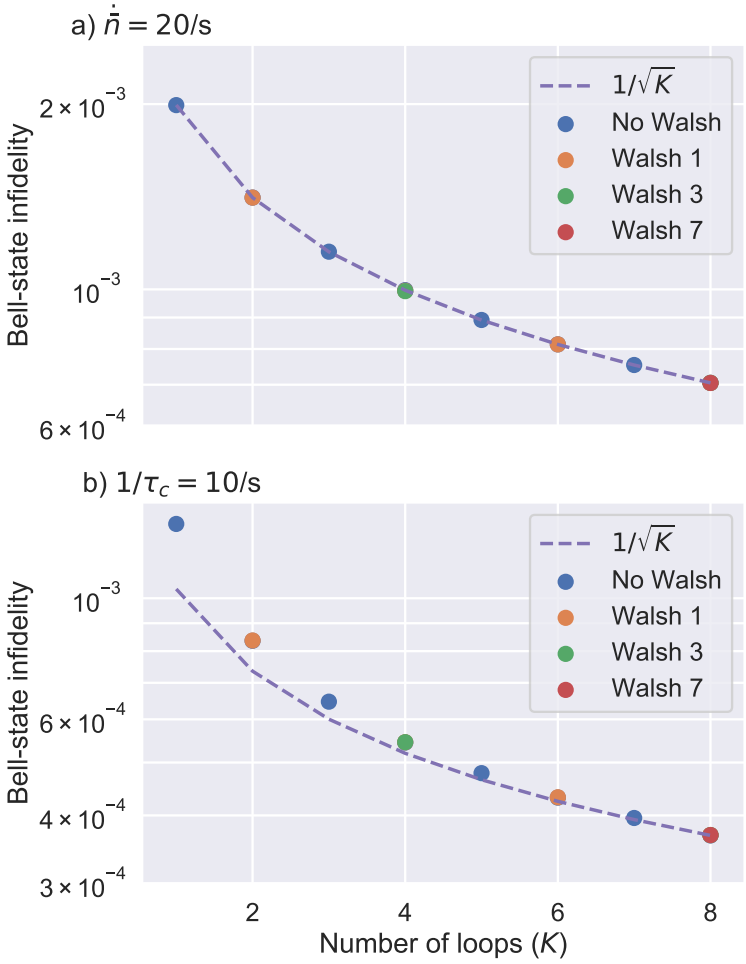

Figure 2.6: Simulations of multi-loop sequences for two types of incoherent motional errors: a) heating rate $\dot{\bar{n}} = 20/s$, b) motional dephasing with $1/\tau_c = 10/s$. For each error, we plot the Bell-state fidelity versus the number of loops for different Walsh sequences: no Walsh (1-8 loops), Walsh 1 (2, 4, 6, 8 loops), Walsh 3 (4, 8 loops), Walsh 7 (8 loops). For all simulations, we use $\Omega_g/2\pi = 1.25\,\text{kHz}$ and adjust the gate duration and detuning according to the number of loops (see equations 2.35 and 2.36). For both errors, we find that increasing the number of loops reduces the error. We find no effect from the Walsh modulation. We additional plot a dashed line showing $1/\sqrt{K}$ scaling for each of the infidelities.

number in Fig. 2.7. For the gate sequence without Walsh modulation, the error increases by almost an order of magnitude going from an $\bar{n}$ of 0 to 4. Walsh modulation significantly reduces this temperature dependence. A more detailed analysis of the sensitivity of different errors to temperature for a Walsh 7 sequence is shown in Fig. 6.4.4. Note that this temperature dependence is more problematic for laser-based interactions.

Figure 2.7: Simulations of Bell-state infidelity for a fixed detuning error versus temperature for different Walsh sequences. The detuning error is 200 Hz, with $\Omega_g/2\pi = 1.25$ kHz for all gates. Walsh modulation significantly reduces the temperature dependence of this error.

2.5.3 Qubit errors

Aside from motional errors, there are also qubit errors that will affect the gate fidelity.

2.5.3.1 Photon scattering

The highest-fidelity entangling gates are the laser-based gates reported in Ref. [Gaebler et al., 2016] and Ref. [Ballance et al., 2016], with fidelities of 0.9992(4) and 0.999(1) respectively. They had photon scattering errors of 5.7×10^{-4} and 4×10^{-4} respectively. This photon scattering comprises both Raman and Rayleigh scattering. Raman scattering is inelastic, destroying the coherence of the qubit, as opposed to Rayleigh scattering which is elastic [Ozeri et al., 2007]. Raman scattering can be reduced by increasing the detuning of the Raman transition further, but at the cost of increasing laser power to maintain the same gate Rabi frequency. Rayleigh scattering on the other hand approaches an asymptotic value.

2.5.3.2 Qubit decoherence

Lastly, the qubit can also suffer from decoherence during the gate sequence. This effect is particularly problematic for field-sensitive qubits. Any changes in the magnetic field can cause shifts in the energy levels of the qubit during the gate. Fortunately for $\hat{\sigma}_z\hat{\sigma}_z$ gates, qubit frequency shifts commute with the gate and can be echoed out.

For MS gates on the other hand, this error does not commute. Even though they can be performed on field sensitive qubits, fluctuations in ac Zeeman or ac Stark shifts can still cause qubit decoherence. This decoherence can be mitigated by an additional dynamical decoupling [Harty et al., 2016]. We discuss dynamical decoupling in more detail in Sec. 6.1.1.

2.5.4 Gate duration errors

Gate duration errors are closely related to detuning errors; they can both cause incomplete closure of the phase-space loop, but gate duration errors can further cause the wrong geometric phase to be acquired. These errors are also mitigated by the Walsh modulation discussed in Sec. 2.5.2. For a fixed gate duration error of 5% we plot the gate infidelity versus detuning in Fig. 2.8. Higher-order Walsh sequences reduce the sensitivity to gate duration errors.

2.6 Non-classical states of motion

While the focus of this chapter has been on spin-motion coupling to generate entanglement between ion spin states via the motion, the ion motional states are also active areas of research in themselves. Non-classical states of motion such as squeezed states [Meekhof et al., 1996, Kienzler et al., 2015, Burd et al., 2019], and Fock-state superpositions [Leibfried et al., 2002, McCormick et al., 2019] have been generated. The motional states of trapped ions can also be used as a qubit in the context of continuous variable quantum computation [Flühmann et al., 2019].

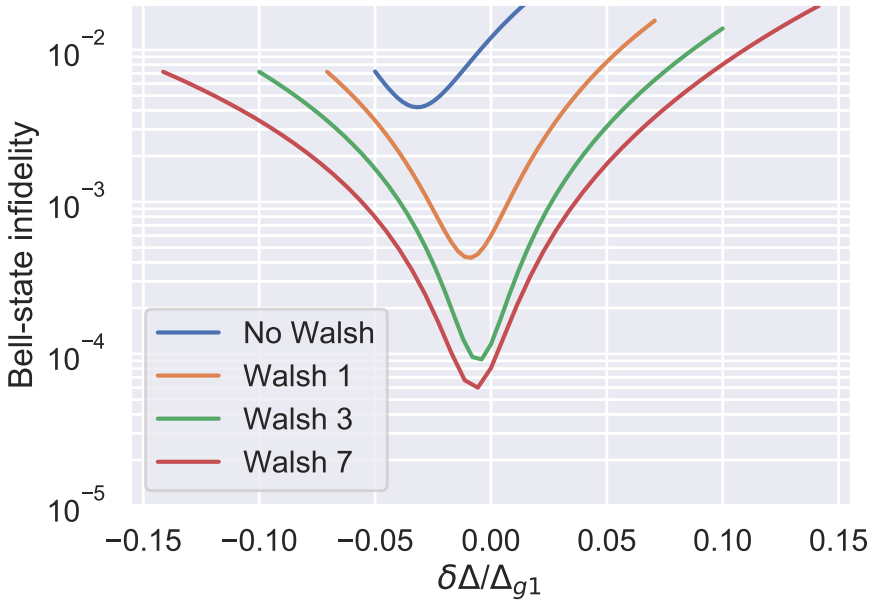

Figure 2.8: Simulations of gate duration errors with Walsh modulation. We have a fixed 5% gate duration error for the different gate sequences, and plot the fidelity versus detuning $(\Delta + \delta\Delta)$, normalized to the one loop detuning Δ_{g1}.

I don't need no money, fortune, or fame (ooh hey hey hey)

I've got all the riches baby one man can claim (oh yes I do)

I guess you'd say

What can make me feel this way?

My girl (my girl, my girl)

Talkin' 'bout my girl (my girl)

The Temptations

3

Apparatus

An experimental thesis would not exist without an apparatus. In this chapter, we discuss key features that enable the experiments described subsequently. The trap fabrication and vacuum assembly was done by Daniel Slichter and David Allcock, while Robert Jördens set up many of the beamlines used in the experiment. Shaun Burd developed a new laser system using vertical external-cavity surface-emitting lasers (VECSELs) that initially were used only for sideband cooling, but were later used for Doppler cooling and detection as well [Burd et al., 2016]. Though this apparatus was redesigned and rebuilt from the ground up in a new lab, it is very much the second generation of the apparatus used in Ref. [Ospelkaus et al., 2008] and Ref. [Warring et al., 2013a], which contain many technical details relevant to this setup.

3.1 Surface electrode trap

At the heart of this apparatus is the surface electrode trap for near-field magnetic-field gradients, or the "magtrap" as shown in Fig. 3.1. This trap was fabricated at the NIST clean room by Daniel Slichter and David Allcock. The trap has a c-cut sapphire substrate and the electrodes

are electroplated gold, with a thickness of 8 μm. A thermal epoxy[1] is used to attach it a pedestal underneath. Ribbon bonds are used to connect the trap to an alumina printed circuit board.

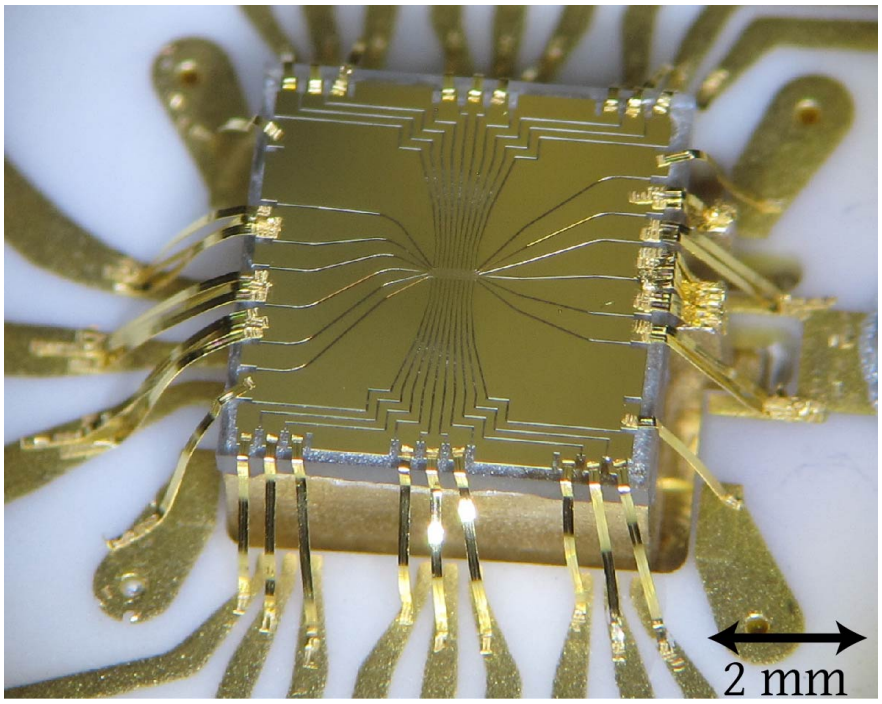

Figure 3.1: Photograph of the "magtrap", the surface electrode trap[2]used in this thesis. The trap is electroplated gold on a sapphire substrate. A thermal epoxy is used to attach it a pedestal underneath. Ribbon bonds connect it to an alumina printed circuit board.

To more clearly see the electrode structure, we display a false color image from a scanning electron microscope (SEM) in Fig. 3.2. Conceptually, it is identical to the trap described in Sec. 2.1, but with all the electrodes in a single plane. The red electrodes are used for the oscillating rf voltage needed to generate a trapping potential. They are connected to the rf resonator on one end and open on the other. We can also apply a dc bias voltage to these electrodes to tilt the ion modes in the radial (y-z) plane. We have 9 pairs of dc electrodes along the trap axis (x) that provide the axial confinement. These electrodes are also used to apply potentials (see Sec. 4.4.1) to compensate for stray electric fields. Additionally, changing the voltages applied to these electrodes enables transport of the ions along the trap axis. As discussed in Sec. 4.9, most of the experiments in this

[1] EPO-TEK H21D.
[2] Even Admiral Ackbar would agree.

thesis were conducted where the ions are loaded as shown in Fig. 3.2.

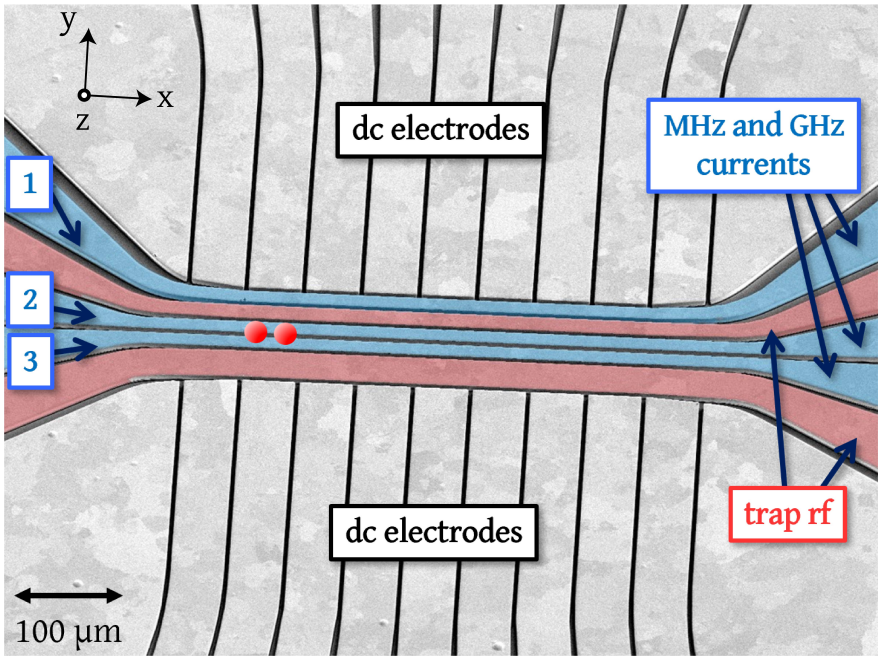

Figure 3.2: False color SEM image of the "magtrap". We apply rf voltages to the red electrodes to generate the trapping potential. Nine pairs of dc electrodes provide confinement along the trap axis (x). The MHz and GHz currents used to the generate the magnetic fields and magnetic field gradients are applied to the electrodes in blue, here labeled 1, 2, and 3.

The most important electrodes for the physics in this thesis are shown in blue. We apply large MHz and GHz currents ($\sim$ 1 A rms) to these electrodes in order to generate magnetic fields and magnetic field gradients. These electrodes are shorted to ground at one end of the chip. By design, the magnetic field gradients are only along the radial (y-z) plane. We have three electrodes for these currents, as did Ref. [Ospelkaus et al., 2011] and Ref. [Allcock et al., 2013], to null the magnetic field at the ion. By adjusting the phase and amplitudes of the currents applied to all three electrodes, we are able to null the magnetic field at the ion while keeping a magnetic field gradient (see Fig. 3.3). At least for the spin-motion coupling scheme described in Sec. 2.3.5, it is advantageous to null the magnetic field while keeping the gradient. Nulling the magnetic field eliminates off-resonant transitions as well as fluctuations in the ac Zeeman shift, improving gate fidelities. Alternative trap structures can be designed to null the magnetic field using only one

electrode such as in Ref. [Hahn et al., 2019]. However, one disadvantage is that it can be challenging to align the rf null to the null of the magnetic field. In contrast, having three electrodes ensures that there are always enough degrees of freedom to null the magnetic field at the ion.

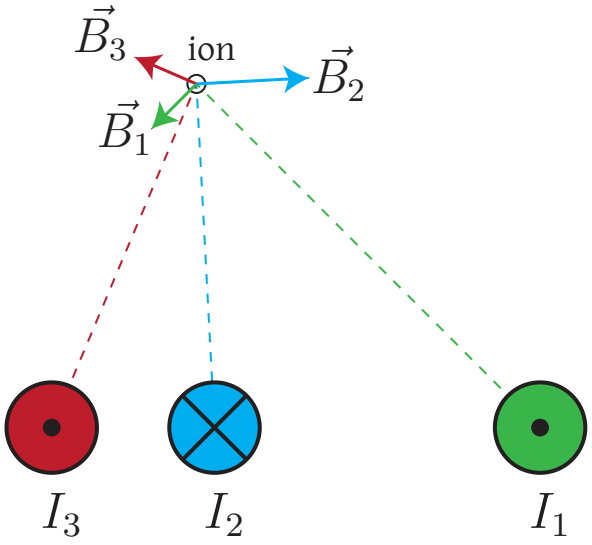

Figure 3.3: Schematic of nulling the magnetic field at the ion. If the current in electrode 2 is π out of phase, and the relative amplitudes adjusted, the magnetic field at the ion is nulled ($\vec{B}_1 + \vec{B}_2 + \vec{B}_3 = 0$). Crucially, the sum of the gradients is not zero ($\vec{\nabla}B_1 + \vec{\nabla}B_2 + \vec{\nabla}B_3 \neq 0$). The direction of the magnetic field gradient from each electrode is along their respective dotted lines.

One consideration for our electrode geometry is the choice of qubit. The magnetic fields that we generate will mostly be linearly polarized. Thus, using a qubit whose transition is only driven by σ^+ polarization results in only using at most half of the linear polarization generated (one must also factor in the direction of the quantization axis). Our apparatus was originally designed to use a "clock" qubit whose transition is driven by a π-polarized magnetic field. This qubit is discussed in more detail in Sec. 4.3. Of course, the experiments we ended up performing took a slight detour from this plan[3] .

[3] Electrodes 1-3 were grounded intentionally to give us the flexibility to pursue different types of gradients.

3.2 Vacuum system

Figure 3.4 shows the gold-plated copper pillbox encasing the trap. The trap as well as the alumina PCB are mounted in this pillbox, which is attached to the base flange of our vacuum system. Our MHz and GHz currents are applied to electrodes 1, 2, and 3 in Fig. 3.2 via the SMA ports and cables shown in Fig. 3.4b) and c) respectively. A copper braid provides the thermal link to the flow cryostat. There are additional resistors and capacitors not indicated on the PCB that provide in-vacuum filtering.

We show the assembled vacuum system on the optical table in Fig. 3.5. The vacuum system itself is obscured by other components, such as as the four argon ion guns attached to the top flange. The guns were intended for *in situ* ion milling, which has been shown to reduce trap heating rates by two orders of magnitude at room temperature [Hite et al., 2012, Daniilidis et al., 2014]. However, more recent results from Ref. [Sedlacek et al., 2018] suggest that ion milling might in fact make heating rates **worse** at cryogenic temperatures. Thus, as we had a fortunately low heating rate to begin with, and ion milling carries the risk of creating electrical shorts between electrodes, we have eschewed ion milling thus far; we have these argon ion guns but have not dared to use them[4] . The other components shown in Fig. 3.5 include the flow cryostat and helium recovery line, the high field coils, the camera, and imaging system which we discuss in subsequent sections.

3.3 Cryogenic operation

Cryogenic operation offers a number of advantages for ion trapping. First, heating rates are typically orders of magnitudes lower [Deslauriers et al., 2006, Chiaverini and Sage, 2014, Brownnutt et al., 2015, Sedlacek et al., 2018]. Second, condensation of residual gasses (cryopumping) in our vacuum system significantly reduces the pressure, increasing the ion lifetime. At room temperature, we have a pressure of $\approx 2\times10^{-10}$ Torr and a single ion lifetime of about 3 min. Operating at closer to 15 K, the pressure drops to below 5×10^{-11} Torr, and our single ion life time is more than 8 hours.

[4] Not Chekhov's argon ion guns. One of the guns is also shorted.

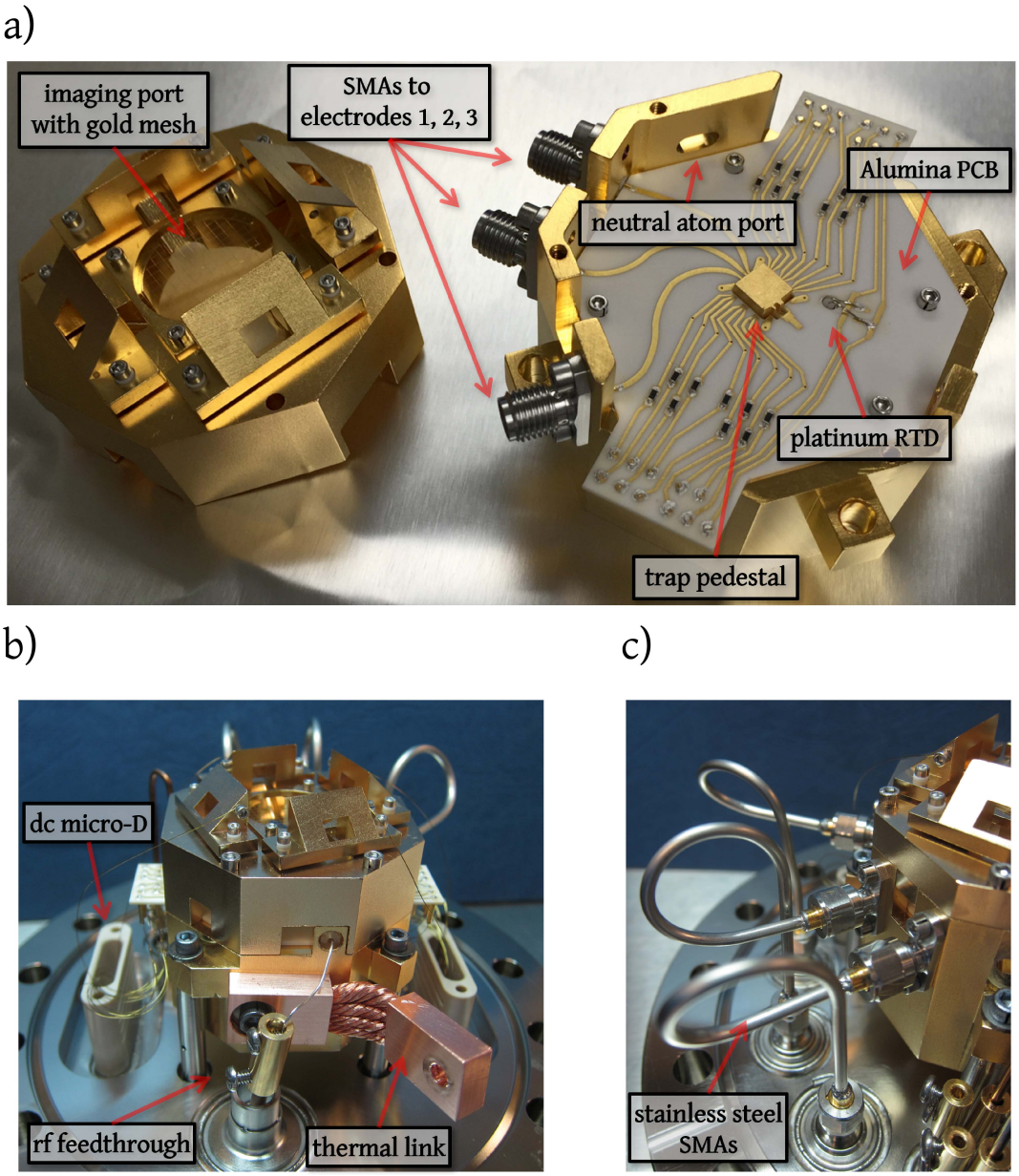

Figure 3.4: a) Pillbox disassembled. On the left we have the lid that has the imaging port with a gold mesh. On the right, we have the trap pedestal and alumina PCB. The alumina PCB has resistors and capacitors for filtering not shown. The high power MHz and GHz currents come in via SMA ports that are connected to electrodes 1, 2, and 3 in Fig. 3.2. We have an on-chip platinum resistance temperature detector (RTD) to measure the temperature close to the trap. The atomic flux from the magnesium oven comes through the neutral atom port. b) and c) show the assembled pillbox attached to the base flange. b) Our connections to the dc electrodes come in via micro-d connectors. Also shown are the rf feedthrough and the copper braid that provides the thermal link to the flow cryostat. c) We indicate the stainless steel SMA cables used for MHz and GHz currents applied to electrodes 1, 2, and 3.

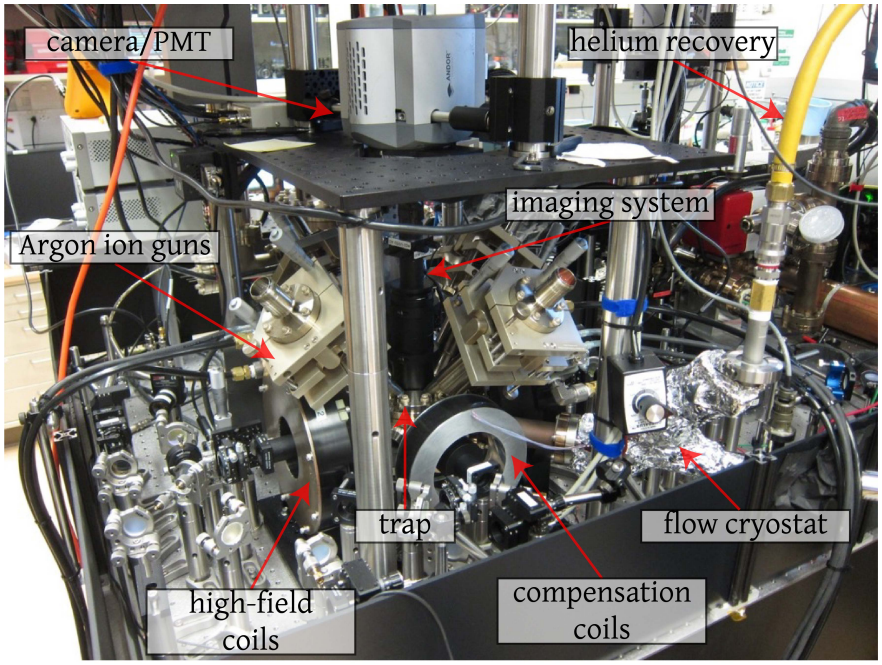

Figure 3.5: Vacuum system on optical table. The trap, within its vacuum system, is at the center of this image. Its top flange has four argon ion guns for *in situ* ion milling. We have large high-field coils for generating our quantization magnetic field, and smaller compensation coils to compensate for stray fields as well as fine adjustment of the magnetic field. An additional compensation coil underneath the vacuum system is not shown. We point out the imaging system, camera, and photomultiplier tube (PMT) used to collect and count photons from the ions. Lastly, we also show the flow cryostat and helium recovery line used for cryogenic operation.

Our two ion lifetime becomes ~ 1 hour, making the entangling gate experiments in later chapters feasible.

The key components of our cryogenic operation are shown in Fig. 3.6 including the Janis ST-400 flow cryostat. When running experiments, we use liquid helium to cool the trap to $\approx 15\,\mathrm{K}$. Helium flows to the trap via a transfer line from a connected dewar ($\approx 80\,\mathrm{L}$) at a pressure of about 10 psi. This pressure is reached naturally by inserting the transfer line into the dewar. A secondary valve ensures that excess pressure is released into the recovery line rather than into the lab. At this temperature, we consume $\approx$ 1 L per hour. When not running experiments, we usually warm up to about 50 K to reduce the helium consumption to $\approx 0.3\,\mathrm{L}$ per hour. We usually consume about

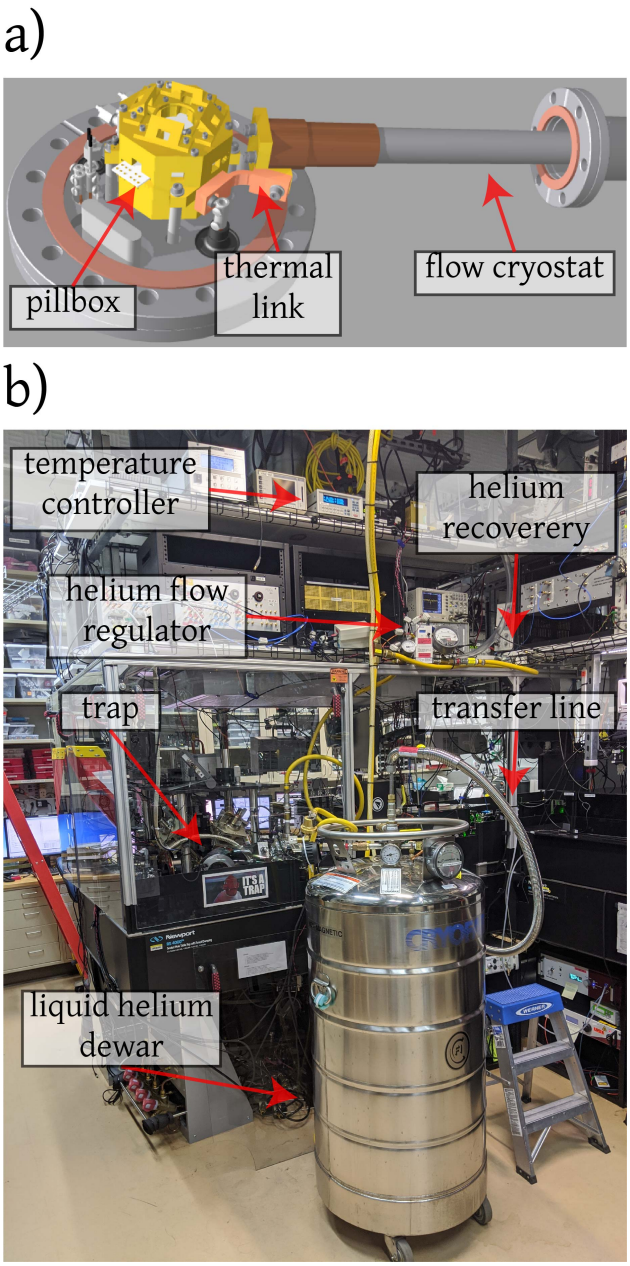

Figure 3.6: Cryogenic operation. a) The flow cryostat makes thermal contact with the copper pillbox via a thermal link. b) Helium dewar connected to the trap. Liquid helium flows via a transfer line to the trap. Warm helium gas goes into the yellow recovery line into the larger NIST helium recovery system. We have a flow regulator for the helium gas flow, controlling the temperature of the trap. A temperature controller enables monitoring of the temperature both at the flow cryostat and at the trap.

100-150 L per week[5] . Approximately 90% of this helium is recovered at NIST[6] . Cycling between

[5] Liquid helium costs more than a graduate student.
[6] In some sense, we have a very large closed-cycle system.

50 K and 15 K, our trap position is maintained within a few μm and our laser beams typically need minimal realignment.

When not running experiments, for example during a global pandemic[7] , we switch over to liquid nitrogen instead. We maintain our trap temperature at about 80 K, consuming approximately 3 L of liquid nitrogen per day. We use liquid nitrogen to minimize costs. We refrain from warming up to room temperature to avoid thermal expansions or contractions of various in-vacuum components.

3.4 High-field coils

For our experiments, we require a fairly large static magnetic field of 212.8 G (see Sec. 4.3) at the trap. We use foil-wound copper coils from Stangenes Industries as shown in Fig. 3.7. We supply about $\approx$ 60 A, with a voltage drop of about 15 V across the two coils connected in series. At this current, these coils require water cooling to stay close to room temperature. We have an interlock that shuts off our power supply if either the water flow is turned off, or if a temperature sensor on the coils reaches 50°C. We measured the magnetic field along the axis of the coils and it is fairly uniform over a region of about 2 mm. Based on Ref. [Merkel et al., 2019], we actively stabilize the current in our trap and also feedforward on the 60 Hz noise in the power supply[8] . With this magnetic field stabilization, we are able to extend our coherence time (T_2^*) on our field sensitive "stretch" qubit from $\sim 100\,\mu$s to $\sim$ ms.

3.4.1 Compensation coils

Aside from the high field coils, we have smaller compensation coils as shown in Fig. 3.5. These coils help to compensate for stray fields at the ion, as well as offer fine adjustment the magnetic field and thus the beam polarization at the ion (see Sec. 4.2.1.1). These coils have axes orthogonal to the high-field coils. We typically apply a current of 0-2 A to each of the coils, generating magnetic fields of 0-2 G at the ion. At these smaller currents, we have neither current stabilization nor water

[7] Our trap has stayed cold thanks to heroic efforts from ACW.
[8] Mainly done by SCB and DTCA.

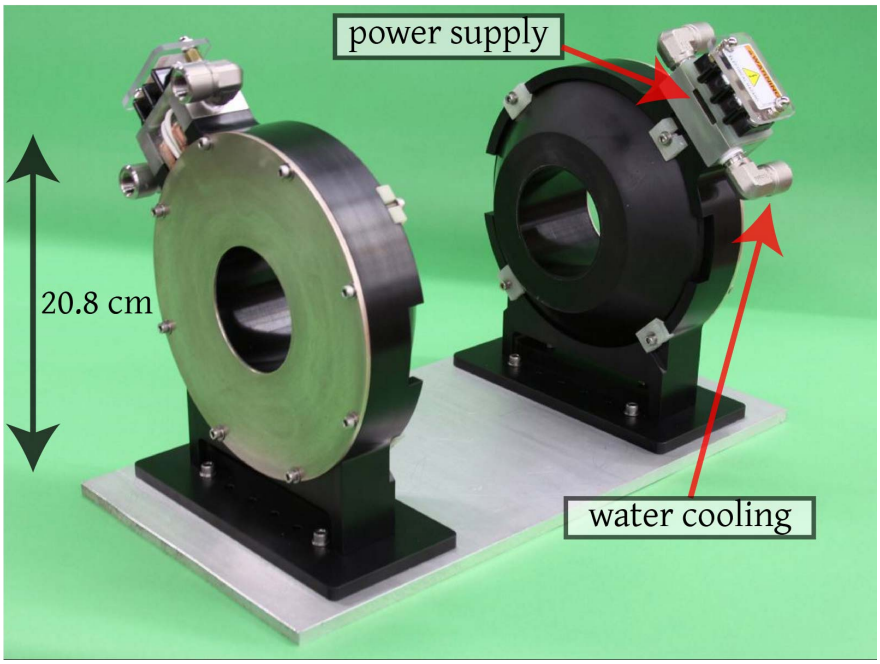

Figure 3.7: Coils to generate magnetic field of 212.8 G. These coils were designed by Stangenes Industries. We indicate where the water cooling and power supply are connected. The height of 20.8 cm refers to the coil diameter.

cooling.

3.5 Laser system

As much as we would like a completely laser-free experiment, we need lasers for photoionization, state preparation (including repumping), and detection. Additionally, we have a pair of Raman beams for sideband cooling. Here, we discuss key details of our laser system. For the rest of this section, we use the following nomenclature[9] for the different laser beams:

(1) Blue doppler (BD) - The laser beam we use for detection close to resonance. We also use it for the final stage of Doppler cooling (≈ 10 MHz red detuned).

(2) Blue doppler detuned (BDD) - Laser beam that is ≈ 370 MHz red detuned from resonance for initialization of the state and preliminary cooling.

[9] Largely historical.

(3) Red doppler (RD) - Laser beam used for repumping (see Fig. 4.1). This beam is $\approx 1302\,\mathrm{MHz}$ red detuned from resonance (but resonant with a different transition, see Fig. 4.1).

(4) Raman beams - The two beams that we use to drive stimulated Raman transitions with σ^+ and π beam polarizations respectively. The two-photon transitions are driven through a virtual state $\sim 50\,\mathrm{GHz}$ blue detuned from the $P_{3/2}$ transition.

On resonance refers to the ${}^2S_{1/2} \leftrightarrow {}^2P_{3/2}$ transition in Fig. 4.1.

3.5.1 Beam orientations

Figure. 3.8 shows the orientation of the beams relative to the trap axis (see Fig. 3.2) and the quantization axis set by the static magnetic field B_0. Our Doppler cooling beams are tilted 22.5° from the y-axis, ensuring cooling of all three motional modes for a single ion. We have two Raman beams, whose net momentum $\Delta\vec{k}$ also has components along all three modes.

3.5.2 BD, BDD, and RD beamlines

We ultimately need UV light at 280 nm for our transitions. However, to generate the BD, BDD, and RD laser beams, we first start in the infrared. For the experiments described in this thesis, the infrared source was first a fiber-laser system[10] that was later replaced by a VECSEL system (see Sec. 3.5.3). From the 1118 nm ($\approx 700\,\mathrm{mW}$) light, we double to the green ($\approx 559\,\mathrm{nm}$) using a periodically poled lithium niobate (PPLN) waveguide[11] for second harmonic generation (SHG). At this point, we have approximately 200 mW of power in the green, $\approx 5\,\mathrm{mW}$ of which we use to lock the laser[12] to an iodine absorption line as an absolute frequency reference. The rest of the green light is sent to a cavity with a BBO (β-BaB_2O_2) crystal for SHG of UV light. This cavity was designed by Christian Ospelkaus based on Ref. [Wilson et al., 2011]. We obtain $\approx 5\,\mathrm{mW}$ of UV light out of the doubler.

[10] Menlo Systems orange one.
[11] NTT electronics.
[12] Mainly done by SCB.

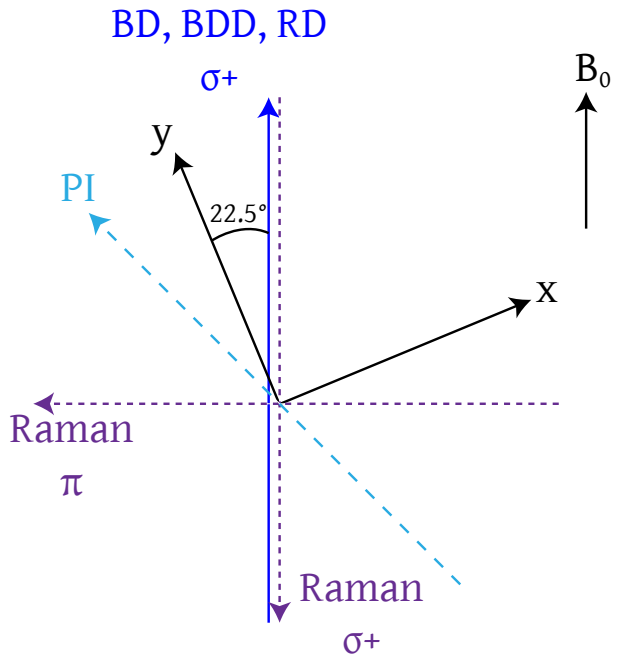

Figure 3.8: Beam orientations. Our BD, BDD, and RD beams (see main text) are all σ^+ polarized, reaching the trap from the same fiber. They are aligned 22.5° to the y-axis in Fig. 3.2, enabling cooling of all three modes of a single ion. We have additional Raman beams with π and σ^+ polarizations that we use for resolved sideband cooling. The static magnetic field B_0 from the high-field coils (Sec. 3.4) defines the quantization axis. We have a photoionization (PI) beam that we use for ionizing neutral magnesium.

This UV light is now used to generate the BD, BDD, and RD beams as shown in Fig. 3.9. This figure is a simplified schematic that does not include all the optical components required. All three laser beams are coupled into the same fiber that takes the light closer to the trap. We use a solarization-resistant, hydrogen-cured fiber as described in Ref. [Colombe et al., 2014]. We typically get $\sim 10\,\mu$W of UV at the trap. We stabilize the intensity of the BD laser beam for detection by picking off part of the light and using a digital servo [Leibrandt and Heidecker, 2015]. The beam waist ($1/e^2$ intensity) for these lasers is $\approx 14\,\mu$m.

3.5.3 VECSEL system for Raman beams

We use a vertical external-cavity surface-emitting laser (VECSEL) system for our Raman beams as described in Ref. [Burd et al., 2016]. This system was designed and built by Shaun Burd.

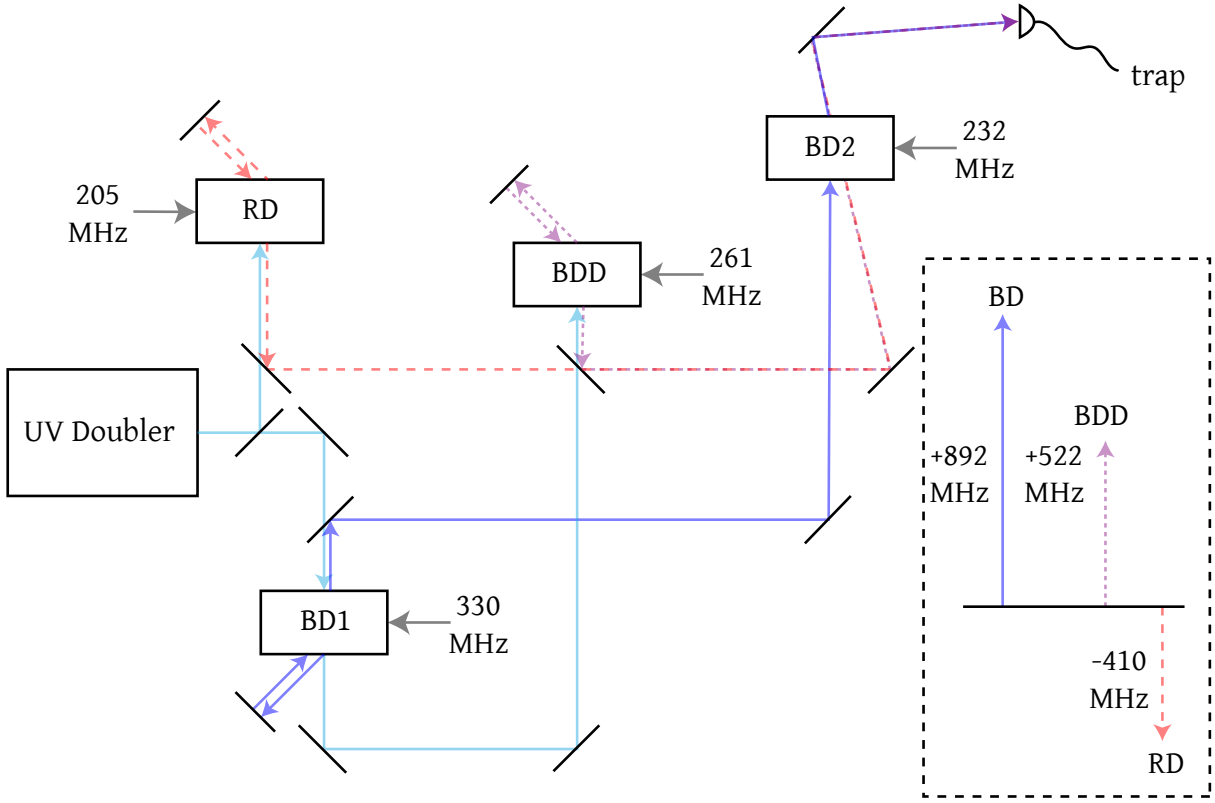

Figure 3.9: Beamlines for blue doppler (BD), blue doppler detuned (BDD), and red doppler (RD) laser beams. The BD beam goes does double pass through the BD1 acousto optic modulator (AOM) ($2 \times 330\,\text{MHz}$ shift) and then a single pass at the BD2 (232 MHz shift) AOM. The BDD only goes through a double pass at the BDD AOM (2×261 MHz shift). Lastly, the RD goes through one double pass ($-2 \times 205\,\text{MHz}$ shift). Both the RD and BDD beams only go through to the fiber when the BD2 AOM is off. The shifts for each of the three beams are shown in the inset. All three beams go through the same fiber to the trap.

Starting at 1118 nm, we follow a similar process to double the light twice to obtain UV light at $\approx$ 280 nm. However, each of the laser beams shown in Fig. 3.8 used for the π and σ^+ is coupled to separate fibers. Each beam has amplitude stabilization as well.

3.5.4 Photoionization

To generate magnesium ions, we employ a two-photon photoionization process. As described in Ref. [Madsen et al., 2000], two 285 nm photons can ionize neutral magnesium, the first photon driving the $3s^2\,{}^1S_0 \leftrightarrow 3s3p\,{}^1P_1$ transition, and the second exciting an electron out to the continuum.

This light is generated using a Raman-fiber-amplifier-based system[13] that first generates 1140 nm light that is doubled to 570 nm. The green light is then sent to a cavity containing a BBO crystal[14] that generates UV light at 285 nm. The UV light is sent to the trap via a fiber, and we obtain ≈ 1 mW of UV light at the trap, which is more than sufficient for loading. We do not lock the laser frequency, instead monitoring it on a wavemeter, and adjusting it accordingly. In the future, we plan on switching to a VECSEL-based system and using a home-built cavity doubler[15] .

3.6 Trapping rf

We need an oscillating potential to trap ions. Our voltage source is an AnaPico APSIN3000 waveform generator set to 68.579 MHz. We stabilize its amplitude following Ref. [Harty, 2013] before it is amplified and sent to a resonator. We use a $\lambda/2$ resonator made from a Heliax cable designed by Daniel Slichter. This resonator has a quality factor of about 90, enabling amplitudes of ≈ 30 V at the trap rf electrodes shown in Fig. 3.2. We can also couple in DC voltages to tilt the ion radial modes, or apply oscillating potentials to perform parametric modulation of the radial motional frequencies [Burd et al., 2019].

3.7 Ion loading

To load ions, we resistively heat a hollow stainless steel tube filled with neutral magnesium. The tube has an aperture drilled in the sidewall for a flux of neutral magnesium atoms to escape. We run about 5.3 A through this wire for one minute, generating a flux of neutral magnesium atoms. We then pulse the PI on while keeping the oven running, periodically checking the counts on the PMT to see if we have loaded. We continue this until the desired number of ions is loaded. We have observed that running the oven continuously for too long a period inhibits loading. We suspect that when the oven is too warm, residual gases in the vacuum that had been cryopumped start to evaporate, increasing the pressure at the trap.

[13] MPB VRFA-SF series.
[14] LAS GmbH WaveTrain
[15] Someday.

Loading multiple ions can occasionally be challenging. We have found that reducing the axial confinement and/or the radial confinement can help. We reduce the axial confinement by multiplying all the voltages on the dc electrodes by a factor (less than 1, excluding shim voltages to compensate for stray fields). We reduce the radial confinement by changing the frequency of the trap rf voltage [16] , thus moving it off resonance and reducing the voltage amplitude at the trap. We typically move it by $\sim 100\,\mathrm{kHz}$ until ions have been loaded and then change it back to its original frequency.

3.8 Clock distribution

Many devices in our apparatus require a reference signal. We have:

(1) APSIN3000 - Trap rf generator.

(2) PDQ[17] - Arbitrary wave form generator based on Ref. [Bowler et al., 2013]. We use these PDQs to:

   (a) Generate rf currents.

   (b) Generate baseband voltages for IQ modulators for pulse shaping microwaves.

(3) Microwave DDS' - AD9914 direct digital synthesizers (DDS') used for microwave sources.

(4) Crate DDS' - DDS' in experimental control "crate" that control acousto-optic modulator (AOM) frequencies, for example.

(5) Field-programmable gate array (FPGA) that controls our experimental sequences.

It would be desirable if the relative phase between all of these reference signals were stable, as drifts in that relative phase would change the relative phase of the fields at the ions and have physical effects.

[16] This technique can also be used to get rid of excess ions, a procedure we call the Knaack maneuver.
[17] Pretty darn quick.

We stabilize these phases using a 10 MHz signal either from a hydrogen maser[18] or a rubidium frequency standard[19] . A schematic for our phase stabilization is shown in Fig. 3.10. We send the 10 MHz signal to our APSIN3000 that generates our trap rf , as well as to a 100 MHz crystal oscillator[20] . This 100 MHz signal is now sent to the various PDQs, as well as a 24× frequency multiplier[21] . The resulting 2.4 GHz signal is now used to clock both the crate and microwave DDS'. The internal clock of one of the crate DDS' at 100 MHz is used as a reference to our experimental control FPGA. This DDS is also used to synchronize the internal clocks of the microwave DDS'(see Sec. 3.9.1).

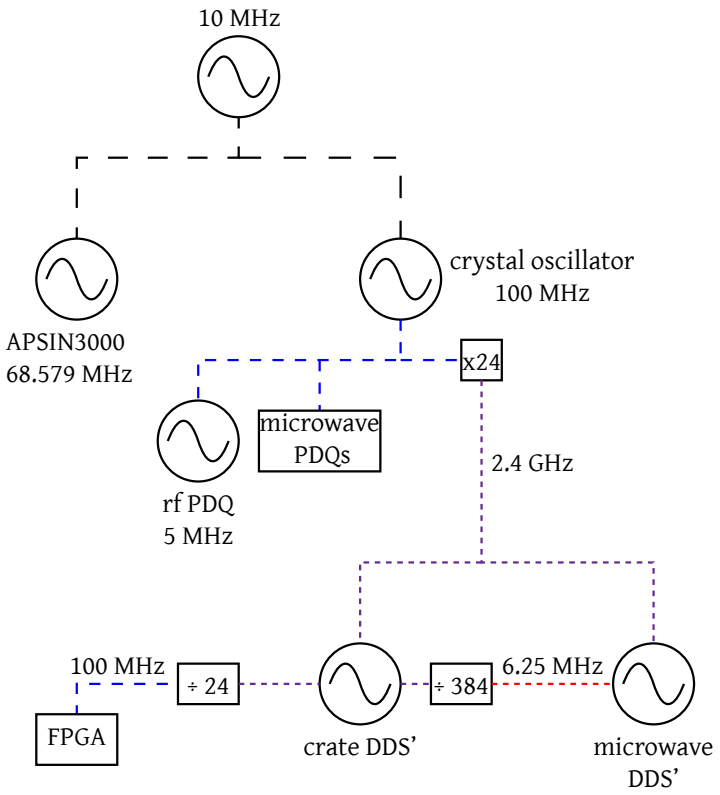

Figure 3.10: Synchronization of devices. Most of the essential devices in the apparatus are synchronised to a 10 MHz signal, see main text for details.

[18] One of the many benefits of working at NIST.
[19] SRS FS 725.
[20] Wenzel 100 MHz-SC.
[21] Wenzel IFM-5R-100-24-13-13.

3.9 Microwave generation

We now describe the generation of the various microwave currents for our experiment. We first explain how the different DDS' are synchronized and then each of the chains[22] for the carrier and sideband drives.

3.9.1 DDS Synchronization

Our microwave sources are AD9914 DDS'. Clocked at 2.4 GHz, we use them to generate microwave tones from 1.3-2.2 GHz for our various transitions. We also use it to generate MHz tones for driving the ion motion or squeezing as shown in Ref. [Burd et al., 2019]. As we use more than one DDS, it is important to sychronize their internal clocks (at 100 MHz) to both each other and the experiment FPGA so all phases are completely deterministic. At every power cycle, the internal clocks of these DDS's are randomly in one of 16 different phases. We synchronize these DDS' following the AN-1254 application note, where we use the "SYNC_OUT" signal at 6.25 MHz[23] from the crate DDS that also references the FPGA (see Fig. 3.10). Figure 3.11 shows the internal clocks of these DDS's before and after the synchronization.

3.9.2 Microwave carrier drive

The microwave components used to generate fields that drive spin-flip transitions are shown in Fig. 3.12. We need to generate tones at 1.3-2.2 GHz; this frequency range is within the second Nyquist zone (using the first Nyquist image) that has a steep power dependence [Analog Devices, 2009]. To minimize the power variation across frequencies, we use a frequency doubler to operate within the first Nyquist zone (using fundamental frequency). Figure 3.12 shows the chain for electrode 1. We have additional switches not shown that let us apply the tone from this chain to electrodes 2 and 3 as well. For electrode 2, we have an additional amplifier that lets us drive faster spin-flip transitions. In contrast, we have an attenuator for electrode 3. This configuration enables

[22] Much of this was put together by DTCA and DHS.
[23] 2.4 GHz/384

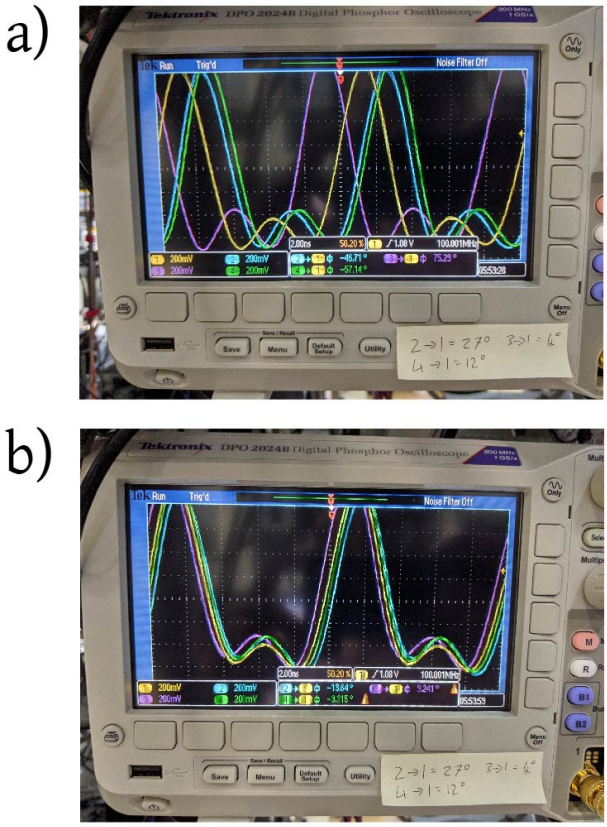

Figure 3.11: DDS synchronization. We synchronize the four DDS' we use for generating our microwave tones to a crate DDS. We monitor their internal clocks at 100 MHz to check their synchronization. a) Their internal clocks are not synchronized and are at one of 16 random phases after a power cycle. b) Their internal clocks are now synchronized.

a wide range of amplitudes to be used within an experimental sequence. We also have additional chains with IQ modulators for electrode 1 that enable pulse shaping of carrier fields used in later chapters.

3.9.3 Microwave sideband drive

The chain for the microwave sideband drive for a single electrode is shown in Fig. 3.13. In contrast to the carrier drive, we only need to generate frequencies within a narrow range of about 10 MHz either side of the "clock" qubit frequency at 1.69 GHz. Thus, we omit the frequency doubler and just operate within the second Nyquist zone (using the first image). We have an IQ modulator

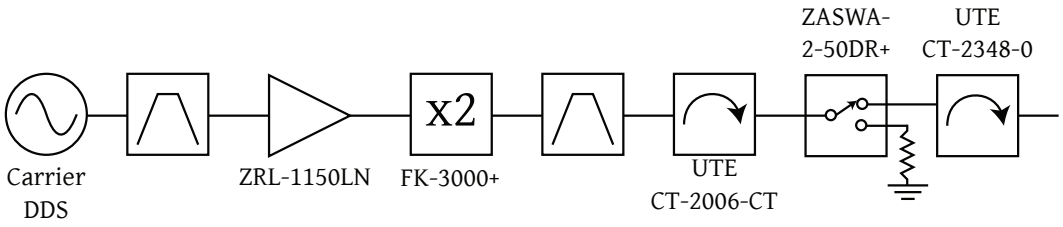

Figure 3.12: Microwave chain for carrier drive, generating microwave fields that drive spin flips at the ion. The unlabeled components are bandpass filters that remove the Nyquist image as well as harmonics from the amplifier and doubler.

that enables pulse shaping, and for adjusting the phase and amplitude of the microwave tone for each electrode. This functionality is essential for the nulling described in Sec. 3.1. The sideband transitions require much more power to drive than the spin flip transitions, hence the higher power amplifier used in this chain.

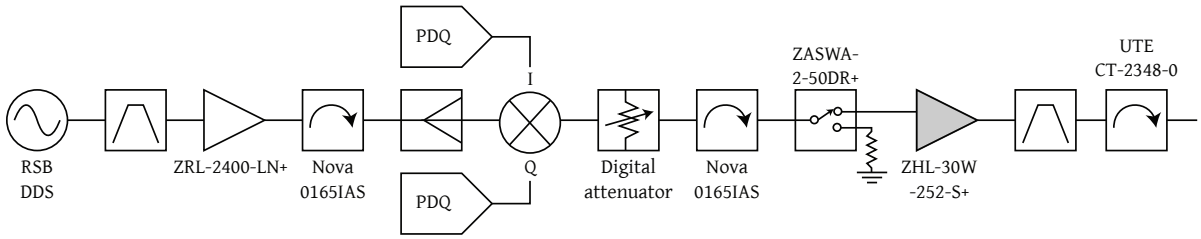

Figure 3.13: Microwave chain for red sideband drive for a single electrode, generating microwave gradients that drive sideband transitions. The unlabeled components are bandpass filters that remove the Nyquist image as well as a narrowband cavity filter after the higher power ZHL-30W-252-S+ amplifier. We have a power splitter (ZC4PD-18-S+) for the chain for the two other electrodes (not shown).

3.9.4 Combining microwave drives

We combine the carrier and sideband drives for each electrode as shown in Fig. 3.14. We use a combination of 3 dB hybrids and directional couplers to combine the different microwave currents for a single electrode.

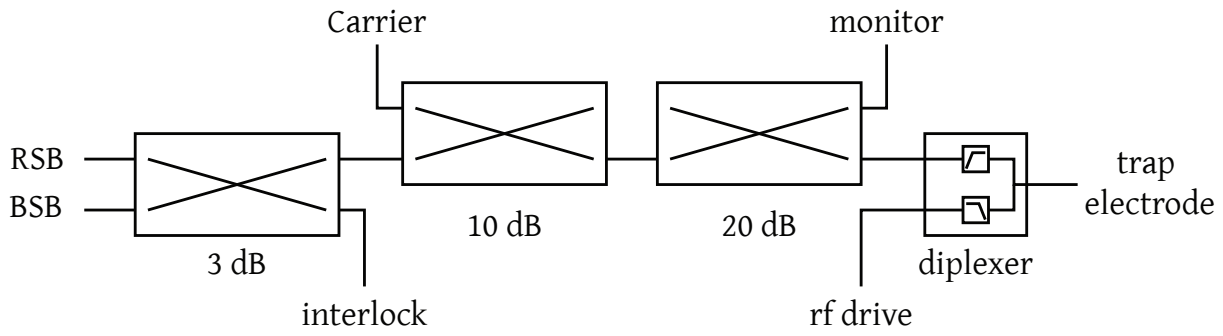

Figure 3.14: Combining carrier and sideband microwave drives. We first use a 3 dB hybrid, then 10 and 20 dB directional couplers. The unused port of the 3 dB hybrid is used is used to monitor the output power and interlock the power amplifiers if the average power delivered to the trap becomes too large.

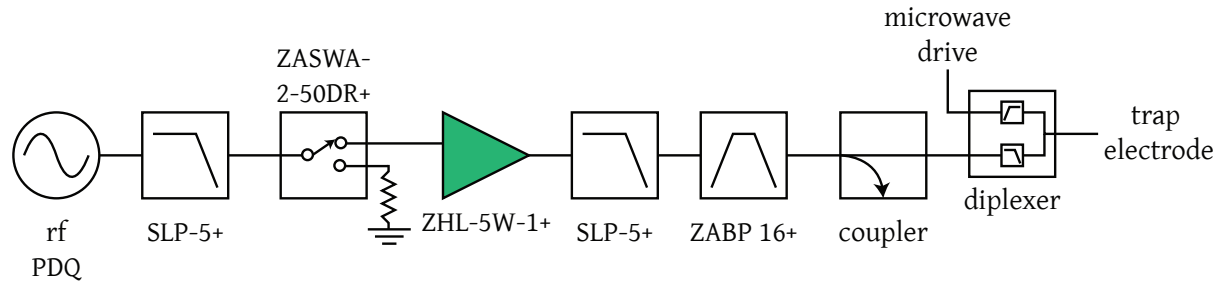

Figure 3.15: Chain to generate high power MHz currents for a single electrode. The coupler enables monitoring of the signals on the scope. The diplexer provides a resonant step up of about 3 in the current for a 5 MHz tone.

3.10 RF generation and delivery

The components required to generate higher power MHz currents for one electrode are shown in Fig. 3.15. We modify one of the PDQs described in Ref. [Bowler et al., 2013] to generate the MHz tones for the radiofrequency gradient. We use a PDQ instead of a DDS as the PDQ very easily allows incorporation of pulse shaping (we need the IQ modulators to do this for the microwave sideband drive). Right before the trap, we use a resonant diplexer[24] that allows a factor of 3 enhancement in the current at the trap electrodes for a 5 MHz tone. Before the diplexer, we have

[24] Designed by DHS.

about 2 W at 5 MHz for each electrode[25] .

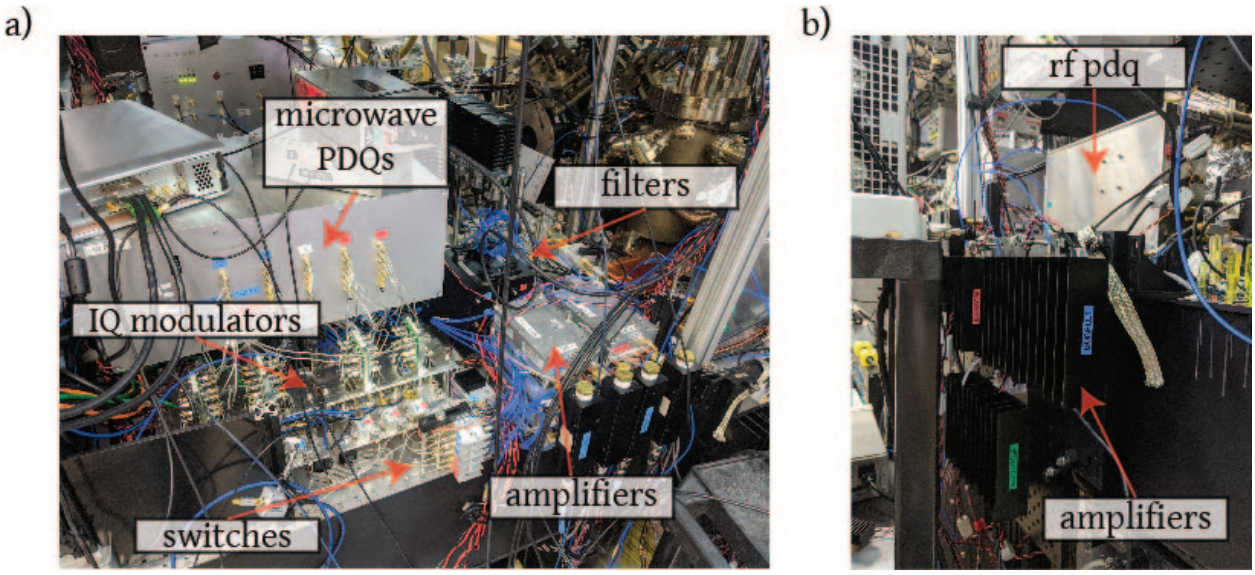

Figure 3.16: Part of microwave and rf setup. a) We show the microwave PDQs, IQ modulators, switches, amplifiers, and filters from Fig. 3.13. b) The rf PDQ and high power amplifiers[26]in Fig. 3.15.

3.11 Imaging

We use custom designed "Slichter optics" for our imaging system, and are able to obtain a magnification of ≈ 44. We are able to collect about 0.5% of the photons on our PMT[27] resulting in about 50 counts per 200 μs detection for a single ion. An image of two ions on the camera[28] is shown in Fig. 3.17.

3.12 Experimental control

If the surface electrode trap is the heart, the FPGA in our control crate[29] is very much the brain. We use a Xilinx Kintex-7 KC705 evaluation board, that is connected to 40 40 digital I/O

[25] HMK has led efforts to increase this to about 5 W.
[26] Blossom, Bubbles, and Buttercup for electrodes 1, 2, and 3 respectively. Originally to be named after Daenerys' dragons but recent events forced a reevaluation.
[27] Hamamatsu R7600P-203. 34% quantum efficiency at 280 nm.
[28] Andor DV887ECS-UVB.
[29] Hardware designed by DHS.

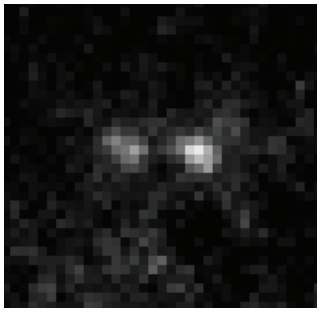

Figure 3.17: Image of two ions on the camera. The ions are approximately 3 μm apart.

(DIO) channels and 12 DDS' via its FPGA mezzanine card (FMC) connectors. We use the DIO channels to trigger rf switches that control our AOMs, and thus the lasers at the ions. We also use rf switches to control which microwave/rf current is pulsed on which electrode. The DIO channels are also used as inputs, such as to record PMT counts. The DDS' in the crate are used primarily to generate the frequencies for the AOMs in our laser beamlines. In addition, we have 4 serial peripheral interface (SPI) channels, which we use for example to program our microwave DDS'.

To program the desired pulse sequences to the FPGA, we use the Advanced Real-Time Infrastructure for Quantum physics (ARTIQ) control system [Bourdeauducq et al., 2016]. Our experiments are Python files that are compiled and sent to the core device, a soft-core CPU on the FPGA, which executes the code. Note that only a subset of Python can be executed on the core device. One big advantage of using Python, aside from its accessibility and readability, is its modularity that easily allows many experiments to share the same code. An important example of this modularity is the drift tracking code used in Sec. 4.7.

For timing, the FPGA has an internal clock at 125 MHz that we bypass using the 100 MHz clock from one of the DDS' (see Fig. 3.10). The timing resolution is $1/8^{\text{th}}$ the clock period which in our case is 1.25 ns. It is important to be aware of this subdivision, as when using other devices such as the rf PDQs or DDS' whose timing resolution is 10 ns (100 MHz clock), we need to ensure that experiments start at the same subdivision for every repetition of the experiment so other devices have the same phase every time.

Every breath you take and every move you make,

Every bond you break, every step you take,

I'll be watching you

The Police

4

Qubit control

In this chapter we introduce the main protagonist[1] of this thesis, $^{25}Mg^{+}$. We describe its energy levels at our operating static magnetic field of 212.8 G that produces a field-independent "clock" qubit, its microwave transitions, and our qubit preparation and readout sequences. We discuss the various calibrations that we perform, including compensating for stray fields that push the ion off the rf null. We also describe how we couple the ion to its motion, using microwave gradients as well as laser-based interactions, for ground-state cooling. We explain how we track both the ions' motional and qubit frequencies within an experimental sequence; the motional frequency tracking especially is an essential component of all remaining experiments described in this thesis. Finally, we have a brief discussion of our even briefer foray into ion transport.

4.1 $^{25}Mg^{+}$ qubit at intermediate magnetic field

The hyperfine Hamiltonian for $^{25}Mg^{+}$ in its electronic ground state is

[1] Sometimes antagonist.

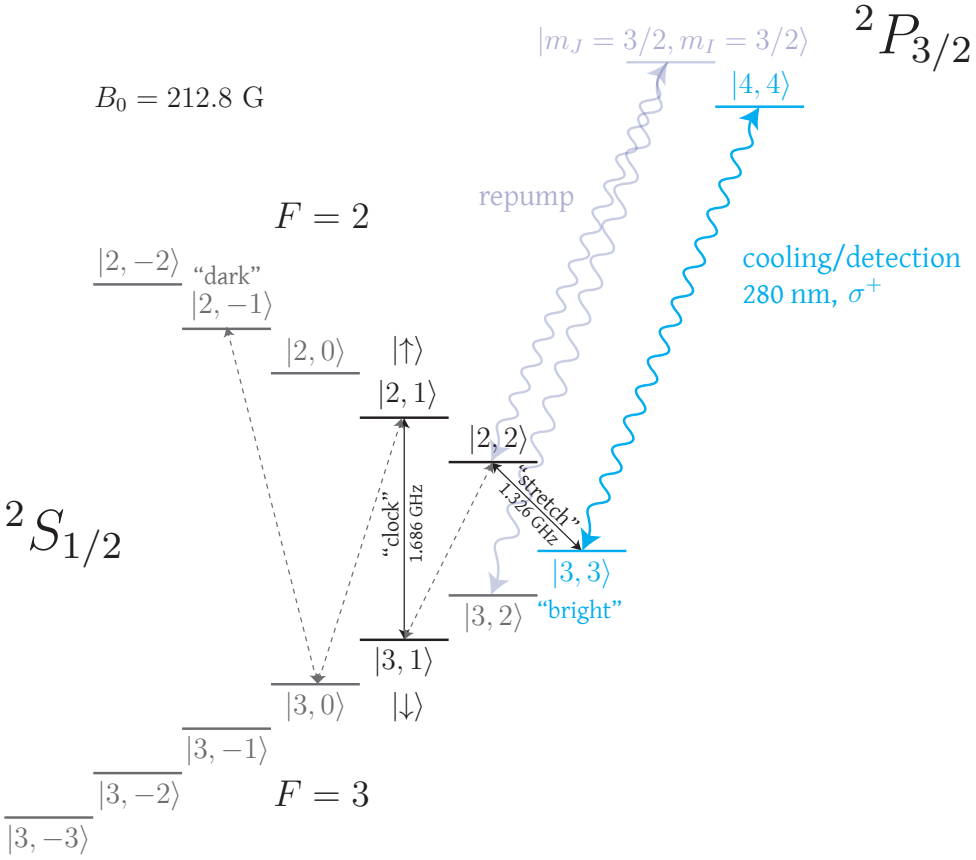

Figure 4.1: Energy level diagram for $^{25}Mg^+$ at a static magnetic field of 212.8 G. We use two sets of qubit states in this thesis. First, the field-sensitive "stretch" qubit transition corresponds to $|F = 3, m_F = 3\rangle \leftrightarrow |2, 2\rangle$. Second the field-insensitive "clock" qubit transition is $|3, 1\rangle \leftrightarrow |2, 1\rangle$. The grey dotted lines indicate additional transitions for shelving to the $|2, -1\rangle$ state for readout. We have an additional repump laser that couples the $|2, 2\rangle$ state to the $^2P_{3/2}\,|m_J = 3/2, m_I = 3/2\rangle$ state. Note that $|m_J = 3/2, m_I = 3/2\rangle$ is an approximate designation; the hyperfine interaction in the P state is much weaker so m_J and m_I are "better" quantum numbers. This repump sends population in the $|2, 2\rangle$ state primarily to the $|3, 2\rangle$ state.

$$\hat{H}_{\text{hfs}} = hA\mathbf{I} \cdot \mathbf{J}, \tag{4.1}$$

where the hyperfine constant is $A = -596.254376$ MHz [Itano and Wineland, 1981] and h is Planck's constant. $\mathbf{J}$ and $\mathbf{I}$ represent the electron and nuclear angular momentum operators respectively. The total angular momentum of the atom is

$$\mathbf{F} = \mathbf{I} + \mathbf{J}. \tag{4.2}$$

Using this result in Eq. 4.1,

$$\hat{H}_{\text{hfs}} = \frac{hA}{2}(\mathbf{F}^2 - \mathbf{I}^2 - \mathbf{J}^2), \tag{4.3}$$

which has eigenstates $|IJFm_F\rangle$, where m_F is the projection of F along a quantization axis [Foot, 2007] defined by a static magnetic field $\mathbf{B}$. For small values of this magnetic field, all states with the same F are degenerate and their energies are

$$E_{\text{hfs}} \simeq \frac{hA}{2}\left(F(F+1) - I(I+1) - J(J+1)\right). \tag{4.4}$$

For $^{25}Mg^{+}$, $I = 5/2$ and $J = 1/2$ in the ground state. The hyperfine splitting between $F = 3$ and $F = 2$ at zero magnetic field is $\Delta E_{\text{hfs}}/h = 3A = -1.78876\,\text{GHz}$. Following Ref. [Woodgate, 1970], the Hamiltonian for an atom with both hyperfine and Zeeman interactions is

$$\hat{H} = hA\mathbf{I}\cdot\mathbf{J} - (\boldsymbol{\mu_J} + \boldsymbol{\mu_I})\cdot\mathbf{B}, \tag{4.5}$$

The magnetic moments are

$$\begin{aligned} \boldsymbol{\mu}_J &= -g_j\mu_B\mathbf{J}, \\ \boldsymbol{\mu}_I &= g_I'\mu_B\mathbf{I}. \end{aligned} \tag{4.6}$$

Its nuclear g factor to electronic g factor ratio is $g_I' = g_I/g_J = 9.299484 \times 10^{-5}$. We operate at an intermediate magnetic field of 212.8 G (21.28 mT), which breaks the degeneracy between the F states, where none of the F, I, or J quantum numbers are good ($m_F = m_I + m_J$ still good). We use the Breit-Rabi [Breit and Rabi, 1931] formula[2] to calculate the energy shifts to our $|F, m_F\rangle$ states

[2] Applies only to $J = 1/2$.

$$\Delta E(F, m_F) = -\frac{\Delta E_{\text{hfs}}}{2(2I+1)} - g'_I \mu_B B m_F \pm \frac{\Delta E_{\text{hfs}}}{2}\sqrt{1 + \frac{4m_F x B}{2I+1} + x^2 B^2}, \tag{4.7}$$

where $x = \frac{(g_j + g'_I)\mu_B}{\Delta E_{\text{hfs}}}$. In Eq. 4.7, + corresponds to $F = I + 1/2$ and − to $F = I - 1/2$. We use this result to calculate the energy levels of the different states shown in Table. 4.1. The magnetic field of 212.8 G was chosen such that the frequency of the $|3,1\rangle \leftrightarrow |2,1\rangle$ transition is first-order insensitive to a change in the quantization axis magnetic field.

Transition ($\|F, m_F\rangle \leftrightarrow \|F, m_F\rangle$)	Frequency f (GHz)	$\mathrm{d}f/\mathrm{d}B$ (MHz/G)	$\mathrm{d}^2f/\mathrm{d}B^2$ (kHz/G^2)
$\|\mathbf{3},\mathbf{3}\rangle \leftrightarrow \|\mathbf{2},\mathbf{2}\rangle$	1.326456	-1.973	1.120
$\|3,2\rangle \leftrightarrow \|2,2\rangle$	1.460516	-1.144	2.240
$\|3,1\rangle \leftrightarrow \|2,2\rangle$	1.573543	-0.572	2.283
$\|3,2\rangle \leftrightarrow \|2,1\rangle$	1.573432	-0.572	2.283
$\|\mathbf{3},\mathbf{1}\rangle \leftrightarrow \|\mathbf{2},\mathbf{1}\rangle$	1.686459	0	2.327
$\|3,0\rangle \leftrightarrow \|2,1\rangle$	1.786044	-0.443	2.100
$\|3,0\rangle \leftrightarrow \|2,-1\rangle$	1.975445	1.252	1.570

Table 4.1: Microwave transition frequencies, first and second order magnetic field sensitivities for $^{25}Mg^+$ at 212.8 G. Our field-sensitive "stretch" qubit ($|3,3\rangle \leftrightarrow |2,2\rangle$) and field-insensitive "clock" qubit ($|3,1\rangle \leftrightarrow |2,1\rangle$) are in bold.

4.2 Field-sensitive "stretch" qubit

We first discuss preparation and readout of our "stretch" qubit on the field-dependent $|F = 3, m_F = 3\rangle \leftrightarrow |F = 2, m_F = 2\rangle$ transition. We call this qubit the "stretch" state qubit as it involves the $|F = 3, m_F = 3\rangle$ state, which has the highest m_I and m_j values. We also describe single-qubit rotations using microwave fields. This qubit is used primarily in the experiments described in this thesis as we require a field-sensitive qubit.

4.2.1 State preparation

We prepare the $|3,3\rangle$ state via optical pumping using the BDD and BD laser described in Sec. 3.5. Using σ^+ polarized light as shown in Fig. 4.1, we should end up in the $|3,3\rangle$ state starting

from any state in the $^2S_{1/2}$ manifold. If this beam is not completely σ^+ polarized or aligned along the quantization axis, we will get imperfect state preparation and leftover population primarily in the $|2,2\rangle$ state. After first adjusting the polarization to maximize the counts as a coarse alignment, we use two additional compensation coils providing fields nominally orthgonal to the quantization axis for finer adjustment.

4.2.1.1 Calibrating compensation fields for beam polarization

We calibrate the currents in the compensation coils (see Sec. 3.4.1) using the following experiment.

(1) Prepare ion nominally in the $|3,3\rangle$ state.

(2) Shelve the $|3,3\rangle$ state to the "dark" $|2,-1\rangle$ state with microwave pulses. Leftover population in the $|2,2\rangle$ state is now in the $|3,3\rangle$.

(3) Turn on a microwave field on the $|3,3\rangle \leftrightarrow |2,2\rangle$ transition for variable duration t.

(4) Shelve the $|2,2\rangle$ state to the $|2,1\rangle$ state.

(5) Detect population in the $|3,3\rangle$ state.

Thus, by looking at the contrast of the Rabi flopping, we have a measure of the population left in the $|2,2\rangle$ state after optical pumping. We adjust the currents in the compensation coils to minimize this contrast. An example scan is shown in Fig. 4.2.

4.2.1.2 Additional state-preparation sequence

Additionally, we perform the following sequence to transfer any residual population in the $|3,2\rangle$ or $|2,2\rangle$ state to the $|3,3\rangle$ state.

(1) $|3,3\rangle \rightarrow |2,2\rangle$ (also transfers population from $|2,2\rangle \rightarrow |3,3\rangle$).

(2) $|2,2\rangle \rightarrow |3,2\rangle$ (population originally in $|3,3\rangle$ now in $|3,2\rangle$).

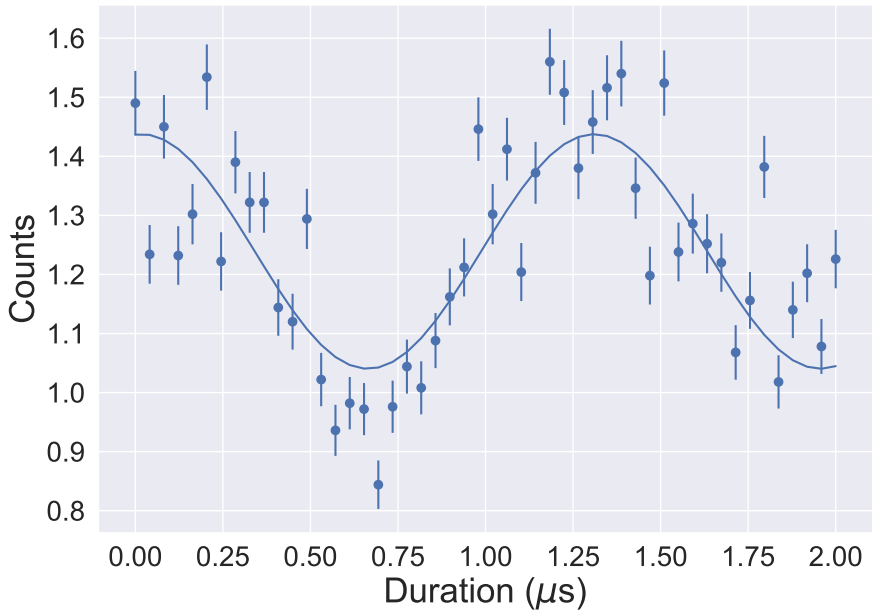

Figure 4.2: Calibration experiment for currents in compensation coils. If the compensation coils are not calibrated, we will have imperfect state preparation and leftover population in the $|2,2\rangle$ state. We pulse a microwave field on resonance with the $|3,3\rangle \leftrightarrow |2,2\rangle$ transition to measure this leftover population. We adjust the currents in the compensation coils to minimize the amplitude of this Rabi flopping.

(3) Pulse repump laser and then drive $|3,3\rangle \rightarrow |2,2\rangle$. We repeat this step 5 times. At this point, the population should be in the $|3,2\rangle$ state.

(4) $|3,2\rangle \rightarrow |2,2\rangle$.

(5) $|2,2\rangle \rightarrow |3,3\rangle$.

The population transfers are performed with microwave π pulses.

4.2.1.3 Repump calibration

Our repump laser sends population in the $|2,2\rangle$ state primarily to the $|3,2\rangle$ state, and secondarily to the $|3,3\rangle$ state (see Fig. 4.1). This repump is used in the state preparation sequence described in the previous section as well as in ground-state cooling. To calibrate the pulse duration for the repump, we prepare the $|2,2\rangle$ state and measure how much of the population is removed from this state as a function of the pulse duration. Experimental data is shown in Fig. 4.3.

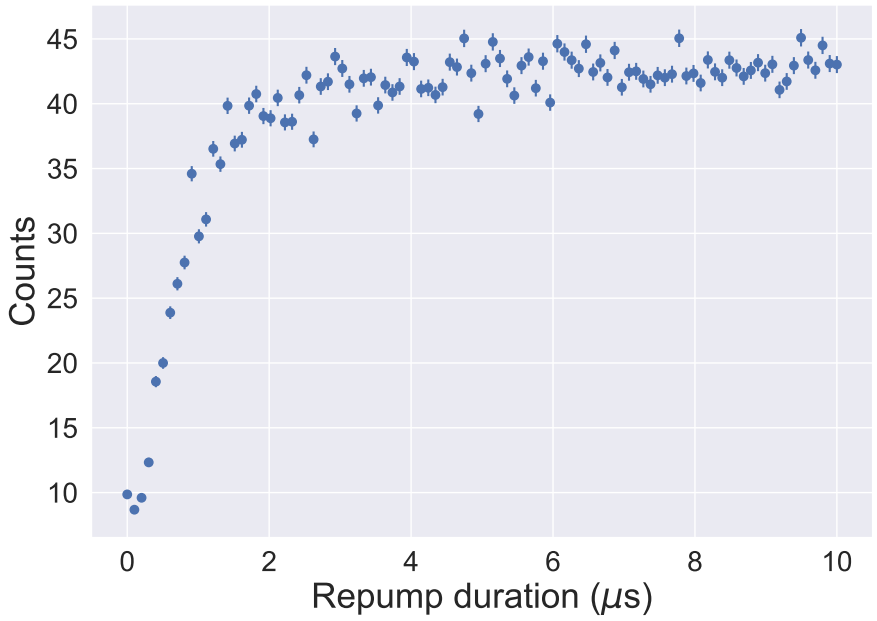

Figure 4.3: Calibration of repump duration. Starting in the $|2,2\rangle$ state which is dark, we pulse the repump laser for a variable duration and subsequently transfer the population in the $|3,2\rangle$ state to the "bright" $|3,3\rangle$ state and then detect. After $5\,\mu$s, most of the state in the $|2,2\rangle$ state is pumped out.

4.2.2 State readout

To read out the state, we first transfer population from the $|2,2\rangle$ state to the $|2,-1\rangle$ state via a sequence of microwave π pulses. We then detect the fluorescence of the $|3,3\rangle$ state by driving a cycling transition to the ${}^2P_{3/2}$ manifold as shown in Fig. 4.1. The microwave shelving sequence is

(1) $|2,2\rangle \rightarrow |3,1\rangle$

(2) $|3,1\rangle \rightarrow |2,1\rangle$

(3) $|2,1\rangle \rightarrow |3,0\rangle$

(4) $|3,0\rangle \rightarrow |2,-1\rangle$

This sequence is shown in Fig. 4.1. This gives us an increased separation between our "bright" $|3,3\rangle$ state and the "dark" $|2,-1\rangle$ which is $\approx 300\,$MHz further away from the $|2,2\rangle$ state. Aside from the detuning, this state also requires more scattered photons to "repump" into the bright state [Langer,

2006]. We apply our detection light for 200 μs. The count histograms for two ions are shown in Fig. 4.4. We typically see about 56 counts (including background counts of about 5) for the one ion bright state and and about 107 counts for the two ion bright states. A more detailed discussion of state preparation and readout errors can be found in Sec. 8.3.2.

For most of the data in this thesis, we use Poissonians to model the counts for the zero ion, one ion, and two ion bright states. This model is then used to extract ion populations from a given set of counts using maximum likelihood estimation[3] .

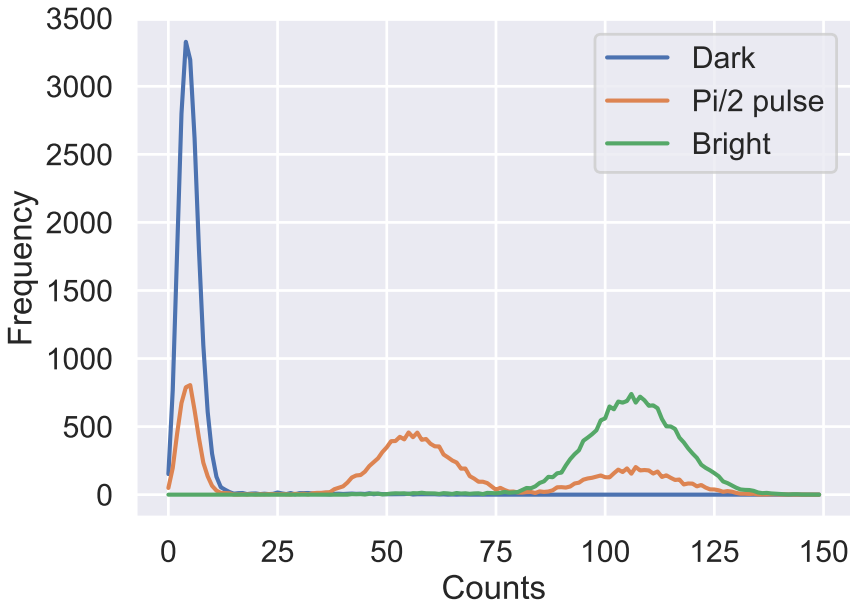

Figure 4.4: Histogram of two ion photon counts. We measure the photon counts with ions in the dark state (blue), after a $\pi/2$ pulse applied to the "stretch" qubit (orange), and in the bright state (green). There are about 19,000 measurements per histogram.

4.2.3 Rabi spectroscopy and Rabi flopping

We perform Rabi spectroscopy by pulsing a microwave field for about 60 μs with a variable detuning from the transition frequency at 1.326 GHz as shown in Fig. 4.5. For these data we apply a current to electrode 3, which generates a lower Rabi frequency of about ≈ 4 kHz. This transition frequency has an approximate linear dependence with the applied magnetic field. We use the

[3] Primarily done by DHS.

difference frequency between the transition we measure and our calculated value as a measure of our magnetic field[4]. Typically, we do not adjust the current to our magnetic field coils unless this difference is larger than 50 kHz. We instead use this transition frequency to track magnetic fields and adjust our microwave frequencies as discussed in more detail in Sec. 4.8.

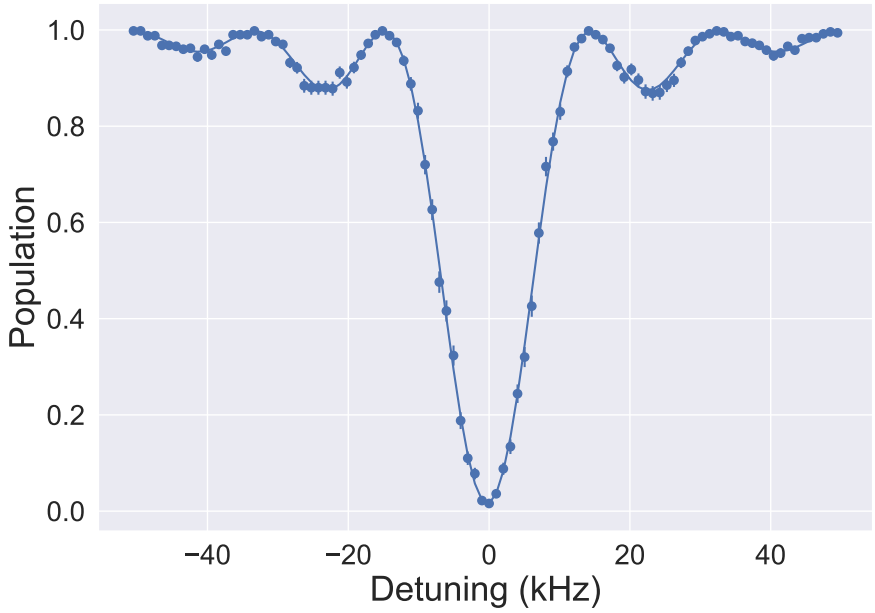

Figure 4.5: Rabi spectroscopy of "stretch" qubit. Starting in the $|3,3\rangle$ state, we pulse a microwave field with a variable detuning for about 60 μs from the $|3,3\rangle \leftrightarrow |2,2\rangle$ transition and measure the population in the $|3,3\rangle$ state.

We also show Rabi flopping on this transition in Fig. 4.6. Here, instead of applying the current to electrode 3, we apply it to electrode 2 which can produce higher Rabi frequencies (due to an additional amplifier in the chain) of about 370 kHz. We use this electrode for fast population transfer during state preparation and readout.

4.3 Field-insensitive "clock" qubit

Our magnetic field produces a field-insensitive "clock" qubit using the $|3,1\rangle$ and $|2,1\rangle$ states. While we do not use this qubit for the new spin-motion coupling technique and entangling gates that we discuss in Chapters 5 and 6, which require a magnetic field sensitive qubit, we do use it for

[4] Note that there will be an offset due to the ac Zeeman shift from an oscillating magnetic field at ω_{rf}.

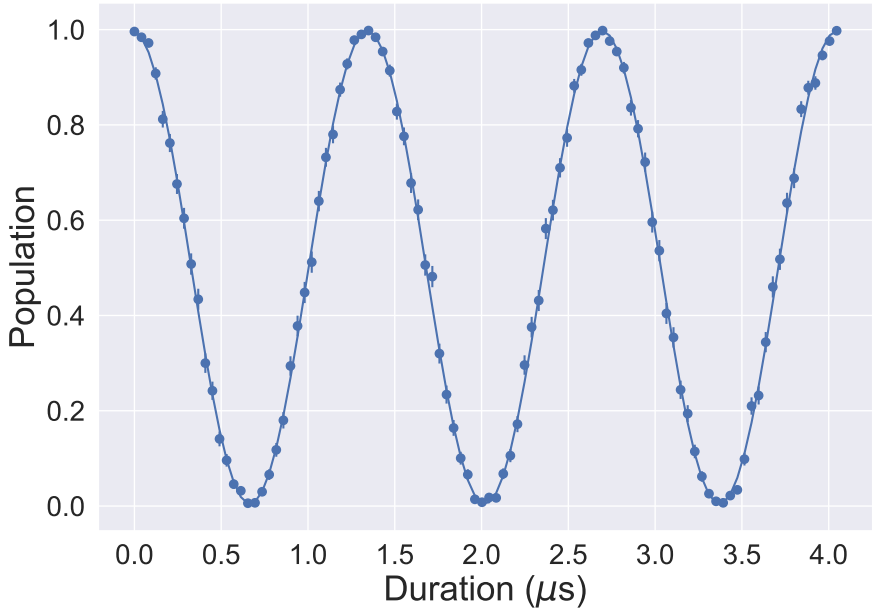

Figure 4.6: Rabi flopping on the "stretch" qubit. Starting in the $|3,3\rangle$ state, we pulse a microwave field driving the $|3,3\rangle \leftrightarrow |2,2\rangle$ transition and measure the population in the $|3,3\rangle$ state.

our microwave sidebands and for some other measurements.

4.3.1 Checking clock state

We check that we have set our magnetic field to the correct value by measuring the frequency of the clock transition as a function of the applied magnetic field. The data is shown in Fig. 4.7. For each of the points, we change the current in our power supply for the high field coils (see Sec. 3.4). For these measurements, the current is varied from 58.89–61.05 A. We then measure the frequency of the "stretch" qubit using Rabi spectroscopy. We use the difference frequency between its measured value and its calculated value at 212.8 G to determine the magnetic field strength. We then perform Rabi spectroscopy on the "clock" qubit to measure its frequency. The minimum is not at 0 due to an ac Zeeman shift from an oscillating magnetic field at ω_{rf}. This field causes an ac Zeeman shift of ≈ 2.5 kHz on the qubit frequency. The magnetic field oscillating at ω_{rf} could be more carefully characterized using the methods outlined in Sec. 5.5.

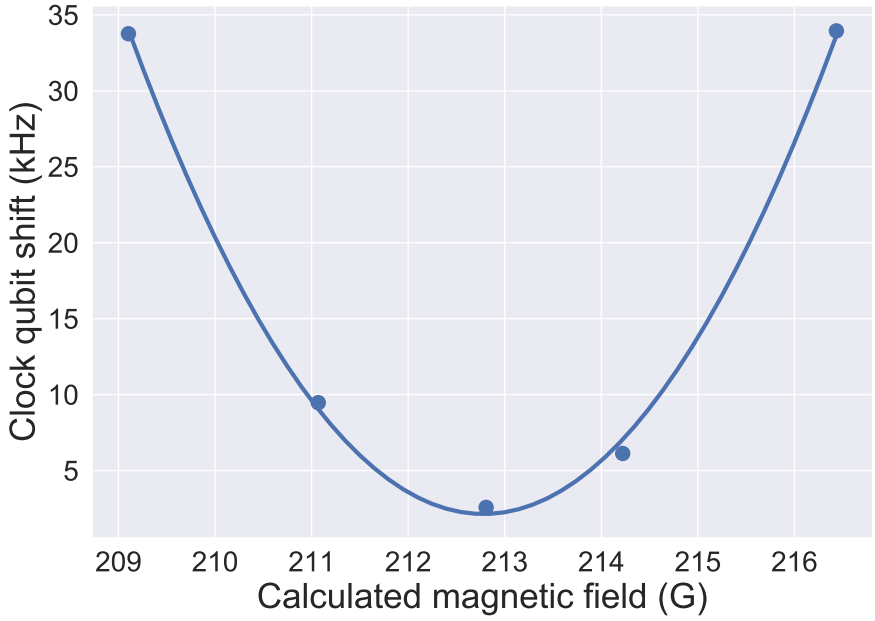

Figure 4.7: Plot of the shift of the "clock" qubit frequency relative to the calculated field-independent frequency versus the applied magnetic field. We vary the strength of the applied magnetic field by changing the current in the magnetic field coils. The value of the magnetic field is calculated using the frequency of the "stretch" qubit. The minimum shift is not 0 due to an additional ac Zeeman shift from a magnetic field at ω_{rf}.

4.3.2 State preparation and readout

To prepare the $|3,1\rangle$ state, we first follow the steps in Sec. 4.2.1 to prepare the $|3,3\rangle$ state. We then transfer from $|3,3\rangle$ to $|3,1\rangle$ using two microwave π pulses that drive the $|3,3\rangle \rightarrow |2,2\rangle$ and $|2,2\rangle \rightarrow |3,1\rangle$ transitions sequentially.

While state preparation is straightforward, state readout is not. With an arbitrary superposition of $|3,1\rangle$ and $|2,1\rangle$, one needs to be careful transferring populations out of these states. For example, the $|3,1\rangle \leftrightarrow |2,2\rangle$ transition frequency is $\approx 100\,\mathrm{kHz}$ away from the $|3,2\rangle \rightarrow |2,1\rangle$ transition frequency. Thus, a π pulse from $|3,1\rangle \rightarrow |2,2\rangle$ can off-resonantly drive population from $|2,1\rangle \rightarrow |3,2\rangle$. This can be mitigated by using a Rabi frequency that is small compared to the difference frequency or by employing pulse-shaping. We use an alternative approach using a composite pulse sequence as follows

(1) $\pi/2$ pulse on $|3,1\rangle \rightarrow |2,2\rangle$ transition.

(2) Wait for a duration t.

(3) $\pi/2$ pulse on $|3,1\rangle \rightarrow |2,2\rangle$ transition.

This sequence will transfer the population from the $|3,1\rangle$ state to the $|2,2\rangle$ state. By adjusting the delay duration t, the part of the amplitude in the $|2,1\rangle$ state that was excited by the initial $\pi/2$ pulse to the $|3,2\rangle$ state will be returned to $|2,1\rangle$. The delay duration t is calibrated experimentally by preparing the state in $|2,1\rangle$ and minimizing the transfer of population to the $|3,2\rangle$ state. An example calibration is shown in Fig. 4.8.

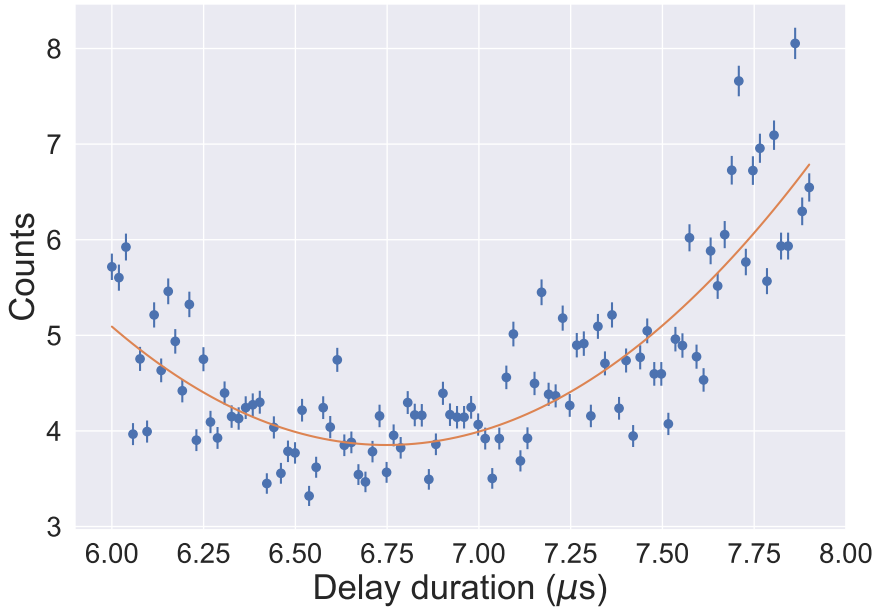

Figure 4.8: Calibration of delay duration in readout of "clock" qubit. We prepare the ion in the $|2,1\rangle$ state and then perform a Ramsey sequence on the $|3,1\rangle \leftrightarrow |2,2\rangle$ transition that off-resonantly drives the $|2,1\rangle \leftrightarrow |3,2\rangle$ transition. We then measure the population transfer to the $|3,2\rangle$ state. By calibrating the delay duration between the two $\pi/2$ pulses in the Ramsey sequence, we can transfer population from $|3,1\rangle \rightarrow |2,2\rangle$ while maintaining the original population of the $|2,1\rangle$ state.

4.3.3 Rabi flopping

We show Rabi flopping on the $|3,1\rangle \leftrightarrow |2,1\rangle$ transition in Fig. 4.9.

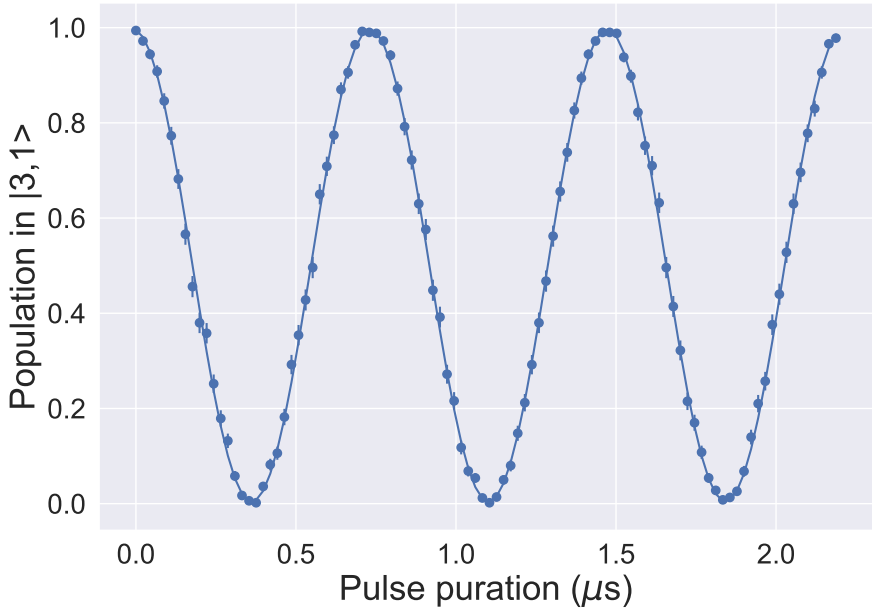

Figure 4.9: Rabi flopping on "clock" qubit. We start in the $|3,1\rangle$ state and pulse a microwave field on resonance with the $|3,1\rangle \leftrightarrow |2,1\rangle$ for a variable duration. We measure the population in the $|3,1\rangle$ state at the end of the sequence.

4.3.4 Qubit coherence

To measure the coherence of the "clock" qubit, we perform a Ramsey experiment. Starting in the $|3,1\rangle$ state we use the following sequence.

(1) $\pi/2$ pulse on $|3,1\rangle \leftrightarrow |2,1\rangle$ transition with phase $\phi = 0$.

(2) Wait time t.

(3) $\pi/2$ pulse on $|3,1\rangle \leftrightarrow |2,1\rangle$ transition with variable phase.

As the qubit decoheres, the contrast in this measurement will decrease. Out to wait times of 100 ms, we see almost no degradation of the qubit contrast on this field-insensitive transition. A plot of the data is shown in Fig. 4.10.

4.4 Calibrations

In this section we outline the calibrations that are performed regularly:

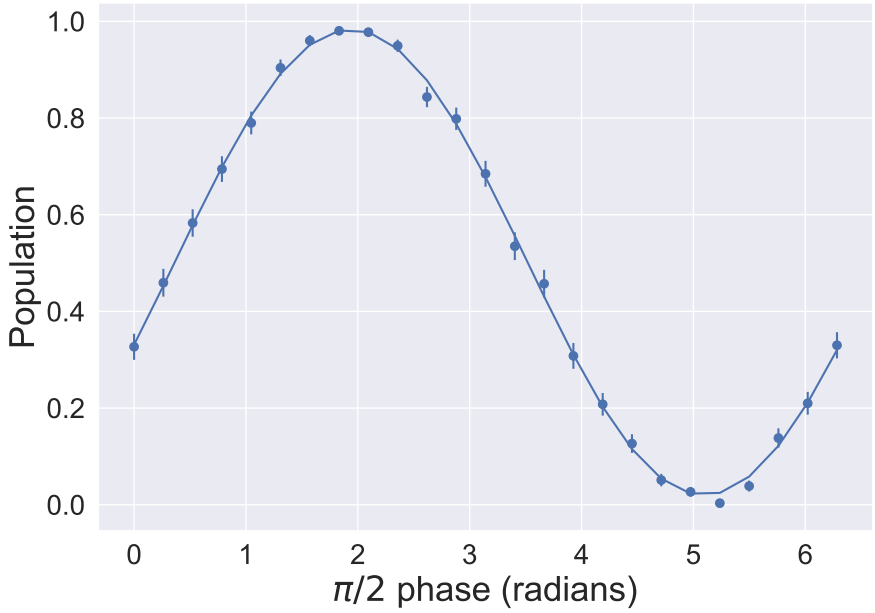

Figure 4.10: Ramsey experiment on "clock" qubit. We start in the $|3,1\rangle$ state and perform a $\pi/2$ pulse on the "clock" transition. We then wait for 100 ms before a second $\pi/2$ pulse with a variable phase. The contrast of this scan is a measure of the qubit coherence. We see almost no loss in contrast with wait times out to 100 ms.

(1) Compensating for ion micromotion in (y) and out of the trap electrode plane (z).

(2) Compensating for stray electric fields along the trap axis (x).

(3) Beam positions on the ions.

(4) Calibrating single-qubit rotations.

The directions of the different axes follow Fig. 3.2. The ion micromotion compensation is typically recalibrated every time ions are loaded due to charging effects from the photoionization beam. The single-qubit rotations are calibrated once a day and the other calibrations less often. Compensating for micromotion first is important to ensure the beams positions are calibrated correctly.

4.4.1 Micromotion compensation

If there are unwanted stray electric fields at the position of the ion, it will be pushed off the rf null and experience micromotion: coherent motion driven by the electric field oscillating at the rf trapping frequency ω_{rf}. We measure the in-plane micromotion using the ion fluorescence and the out of plane micromotion using magnetic field gradients. We compensate for this micromotion by changing the potentials on the dc electrodes to move the ion towards the rf null. The axes follow those in Fig. 3.2.

4.4.1.1 In-plane micromotion

As described in Ref. [Berkeland et al., 1998], micromotion will cause a modulation of the ion fluorescence on resonance due to a Doppler-shift-induced frequency modulation. Thus, maximizing the ion fluorescence allows us to minimize the micromotion. We use simulations to generate a set of voltages[5] on the dc electrodes that provide an electric field at the ion in the plane of the trap along the y direction. We scan the ion fluorescence as a function of this compensating electric field. Data are shown in Fig. 4.11.

4.4.1.2 Out-of-plane micromotion

Our laser beams are orthogonal to the motion of the ion out of the plane of the trap. Ion fluorescence is not affected by micromotion in this direction and we need to use another method. We use the technique described in Ref. [Warring et al., 2013a], using a microwave magnetic field gradient. If the ion is not at the rf null, the electric field at the trapping rf frequency ω_{rf} will drive ion motion at that frequency. If we have a microwave field gradient that is detuned from the qubit frequency ω_0 by ω_{rf}, we can drive micromotion sideband transitions that flip the ion spin. The Rabi frequency of this transition is

[5] Thanks DHS!

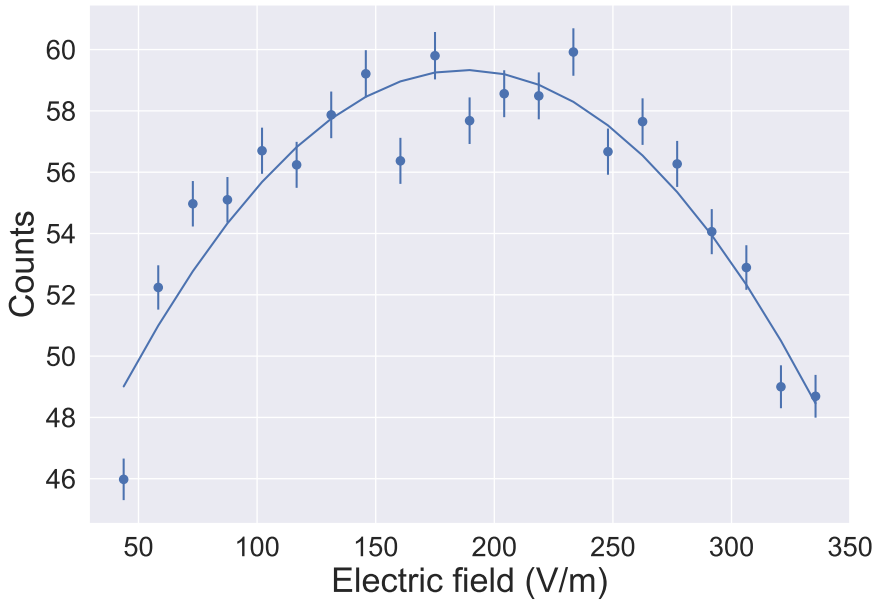

Figure 4.11: Calibration of in-plane micromotion. We measure the ion fluorescence as a function of the electric field along the $\hat{y}$ direction. When the electric field we apply compensates for stray electric fields at the ion and minimizes the in-plane micromotion, we see maximum fluorescence.

$$\Omega_{\mathrm{mm}} = \frac{B'\mu_B}{4\hbar} r_{\mathrm{mm}}, \tag{4.8}$$

where B' is the magnitude of the magnetic field gradient (π-component) we apply along the direction of the micromotion, μ_B is the Bohr magneton[6]and r_{mm} is the amplitude of the ion micromotion at ω_{rf}. Thus, by adjusting the shim voltages to (ideally) null Ω_{mm}, we can compensate the ion position out of the plane of the trap. We note that the exact detuning of the field gradient from ω_0 is shifted slightly from ω_{rf} due to the ac Zeeman shift from the detuned microwave field (see Sec. 4.3.1). Rabi oscillations at the micromotion sideband are shown in Fig. 4.12 for three different values of the shim voltage. While in principle we could use a microwave gradient detuned from any microwave transition, we use the field-insensitive "clock" qubit for its longer coherence time, which allows sensing of smaller Ω_{mm} and thus better micromotion compensation. Additionally, a field-sensitive transition would also be sensitive to an oscillating magnetic field at ω_{rf} that can also cause spin-flip transitions (see Sec. 5.2).

[6] The astute reader might wonder where the matrix element went. It has been factored in, but for the "clock"

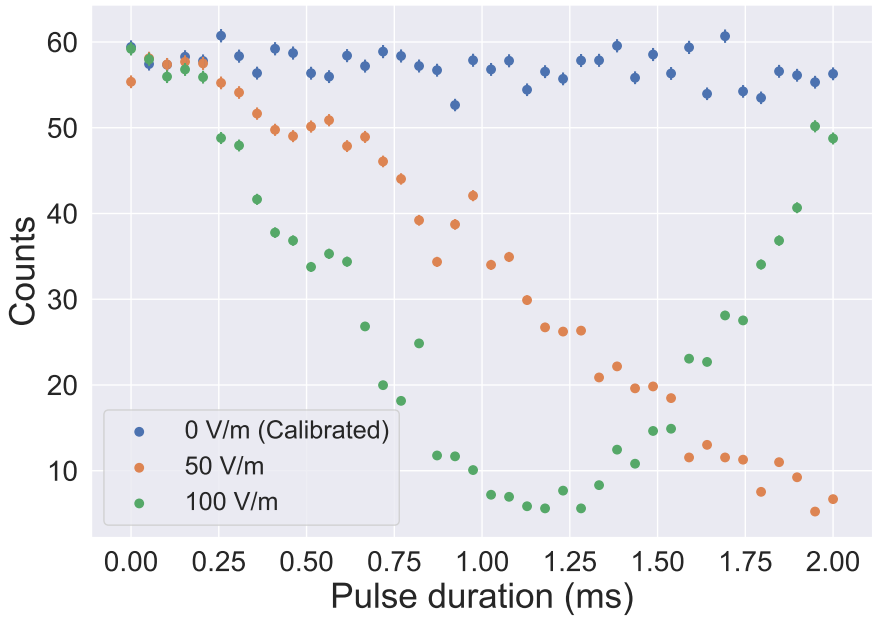

Figure 4.12: Calibration of out-of-plane micromotion with microwave gradient. We pulse a microwave gradient detuned from the "clock" qubit frequency ω_0 by the trap rf frequency ω_{rf}. We perform this experiment for three different values of the compensation voltages applied: at the calibrated value (blue), 50 V/m off (orange) and 100 V/m off the calibrated value (green points). When the ion is displaced from the rf null, the Rabi frequency of this transition increases.

4.4.2 x shim

Stray electric fields along the trap axis will push the ion off the center of the trap but not cause micromotion since the rf electric field is zero along the rf null line, parallel to the trap axis. However, it is still desirable to have the ion at the nominal trap center. Our shim voltages are calculated at this point, and it should minimize anharmonicities, improving the ion lifetime. To compensate for stray fields along this direction, we measure the ion position as a function of the axial confinement. For a harmonic oscillator,

$$F = -kx, \tag{4.9}$$

where here, F is the force from a stray field, k is the spring constant, and x is the displacement of the ion from its equilibrium position without any stray fields. By changing the axial confinement

transition, that corresponds to $\approx 1.001\mu_B$ [Warring et al., 2013a].

strength, we change the value of the spring constant. The displacement $x = -F/k$. Thus, if the ion position x is constant for different values of k, we have $F = 0$. We measure the ion position by looking at the peak of its fluorescence versus beam position as shown as shown in Sec. 4.4.3. We change the axial confinement by changing all of our dc voltages (without compensation) by the same scale factor. The two scaling factors for the data in Fig. 4.13 are 0.36 and 0.76.

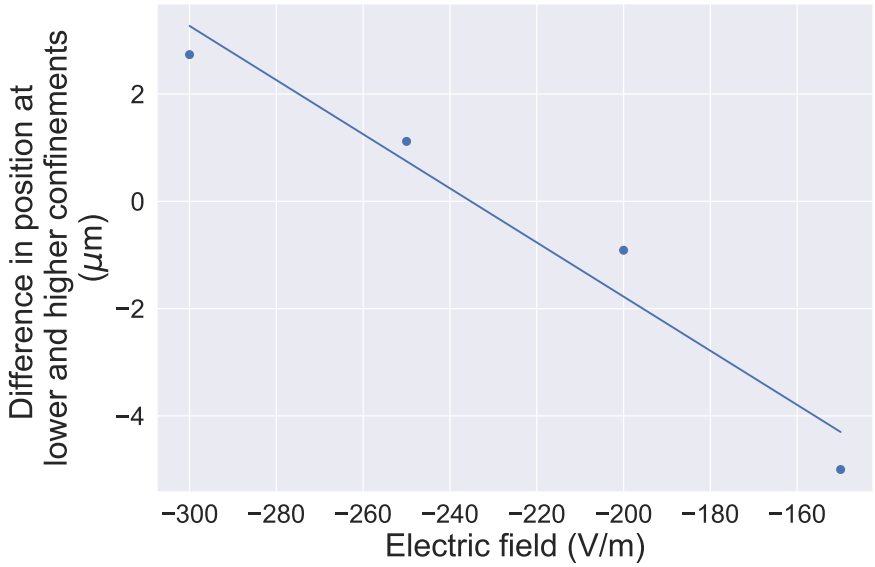

Figure 4.13: Calibration of compensation voltages along trap axis. We measure the ion position at two values of the axial confinement. We plot the difference in position at those two values as a function of the electric field applied along the trap axis. When the ion is well-compensated, the difference will be 0.

4.4.3 Detection beam positions

Our beams for detection, Doppler cooling, repumping, and optical pumping follow the same path to the ion after the same fiber. Thus, aligning one of the beams on the ion aligns all of them. The horizontal alignment is controlled using a motorized actuator whose position we scan. Using the ion, we optimize the beam position by maximizing its fluorescence as shown in Fig. 4.14.

The vertical (out-of-plane) alignment is controlled via a mirror mount with a piezoelectric adjuster. Changing the applied voltage changes the vertical position of the beam. To distinguish between ion fluorescence and scatter from the surface, we measure the counts with the ion in its

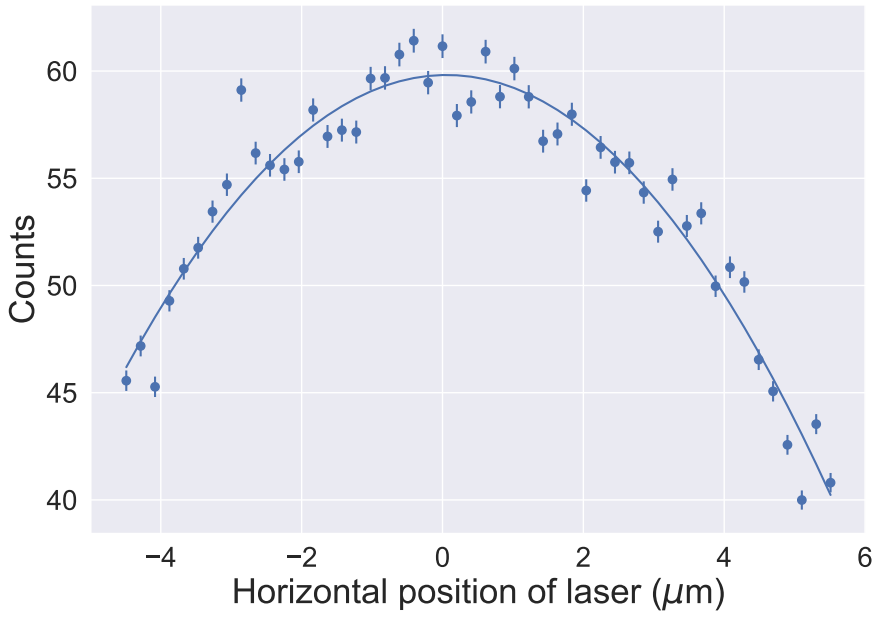

Figure 4.14: Calibration of in-plane position of detection beam. We measure the ion fluorescence as a function of the beam position which is varied using a motorized actuator. We use a quadratic fit to determine the position at the maximum.

bright state and in its dark state. We pick the point with the highest difference between bright and dark state counts as shown in Fig. 4.15.

4.4.4 Single qubit rotations

We use our microwave fields to perform single-qubit rotations. For example, we perform $\pi/2$ pulses for Ramsey sequences, two-qubit gates, and π pulses for spin-echos, state initialization, and shelving sequence for state readout. To perform these single-qubit rotations accurately, we need to calibrate the duration of the pulses. A coarse calibration is done using Rabi oscillations as shown in Fig. 4.6. However, the π-pulse duration extracted from Rabi oscillations does not take into account the rise and fall times of our microwave switches that also induce some rotation.

To more precisely calibrate the duration of π or $\pi/2$ pulses, we perform a sequence of pulses with a short delay in between. As shown in Fig. 4.16, we measure the qubit population as we perform a sequence of 200 π pulses in a row with a 5 μs gap between pulses on the "stretch" qubit. This gap also mitigates duty cycle effects to a certain extent. Starting in $|\uparrow\rangle$, we perform an even

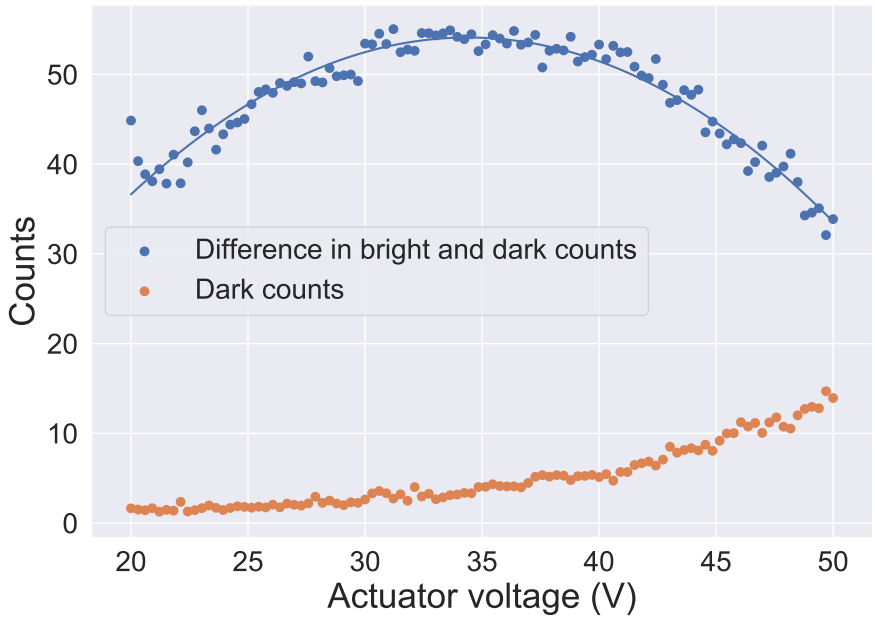

Figure 4.15: Calibration of the out-of-plane position of the detection beam. We measure the ion fluorescence as a function of the beam position which is varied by changing the actuator voltage. We measure both the bright and dark state counts and plot the difference as well as the dark state counts as a function of voltage. We fit a quadratic to the difference and set the voltage to the maximum.

number of π pulses so the ion should ideally be returned to its initial dark population. If the pulse duration is too long or too short, we get an over or under rotation that we measure with longer sequences. Based on this measurement, we can apply a correction ϵ_t to the π pulse duration

$$\epsilon_t = \frac{t_\pi}{\text{No. of pulses for } \pi \text{ rotation error}}. \tag{4.10}$$

For the data in Fig. 4.16, about 118 pulses resulted in a π rotation error, or a complete transfer from dark to bright. From a π pulse duration t_π of about 0.673 μs, this corresponds to a timing error of about 6 ns. As we cannot distinguish between an under or over rotation, we experimentally try both adding and subtracting this correction and choose the time that results in a reduction of the error. The initial coarse calibration of this π pulse duration was done via Rabi flopping; we attribute the 6 ns discrepancy to the rise and fall times of the switches. We perform a similar calibration for the $\pi/2$ pulses, which are not simply half the π time, again due to the switches.

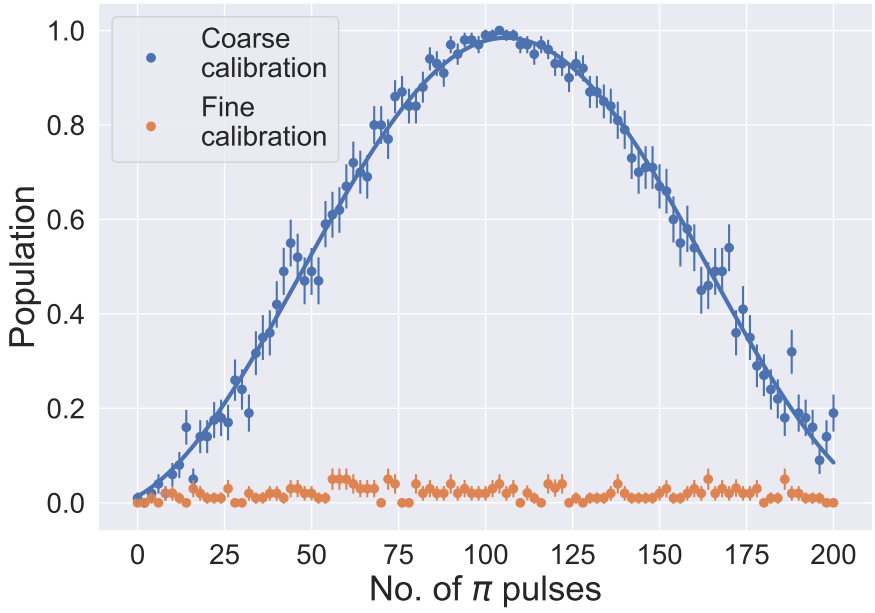

Figure 4.16: Calibration of π-pulse times using microwaves for single-qubit rotations on the "stretch" qubit. We plot the population versus the number of π pulses applied. Starting in the dark $|2,2\rangle$ state, we apply an even number of π pulses. If the timing of the π pulse is incorrect, we will see coherent excitation to the $|3,3\rangle$ state which we measure. Based on the number of pulses that transfer $|2,2\rangle \rightarrow |3,3\rangle$, we can determine the timing offset. Based on the data in the blue points which produced an error, we applied a 6 ns correction to the π time as shown in the orange points.

Transition ($\|F, m_F\rangle \leftrightarrow \|F, m_F\rangle$)	π pulse duration (μs)
$\|3,3\rangle \leftrightarrow \|2,2\rangle$	0.673
$\|3,2\rangle \leftrightarrow \|2,2\rangle$	0.299
$\|3,1\rangle \leftrightarrow \|2,2\rangle$	2.329
$\|3,1\rangle \leftrightarrow \|2,1\rangle$	0.366
$\|3,0\rangle \leftrightarrow \|2,1\rangle$	2.628
$\|3,0\rangle \leftrightarrow \|2,-1\rangle$	4.254

Table 4.2: π pulse durations for single-qubit rotations for state preparation and readout. These transitions are driven by a current applied to electrode 2.

The π times for the transitions used in the state preparation and shelving sequence are listed in Table. 4.2. Each of these π pulse durations are calibrated using the method outlined previously.

4.5 Laser-based spin-motion coupling

As described in Sec. 3.5.3, we use a VECSEL based system for implementing stimulated Raman transitions. We drive coherent two-photon $|3,3\rangle \leftrightarrow |2,2\rangle$ transitions via the intermediate P states. As the effective k vector for this transition has an overlap with all three motional modes of a single ion, we can use these lasers for 3D ground-state cooling [Burd et al., 2016]. For the experiments described in this thesis, we use this transition to cool the out-of-phase axial mode and sometimes the radial modes.

To align each beam on the ions, we maximize the ac Stark shift on the ions due to the Raman beams, as measured using a microwave Ramsey experiment. With two ions, the beams might need slight readjustment from the one ion calibration to ensure they are equally illuminating both ions.

4.5.1 Ground state cooling

We use the Raman beams to cool the out-of-phase axial mode ($\approx$3.8 MHz) as shown in Fig. 4.17. Cooling this mode is important for the gates we perform in chapter 6.

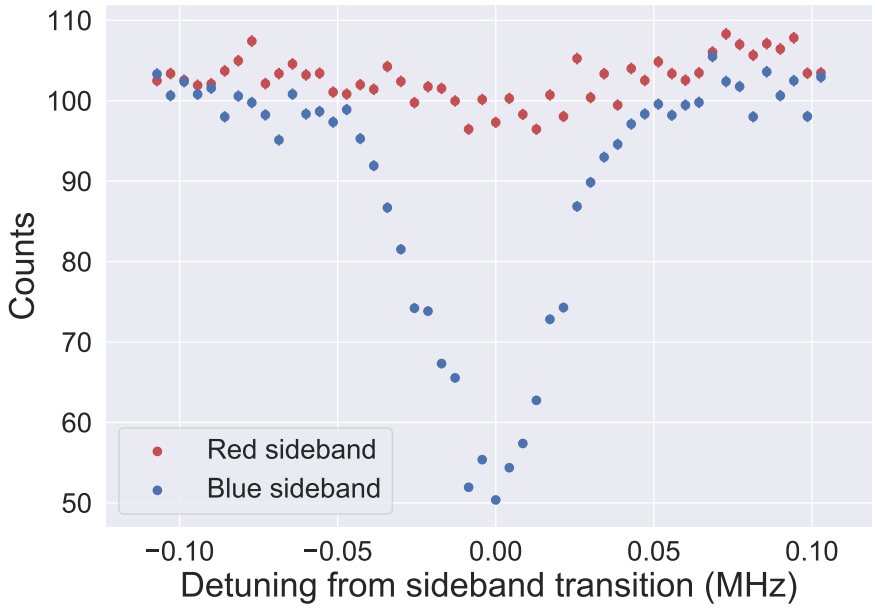

Figure 4.17: Verification of ground-state cooling of the out-of-phase axial mode with Raman beams. We scan across the sideband transitions after cooling the mode, exciting the blue sideband but not the red. This asymmetry indicates that the mode is close to its ground state (Eq. 4.11).

4.5.2 Heating rate measurements

After ground-state cooling, we can add in a variable wait duration before measuring the sideband asymmetry as shown in the previous section. Following Ref. [Leibfried et al., 2003] for a single ion, the mean thermal occupation $\bar{n}$ is

$$\bar{n} = \frac{R}{1-R}, \tag{4.11}$$

where R is the ratio of the red to blue sideband excitation probabilities.

$$R = \frac{P_{\mathrm{rsb}}}{P_{\mathrm{bsb}}}. \tag{4.12}$$

We note that this relation holds for a thermal state regardless of the duration for which each of the blue or red sideband pulse is applied. Typically, this is adjusted to the π time of the blue sideband transition from the ground state to maximize the contrast. Thus, by measuring the sideband asymmetry as a function of wait duration after ground state cooling, we have a measure of $\bar{n}$ as a function of time and can determine the heating rate. The heating rates of the different modes measured in this setup are shown in Table. 4.3.

Mode	Frequency (MHz)	Heating rate (quanta/s)
Axial center-of-mass	2.4	60
Radial center-of-mass	7.3	18
Radial out-of-phase	7.2	<2

Table 4.3: Heating rates for different motional modes.

4.5.3 Photon scattering

The Raman beams cause photon scattering (Raman and Rayleigh), sometimes causing transitions out of the "stretch" qubit manifold. When using the Raman beams for ground-state cooling in other experiments, such as our two-qubit gates, we find that we need to add an extra π

pulse on the $|3,1\rangle \leftrightarrow |2,2\rangle$ transition before performing the state preparation sequence in Sec. 4.2.1.2. This extra pulse helps recover any population lost from the ground state cooling to the $|3,1\rangle$ state and return it to the $|3,3\rangle$ state.

4.6 Microwave spin-motion coupling

Similar to Ref. [Ospelkaus et al., 2011], we can drive sideband transitions using a magnetic field gradient oscillating close to the "clock" qubit frequency as described in Sec. 2.3.5.

4.6.1 Nulling the microwave magnetic field

As described in Ref. [Ospelkaus et al., 2008], we first null the microwave magnetic field at the ion's position. When we apply a current to the electrode, we generate a magnetic field B and a magnetic field gradient. While we need a magnetic field gradient to drive sideband transitions, nulling the magnetic field B is desirable as it minimizes the ac Zeeman shift at the ions which is proportional to B^2. A static ac Zeeman shift can be calibrated out, but fluctuations in this ac Zeeman shift will cause qubit decoherence, even though the qubit itself is insensitive to fluctuations in the quantization magnetic field. These fluctuations could be due to Rabi frequency fluctuations of the microwave fields. Operating at the B field null reduces the sensitivity as

$$\begin{aligned} \Delta_{ac} &\propto B^2, \\ \delta\Delta_{ac} &\propto B\delta B. \end{aligned} \tag{4.13}$$

Nulling the microwave magnetic field also minimises off-resonant transitions, for example for the $|3,1\rangle \leftrightarrow |2,2\rangle$ transition[7] .

In our trap, nulling the magnetic field involves applying currents of a given frequency to multiple electrodes, and adjusting the phases and amplitudes of each current to cancel the magnetic field at the ion. Other traps instead incorporate an electrode geometry with a meander to null the

[7] Off-resonant transitions can also be mitigated by pulse shaping.

magnetic field automatically [Hahn et al., 2019], though successfully overlapping the B field null and the rf null requires both complex finite element analysis simulations and accurate microfabrication.

To null the magnetic field, we first apply currents at the qubit frequency ω_0 to both electrodes 2 and 3 (see Fig. 3.2). On resonance, the magnetic field will drive carrier transitions. We adjust the relative phase and amplitudes of the currents to minimize the Rabi frequency Ω_μ of this transition. As $\Omega_\mu \propto B$, this measurement is first order sensitive to the magnetic field. Note that this measurement is only sensitive to B field polarizations that drive the qubit transition, which in this case requires π polarization. The effect of this nulling is shown in Fig. 4.18. With currents applied to both electrodes 2 and 3, the Rabi flopping seen with just electrode 3 is reduced considerably. However, going to longer pulse durations we see some flopping likely due to duty cycle effects.

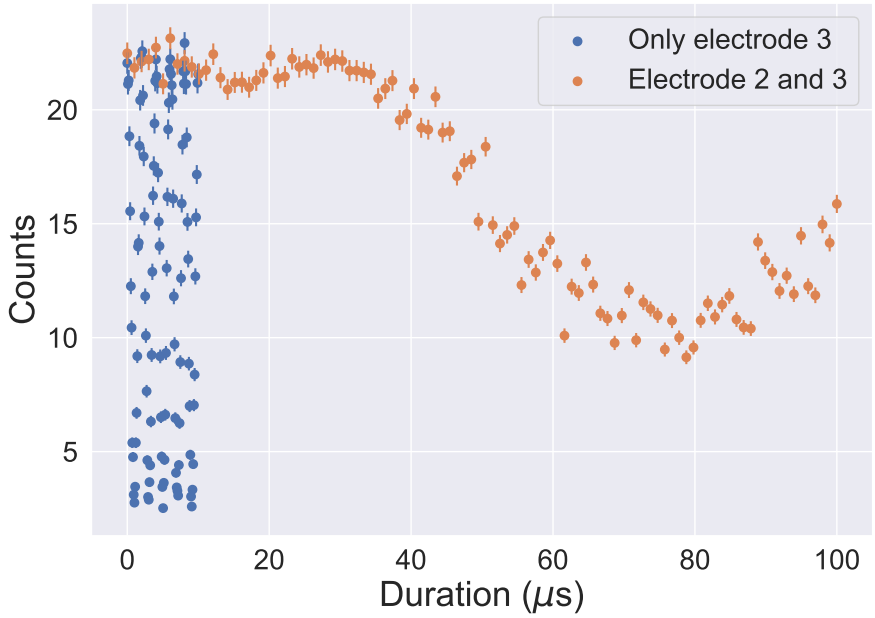

Figure 4.18: The magnetic field oscillating at the qubit frequency ω_0 is nulled by applying currents to multiple electrodes. With a current applied only to electrode 3, we see fast Rabi flopping as seen by the blue points. By applying a current to electrode 2 as well, with an amplitude of 0.77 and phase of 0.92π relative to electrode 3, we are able to minimize the Rabi flopping. We start to see flopping at longer timescales most probably due to thermal duty cycle effects that shift the relative phases and amplitudes slightly. The counts are lower in this plot as a 100 μs detection time was used.

Compared to using a current at ω_0 to calibrate the nulling, there might be slight variations in

the phase and amplitudes required when the microwave current is applied at $\omega_0 \pm \omega_r$ for sideband transitions. This variation can be verified by measuring the ac Zeeman shift on the "clock" qubit that varies as B^2. The ac Zeeman shifts on other transitions such as $|3,1\rangle \leftrightarrow |2,2\rangle$ offer measures of the other polarization components of the B field [Warring et al., 2013b].

4.6.2 Microwave sidebands

After nulling the magnetic field, we then drive sideband transitions by applying a current at $\omega_0 \pm \omega_r$ where +(-) corresponds to the blue(red) sideband. An example sideband transition is shown in Fig. 4.19. These sideband transitions are used for the motional frequency tracking in the next section.

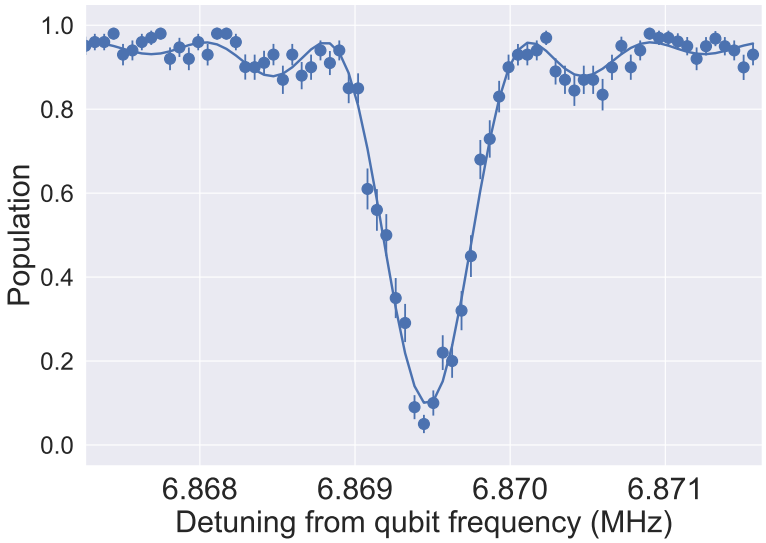

Figure 4.19: Blue sideband transition using a microwave magnetic field gradient oscillating at $\omega_0 + \omega_r$. The population excited from the $|\downarrow\rangle$ ($|3,1\rangle$) state is shown a a function of detuning from the qubit frequency. Starting in the ground state of motion, we are able to completely flip the spin while adding a motional quantum. The sideband was pulsed on for 770 μs.

4.7 Motional frequency tracking

Most quantum information experiments with trapped ions involve coupling their internal spin-states to their motion. In order to do this, one most know the motional frequency to some precision. Unfortunately, for our system this frequency drifts quite substantially. These drifts are primarily due to the proximity of our ions to the surface; being close to the surface increases the strength of our gradients and thus the spin-motion coupling, but also makes us more sensitive to surface effects such as charging which can change the motional frequencies. This charging is caused by the 280 and 285 nm light that we use with $^{25}Mg^{+}$. In this section, we describe how we keep track of the drifts in the motional frequencies as we conduct our experiments. This drift tracking is used for practically every experiment that involves the ions' motion in this apparatus.

4.7.1 Overview

We created a drift tracking (DT) module that could be easily imported into different experiments. The DT is interleaved in between repetitions of a particular experiment; the number of repetitions is a parameter that can be set. When the DT is run, it records the time at which it is running, measures the motional frequency and then outputs that frequency.

We keep track of all frequencies measured as a function of time and perform a simple linear fit to predict what the frequency will be in the future. Setting the frequency to the most recent estimate, without including linear extrapolation of the current drift trend, produced less accurate predictions of the motional frequency. Empirically, fitting the 5 most recent points works well; too few points and the DT becomes vulnerable to fast fluctuations, too many and the DT is unable to adapt to changes.

An overview of each sequence of the DT procedure is shown in Fig. 4.20[8]. The steps are

(1) Initialize hardware: We set the parameters for the drift tracking, namely the attenuation values for the digital attenuators controlling the strength of the sidebands we apply. In

[8] HMK points out that no Boulder thesis is complete without a 420 reference.

some experiments, where IQ baseband voltages are also modified from their values for the microwave sideband used for drift tracking, the IQ parameters will also need to be set.

(2) Based on previous measurements, we calculate the predicted motional frequency. Subsequent measurements use this calculated value.

(3) We now begin measurements of the motional frequency, starting with preparing the ion in the $|\downarrow\rangle$ state of the "clock" qubit.

(4) We now pulse the microwave blue sideband on either side of the center frequency, determined in step 2, where there is a steeper response. We perform these measurements in an interleaved fashion, alternating between negative and positive detunings. The detuning values used here are based on the calibration of the sideband that is done beforehand.

(5) We perform state readout, and perform thresholding of the measured counts to determine the qubit populations.

(6) We then reset the hardware so the subsequent experimental measurements can be done. Steps 3-5 are repeated, typically for a total of 100 repetitions per negative and positive detuning.

(7) We perform analysis of the measured qubit populations. This step is done on the host computer, not the FPGA. Here, we calculate the ratio of the populations measured on either side of the detuning, and based on the ratio, the actual motional frequency. We now include the most recent measurement of the motional frequency into our linear fit. We save the new fit parameters which are used for subsequent calculations of the motional frequency.

4.7.2 Calibration

To calibrate the drift tracking parameters, we run a sideband scan similar to that shown in Fig. 4.19. However, instead of a ground- state cooled ion, we typically perform our drift tracking

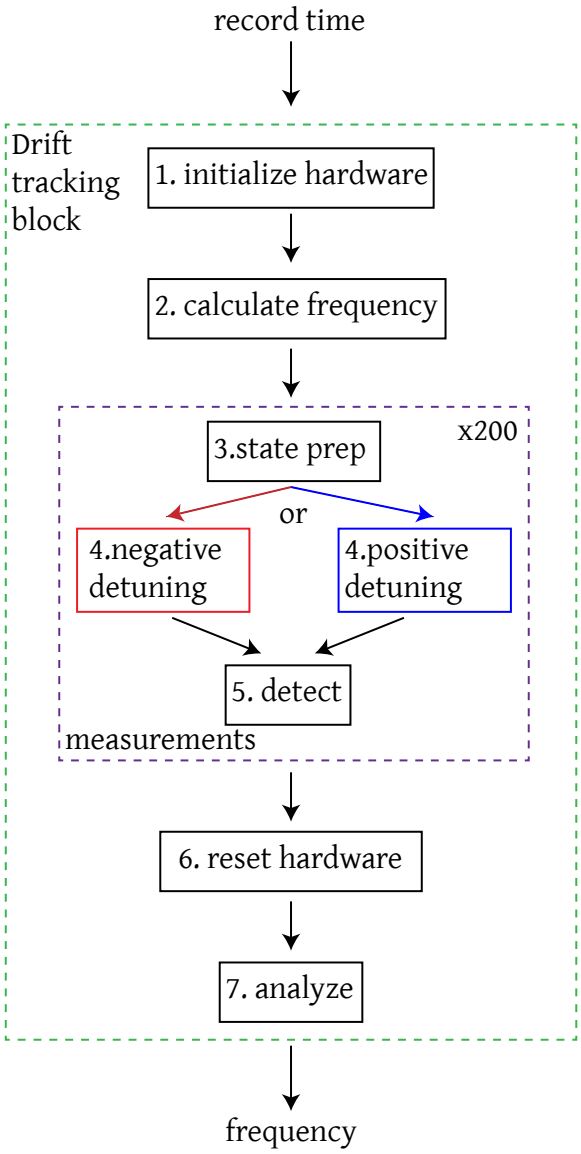

Figure 4.20: Overview of motional frequency tracking. See main text for details.

with Doppler cooled ions. While ground-state cooled ions would offer increased contrast, the duty cycle of the experiment would be reduced due to the ground state cooling. Furthermore, if the ground state cooling is performed with lasers, there might be additional charging as well.

Sample calibration scans for three different pulse durations of 400, 800 and 1600 μs are shown in Fig. 4.21a. In applying the microwave sidebands for these different durations, the only parameter that is changed is the attenuation on the digital attenuator in 6 dB steps. Renulling of the magnetic

field is not done. In addition, a separate experiment is performed to measure the ac Zeeman shift from the residual magnetic field as described in Sec. 4.6.1. This shift would generate a systematic shift to any measured motional frequencies. We typically measure this once, and only recalibrate this shift if there are hardware changes to the microwave lines.

From the counts measured in the calibration experiment, we determine the ion populations as shown in Fig. 4.21b. Simple thresholding is used to determine the populations. The data shown in Fig. 4.21b uses a threshold of 20 and 72 for the zero ion bright and two ion bright populations respectively. Any count below 20 is classified as population 0, between 20 and 72 population 1, and above 72 as two.

From the population points, we fit a resonance line to determine the slope at the population point halfway in between the minimum and maximum and its corresponding detuning. For the data shown, this point occurs at a population of 1.6. These parameters are used for subsequent tracking.

4.7.3 Seeding

We typically interleave measurements of the motional frequency with the experiment we want to run. However, to ensure the drift tracking "locks", we usually seed the drift tracking. This seeding involves running the drift tracking continuously without any experimental measurements to determine the parameters for the linear fit before the experiment starts. This typically involves measuring the frequency about 20 times. The first five measurements have no feedforward; subsequent points use the linear fit to predict future points. This seeding is usually used in conjunction with "dummy" points of the experiments which allows the drift tracking to adapt to the duty cycle of the experiment and keep lock.

4.7.4 Example operation

As an example operation, we show the drift tracking data from one of the two-qubit entangling gates discussed in Sec. 8.1.1 in Fig. 4.22. The population data from measurements made on either side of the predicted motional frequency are shown in Fig. 4.22a. The drift tracking is "locked"

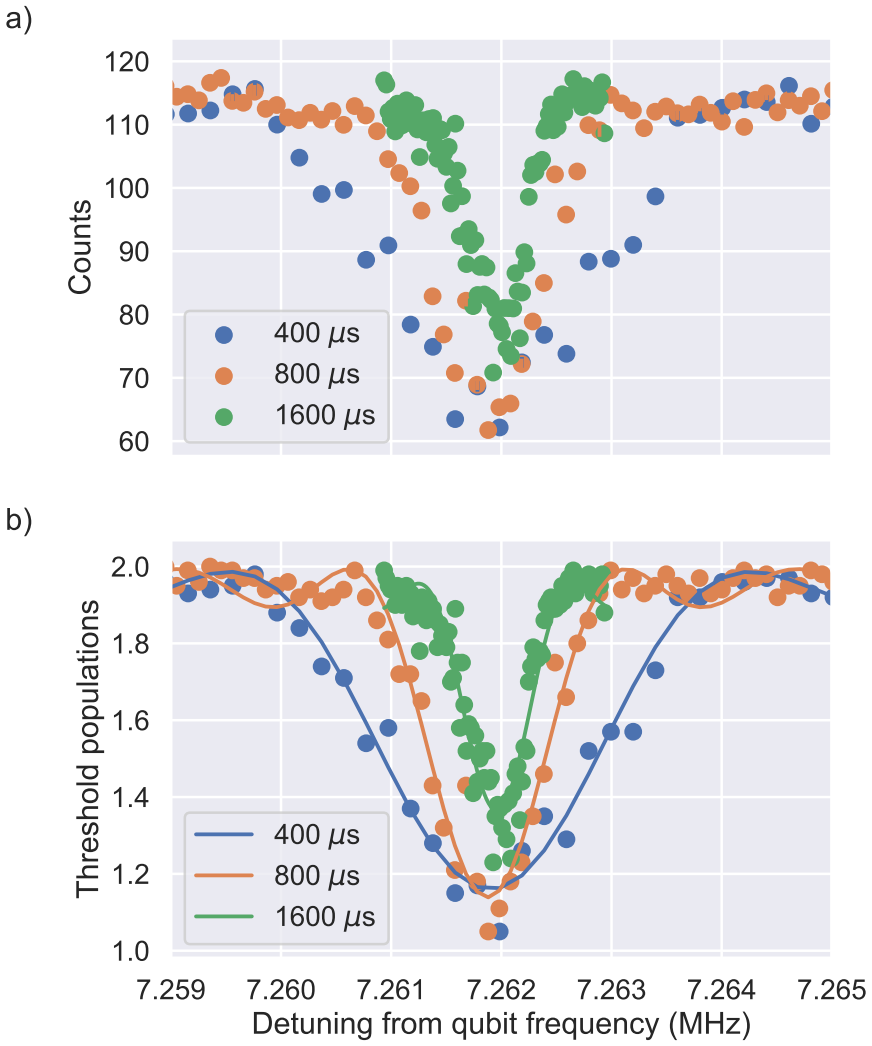

Figure 4.21: Sample calibration scans of microwave sidebands for drift tracking for three different sideband pulse durations of 400, 800 and 1600 μs. a) Plot of raw counts versus detuning. b) Plot of qubit populations derived from thresholds and resulting fits. The parameters extracted from the fit are used for subsequent tracking.

as the populations are close to 1.5. If the drift tracking is "unlocked" both of these population measurements would be closer to 2, i.e. the sideband is far off resonance and causes no spin flips. The drift of the motional mode over the course of normal operation is shown in Fig. 4.22b. Here we see a drift of about 1.2 kHz over 6 min. Larger drifts of about 10 kHz have also been observed.

The precision of our drift tracking, where we plot the difference between the predicted and measured value, is shown in Fig. 4.23. From the histogram, we extract a mean of -2.4 Hz and a

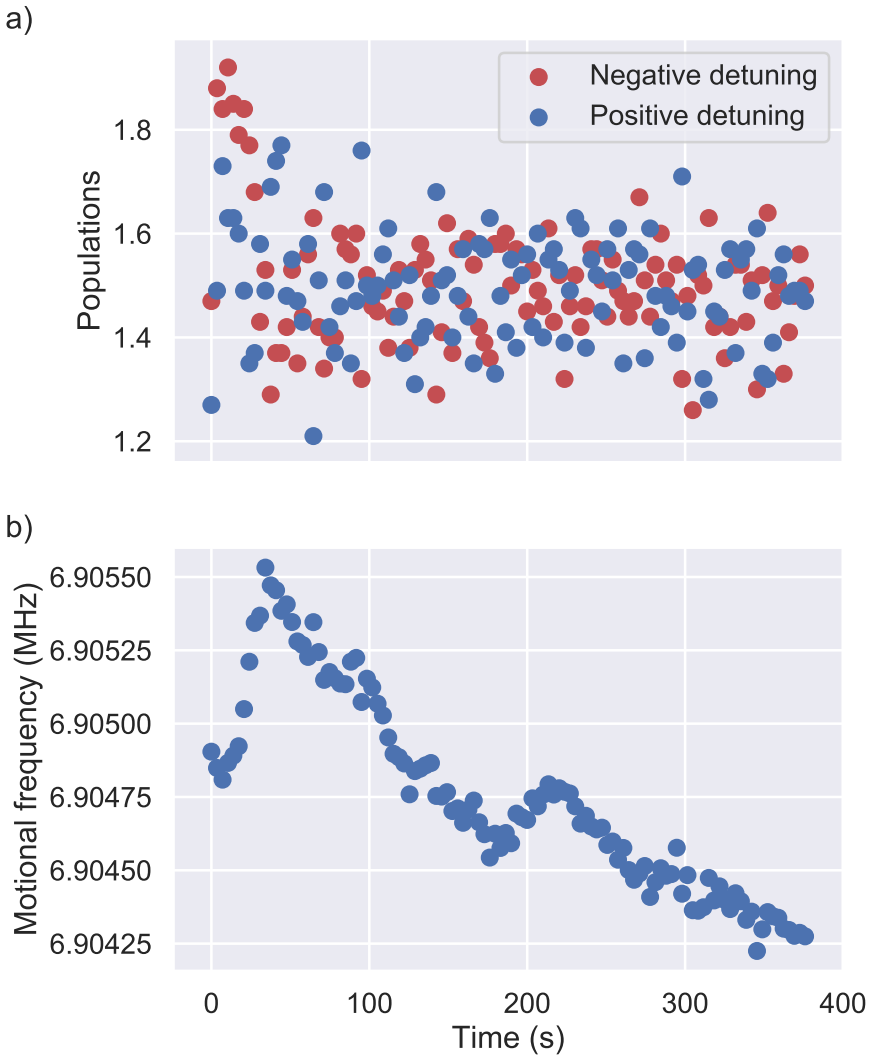

Figure 4.22: Example motional frequency tracking data from a gate experiment. a) Population measurements versus time. These populations are measured on either side of the predicted central peak. The red points correspond to a negative detuning while the blue points to a positive detuning. b) Motional frequency versus time. We plot the motional frequency versus time. Here we see about a 1.25 kHz drift over the course of a typical entangling gate experiment. Each point of the drift tracking precedes 200 repetitions of the entangling gate experiment.

standard deviation of 67 Hz. This measurement was taken using a sideband probe duration of 1.6 ms. Longer times can be used, but there is a trade off between the length of the probe and how reliably the drift tracking stay locked, as the time intervals between frequency updates become too long. Empirically, 1.6 ms is about as long a probe duration as can be used in practice. For coarser scans where the precision is not as important we use 400 μs probes.

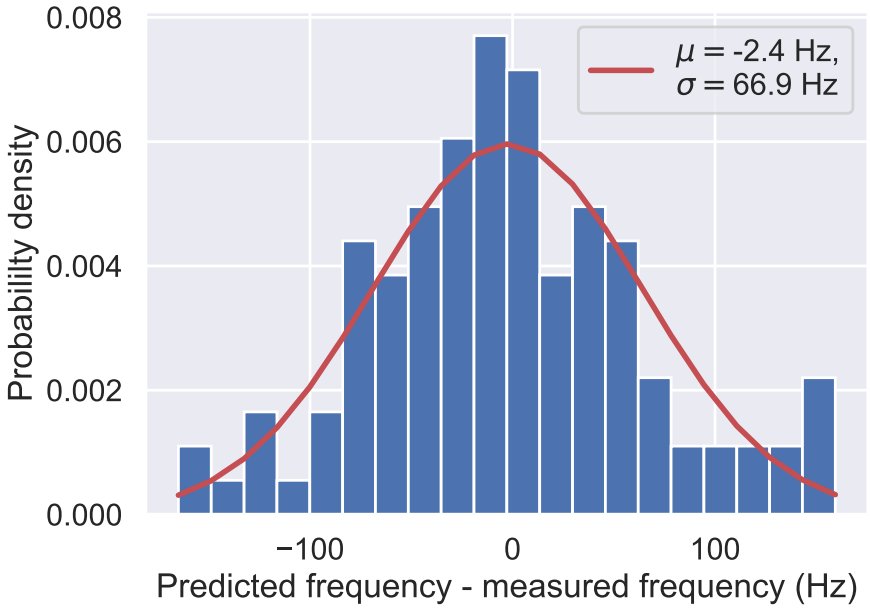

Figure 4.23: Histogram of difference between predicted and measured motional frequency from data in Fig. 4.22. We plot the probability density of measuring a particular frequency difference in red. The mean is close to 0 and the standard deviation of about 67 Hz.

4.7.5 Laser-induced charging

When we first discovered drifts in the motional frequency when performing gate experiments, we were somewhat perplexed. We eventually tracked it down to duty cycle effects from the laser beams and implemented several iterations of the drift tracking before it reached the version described in this thesis. With the drift tracking, we examined the laser-induced charging more concretely as shown in Fig. 4.24.

With a single ion, we measure the motional frequency as a function of time. However, after some number of measurements, we pulse our Raman beams on but detuned from any transition during our drift tracking before measuring the frequency. We see large fluctuations in the motional frequency on the order of 100 Hz that are correlated with the application of the Raman beams. These fluctuations also have fast time scales, causing spikes over a few seconds. When running the drift tracking, we usually try to keep the duty cycle of the laser (Doppler cooling and or Raman) consistent with the main experiment. This can be controlled by changing the amount of Doppler

cooling before the measurement is performed during the drift tracking.

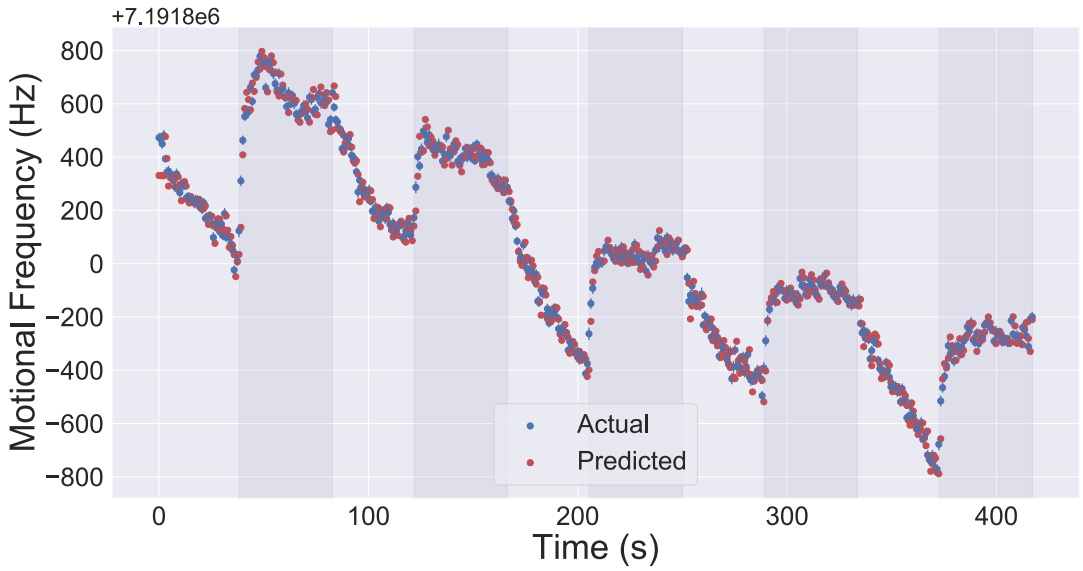

Figure 4.24: Effect of charging from Raman beams on a radial frequency. We measure the motional frequency on a radial mode versus time. The darker regions indicate when Raman beams were also pulsed during the drift tracking sequence. We see sharp increases when the Raman beams are first applied that decreases when they are turned off. We attribute these fluctuations to charging of contaminants on the surface of our electrodes from the laser.

4.7.6 Future improvements

$^{25}Mg^{+}$ is not as light as $^{9}Be^{+}$ and uses 280 nm for cooling and detection as opposed to 313 nm, which should cause less charging. Other experiments in our group that use $^{9}Be^{+}$ close to the surface see weaker effects from charging. Thus, one way to improve our drift tracking would be to reduce the drifts in the first place by using a different ion. Fortunately, this apparatus also has Ca ovens; Ca^{+} ions will hopefully enable mixed-species operations that minimize the use of Mg lasers.

Additionally, we typically require a scan of the motional frequency to initialize the drift tracking i.e. a starting point before the seeding occurs. This step could be eliminated by a continuous monitoring of the motional frequency in between experiments.

Furthermore, more advanced algorithms to predict the motional frequency could also be used.

In particular, we find that the drift tracking has consistent behaviour for identical experimental sequences outside of the drift tracking. If motional frequency drifts from previous runs of the experiments could also be incorporated in the tracking, it might help to track the drifts in subsequent runs of the experiments more precisely. Since all the drift tracking data is stored for every experimental run, different algorithms could be tested with existing data.

4.8 Qubit frequency tracking

Aside from motional frequency drifts, we also employ a similar procedure for tracking the magnetic-field-sensitive "stretch" qubit frequency. The qubit frequency would drift due to changes in our nominally static quantization field. An example of qubit frequency tracking is shown in Fig. 4.25. Instead of using Rabi spectroscopy on the sideband transition, we instead use the spin-flip transition as shown in Fig. 4.5. We increase the π-pulse duration of this transition to about 1 ms by reducing the microwave amplitude in order to increase the precision. We are usually able to predict the qubit frequency to about 50 Hz, which corresponds to a magnetic field shift of 2.3×10^{-5} G (2.3 nT). These fluctuations are small. In fact, while running these experiments we often saw qubit frequency shifts when routine tasks such as opening cupboards or drawers close to the experiment. We also observed shifts due to cryogen dewars being transported outside the lab.[9] .

4.9 Ion transport

As shown in Fig. 3.2, there are multiple trap zones that could be used for experiments. The advantage of performing experiments away from the load zone would be to minimize the effects of charging from the higher power 285 nm beams used for loading. However, for the majority of the experiments in the thesis, we only performed experiments in the load zone. One does not simply transport ions into the experiment zone[10].

[9] Even if we don't end up with a quantum computer with our setup, at least we have a very expensive magnetic field sensor.

[10] Even Boromir would agree walking into Mordor is easier.

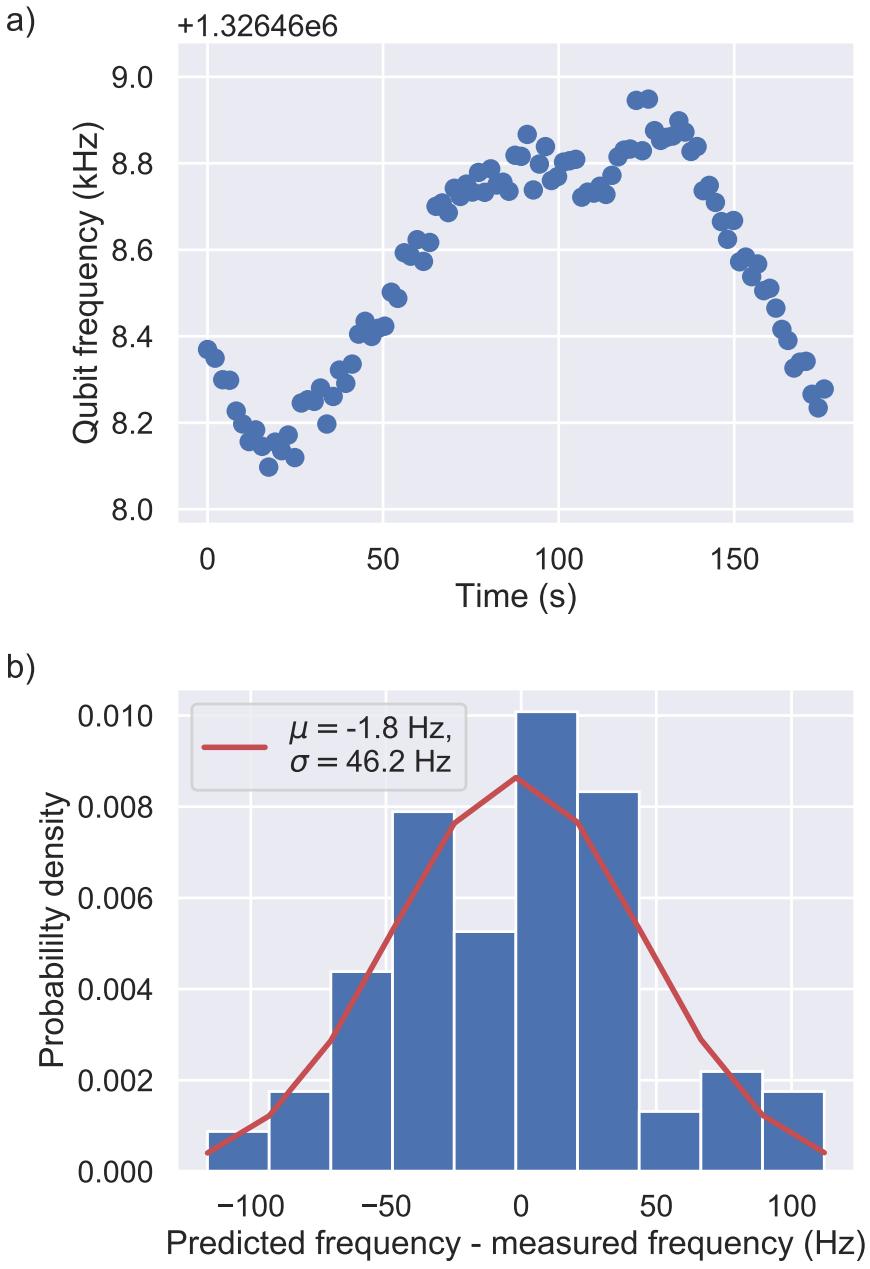

Figure 4.25: Example qubit frequency tracking. a) Plot of qubit frequency versus time. We see drifts on the kHz level over a period of about 3 minutes. b) Histogram of the difference between the predicted and measured frequencies. The mean μ is -1.8 Hz and the standard deviation σ is about 46 Hz.

Ion transport involves changing the potentials[11] of the DC electrodes, moving the minimum of the axial confining potential along the trap axis. We only attempted transport that was well into

[11] Transport potentials generated by DHS. This is just a statement of fact, not assigning blame for our transport woes.

the adiabatic regime on the millisecond timescale. We were initially successful in this and were able to transport up to two ions reliably. Figure 4.26 shows one of our more successful attempts moving a single ion three electrodes over or by a distance corresponding to$\approx 165\,\mu$m from its initial position.

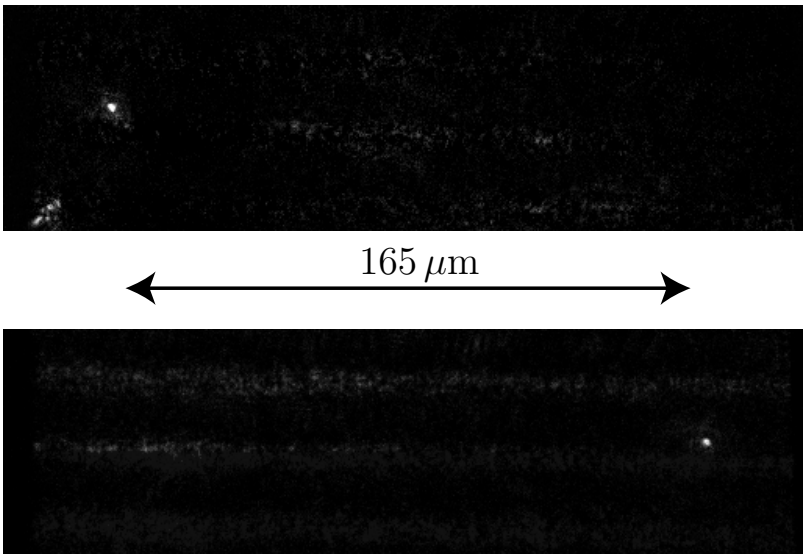

Figure 4.26: Transport of a single ion from the load zone to the experiment zone. The bright dot indicates the ion position, which has moved about $165\,\mu$m.

Unfortunately, that reliability was short-lived. We eventually started losing ions during the transport. Instead of moving the ion all $165\,\mu$m at once, we broke the transport into smaller steps. We noticed that the ion was getting severely decompensated during the transport, as evidenced by the shim voltages required. We adjusted the shim voltages at smaller intervals as shown in Fig. 4.27. Large changes in the z-shim, on the order of kV/m were required. We attribute this large spatial variation to charging of the trap surface. Debugging transport is somewhat of a vicious cycle as if the ion is lost, reloading will make the transport even harder due to the charging from the photoionization beam.

We suspect our transport became more unreliable due to a degradation of our UV fiber, resulting in a loss of power for Doppler cooling. Reducing the amount of cooling meant the ion was more likely to leave the trap if it were uncompensated. However, changing the fiber did not fix this issue and we eventually stopped working on transport altogether to focus on experiments in

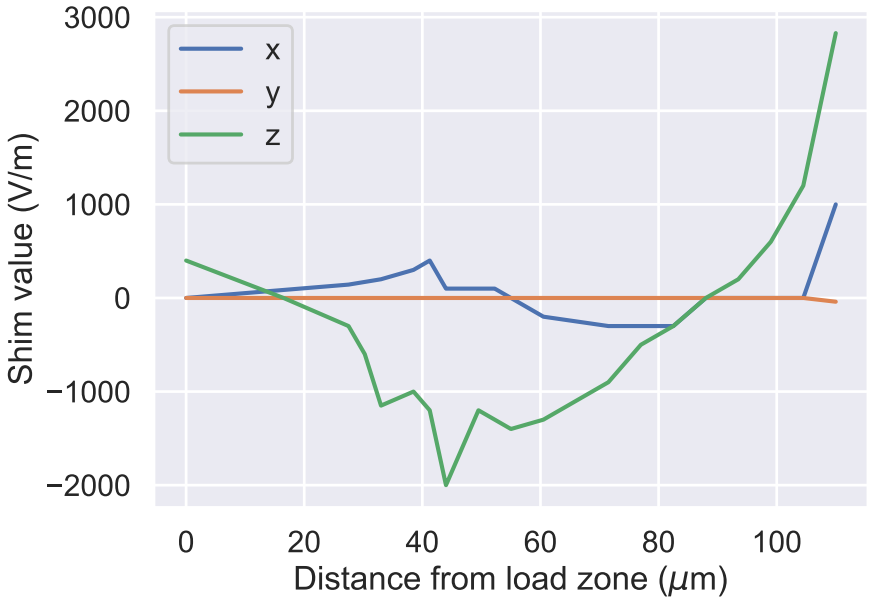

Figure 4.27: We plot the compensation voltages required during the ion transport as a function of its position from the load zone (0 μm is at the load zone). We found that there were large changes in the required z-shim.

the load zone. This provides a good juncture to terminate the transport discussion and focus on experiments in the subsequent chapters.

All we hear is radio ga ga,

Radio blah blah,

Radio, what's new?

Someone still loves you

Queen

5

Spin-motion coupling with a radiofrequency magnetic field gradient

In this chapter, we discuss a new method of laser-free spin-motion coupling that uses an oscillating magnetic-field gradient close to the motional frequency, at radio frequency. This technique was developed during this Ph.D. and addresses some of the challenges present in previous laser-free methods. We discuss the physics underlying this mechanism, demonstrate sidebands using this technique, and use those sidebands to cool a motional mode close to its ground state. The results presented in this chapter were published in [Srinivas et al., 2019]. We note that similar physics was observed using an intensity gradient of a running optical lattice [Ding et al., 2014], which inspired this work.

5.1 Spin-motion coupling with an oscillating magnetic-field gradient

In this section, we derive the sideband interaction that couples the spin to the motion using an oscillating gradient. For simplicity, we first assume the ion experiences only a gradient oscillating at ω_g and a microwave field close to its qubit frequency. We discuss the effects of an additional

oscillating magnetic field at ω_g in section 5.2. The Hamiltonian can be written as

$$\begin{aligned}\hat{H}(t) =& \frac{\hbar\omega_0}{2}\hat{\sigma}_z + \hbar\omega_r\hat{a}^\dagger\hat{a} \\ &+ 2\hbar\Omega_g\cos(\omega_g t)\hat{\sigma}_z(\hat{a}+\hat{a}^\dagger) \\ &+ 2\hbar\Omega_\mu\cos\big((\omega_0+\delta)t\big)\hat{\sigma}_x.\end{aligned} \tag{5.1}$$

The first two terms correspond to the ion's qubit and motional energies, with frequencies ω_0 and ω_r respectively. The next term corresponds to the spin-dependent force arising from a magnetic field gradient with a Rabi frequency Ω_g that is oscillating at ω_g. The last term corresponds to the microwave field with spin-flip Rabi frequency Ω_μ oscillating close to the qubit frequency ω_0 with a detuning δ. The Rabi frequency from the gradient[1] Ω_g is defined as

$$\Omega_g \equiv \frac{r_0(\hat{r}\cdot\nabla B_g)}{4}\frac{d\omega_0}{dB_z}\Big|_{B_z=|\vec{B}_0|}. \tag{5.2}$$

A quantization axis $\hat{z}$ is defined by a static magnetic field $\vec{B}_0$. The sensitivity of the qubit frequency ω_0 to changes in an additional magnetic field B_z along this quantization axis is described by $d\omega_0/dB_z$. This sensitivity in general depends on the magnitude of $\vec{B}_0$ as well. The gradient of the magnetic field oscillating at ω_g is described by ∇B_g, where B_g is the magnetic field along the quantization axis oscillating at ω_g. The ground-state extent of the ion's wave function for the motional mode along the $\hat{r}$ direction is characterized by $r_0 = \sqrt{\hbar/2M\omega_r}$ for ion mass M. This gives an implicit $\omega_r^{-1/2}$ dependence to Ω_g. This dependence is present in all types of spin-motion coupling, including laser-based methods.

The microwave Rabi frequency[2] Ω_μ is

$$\Omega_\mu = \frac{B_x}{2\hbar}\left\langle\downarrow\right|\mu_x\left|\uparrow\right\rangle, \tag{5.3}$$

[1] This is equivalent to $\Omega^z_{j,n}$ in Ref. [Ospelkaus et al., 2008].
[2] This corresponds to Ω^x in Ref. [Ospelkaus et al., 2008].

where B_x is the component of the oscillating microwave magnetic field perpendicular to the quantization axis and μ_x is the component of the ion's magnetic moment along the same direction.

The dynamics of this Hamiltonian in the lab frame can be difficult to analyze. To elucidate the physical mechanism, let us first look at the static gradient case by setting $\omega_g = 0$. Going into the interaction picture with respect to the Hamiltonian corresponding to the qubit frequency, $H_0 = \frac{\hbar\omega_0}{2}\hat{\sigma}_z$, our interaction picture Hamiltonian is

$$\begin{aligned} \hat{H}_{\text{static}}(t) = 2\hbar\Omega_g\hat{\sigma}_z(\hat{a}+\hat{a}^\dagger) & \qquad \text{spin-dependent displacement} \\ +\hbar\omega_r\hat{a}^\dagger\hat{a} & \qquad \text{motional frequency} \\ +\hbar\Omega_\mu\left(\hat{\sigma}_+e^{-i\delta t}+\hat{\sigma}_-e^{i\delta t}\right). & \qquad \text{microwave term} \end{aligned} \tag{5.4}$$

The first term corresponds to a spin-dependent displacement, the second term to the motional frequency, and the last term to the microwave fields which drive spin flips, where $\hat{\sigma}_+ = |\uparrow\rangle\langle\downarrow|$ and $\hat{\sigma}_- = |\downarrow\rangle\langle\uparrow|$.

In the absence of the spin-dependent displacement, the microwave field can only drive spin-flip transitions[3] . Sideband transitions where $\Delta n \neq 0$ are forbidden as the different $|n\rangle$ Fock states are orthogonal. However, if $|\uparrow\rangle$ is displaced relative to $|\downarrow\rangle$, spatial overlap between the motional wavefunctions for different spin states is modified, enabling sideband transitions [Förster et al., 2009]. In order to drive these transitions, the microwave field would have to be detuned by the motional frequency with $\delta = \pm\omega_r$. This process is illustrated in Fig. 5.1(a). This effect can also be viewed as similar to Franck-Condon factors that appear in molecular spectroscopy [Förster et al., 2009, Hu et al., 2011].

The dynamics with an oscillating gradient in Eq. 5.1 are similar to the static gradient case when going into a frame of reference oscillating at the qubit frequency ω_0 and the oscillating gradient frequency ω_g. This transformation is accomplished by going into an interaction picture with respect to $H_0 = \frac{\hbar\omega_0}{2}\hat{\sigma}_z + \hbar\omega_g\hat{a}^\dagger\hat{a}$. We obtain the interaction picture Hamiltonian $H_{\omega_g}(t)$,

[3] We refer to the microwave **field**. A microwave **gradient** detuned by $\pm\omega_r$ can also drive sideband transitions but this is a different mechanism altogether. See Eq. 2.26.

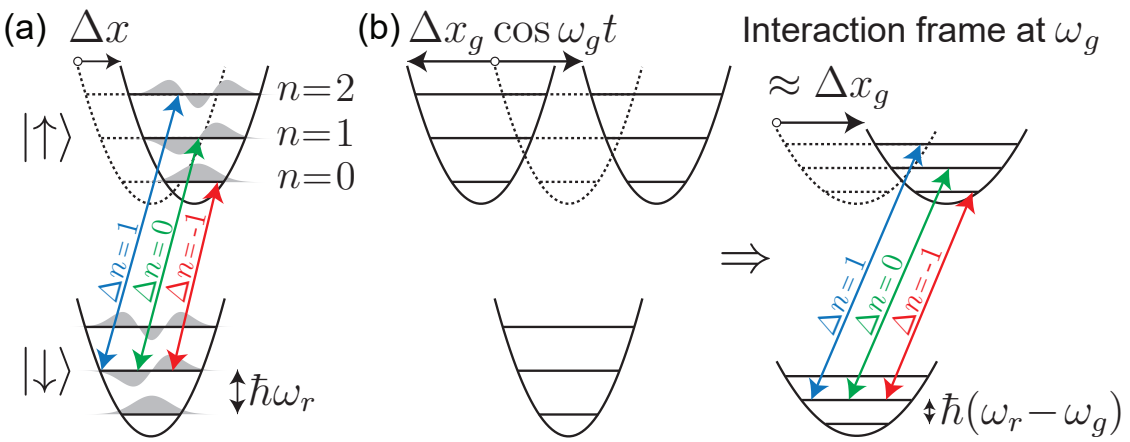

Figure 5.1: Schematic of a qubit coupled to a harmonic oscillator with a spin-dependent displacement from (a) a static gradient or (b) an oscillating gradient[4]. An additional microwave field drives $|\downarrow\rangle \leftrightarrow |\uparrow\rangle$ transitions. (a) For a static gradient, detuning the microwave field by $\pm\omega_r$ drives sideband transitions with $\Delta n = \pm 1$. (b) An oscillating gradient at ω_g is formally equivalent to a static gradient in the interaction frame oscillating at ω_g, ignoring fast-oscillating terms. The sideband transitions now occur at detunings $\pm(\omega_r - \omega_g)$. A more detailed discussion of the different displacements can be found in appendix C.

$$
\begin{aligned}
\hat{H}_{\omega_g}(t) =& \hbar\Omega_g\hat{\sigma}_z\big[(\hat{a}+\hat{a}^\dagger) && \text{spin-dependent displacement}\\
&+(\hat{a}e^{-2i\omega_g t}+\hat{a}^\dagger e^{2i\omega_g t})\big] && \text{counter-rotating terms}\\
&+\hbar(\omega_r-\omega_g)\hat{a}^\dagger\hat{a} && \text{modifed ``motional frequency''}\\
&+\hbar\Omega_\mu\left(\hat{\sigma}_+e^{-i\delta t}+\hat{\sigma}_-e^{i\delta t}\right). && \text{microwave term}
\end{aligned}
\tag{5.5}
$$

In this interaction frame, we effectively get a static spin-dependent displacement. However, instead of the microwave field driving sideband transitions at detunings of $\pm\omega_r$, they now occur at detunings of $\delta = \pm(\omega_r - \omega_g)$. We have an additional counter-rotating term shown in the second line which can be ignored if $\omega_g \gg \Omega_g$.

To obtain the sideband transitions, we transform Eq. 5.5 into a second interaction picture with respect to the term $\hbar(\omega_r - \omega_g)\hat{a}^\dagger\hat{a}$. One can also go straight into the interaction picture with respect to $H_0 = \frac{\hbar\omega_0}{2}\hat{\sigma}_z + \hbar\omega_r\hat{a}^\dagger\hat{a}$ from Eq. 5.1. The order in the text is chosen for pedagogical

[4] This figure is **significantly** out of scale. The ion's ground state extent is $\sim 5.7\,\text{nm}$, while the displacements are $\sim 30\,\text{pm}$. Artistic liberty was exercised to make the displacement more than a pixel. More detail on how the displacement can be estimated can be found in appendix C.

reasons. We obtain the interaction Hamiltonian $H_I(t)$,

$$\begin{aligned}\hat{H}_I(t) =&\hbar\Omega_g\hat{\sigma}_z\Big[(\hat{a}e^{-i(\omega_r-\omega_g)t}+\hat{a}^\dagger e^{i(\omega_r-\omega_g)t})\\ &+(\hat{a}e^{-i(\omega_r+\omega_g)t}+\hat{a}^\dagger e^{i(\omega_r+\omega_g)t})\Big]\\ &+\hbar\Omega_\mu\left(\hat{\sigma}_+e^{-i\delta t}+\hat{\sigma}_-e^{i\delta t}\right).\end{aligned} \tag{5.6}$$

In order to transfer into the interaction picture with respect to the gradient term (corresponding to Ω_g), we derive the propagator using the first term of the Magnus expansion. This step is required as the commutator of $\hat{H}_I(t)$ with itself at different times is not zero, i.e. $[\hat{H}_I(t),\hat{H}_I(t')]\neq 0$. The second term in the Magnus expansion is just a global phase, which is ignored. Terms that are higher order in the Magnus expansion are thus vanishing. A detailed derivation is in appendix D. The propagator $\hat{U}_g^\dagger(t)$ is

$$\begin{aligned}\hat{U}_g^\dagger(t) = \exp\Big[&\frac{\Omega_g}{\omega_r-\omega_g}\hat{\sigma}_z\big(-\hat{a}(e^{-i(\omega_r-\omega_g)t}-1)\\ &+\hat{a}^\dagger(e^{i(\omega_r-\omega_g)t}-1)\big)+\\ &\frac{\Omega_g}{\omega_r+\omega_g}\hat{\sigma}_z\big(-\hat{a}(e^{-i(\omega_r+\omega_g)t}-1)\\ &+\hat{a}^\dagger(e^{i(\omega_r+\omega_g)t}-1)\big)\Big].\end{aligned} \tag{5.7}$$

Using this propagator, we derive the interaction Hamiltonian with respect to the gradient term $\hat{H}_{I'}(t)$,

$$\hat{H}'_I(t) =\hat{U}_g^\dagger(t)\hbar\Omega_\mu(\hat{\sigma}_+e^{-i\delta t}+\hat{\sigma}_-e^{i\delta t})\hat{U}_g(t). \tag{5.8}$$

Making use of the Baker-Campbell-Hausdorff theorem (appendix A), keeping only the lowest order terms, we obtain $\hat{H}_{I'}(t)$,

$$\begin{aligned}\hat{H}_I'(t) \simeq & \hbar\Omega_\mu(\hat{\sigma}_+ e^{-i\delta t} + \hat{\sigma}_- e^{i\delta t}) \\ & + 2\hbar\Omega_g\Omega_\mu(\hat{\sigma}_+ e^{-i\delta t} - \hat{\sigma}_- e^{i\delta t}) \\ & \times \Big\{\frac{1}{\omega_r - \omega_g}\big(\hat{a}^\dagger(e^{i(\omega_r-\omega_g)t} - 1) - \hat{a}(e^{-i(\omega_r-\omega_g)t} - 1)\big) \\ & + \frac{1}{\omega_r + \omega_g}\big(\hat{a}^\dagger(e^{i(\omega_r+\omega_g)t} - 1) - \hat{a}(e^{-i(\omega_r+\omega_g)t} - 1)\big)\Big\}.\end{aligned} \tag{5.9}$$

We obtain sideband transitions when $\delta = \pm(\omega_r - \omega_g)$, where (+) corresponds to blue sideband transitions and (-) corresponds to red sideband transitions. We obtain the Hamiltonian $\hat{H}_{\text{sb}}$,

$$\hat{H}_{\text{sb}} = \pm\frac{2\hbar\Omega_g\Omega_\mu}{\omega_r - \omega_g}(\hat{\sigma}_\pm\hat{a}^\dagger + \hat{\sigma}_\mp\hat{a}), \tag{5.10}$$

where the sideband Rabi frequency Ω_{sb} is

$$\Omega_{\text{sb}} = \frac{2\Omega_g\Omega_\mu}{\omega_r - \omega_g}. \tag{5.11}$$

For Eqs. 5.10 and 5.11, we have neglected fast-rotating terms corresponding to a detuned carrier field and the additional sideband at $\omega_r + \omega_g$, which are detuned by δ and $2\omega_g$, respectively. Errors caused by these terms are coherent, and can be mitigated, by for example ramping the gradient and microwaves on and off adiabatically. Note that the additional sidebands for $\delta = \pm(\omega_r + \omega_g)$ will have a sideband Rabi frequency that is proportional to $1/(\omega_r + \omega_g)$, and thus will be significantly weaker than the sidebands at $\delta = \pm(\omega_r - \omega_g)$ when ω_g is close to ω_r.

5.2 Residual oscillating magnetic field

To generate the gradient for the sideband interactions, we apply a current oscillating at ω_g to our trap electrodes. However, the current will not only give us an oscillating magnetic-field gradient, but also an oscillating magnetic field at the ion. This oscillating magnetic field will modulate the frequency of our field-sensitive qubit which gives rise to some interesting effects. To simplify the analysis, we ignore the effect of the gradient and the motion. Our Hamiltonian is then

$$\begin{aligned}\hat{H}_0(t) =& \frac{\hbar\omega_0}{2}\hat{\sigma}_z + 2\hbar\Omega_z \cos(\omega_g t)\hat{\sigma}_z \\ &+2\hbar\Omega_\mu \cos\big((\omega_0+\delta)t\big)\hat{\sigma}_x.\end{aligned} \tag{5.12}$$

The term with Ω_z corresponds to the magnetic field oscillating at ω_g, where Ω_z is

$$\Omega_z \equiv \frac{B_g}{4}\frac{d\omega_0}{dB_z}\Big|_{B_z=|\vec{B}_0|}. \tag{5.13}$$

The terms in Ω_z follow the same definitions as Eq. 5.2, with B_g the magnitude of the magnetic field along the quantization axis oscillating at ω_g. Effectively, this term causes a modulation of the qubit frequency with frequency ω_g and amplitude Ω_z. To see this frequency modulation more clearly, we go into the interaction picture with respect to the first two terms of Eq. 5.12, deriving the propagator $\hat{U}_I(t)$,

$$\begin{aligned}\hat{U}_I^\dagger(t) &= \exp\Big(\frac{i}{\hbar}\int_0^t \Big[\frac{\hbar\omega_0}{2}\hat{\sigma}_z + 2\hbar\Omega_z\cos(\omega_g t')\hat{\sigma}_z\Big]dt'\Big) \\ &= \exp\Big(\frac{i\omega_0 t}{2}\hat{\sigma}_z + \frac{2i\Omega_z}{\omega_g}\sin(\omega_g t)\hat{\sigma}_z\Big).\end{aligned} \tag{5.14}$$

We thus obtain the interaction Hamiltonian for the last term in Eq. 5.12,

$$\hat{H}_I(t) = \hbar\Omega_\mu\left(e^{-i\delta t}\hat{\sigma}_+\sum_{m=-\infty}^{\infty} J_m\left(\frac{4\Omega_z}{\omega_g}\right)e^{im\omega_g t}\right) + \text{H.c}, \tag{5.15}$$

where we use the Jacobi-Anger expansion,

$$e^{iz\sin\theta} = \sum_{m=-\infty}^{\infty} J_m(z)e^{im\theta}. \tag{5.16}$$

When $\delta = m\omega_g$, we implement spin-flip transitions described by the Hamiltonian $\hat{H}_m$,

$$\hat{H}_m = \hbar\Omega_\mu J_m\left(\frac{4\Omega_z}{\omega_g}\right)(\hat{\sigma}_+ + \hat{\sigma}_-), \tag{5.17}$$

where we have dropped the fast-rotating terms. This applies for any oscillating magnetic field, including those generated by rf trapping potentials [Meir et al., 2018]. The Rabi frequency Ω_m of these transitions is

$$\Omega_m = \Omega_\mu J_m \left(\frac{4\Omega_z}{\omega_g} \right). \tag{5.18}$$

Thus, the oscillating magnetic field would modify the microwave term from the previous section and would need to be considered for the sideband transitions as well. Modifying Eq. 5.10,

$$\hat{H}_{\mathrm{sb},m} = \pm \frac{2\hbar\Omega_g\Omega_\mu}{\omega_r - \omega_g} J_m \left(\frac{4\Omega_z}{\omega_g} \right) (\hat{\sigma}_\pm \hat{a}^\dagger + \hat{\sigma}_\mp \hat{a}). \tag{5.19}$$

The largest sideband Rabi frequency corresponds to the largest value of the Bessel function $J_m\left(\frac{4\Omega_z}{\omega_g}\right)$. This value occurs for $J_0(0)$, which is achieved when $B_g = 0$, i.e. the oscillating magnetic field along the quantization is nulled. We explain this nulling process in detail in section 5.5.

5.3 Experimental implementation

For these experiments, we use a field-sensitive "stretch qubit" with a transition frequency of $\omega_0/2\pi = 1.326\,\mathrm{GHz}$ as described in section 4.2.1. The magnetic field sensitivity of this transition is $(d\omega_0/dB_z)/2\pi = -19.7\,\mathrm{MHz/mT}$. The qubit preparation and readout is described in Sec. 4.2. For these experiments with a single ion, the motional frequencies are $(\omega_a, \omega_{r_1}, \omega_{r_2})/2\pi \approx (3.2, 6.2, 7.6)\,\mathrm{MHz}$, where $\vec{a}$ is along the axis of the trap, and $\vec{r}_1$, $\vec{r}_2$ lie in the radial plane (Fig.5.2). By design, the magnetic field gradient is only in the radial plane and thus the spin-motion coupling is only for the two radial modes.

To realize spin-motion coupling, we apply simultaneous currents (which are ramped on and off over 10 μs) to the trap electrodes at two frequencies, ω_g and $\omega_0 + \delta$. We apply up to 0.5(1) A rms per electrode at $\omega_g/2\pi = 5\,\mathrm{MHz}$, corresponding to 6(1) mW of dissipation in the trap electrodes[5] ;

[5] These electrodes are shorted to ground at their far end, so most of the power is reflected. See Sec. 3.1 for details.

dissipation from the drive at $\omega_0 + \delta$ is $\ll 1\,\mathrm{mW}$. Currents oscillating at ω_g are applied to electrodes 1, 2 and 3 as shown in Fig. 5.2. The microwave currents close to the qubit frequency are applied to either electrode 1 or 2 for the experiments described here.

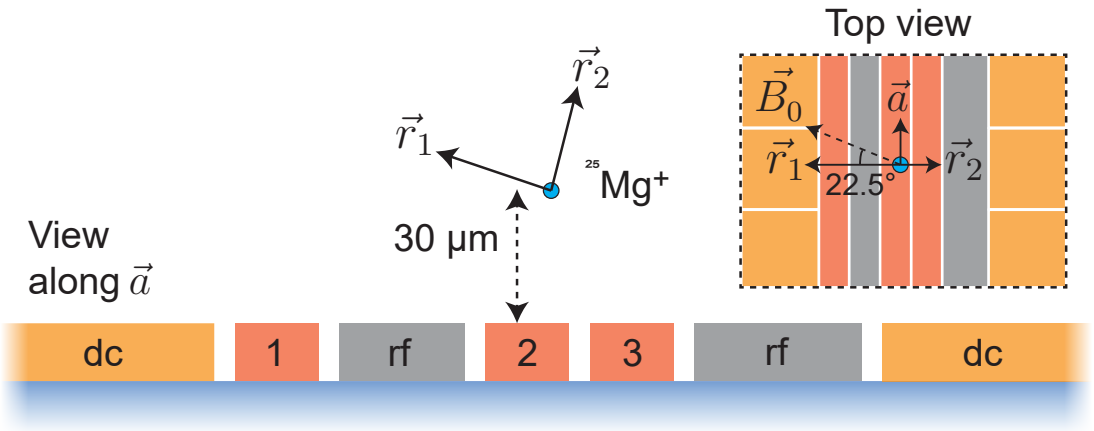

Figure 5.2: Schematic of the surface electrode trap with the relevant details for the experiments discussed in this chapter. Oscillating currents in electrodes 1, 2, and 3 generate magnetic fields and magnetic field gradients at the ion. A static magnetic field $\vec{B}_0$ parallel to the surface of the trap defines the quantization axis $\hat{z}$. From the electrode geometry, the relevant gradients oscillating at ω_g are only along the radial modes $\vec{r_1}$ and $\vec{r_2}$. Thus, sideband transitions are only observed for those modes using the technique described in this chapter.

5.4 Spectroscopy with an oscillating magnetic field gradient

We first perform microwave spectroscopy with the oscillating gradient applied. The microwave pulse is applied for $500\,\mu$s and the detuning δ is varied. The ion is initialised in $|{\downarrow}\rangle$ to its Doppler temperature ($\bar{n} \approx 2$) so both motion-adding blue sideband ($\Delta n = 1$) and motion-subtracting red sideband ($\Delta n = -1$) transitions could be observed. A reduced spectrum with the strongest sidebands for each of the radial modes is shown in Fig. 5.3. For $\delta = 0$, the spin-flip transition is driven resonantly. The blue (red) sideband transitions occur when $\delta = +[\omega_{ri} - \omega_g]$ ($\delta = -[\omega_{ri} - \omega_g]$), where ω_{ri} is the frequency of the radial mode $\vec{r}_1$ or $\vec{r}_2$.

However, the full spectroscopy shows additional spin-flip transitions, as shown in Fig.5.4. We see spin-flip transitions at $\delta = m\omega_g$, as the magnetic field $B_g \neq 0$ as described in Eq. 5.17.

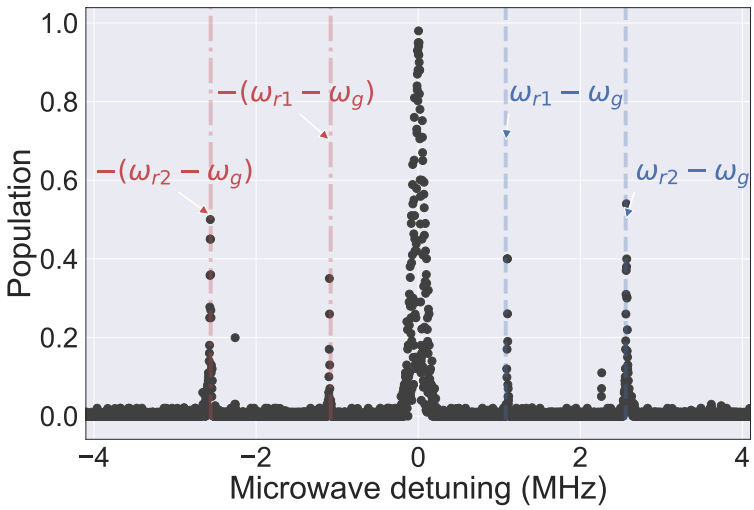

Figure 5.3: Sideband transitions with microwaves and an oscillating magnetic field gradient. In addition to a magnetic field gradient oscillating at ω_g, an additional microwave pulse with detuning δ is applied. Blue (red) sideband transitions with $\Delta n = 1$ ($\Delta n = -1$) occur when $\delta = +[\omega_{ri} - \omega_g]$ ($\delta = -[\omega_{ri} - \omega_g]$).[6]

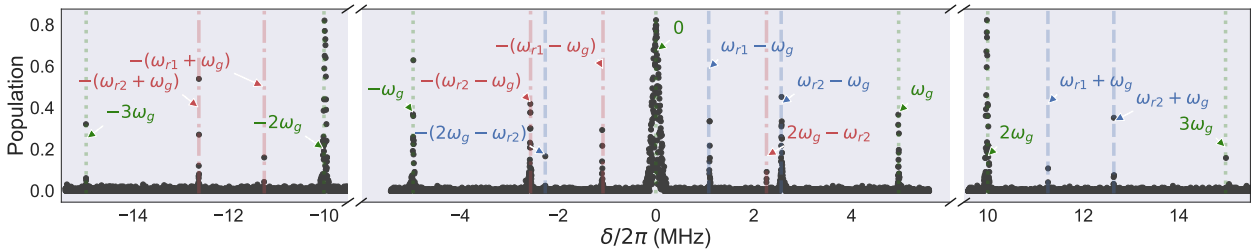

Figure 5.4: Microwave spectroscopy with an applied magnetic field gradient oscillating at $\omega_g/2\pi = 5\,\text{MHz}$. The microwave field has a detuning δ which is varied. Spin-flip transitions that leave the motional state unchanged ($\Delta n = 0$), denoted by the green-dotted lines, occur when $\delta = \pm m\omega_g$. Blue sideband transitions with $\Delta n = 1$ (blue dashed lines) occur when $\delta = +(\omega_{ri} \pm \omega_g)$. Red sideband transitions with $\Delta n = -1$ (red dash-dotted lines) occur when $\delta = -(\omega_{ri} \pm \omega_g)$.

In addition to the blue (red) transitions at $\delta = +(-)[\omega_{ri} - \omega_g]$, we see sideband transitions at $\delta = +(-)[\omega_{ri} + \omega_g]$. We also observe weaker higher-order transitions due to the frequency modulation of the qubit frequency as described in Eq. 5.19.

[6] The eagle-eyed reader might observe that these transitions are slightly shifted from the exact values of $\delta = \pm[\omega_{ri} - \omega_g]$). This shift is due to the ac Zeeman shift from the detuned microwave fields as described in Sec. 5.6.1.

5.5 Measuring and nulling the oscillating magnetic field

We characterize the effect of the oscillating magnetic field by measuring the Rabi frequency of the spin-flip transitions Ω_m as a function of B_g following Eq. 5.17. We apply a current oscillating at ω_g to only electrode 2, in addition to a microwave field on resonance with Rabi frequency $\Omega_\mu/2\pi = 375\,\text{kHz}$. This microwave field is also generated by a current applied to electrode 2, and this Rabi freuqency is measured without any applied current at ω_g ($B_g = 0$). We vary the amplitude of the current at ω_g and measure the Rabi frequency of the spin-flip transitions as a function of this amplitude. We perform this first for the J_0 transition.

For each amplitude of the oscillating magnetic field B_g, we measure the Rabi frequency of the J_0 transition. An example measurement is shown in Fig. 5.5 for $B_g = 0$. From these data, we extract a Rabi frequency. We repeat this process for different values of B_g as shown in Fig. 5.6. While increasing the value of B_g, the frequency of the spin-flip transition shifts slightly due to an ac Zeeman shift from B_g. This shift must be accounted for to keep the spin-flip transitions on resonance. We scan the microwave detuning δ to calibrate this shift. A fit of the Rabi frequencies as a function of B_g to the J_0 Bessel function gives a scaling factor from the amplitude of the applied current oscillating at ω_g to the amplitude of the oscillating magnetic field B_g at the ion.

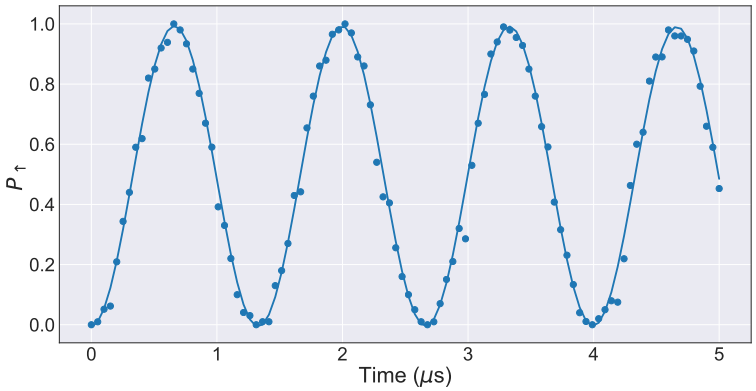

Figure 5.5: Example Rabi flopping data for the J_0 transition. For these data the amplitude of B_g was set to 0 and $\Omega_0/2\pi$ was 375 kHz. The ion was initialized to $|\downarrow\rangle$ and the microwave field drives the $|\downarrow\rangle \leftrightarrow |\uparrow\rangle$ transition.

We repeat the measurements for the $m = \{1, 2, 3, 4, 5\}$ transitions, changing the detuning of

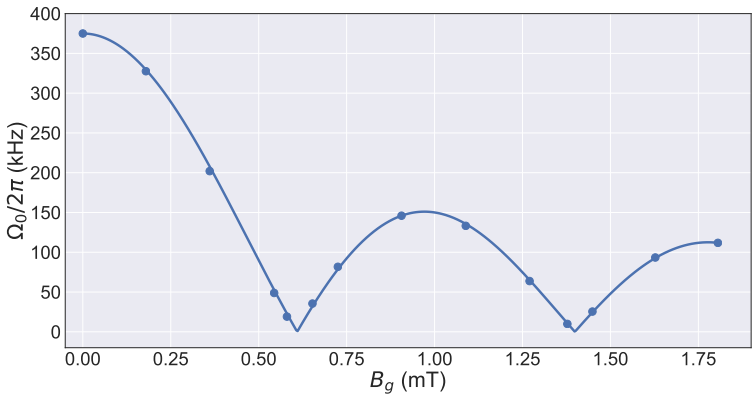

Figure 5.6: Spin-flip transition Rabi frequency Ω_0 as a function of magnetic field B_g oscillating at ω_g. For these data, the microwave field is nominally on resonance after taking into account the additional ac Zeeman shift ($\delta = 0$).

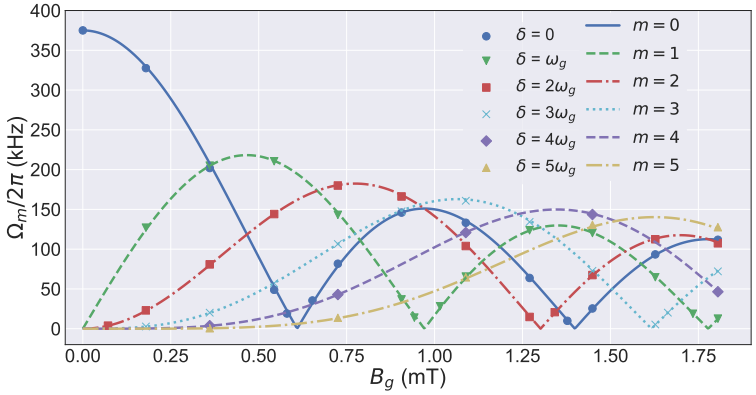

Figure 5.7: Plot of the spin-flip Rabi frequency Ω_m versus the amplitude of the oscillating magnetic field B_g. Spin-flip transitions occur when the detuning of the microwave field $\delta = m\omega_g$. The theory curves indicated by the dashed lines have no free parameters. Error bars are smaller than the data points.

the microwave field to $\delta = m\omega_g$ accordingly. As before, there is a slight offset to the exact detuning, with an additional contribution to the ac Zeeman shift from the detuned microwave field which is accounted for. The results are shown in Fig. 5.7. Note that for the $m > 0$ transitions, the theory lines have no free parameters. We use the same scaling factor that we determined from the J_0 transition. We see that the data seem to fit Eq. 5.17 well[7] .

In order to maximize the sideband Rabi frequency Ω_{sb}, we set $B_g = 0$ and thus Ω_z to zero

[7] Would calculating Bessel functions be a more practical application of near-term quantum computers than factoring? Certainly for our system.

as shown in Eq. 5.19. We set $B_g = 0$ by minimizing the value of Ω_1 by adjusting the phases and amplitudes of the currents oscillating at ω_g for all three electrodes 1, 2, and 3. As $B_g \to 0$, Ω_1 is proportional to ${B_g}^8$. At $J_0(0)$, the sideband Rabi frequency is insensitive to variations in B_g to first order. We note that nulling B_g does not mean that all components of the oscillating magnetic field are also nulled. However, only the component of the magnetic field along the quantization field will create this frequency modulation effect; other perpendicular components produce an ac Zeeman shift of less than 100 kHz for the experiments in this chapter.

5.6 Sideband Rabi frequency

In addition to the magnitude of B_g, the sideband Rabi frequency also depends on the Rabi frequency of the microwave field Ω_μ. Setting $J_0 = 0$ in Eq. 5.19 to achieve the largest sideband Rabi frequency, we obtain our initial expression for the sideband Rabi frequency in Eq. 5.11 where

$$\Omega_{\text{sb}} = \frac{2\Omega_g \Omega_\mu}{\omega_r - \omega_g}.$$

At first glance, it may seem that we can make this Rabi frequency arbitrarily large by increasing the microwave Rabi frequency Ω_μ, which would be easy to do in our system without large currents. However, an important effect that needs to be considered is the ac Zeeman shift from this microwave field.

5.6.1 ac Zeeman shift from microwave fields

To drive the blue (red) sideband transition, a microwave field detuning of $\delta = +(-)[\omega_r - \omega_g]$ is required. For $\omega_r - \omega_g > 0$, a blue (red) detuned microwave field will generate a negative (positive) ac Zeeman shift that will need to be accounted for. This shift will push the absolute value of the detuning from the unshifted qubit frequency closer to 0 as Ω_μ is increased (Eq.5.21). This effect ultimately limits the value of Ω_μ that can be used. The ac Zeeman shift Δ_{ac} from a detuned field δ is

[8] $J_1(x) \propto x, x \to 0$

$$\Delta_{ac} = \delta \mp \sqrt{\delta^2 + 4\Omega_\mu^2}, \tag{5.20}$$

where - (+) corresponds to a blue (red) detuned field respectively [Foot, 2007]. This shift would modify the actual detuning required to $\delta = \pm(\omega_r - \omega_g) + \Delta_{ac}$. Solving for δ we obtain,

$$\delta = \pm\sqrt{(\omega_r - \omega_g)^2 - 4\Omega_\mu^2}. \tag{5.21}$$

Thus, $2\Omega_\mu < |\omega_r - \omega_g|$ and $\Omega_{\rm sb} \leq \Omega_g$ when using an oscillating gradient.[9] . As $2\Omega_\mu$ approaches $\omega_r - \omega_g$, the microwave field is shifted closer to resonance, driving spin-flip transitions.

5.6.2 Characterizing the sideband Rabi frequency

We experimentally verify Eq. 5.11, keeping Ω_g constant but varying the microwave Rabi frequency Ω_μ. For each value of Ω_μ, we first measure the ac Zeeman shift by scanning the detuning of the microwave field from the qubit frequency ω_0 and looking for the sideband transition. We measure $\Omega_{\rm sb}$ for the r_1 mode by first cooling to its ground state, then driving the blue sideband transition. Example data is shown in Fig. 5.8. For these experiments $\omega_{r1} - \omega_g/2\pi \approx 1.2\,\text{MHz}$.

We repeat these measurements for different values of Ω_μ, and a plot of both the sideband Rabi frequency Ω_{sb} and the microwave detuning δ to drive the blue sideband transition is shown in Fig. 5.9. We see a linear variation in $\Omega_{\rm sb}$, and as $2\Omega_\mu \to (\omega_{r1} - \omega_g)$, $\delta \to 0$. From a linear fit of the data, we determine that $\Omega_g/2\pi$ =1.383(6) kHz. We can use this Rabi frequency to determine the magnetic field gradient. Following Eq. 5.2.

$$\hat{r} \cdot \nabla B_g = \frac{4\Omega_g}{r_0} \left(\frac{d\omega_0}{dB_z}\Big|_{B_z=|\vec{B}_0|} \right)^{-1}. \tag{5.22}$$

For these experiments, $r_0 \approx 5.7\,\text{nm}$, and the frequency sensitivity of the transition is $\approx 19.7\,\text{GHz/T}$, yielding a peak magnetic field gradient[10]of 49.4(2) T/m along the mode $\vec{r}_1$.

[9] There has to be some conservation principle here, but generating sidebands is hard and being able to crank up the microwave Rabi frequency would have been too easy a way out.

[10] For the gate experiments we perform later, we increase this gradient to $\approx 120\,\text{T/m}$!

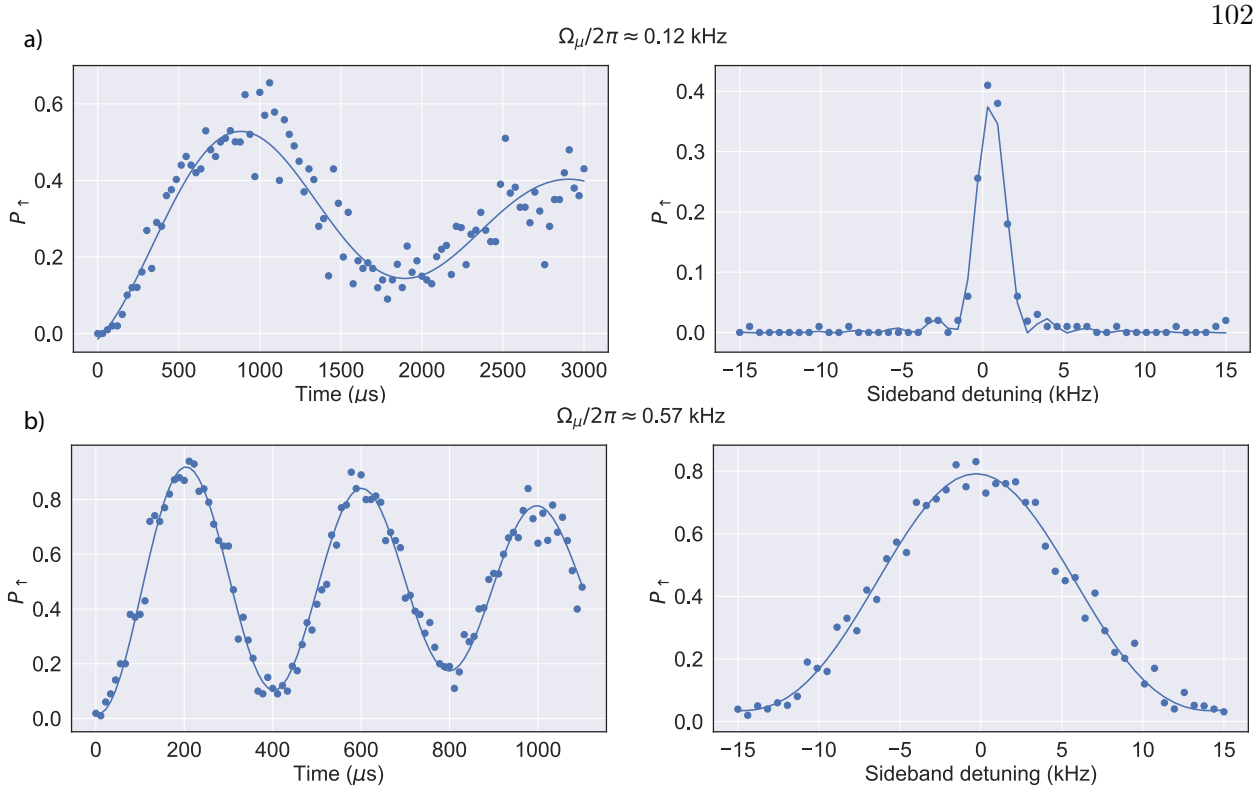

Figure 5.8: Example time and frequency scans on the blue sideband transition for two microwave Rabi frequencies **a)** $\Omega_\mu/2\pi \approx 0.12\,\text{kHz}$ and **b)** $\Omega_\mu/2\pi \approx 0.57\,\text{kHz}$. On the left, we show Rabi flopping on the sideband transition and on the right a detuning scan over the transition. The detuning scan is used to determine the frequency of the ac Zeeman shift and the time scan is used to determine the sideband Rabi frequency Ω_{sb}. An exponentially decaying sine function is fit to the time scan data to account for qubit decoherence due to fluctuating magnetic fields. As Ω_μ is increased, the sideband Rabi frequency Ω_{sb} is increased.

5.7 Sideband cooling

Finally, we use the resolved sideband at $\delta \approx -(\omega_{r1} - \omega_g)$ to cool the r_1 mode, as shown in Fig. 5.10. Starting from a Doppler-cooled mean phonon occupation of $\bar{n} \approx 2$, we use a sequence of twelve $150\,\mu$s red sideband pulses with interleaved optical repumping to reach $\bar{n} = 0.09(7)$. The total cooling duration is $\approx 2.5\,$ms, more than an order of magnitude faster than previous demonstrations of microwave cooling using the static gradient scheme [Weidt et al., 2015, Sriarunothai et al., 2018]. This speed-up is partly from using higher motional frequencies, which results in a lower initial thermal occupation after Doppler cooling. For the data in this section, we use only one microwave field in addition to the gradient to perform this cooling. We extend this technique to two microwave

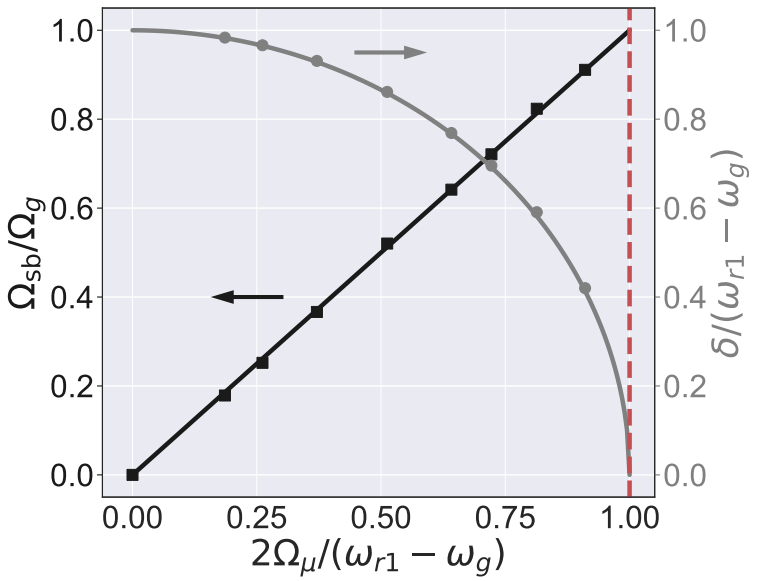

Figure 5.9: We plot the normalized blue sideband Rabi frequency $\Omega_{\rm sb}/\Omega_g$ (black squares, left axis) and the normalized microwave detuning $\delta/(\omega_{r1}-\omega_g)$ from Eq. (5.21) (gray circles, right axis) as a function of $2\Omega_\mu/(\omega_{r1}-\omega_g)$. Error bars are smaller than the data points. The red dashed line denotes the limit on Ω_μ described in the text. The black line is a linear fit to the data; the gray line is a theoretical plot following Eq. 5.21.

fields in Sec. 6.2.5.

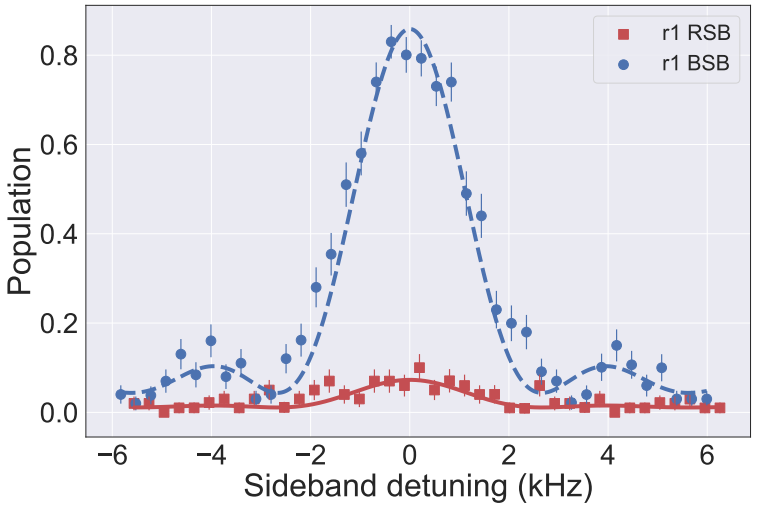

Figure 5.10: Populations in $|\uparrow\rangle$ after blue (BSB, circles) and red (RSB, squares) sideband analysis pulses on a ground-state-cooled ion initialised in $|\downarrow\rangle$ versus the detuning of the microwaves from the r_1 sideband transition. Both the cooling and the analysis pulses are performed using the oscillating gradient sidebands. Lines are fits giving a final Fock state population of $\bar{n} = 0.09(7)$.

5.8 Pulse shaping

For the data in this section, we operate in a limit where our microwave Rabi frequency Ω_μ is of the same order of magnitude as its detuning δ. Using a square pulse for the microwave would thus result in significant off-resonant excitation. To minimize this effect, we employ pulse-shaping of our microwave fields.

Specifically, we use a Blackman envelope [Harris, 1978] to adiabatically ramp the microwave pulse on and off over $10\,\mu$s. This pulse shaping allows us to operate with $2\Omega_\mu/(\omega_r - \omega_g) = 0.9$, and Ω_{sb} close to its maximum value of Ω_g as shown in the previous section. We program an approximation of the Blackman envelope to our IQ modulator, which controls the amplitude of the microwave field. An example waveform is shown in Fig. 5.11.

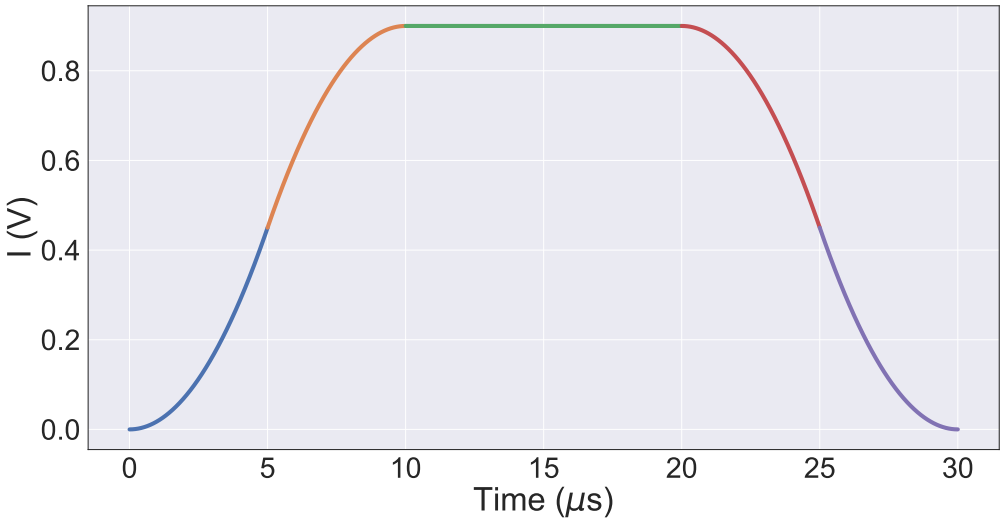

Figure 5.11: Plot of voltage versus time for the I port (I) of the IQ modulator. The voltage I is directly proportional to the microwave field amplitude at the ion. The microwave field is ramped on (blue and orange segments) and off (red and purple segments) over $10\,\mu$s. The field has a constant amplitude for a duration of $10\,\mu$s (green segment).

We plot the spectroscopy data from Fig. 5.3, but this time include data without pulse shaping in Fig. 5.12. We see that without the pulse shaping, there is significant off-resonant excitation. This excitation is purely an effect on the spin transition, and for the parameters of the experiment obscures the sideband transitions.

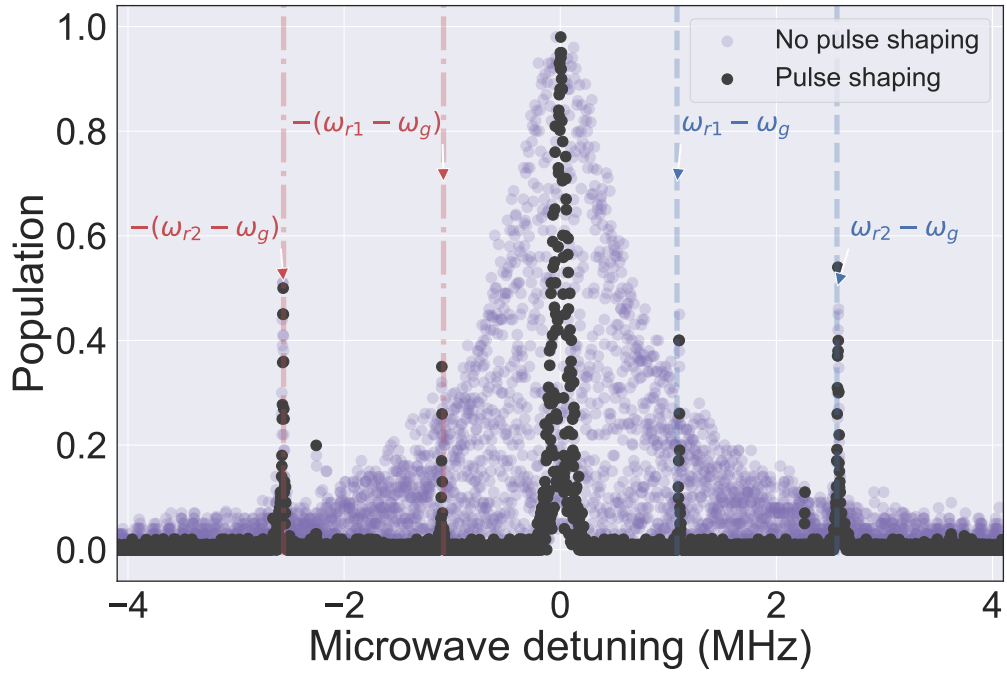

Figure 5.12: Identical plot to Fig. 5.3, except the data without pulse shaping are included. Pulse shaping significantly reduces the off-resonant excitation of the spin, allowing us to resolve the sideband transitions.

Section 6.1.2 contains a more detailed discussion on pulse shaping, especially for a bichromatic microwave field.

5.9 Comparison to static gradient scheme

The sideband Rabi frequency using an oscillating gradient is $\Omega_{\text{sb}} = \frac{2\Omega_g\Omega_\mu}{\omega_r-\omega_g}$ from Eq. 5.11. For a static gradient, the Ω_{sb} is instead,

$$\Omega_{\text{sb}} = \frac{4\Omega_g\Omega_\mu}{\omega_r}. \tag{5.23}$$

The microwave field detuning required to drive this sideband transition would be $\delta = \omega_r$, without considering the effects of ac Zeeman shifts. Following the discussion in Sec. 5.6.1, $2\Omega_\mu \leq \omega_r$, and the maximum value of the sideband Rabi frequency using a static gradient is $2\Omega_g$. The maximum value using an oscillating magnetic field gradient is Ω_g, as half of the gradient strength is lost as

a counter-rotating term that does not participate in the interaction(Eq. 5.5). However, $\Omega_{\mathrm{sb}} = \Omega_g$ is obtained for a lower microwave Rabi frequency Ω_μ using an oscillating gradient as opposed to a static gradient. Using an oscillating gradient, $2\Omega_\mu = \omega_r - \omega_g$ as opposed to $2\Omega_\mu = \omega_r/2$ for the static gradient. For surface traps especially, this is the difference between $2\Omega_\mu/2\pi \approx 1\,\mathrm{MHz}$ or $2\Omega_\mu/2\pi \approx 3\,\mathrm{MHz}$ for the oscillating and static gradients respectively, an order of magnitude in the microwave power. In principle, $\omega_r - \omega_g$ could be made smaller by setting ω_g closer to ω_r, but this is limited by the electric field at ω_g as discussed in sec 5.11.

5.10 Comparison to near-qubit-frequency oscillating gradient scheme

Compared to the near-qubit-frequency oscillating gradient scheme that requires gradients at GHz frequencies, it is much easier to generate large currents at radio frequencies. The maximum current that can be applied will likely be limited by Joule heating in the trap electrodes. This heating is significantly lower for a current at megahertz frequencies than at gigahertz frequencies due to the larger skin depth. From [Pozar, 2009], the skin depth δ_s for a conductor is defined as

$$\delta_s = \sqrt{\frac{2}{\omega\mu\sigma}}, \tag{5.24}$$

where ω is the angular frequency of the current, μ the magnetic permeability and σ the conductivity. For gold, $\mu = \mu_0 = 4\pi \times 10^{-7}\,\mathrm{N/A^2}$ and $\sigma = 4.098 \times 10^7\,\mathrm{S/m}$. For, $\omega/2\pi = 1.7\,\mathrm{GHz}$, the skin depth $\delta_s \approx 2\,\mu\mathrm{m}$. For, $\omega/2\pi = 5\,\mathrm{MHz}$, the skin depth $\delta_s \approx 35\,\mu\mathrm{m}$. For our $8\,\mu\mathrm{m}$ thick electrodes, operating at 5 MHz is effectively dc as far as heat dissipation goes. Furthermore, the magnitude of induced return currents in neighboring electrodes [Warring et al., 2013a] is reduced at lower frequencies, yielding a larger gradient at the ion for a given applied current.

An additional challenge is that one near-field gradient, and hence one large GHz oscillating current, is needed per sideband. Thus, for a typical Mølmer-Sørensen like interaction, two such gradients, from two large GHz currents, would be required.

5.11 Oscillating electric field

The finite impedance of the current-carrying electrodes results in an oscillating potential on these electrodes at ω_g. The resulting gradient in this potential at the ions gives rise to an electric field that drives the ion's motion. As for a classical oscillator, the amplitude of this motion is $\propto (\omega_r^2 - \omega_g^2)^{-1}$. As $\omega_g \to \omega_r$, the amplitude of this motion gets larger, causing the ion to sample increasingly anharmonic regions of the trap, and may even cause the ion to leave the trap altogether. These effects will set a practical limit on how close ω_g can be set to ω_r.

5.11.1 Measuring electric field

In order to measure the electric field, we use a technique described in [Warring et al., 2013a]. This technique is similar to what we use for compensating excess micromotion out of the plane of the trap as described in Sec. 4.4.1.2. An oscillating electric field at ω_g will cause ion motion oscillating at the same frequency. This motion enables a microwave magnetic field gradient to cause spin-flip transitions when detuned from the qubit frequency by $\pm\omega_g$. Following the discussion in Sec. 5.2, we note that an oscillating magnetic field B_g at ω_g can also give rise to spin flips when a microwave magnetic field with detuning ω_g from the qubit frequency is applied. To isolate the contribution to the Rabi frequency due to electric fields at ω_g, we perform the measurement using our "clock" qubit, the hyperfine transition ($|F = 3, m_F = 1\rangle \leftrightarrow |F = 2, m_F = 1\rangle$) which is first-order insensitive to magnetic field fluctuations at our applied magnetic field of $|\vec{B}_0| = 21.3\,\mathrm{mT}$. This yields $\Omega_z \approx 0$ even if there is an oscillating magnetic field B_g at ω_g at the ion, and as a result will not cause spin flips. The Rabi frequency of the spin flips due to the electric field is given by,

$$\Omega_{\text{spin-flip}} = \frac{2\Omega_{\mu\text{sb}}\Omega_e\omega_r}{(\omega_r^2 - \omega_g^2)}, \tag{5.25}$$

where $\Omega_e = qEr_0/2\hbar$ and $\Omega_{\mu\text{sb}}$ is the Rabi frequency of the sideband from the oscillating gradient close to the qubit frequency. The amplitude of the oscillating electric field at the ion is E and q is the elementary charge (Appendix D.6). Using the same parameters for the phases and amplitudes

when the magnetic field at ω_g is nulled at the ion, $\Omega_{\text{spin-flip}}/2\pi \approx 3.7\,\text{kHz}$. The Rabi frequency corresponding to the microwave magnetic field gradient $\Omega_{\mu\text{sb}}/2\pi \approx 0.5\,\text{kHz}$. Using these values, we estimate the electric field amplitude to be $\approx 10\,\text{V/m}$ at the ion.

5.11.2 Effect of electric field on ac Zeeman shift

The electric field oscillating at ω_g also has an effect on the ac Zeeman shift due to the magnetic field oscillating at ω_g. While we null the magnetic field to a large extent, the electric field would cause the ion to oscillate around the null point with amplitude r_e, where $r_e \propto (\omega_r^2 - \omega_g^2)^{-1}$. This will cause the ion to sample a magnetic field whose maximum value is proportional to this amplitude, $B \approx \nabla B r_e$. Since the ac Zeeman shift Δ_{ac} is proportional to B^2,

$$\begin{aligned} \Delta_{\text{ac}} &\propto r_e^2, \\ \therefore \Delta_{\text{ac}} &\propto \left(\frac{1}{\omega_r^2 - \omega_g^2}\right)^2. \end{aligned} \tag{5.26}$$

We measured the ac Zeeman shift as a function of the radial mode frequency ω_r and use this simple model to fit the data, which is shown in Fig. 5.13. We see good agreement between the data and the fit. However, this model only accounts for the coupling of the electric field to one mode of motion. Other modes which have an overlap with the electric field would have additional shifts with a similar scaling as Eq. 5.26, except that ω_r is replaced by the particular mode frequency.

5.11.3 Shift on motional frequency

Finally, the electric field also gives rise to a pseudopotential that modifies the curvature of the electric fields at the ion, and thus the motional frequencies. For these experiments, the shift[12] on ω_r was about 4 kHz. We measure this shift by comparing the motional frequency with and without

[11] We were puzzled for a long time that we couldn't null the ac Zeeman shift closer to 0. However, once we figured out this effect, the ac Zeeman shifts were not really problematic for any experiments we wanted to as long as we could calibrate it so we did not investigate this further.

[12] This shift increases to about 15 kHz in later experiments as we increased the current at ω_g.

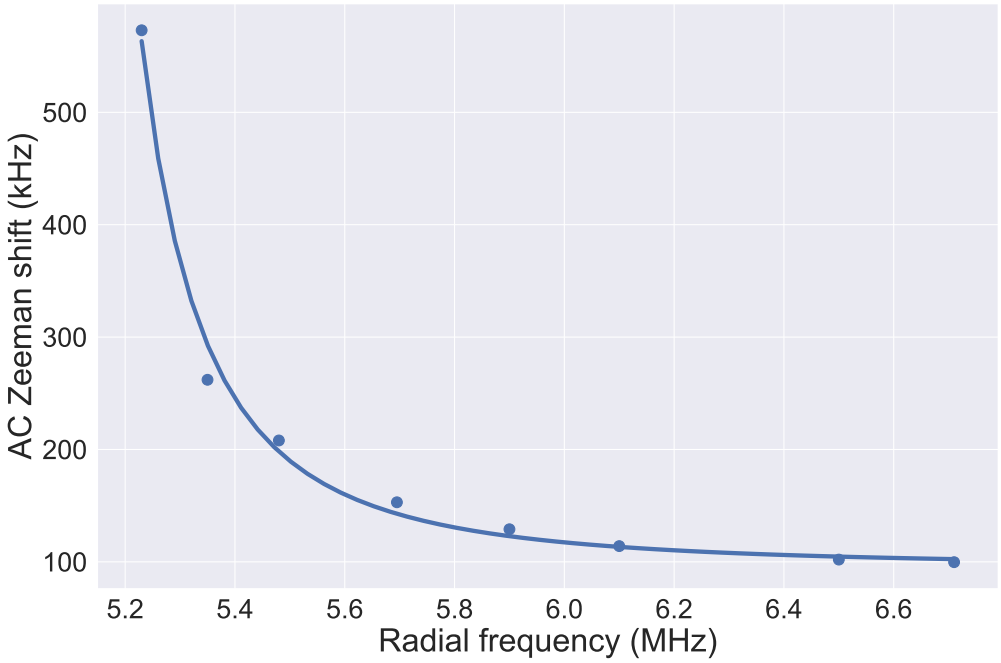

Figure 5.13: Plot of the ac Zeeman shift due to the electric field[11]at ω_g versus the radial mode ω_r. The data are shown by the blue points and the blue line is a fit following Eq. 5.26. For these experiments, $\omega_g/2\pi = 5$ MHz.

the application of currents oscillating at ω_g. A similar effect was seen due to microwave electric fields in [Warring et al., 2013a], with shifts of about 3 kHz on the motional frequencies.

5.11.4 Reducing the effect of the electric field

The effects from these electric fields can be reduced in a number of ways. First, with multiple ions, differential motional modes which are not excited by a uniform electric field can be used. In addition, one can compensate these oscillating electric fields by applying electric potentials oscillating at the same frequency to the electrodes. One can also use trap designs which place the current-carrying electrodes beneath a conducting layer [Welzel et al., 2019] which shields electric fields more strongly than magnetic fields.

5.12 Higher-order interactions

As seen in Sec. 5.1, a spin-dependent displacement can cause a non-zero overlap between otherwise orthogonal motional wavefunctions for the different spin states. For small displacements, this allows sideband interactions that change the Fock state by $\Delta n = \pm 1$ using an additional microwave field. To allow higher order transitions, for example $\Delta n = \pm 2$, a larger displacement would be required. Using a static gradient, this would simply correspond to a larger gradient. However, using an oscillating gradient, we can exploit the additional degree of freedom of being able to set ω_g relative to ω_r to obtain a larger displacement without increasing the magnitude of the field gradient.

Analogous to a classical harmonic oscillator, driving it close to resonance allows larger displacements without a larger force. One application which we explore in this section is the generation of higher-order interactions in a and $a^\dagger$ by tuning the oscillation frequency of the gradient close to the oscillation frequency of the harmonic oscillator, i.e. setting ω_g close to ω_r.

5.12.1 Oscillating gradient interaction

Since we will be operating in a regime where $\omega_g \to \omega_r$, we will ignore the term $\propto 1/(\omega_r + \omega_g)$ in Eq. 5.7 and the propagator simplifies to

$$\begin{aligned} U_g^\dagger(t) \approx \exp\Big[\frac{\Omega_g}{\omega_r - \omega_g}\sigma_z\big(- \hat{a}(e^{-i(\omega_r-\omega_g)t} - 1) \\ + \hat{a}^\dagger(e^{i(\omega_r-\omega_g)t} - 1)\big)\Big]. \end{aligned} \tag{5.27}$$

We now use the BCH theorem to transform the microwave term into the interaction picture with respect to the gradient term.

$$e^{AC}Be^{-AC} = B + [AC, B] + \frac{1}{2}[AC, [AC, B]]... \tag{5.28}$$

where $A = \frac{\Omega_g}{\omega_r-\omega_g}\sigma_z$, $C = \big(-a(e^{-i(\omega_r-\omega_g)t} - 1) + a^\dagger(e^{i(\omega_r-\omega_g)t} - 1)\big)$ and $B = \hbar\Omega_\mu(\sigma_+ e^{-i\delta t} + \sigma_- e^{i\delta t})$. To evaluate the commutator we make use of,

$$[\sigma_z, \sigma_+] = 2\sigma_+$$

$$[\sigma_z, \sigma_-] = -2\sigma_-,$$

and

$$[B, C] = 0$$

$$[A, C] = 0.$$

Using the result from appendix A.1.3,

$$\begin{aligned} H_g &= e^{AC} B e^{-AC} \\ &= \hbar\Omega_\mu \Big(\sigma_+ e^{-i\delta t} \exp\Big(\frac{2\Omega_g}{\omega_r - \omega_g}\big(- a(e^{-i(\omega_r-\omega_g)t} - 1) + a^\dagger (e^{i(\omega_r-\omega_g)t} - 1)\big)\Big) \\ &+ \sigma_- e^{i\delta t} \exp\Big(\frac{-2\Omega_g}{\omega_r - \omega_g}\big(- a(e^{-i(\omega_r-\omega_g)t} - 1) + a^\dagger (e^{i(\omega_r-\omega_g)t} - 1)\big)\Big)\Big) \\ &= \hbar\Omega_\mu \big(\sigma_+ e^{-i\delta t} D(\alpha) + \sigma_- e^{i\delta t} D(-\alpha)\big), \end{aligned} \tag{5.29}$$

where the displacement operator $D(\alpha)$ is

$$D(\alpha) = \exp\left(\alpha a^\dagger - \alpha^* a\right), \tag{5.30}$$

with α

$$\alpha = \frac{2\Omega_g}{\omega_r - \omega_g}(e^{i(\omega_r-\omega_g)t} - 1). \tag{5.31}$$

5.12.2 Sideband interactions

We can expand the displacement operator to obtain sideband interactions. Keeping up to the second order terms gives

$$
\begin{aligned}
D(\alpha) &= \exp\left(\alpha a^\dagger - \alpha^* a\right) \\
&\approx 1 + (\alpha a^\dagger - \alpha^* a) + \frac{1}{2}(\alpha^2 a^{\dagger 2} - |\alpha|^2(a^\dagger a + a a^\dagger) + \alpha^{*2} a^2).
\end{aligned}
$$

5.12.3 Single sideband interactions

Just keeping the first order terms, we obtain the first sideband interaction where,

$$
\begin{aligned}
H_{sb} &= \hbar\Omega_\mu(\sigma_+ e^{-i\delta t} - \sigma_- e^{i\delta t})(\alpha a^\dagger - \alpha^* a) \\
&= \frac{2\hbar\Omega_\mu\Omega_g}{\omega_r - \omega_g}(\sigma_+ e^{-i\delta t} - \sigma_- e^{i\delta t})(a^\dagger(e^{i(\omega_r-\omega_g)t} - 1) - a(e^{-i(\omega_r-\omega_g)t} - 1))
\end{aligned}
\tag{5.32}
$$

When $\delta = \omega_r - \omega_g$ we obtain the blue sideband interaction and when $\delta = -(\omega_r - \omega_g)$ we obtain the red sideband interaction as described by Eq. 5.10.

As discussed in Sec. 5.6.1, the detuned microwave causes an ac Zeeman shift. Thus, the Rabi frequency of the microwave can only be as large as the detuning for the single sideband due to the ac Zeeman shift ($2\Omega_\mu < \omega_r - \omega_g$). Thus, the maximum sideband Rabi frequency is Ω_g.

5.12.3.1 Second sideband interaction

The second order terms give us the second sideband interaction. Dropping the $a^\dagger a$ and $aa^\dagger$ terms that are at different detunings,

$$
\begin{aligned}
H_{ssb} &= \frac{\hbar\Omega_\mu}{2}(\sigma_+ e^{-i\delta t} + \sigma_- e^{i\delta t})(\alpha^2 a^{\dagger 2} + \alpha^{*2} a^2) \\
&\approx \frac{\hbar\Omega_\mu}{2}\Big(\frac{2\Omega_g}{\omega_r - \omega_g}\Big)^2(\sigma_+ e^{-i\delta t} + \sigma_- e^{i\delta t})(a^{\dagger 2}(e^{2i(\omega_r-\omega_g)t} - 2e^{i(\omega_r-\omega_g)t} + 1) \\
&\qquad\qquad + a^2(e^{-2i(\omega_r-\omega_g)t} - 2e^{-i(\omega_r-\omega_g)t} + 1)).
\end{aligned}
$$

When $\delta = 2(\omega_r - \omega_g)$, we get the second blue sideband and when $\delta = -2(\omega_r - \omega_g)$ we get the second red sideband. Similarly, because of the ac Zeeman shift, the maximum Rabi frequency of this second sideband is $\Omega_g^2/(\omega_r - \omega_g)$.

These interactions can be enhanced simply by tuning ω_g closer to ω_r i.e they can exist even without a second order spatial derivative of the magnetic field; Ω_g only depends on the first order derivative. Of course, one must be careful of the electric field oscillating at ω_g; as $\omega_g \to \omega_r$, the electric field also gets closer to resonance. The frequency difference $\omega_r - \omega_g \sim \Omega_g$ for this interaction to have non-negligible strength.

There are two colours in my head

Radiohead

6

Entangling gates with a radiofrequency oscillating magnetic field gradient

In the previous chapter, we discussed how one can use a radiofrequency magnetic field gradient with **one** microwave field to couple an ion's spin to its motion. In this chapter, we extend that technique to implementing two-qubit entangling gates that use **two** microwave fields symmetrically detuned from the qubit frequency. We analyze the dynamics of these fields in the "bichromatic" interaction picture: the interaction picture with respect to the two microwave fields. We show that we can choose between $\hat{\sigma}_y\hat{\sigma}_y$ Mølmer-Sørensen-type gates and $\hat{\sigma}_z\hat{\sigma}_z$ gates simply by changing the detuning of the microwave fields. In addition, by appropriately choosing the Rabi frequency of the microwave fields, we can make the gate less sensitive to qubit frequency fluctuations without additional fields, known as intrinsic dynamical decoupling (IDD). These theoretical results were published in [Sutherland et al., 2019].

Next, we experimentally demonstrate two-qubit entangling gates using a radiofrequency magnetic field gradient. We implement both $\hat{\sigma}_y\hat{\sigma}_y$ and $\hat{\sigma}_z\hat{\sigma}_z$ gates, the latter being the focus of this chapter. By tuning the microwave fields to the IDD point, we show an improvement in our

qubit coherence by more than an order of magnitude. We also measure the insensitivity of the two-qubit gate to qubit frequency offsets, which enables the single-ion addressing presented in the next chapter.

6.1 Bichromatic interaction picture

We first consider a general Hamiltonian for laser-free gates comprising an interaction with a bichromatic microwave field whose components are symmetrically detuned from the qubit frequency in addition to a magnetic field gradient that couples the ions' spin to one mode of their motion. The Hamiltonian is

$$\begin{aligned}\hat{H}_{\text{lab}}(t) = \frac{\hbar\omega_0}{2}\hat{S}_z + \hbar\omega_r\hat{a}^\dagger\hat{a} + 2\hbar\Omega_\mu\hat{S}_i\Big\{\cos([\omega_0+\delta]t) + \cos([\omega_0-\delta]t)\Big\} \\ + 2\hbar\Omega_g f(t)\hat{S}_j\Big\{\hat{a}+\hat{a}^\dagger\Big\}.\end{aligned} \tag{6.1}$$

This Hamiltonian is for an N-ion string[1], where the spin operators are $\hat{S}_i \equiv \sum_n^N \hat{\sigma}_{i,n}$, with $i \in \{x, y\}$ and $j \in \{x, y, z\}$. We assume for now that we are using the center-of-mass mode, so all ions participate equally in the motion[2]. The Ω_μ term describes two microwave fields with the same Rabi frequency, one with a detuning $+\delta$ and one with a detuning $-\delta$ from the qubit frequency ω_0. The Ω_g term represents a field gradient that couples the ions' internal states to their motion, which is characterized by creation and annihilation operators $\hat{a}$ and $\hat{a}^\dagger$ and frequency ω_r. The function $f(t)$ describes the time dependence of the field gradient, which we take to be either static or oscillating sinusoidally.

We transform from Eq. 6.1 into an interaction picture with respect to $\hat{H}_0 = \hbar\omega_0\hat{S}_z/2 + \hbar\omega_r\hat{a}^\dagger\hat{a}$, i.e. the qubit and motional frequency. Making use of the results in Sec. A.1 including the rotating wave approximation, we obtain the Hamiltonian,

[1] In other sections, n is used to identify the motional Fock state $|n\rangle$. However, in this chapter we use it to denote the number of ions to maintain consistency with the paper in which these results were published [Sutherland et al., 2019].

[2] For other modes of motion, we would need to add coefficients b_n to the spin operator for the gradient term such that $\hat{S}_i \equiv \sum_n b_n\hat{\sigma}_{i,n}$. For the simple case of two identical ions, on the center of mass modes, $b_1 = b_2 = 1$. On the out-of-phase modes, $b_1 = 1 = -b_2$.

$$\begin{aligned}\hat{H}(t) &= \hat{H}_\mu(t) + \hat{H}_g(t) \\ &= 2\hbar\Omega_\mu \hat{S}_i \cos(\delta t) + 2\hbar\Omega_g f(t)\hat{S}_j\Big\{\hat{a}e^{-i\omega_r t} + \hat{a}^\dagger e^{i\omega_r t}\Big\}. \end{aligned} \tag{6.2}$$

We identify two main components of the Hamiltonian, $\hat{H}_\mu(t)$ and $\hat{H}_g(t)$, which we refer to as the *microwave field term* and the *gradient term*, respectively. To more explicitly derive $\hat{H}_\mu$, let us first analyze the case of $\hat{S}_i = \hat{S}_x$,

$$\begin{aligned} & 2\hbar\Omega_\mu \hat{S}_x\Big\{\cos([\omega_0+\delta]t) + \cos([\omega_0-\delta]t)\Big\} \\ & \rightarrow \hbar\Omega_\mu\Big\{\sum_n \hat{\sigma}_{+,n}e^{-i\delta t} + \sum_n \hat{\sigma}_{-,n}e^{i\delta t} && \text{blue-detuned microwave field} \\ & \quad + \sum_n \hat{\sigma}_{+,n}e^{i\delta t} + \sum_n \hat{\sigma}_{-,n}e^{-i\delta t}\Big\} && \text{red-detuned microwave field,} \\ & = 2\hbar\Omega_\mu \hat{S}_x \cos(\delta t), \end{aligned} \tag{6.3}$$

where we make use of $e^{i\delta t} + e^{-i\delta t} = 2\cos(\delta t)$ as we transform into rotating frame of the qubit. We dropped the fast-rotating terms through the rotating wave approximation. A similar result can be shown for $\hat{S}_i = \hat{S}_y$ and is left as an exercise for the reader[3] . We assume that all ions are identical with the same qubit frequencies, and can all be addressed with a single pair of microwave fields. We can generalize this formalism to the case of multiple qubit frequencies, either for different ion species, or for ions of the same species with different qubit frequencies as discussed for example in [Khromova et al., 2012], by using multiple pairs of microwave fields. Note that the result in Eq. 6.2 is valid unconditionally for $\hat{S}_j = \hat{S}_z$. This result also holds for specific cases $j \in \{x, y\}$, such as the gradient term comprising two gradients oscillating with frequencies symmetrically detuned from the qubit, i.e. $f(t) = \cos([\omega_0 + \delta']t) + \cos([\omega_0 - \delta']t)$.

We transform Eq. 6.2 into the bichromatic interaction picture, the interaction picture with respect to $\hat{H}_\mu$. In performing this step, we make use of the formalism developed in [Roos, 2008] for laser-driven gates. We first derive the propagator from H_μ,

[3] I've always wanted to say that.

$$\begin{aligned}\hat{U}_\mu(t) &= \exp\Big\{-\frac{i}{\hbar}\int_0^t dt' H_\mu(t')\Big\} \\ &= \exp\Big\{-2i\Omega_\mu \hat{S}_i \int_0^t dt' \cos(\delta t')\Big\} \\ &= \exp\Big\{-iF(t)\hat{S}_i\Big\}, \end{aligned} \tag{6.4}$$

with $F(t) \equiv \frac{2\Omega_\mu \sin(\delta t)}{\delta}$. The interaction picture Hamiltonian is then,

$$\begin{aligned}\hat{H}_I(t) &= \hat{U}_\mu^\dagger(t)\hat{H}_g(t)\hat{U}_\mu(t) \\ &= 2\hbar\Omega_g f(t)\Big\{\hat{a}e^{-i\omega_r t} + \hat{a}^\dagger e^{i\omega_r t}\Big\}e^{iF(t)\hat{S}_i}\hat{S}_j e^{-iF(t)\hat{S}_i}, \end{aligned} \tag{6.5}$$

where the terms corresponding to the motion commute with the terms corresponding to the qubit. All the interesting dynamics are in the qubit term with only spin operators, which we can simplify by using $e^{ib\hat{\sigma}_i} = \hat{I}\cos(b) + i\hat{\sigma}_i \sin(b)$, where b is scalar quantity. First, using the commutativity of the different ion operators,

$$e^{iF(t)\hat{S}_i}\hat{S}_j e^{-iF(t)\hat{S}_i} = \sum_n e^{iF(t)\hat{\sigma}_{i,n}}\hat{\sigma}_{j,n}e^{-iF(t)\hat{\sigma}_{i,n}}. \tag{6.6}$$

Now focusing on the single-ion operators and dropping the n subscript for simplicity,

$$\begin{aligned}&e^{iF(t)\hat{\sigma}_i}\hat{\sigma}_j e^{-iF(t)\hat{\sigma}_i} \\ =&\Big\{\hat{I}\cos(F(t)) + i\hat{\sigma}_i\sin(F(t))\Big\}\hat{\sigma}_j\Big\{\hat{I}\cos(F(t)) - i\hat{\sigma}_i\sin(F(t))\Big\} \\ =&\hat{\sigma}_j\cos^2(F(t)) - i\hat{\sigma}_j\hat{\sigma}_i\cos(F(t))\sin(F(t)) + i\hat{\sigma}_i\hat{\sigma}_j\cos(F(t))\sin(F(t)) + \hat{\sigma}_i\hat{\sigma}_j\hat{\sigma}_i\sin^2(F(t)) \\ =&\hat{\sigma}_j\cos^2(F(t)) + i[\hat{\sigma}_i,\hat{\sigma}_j]\cos(F(t))\sin(F(t)) + ([\hat{\sigma}_i,\hat{\sigma}_j] + \hat{\sigma}_j\hat{\sigma}_i)\hat{\sigma}_i\sin^2(F(t)) \\ =&\hat{\sigma}_j\left(\cos^2(F(t)) + \sin^2(F(t))\right) + [\hat{\sigma}_i,\hat{\sigma}_j]\sin(F(t))\left(i\cos(F(t)) + \hat{\sigma}_i\sin(F(t))\right) \\ =&\hat{\sigma}_j + i[\hat{\sigma}_i,\hat{\sigma}_j]\sin(F(t))\left(\cos(F(t)) - i\hat{\sigma}_i\sin(F(t))\right) \\ =&\hat{\sigma}_j + i[\hat{\sigma}_i,\hat{\sigma}_j]\sin(F(t))e^{-iF(t)\hat{\sigma}_i}, \end{aligned} \tag{6.7}$$

where we have also made use of $\hat{\sigma}_i^2 = \hat{I}$. Using this result in Eq. 6.5 gives

$$\hat{H}_I(t) \quad = \quad 2\hbar\Omega_g f(t)\Big\{\hat{a}e^{-i\omega_r t} + \hat{a}^\dagger e^{i\omega_r t}\Big\}\Big\{\hat{S}_j + i[\hat{S}_i, \hat{S}_j]\sin(F(t))e^{-iF(t)\hat{S}_i}\Big\}.$$

If $i = j$, then Eq. 6.7= $\hat{\sigma}_j$, and $\hat{H}_I(t) = \hat{H}_g(t)$. However, if $i \neq j$, Eq. 6.7 becomes

$$\begin{aligned}
&\hat{\sigma}_j + i[\hat{\sigma}_i, \hat{\sigma}_j]\sin(F(t))e^{-iF(t)\hat{\sigma}_i}, \\
=&\hat{\sigma}_j - 2\epsilon_{ijk}\hat{\sigma}_k \sin(F(t))e^{-iF(t)\hat{\sigma}_i}, \\
=&\hat{\sigma}_j - 2\epsilon_{ijk}\hat{\sigma}_k \sin(F(t))(\cos(F(t)) - i\sin(F(t))\hat{\sigma}_i), \\
=&\hat{\sigma}_j - 2\epsilon_{ijk}\hat{\sigma}_k \sin(F(t))\cos(F(t)) + 2i\epsilon_{ijk}\hat{\sigma}_k\hat{\sigma}_i \sin^2(F(t)), \\
=&\hat{\sigma}_j - \epsilon_{ijk}\hat{\sigma}_k \sin(2F(t)) - 2\hat{\sigma}_j \sin^2(F(t)), \\
=&\hat{\sigma}_j \cos(2F(t)) - \epsilon_{ijk}\hat{\sigma}_k \sin(2F(t)),
\end{aligned} \tag{6.8}$$

where we understand that $\hat{\sigma}_k\hat{\sigma}_i = i\hat{\sigma}_j$ and ϵ_{ijk} is the Levi-Civita symbol. We can use the Jacobi-Anger expansion [Abramowitz and Stegun, 1972], to simplify this further.

$$\begin{aligned}
\cos(z\sin\theta) &= J_0(z) + 2\sum_{n=1}^{\infty} J_{2n}(z)\cos(2n\theta), \\
\sin(z\sin\theta) &= 2\sum_{n=0}^{\infty} J_{2n+1}(z)\cos((2n+1)\theta),
\end{aligned}$$

where J_n is the n^{th} Bessel function[4]. Finally, using $z = \frac{4\Omega_\mu}{\delta}$, $\theta = \delta t$, and putting back the summation $\hat{S}_i = \sum_n^N \hat{\sigma}_{i,n}$ in Eq. 6.5 we obtain

$$\begin{aligned}
\hat{H}_I(t) = \quad & 2\hbar\Omega_g f(t)\Big\{\hat{a}e^{-i\omega_r t} + \hat{a}^\dagger e^{i\omega_r t}\Big\}\Big\{\hat{S}_j\Big[J_0\Big(\frac{4\Omega_\mu}{\delta}\Big) + 2\sum_{n=1}^{\infty} J_{2n}\Big(\frac{4\Omega_\mu}{\delta}\Big)\cos(2n\delta t)\Big] \\
& -2\epsilon_{ijk}\hat{S}_k \sum_{n=1}^{\infty} J_{2n-1}\Big(\frac{4\Omega_\mu}{\delta}\Big)\sin([2n-1]\delta t)\Big\},
\end{aligned} \tag{6.9}$$

This is the main result from [Sutherland et al., 2019]. One interpretation of this result is that the $\hat{H}_\mu$ term effectively provides a frequency modulation of the gradient term $\hat{H}_g$. When $i \neq j$, we

[4] Not to be confused with the n in $\hat{S}_i = \sum_n^N \hat{\sigma}_{i,n}$ which refers to the ion number. We stick with n here to be consistent with Ref. [Sutherland et al., 2019].

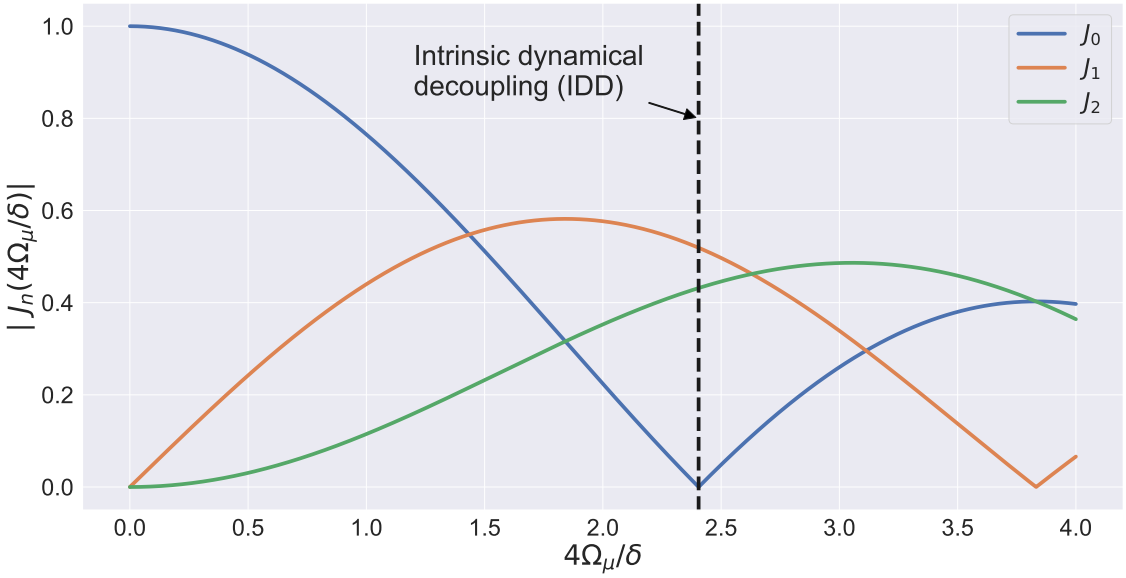

Figure 6.1: Plot of $|J_n(4\Omega_\mu/\delta)|$ versus $4\Omega_\mu/\delta$. The interactions described in Eq. 6.9 are proportional to Bessel functions J_n; J_0, J_1, and J_2 are plotted. Each of those interactions correspond to a different condition on δ and different spin operators. Any qubit frequency error would be scaled by the J_0 function as described in Sec. 6.1.1. By choosing $4\Omega_\mu/\delta$ such that $J_0 = 0$, we perform intrinsic dynamical decoupling (IDD). The $\hat{\sigma}_z\hat{\sigma}_z$ gate that we perform experimentally has a gate Rabi frequency that is proportional to J_2.

obtain an infinite series of resonances which can be used to implement different spin-spin interactions between ions, with a suitable choice of parameters. Even resonances ($2n$) produce an interaction corresponding to the spin term $\hat{S}_j$ in $\hat{H}_g$. Odd resonances ($n = 2n - 1$) correspond to $[\hat{S}_i, \hat{S}_j]$, the commutator of the spin-terms in $\hat{H}_g$ and $\hat{H}_\mu$. The strengths of these interactions correspond to the Bessel functions J_n as shown in Fig. 6.1. We can choose which interaction to implement by choosing the value of δ, the detuning of the bichromatic fields. We assume that the Rabi frequency of the gradient term $\Omega_g \ll \delta$, such that when we pick one resonance we can ignore the others[5]. The other interactions will have excitations proportional to $\left(\frac{\Omega_g}{\delta}\right)^2$. We analyze three different implementations $\hat{H}_g$ in Sec. 6.1.3; a static magnetic field gradient, a magnetic field gradient oscillating at near-qubit frequencies, and finally what we implement in this thesis, a radiofrequency magnetic field gradient near the motional frequency.

[5] For our experiments, $\Omega_g/2\pi \sim$kHz and $\delta/2\pi \sim$MHz.

6.1.1 Intrinsic dynamical decoupling

Aside from elucidating the dynamics of the spin-dependent force term $\hat{H}_g$ in the presence of large bichromatic microwave fields, the bichromatic interaction picture also reveals important dynamics of qubit frequency errors. This analysis shows that we can perform dynamical decoupling of the qubit without any additional fields. Dynamical decoupling is useful for error suppression [Viola and Lloyd, 1998, Viola et al., 1999, Uhrig, 2007] and has been used in a number of different ion trapping experiments such as [Biercuk et al., 2009, Timoney et al., 2011, Tan et al., 2013] and more specifically in laser-free gates such as demonstrated in Ref. [Weidt et al., 2016, Harty et al., 2016]. In contrast to those implementations, we do not require additional fields for dynamical decoupling.

To illustrate this intrinsic dynamical decoupling (IDD), we add an error term to our Hamiltonian in Eq. 6.9

$$\hat{H}_z = \frac{\hbar\epsilon}{2}\hat{S}_z, \tag{6.10}$$

where ϵ is the magnitude of the qubit frequency shift, which we assume is the same for all the ions. This qubit frequency shift can arise from a shift in the quantization axis magnetic field, changes in the ac Zeeman shift from the microwave fields, or just an error in calibrating the qubit frequency. This shift can be static or time-varying (slowly compared to $1/\delta$). This error term transforms into the bichromatic interaction picture as

$$\begin{aligned}\hat{H}_{I,z} = \quad & \tfrac{\hbar\varepsilon}{2}\Big\{\hat{S}_z\Big[J_0\Big(\tfrac{4\Omega_\mu}{\delta}\Big) + 2\textstyle\sum_{n=1}^{\infty} J_{2n}\Big(\tfrac{4\Omega_\mu}{\delta}\Big)\cos(2n\delta t)\Big] \\ & +2\epsilon_{ikz}\hat{S}_k \textstyle\sum_{n=1}^{\infty} J_{2n-1}\Big(\tfrac{4\Omega_\mu}{\delta}\Big)\sin([2n-1]\delta t)\Big\}.\end{aligned} \tag{6.11}$$

As long as ϵ does not have frequency components near $n\delta$, most of the terms in Eq. 6.11 will be varying quickly with time and can be ignored. As n gets larger, J_n also in general gets smaller. Thus, the leading error term, especially if ϵ is static, is proportional to $J_0\Big(\frac{4\Omega_\mu}{\delta}\Big)$. Thus, by choosing $4\Omega_\mu/\delta \approx 2.405$ such that $J_0\Big(\frac{4\Omega_\mu}{\delta}\Big) = 0$, we are only left with the higher order terms that oscillate

quickly. At this point, the J_1 and J_2 values are approximately 0.519 and 0.432, as opposed to their peak values of 0.582 and 0.486 respectively. Thus, choosing the IDD point will come at a slight cost to the interaction strength. We investigate IDD experimentally in Sec. 6.2.1.1.

6.1.2 Pulse shaping

In this chapter, we have explained how analyzing our Hamiltonians in the bichromatic interaction picture has simplified the dynamics. Here, we show how we can employ pulse shaping of the microwave fields to move smoothly in and out of the interaction picture, such that the dynamics in the original interaction picture (with respect to the qubit and motion) are identical to the dynamics in the bichromatic interaction picture.

As shown in Eq. 6.2, our Hamiltonian is composed of two parts,

$$\hat{H}(t) = \hat{H}_\mu(t) + \hat{H}_g(t), \tag{6.12}$$

where $\hat{H}_\mu(t)$ is our bichromatic microwave term and $\hat{H}_g(t)$ is the gradient term. We assume $\hat{H}_\mu$ commutes with itself at all times so its propagator can be determined simply as

$$\hat{U}(t) \;=\; \exp\Big\{-\frac{i}{\hbar}\int_0^t dt'\hat{H}_\mu(t')\Big\}. \tag{6.13}$$

The Hamiltonian in the bichromatic interaction picture $\hat{H}_I(t)$ is

$$\hat{H}_I(t) = \hat{U}^\dagger(t)\hat{H}_g(t)\hat{U}(t). \tag{6.14}$$

In this interaction frame, our initial state $|\psi(t)\rangle \rightarrow |\phi(t)\rangle = \hat{U}^\dagger|\psi(t)\rangle$, whose time evolution is governed by,

$$i\hbar\,|\dot{\phi}(t)\rangle = \hat{H}_I(t)\,|\phi(t)\rangle\,. \tag{6.15}$$

Solving this equation, we obtain the time evolution operator $\hat{T}_I(t)$ such that $|\phi(t)\rangle = \hat{T}_I(t)\,|\phi(0)\rangle$. The final state in our original frame is

$$\begin{aligned} |\psi(t_f)\rangle &= \hat{U}(t_f)\,|\phi(t_f)\rangle \\ &= \hat{U}(t_f)\hat{T}_I(t_f)\,|\phi(0)\rangle \\ &= \hat{U}(t_f)\hat{T}_I(t_f)\hat{U}^\dagger(0)\,|\psi(0)\rangle\,. \end{aligned} \tag{6.16}$$

$\hat{U}^\dagger(0) = \hat{I}$, so if $\hat{U}(t_f) \to \hat{I}$, we find that

$$|\psi(t_f)\rangle \to \hat{T}_I(t_f)\,|\psi(0)\rangle\,, \tag{6.17}$$

and the state in the bichromatic interaction picture and the ion frame (with respect to qubit and motion) are identical. We achieve this condition of $\hat{U}(t_f) \to \hat{I}$ by pulse shaping our microwave fields, turning the microwave fields on and off smoothly in a time τ that is long compared to $2\pi/\delta$. We add time dependence to Ω_μ in $\hat{H}_\mu(t)$ such that

$$\hat{H}_\mu(t) \to 2\Omega_\mu g(t)\cos(\delta t)\hat{S}_i. \tag{6.18}$$

We impose the following boundary conditions on $g(t)$

$$\begin{aligned} g(0) = g(t_f) = 0, \\ g(\tau \le t \le t_f - \tau) = 1, \end{aligned} \tag{6.19}$$

i.e. our microwaves are off at the start and end of the gate sequence and between the ramps they have a constant amplitude. We now evaluate $\hat{U}(t_f)$,

$$\begin{aligned} \hat{U}(t_f) &= \exp\Big\{ -i\int_0^{t_f} \mathrm{d}t' 2\Omega_\mu g(t')\cos(\delta t')\hat{S}_i\Big\}, \\ &= \exp\Big\{\frac{2i\Omega_\mu}{\delta}\Big(\int_0^{\tau} dt'\dot{g}(t')\sin(\delta t') + \int_{t_f-\tau}^{t_f} dt'\dot{g}(t')\sin(\delta t')\Big)\hat{S}_i\Big\}, \end{aligned} \tag{6.20}$$

where we have integrated by parts and made use of the boundary conditions on $g(t)$. If $\dot{g}(t)$ is small compared to δ, then the value of the integrals will be roughly proportional to $2\pi/(\tau\delta)$, so for $\tau \gg 2\pi/\delta$, these integrals will vanish and $\hat{U}(t_f) \to \hat{I}$. This condition can also be fulfilled by picking ramp times such that $\delta\tau = 2n\pi$. We note that the pulse shaping will change the optimal gate time slightly as there are some gate dynamics during the ramps. In practice, we do not fulfill $\tau \gg 2\pi/\delta$ to reduce the ramp times, which is discussed in more detail in Sec. 6.4.6.

6.1.3 Physical implementations

Using the formalism that we have discussed so far, we describe three different types of laser-free entangling gates using three different types of magnetic field gradients: a static magnetic field gradient, a magnetic field gradient oscillating at near-qubit frequencies, and a magnetic field gradient oscillating at radio frequencies close to the motional frequency. The latter method was discussed in the previous chapter and is used for the gates we perform in this chapter. Each of these three implementations will have different spin operators $\hat{S}_i$ and $\hat{S}_j$ and time dependencies of the gradient $f(t)$.

6.1.3.1 Static magnetic field gradient

We study a static magnetic field gradient with a pair of microwave fields symmetrically detuned from the qubit frequency as described in [Lake et al., 2015]. Equation 6.2, with $\hat{S}_i = \hat{S}_x$, $\hat{S}_j = \hat{S}_z$ and $f(t) = 1$, becomes

$$\hat{H}(t) = 2\hbar\Omega_\mu \hat{S}_x \cos(\delta t) + 2\hbar\Omega_g \hat{S}_z \Big\{ \hat{a}e^{-i\omega_r t} + \hat{a}^\dagger e^{i\omega_r t} \Big\}. \tag{6.21}$$

In the bichromatic interaction picture, this Hamiltonian transforms as,

$$\hat{H}_I(t) = 2\hbar\Omega_g\Big\{\hat{a}e^{-i\omega_r t} + \hat{a}^\dagger e^{i\omega_r t}\Big\}\Big\{\hat{S}_z\Big[J_0\Big(\frac{4\Omega_\mu}{\delta}\Big) + 2\sum_{n=1}^{\infty} J_{2n}\Big(\frac{4\Omega_\mu}{\delta}\Big)\cos(2n\delta t)\Big] + 2\hat{S}_y\sum_{n=1}^{\infty} J_{2n-1}\Big(\frac{4\Omega_\mu}{\delta}\Big)\sin([2n-1]\delta t)\Big\}. \quad (6.22)$$

We obtain a $\hat{\sigma}_y\hat{\sigma}_y$ interaction for $(2n-1)\delta \approx \omega_r$ and a $\hat{\sigma}_z\hat{\sigma}_z$ interaction for $2n\delta \approx \omega_r$.

6.1.3.2 Magnetic field gradient oscillating at near-qubit frequencies

We next study a magnetic field gradient oscillating close to the qubit frequency [Ospelkaus et al., 2011, Harty et al., 2016]. We consider the case that the microwave fields are not nulled and are oscillating at the same frequencies and have the same spin-operator as the gradient. This corresponds to $\hat{S}_i = \hat{S}_x$, $\hat{S}_j = \hat{S}_x$, and $f(t) = \cos(\delta t)$ in Eq. 6.2. The interaction Hamiltonian for this system is,

$$\hat{H}(t) = 2\hbar\Omega_\mu\cos(\delta t)\hat{S}_x + 2\hbar\Omega_g\cos(\delta t)\hat{S}_x\Big\{\hat{a}e^{-i\omega_r t} + \hat{a}^\dagger e^{i\omega_r t}\Big\}. \quad (6.23)$$

We note that the microwave term commutes with the gradient term, giving the bichromatic interaction picture Hamiltonian

$$\hat{H}_I(t) = 2\hbar\Omega_g\cos(\delta t)\hat{S}_x\Big\{\hat{a}e^{-i\omega_r t} + \hat{a}^\dagger e^{i\omega_r t}\Big\}. \quad (6.24)$$

This Hamiltonian results in a $\hat{\sigma}_x\hat{\sigma}_x$ interaction. While previous implementations nulled the oscillating magnetic fields at the ion, we show that those fields can be used for intrinsic dynamical decoupling.

6.1.3.3 Magnetic field gradient oscillating at near-motional frequencies

We extend the technique developed in the previous chapter to two microwave fields in addition to the oscillating magnetic field gradient close to the motional frequency at radio frequency. The

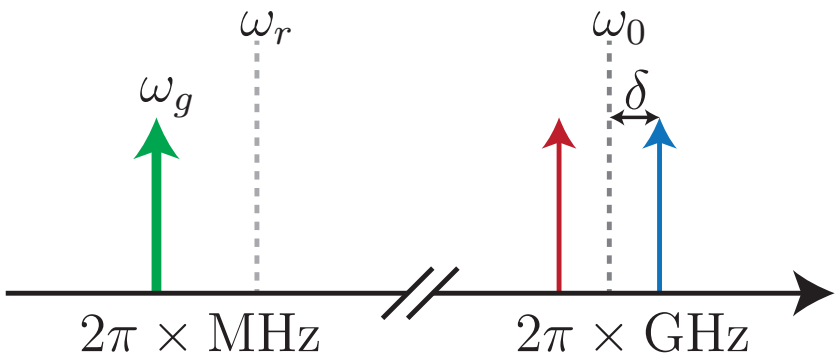

Figure 6.2: Spectrum of applied fields for two-qubit entangling gates. We have a strong radiofrequency magnetic field gradient oscillating at ω_g close to the motional mode frequency ω_r. At the gigahertz end of the spectrum, we have two microwave fields that are symmetrically detuned by δ from the qubit frequency ω_0.

spectrum of fields used is shown in Fig. 6.2. With $\hat{S}_i = \hat{S}_x$, $\hat{S}_j = \hat{S}_z$, and $f(t) = \cos(\omega_g t)$, Eq. 6.2 becomes

$$\hat{H}(t) = 2\hbar\Omega_\mu \cos(\delta t)\hat{S}_x + 2\hbar\Omega_g \cos(\omega_g t)\hat{S}_z\Big\{\hat{a}e^{-i\omega_r t} + \hat{a}^\dagger e^{i\omega_r t}\Big\}, \tag{6.25}$$

where we follow the same definitions for Ω_μ and Ω_g as in Sec. 5.1. Note that this reduces to Eq. 6.21 for $\omega_g = 0$. In the bichromatic interaction picture, our Hamiltonian is

$$\begin{aligned}\hat{H}_I(t) \;=\; & 2\hbar\Omega_g \cos(\omega_g t)\Big\{\hat{a}e^{-i\omega_r t} + \hat{a}^\dagger e^{i\omega_r t}\Big\}\Big\{\hat{S}_z\Big[J_0\Big(\frac{4\Omega_\mu}{\delta}\Big) \\ & +2\sum_{n=1}^{\infty} J_{2n}\Big(\frac{4\Omega_\mu}{\delta}\Big)\cos(2n\delta t)\Big] + 2\hat{S}_y\sum_{n=1}^{\infty} J_{2n-1}\Big(\frac{4\Omega_\mu}{\delta}\Big)\sin([2n-1]\delta t)\Big\}.\end{aligned} \tag{6.26}$$

Compared to the static gradient case, the resonant interactions occur when $n\delta = |\omega_r \pm \omega_g|$ as opposed to $n\delta = \omega_r$. For smaller values of δ, lower microwave Rabi frequencies Ω_μ are required to achieve the same argument of the Bessel functions $4\Omega_\mu/\delta$. We can view the microwave term in Eq. 6.25 as providing a frequency modulation to the gradient term δ as illustrated in Fig. 6.3. Because the term providing the frequency modulation does not commute with the gradient term,

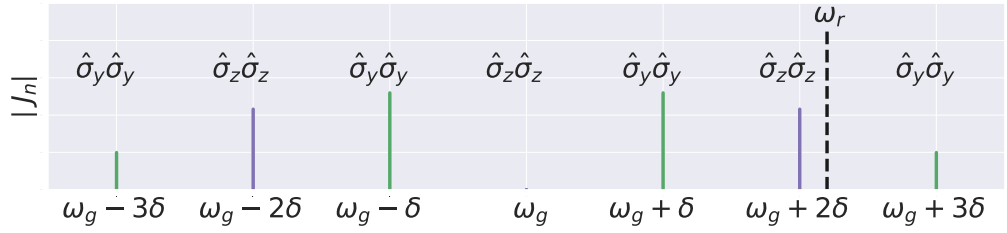

Figure 6.3: Spectrum of frequency modulation of the spin-dependent force term. The microwave term in Eq. 6.25 provides a frequency modulation at the microwave detuning δ of the gradient term which provides the spin-dependent force. Even terms correspond to an effective $\hat{\sigma}_z\hat{\sigma}_z$ interaction and odd terms correspond to an effective $\hat{\sigma}_y\hat{\sigma}_y$ interaction. When one of the frequency modulation terms is close to the motional frequency ω_r, we can drive an entangling interaction. We operate at the IDD point where $J_0\left(\frac{4\Omega_\mu}{\delta}\right) = 0$.

odd resonances ($(2n+1)\delta \approx |\omega_r \pm \omega_g|$) implement a $\hat{\sigma}_y\hat{\sigma}_y$ interaction while even resonances ($2n\delta \approx |\omega_r \pm \omega_g|$) implement a $\hat{\sigma}_z\hat{\sigma}_z$ interaction.

For our gate demonstrations, we use the J_2 resonance where $2\delta \approx \omega_r - \omega_g$ which corresponds to

$$\hat{H}_{\mathrm{zz}} = \hbar\Omega_g J_2\left(\frac{4\Omega_\mu}{\delta}\right)(\hat{\sigma}_{z1} - \hat{\sigma}_{z2})\left\{\hat{a}e^{i\Delta t} + \hat{a}^\dagger e^{-i\Delta t}\right\}, \tag{6.27}$$

where the gate Rabi frequency (following Eq. 2.31) is $\Omega_g J_2\left(\frac{4\Omega_\mu}{\delta}\right)$ and $\Delta = 2\delta - (\omega_r - \omega_g)$. We have also replaced $\hat{S}_z$ with the spin operators for each of the two ions for the out-of-phase radial mode. This gate is the focus of the rest of the chapter. However, we also briefly discuss the Mølmer-Sørensen-type $\hat{\sigma}_y\hat{\sigma}_y$ interaction in Sec. 6.5 which occurs when $\delta \approx \omega_r - \omega_g$, and

$$\hat{H}_{\mathrm{ms}} = i\hbar\Omega_g J_1\left(\frac{4\Omega_\mu}{\delta}\right)(\hat{\sigma}_{y1} + \hat{\sigma}_{y2})\left\{-\hat{a}e^{i\Delta t} + \hat{a}^\dagger e^{i\Delta t}\right\}, \tag{6.28}$$

where the gate Rabi frequency is $\Omega_g J_1\left(\frac{4\Omega_\mu}{\delta}\right)$ and $\Delta = \delta - (\omega_r - \omega_g)$ and we have replaced $\hat{S}_y$ with the individual spin operators for the center of mass mode on which the gate was performed.

6.1.4 $\hat{\sigma}_z\hat{\sigma}_z$ interaction without microwave fields

From Eq. 6.25, we note that we could drive a $\hat{\sigma}_z\hat{\sigma}_z$ interaction directly by removing the microwave fields and just having our gradient frequency ω_g close to the motional frequency ω_r. In this case, our Hamiltonian would be,

$$\hat{H}(t) = 2\hbar\Omega_g \cos(\omega_g t)\hat{S}_z\Big\{\hat{a}e^{-i\omega_r t} + \hat{a}^\dagger e^{i\omega_r t}\Big\}. \tag{6.29}$$

This type of gate has been proposed in [Leibfried et al., 2007, Ospelkaus et al., 2008]. However, this gate is challenging to implement as there is a spin-independent electric field that will be oscillating at ω_g. This electric field can excite the ion motion and cause other adverse affects as described in Sec. 5.11. This gate has been implemented in our apparatus [Burd, 2020], with a highest Bell-state fidelity of approximately 0.8.

6.1.5 Rabi frequency imbalance of microwave fields

Thus far, we have assumed that our bichromatic field comprises two microwave fields with equal amplitude. In this section, we analyze the effect of an amplitude imbalance between the two fields. For this analysis, we ignore the gradient term. From Eq. 6.3, our Hamiltonian is

$$\begin{aligned}
&2\hbar\Omega_\mu\hat{S}_x\cos([\omega_0+\delta]t) + 2(\hbar\Omega_\mu+\hbar\epsilon)\hat{S}_x\cos([\omega_0-\delta]t) \\
\rightarrow\ &\hbar\Omega_\mu\Big\{\sum_n \hat{\sigma}_{+,n}e^{-i\delta t} + \sum_n \hat{\sigma}_{-,n}e^{i\delta t} && \text{blue-detuned microwave field} \\
&\quad + \sum_n \hat{\sigma}_{+,n}e^{i\delta t} + \sum_n \hat{\sigma}_{-,n}e^{-i\delta t}\Big\} && \text{red-detuned microwave field} \\
&+\hbar\epsilon\Big(\sum_n \hat{\sigma}_{+,n}e^{i\delta t} + \sum_n \hat{\sigma}_{-,n}e^{-i\delta t}\Big) && \text{red-detuned field with amplitude } \epsilon \\
&= 2\hbar\Omega_\mu\hat{S}_x\cos(\delta t) + \hbar\epsilon\left(\hat{S}_x\cos(\delta t) - \hat{S}_y\sin(\delta t)\right),
\end{aligned}$$

where the red-detuned microwave field has a slightly different Rabi frequency $\Omega_\mu + \epsilon$. We now

transform to the bichromatic interaction picture with respect to the Ω_μ term and obtain

$$\begin{aligned}\hat{H}_{I,}(t) = \hbar\epsilon\hat{S}_x\cos(\delta t)\\ +\hbar\epsilon\Big\{\hat{S}_y\sin(\delta t)\Big[J_0\Big(\frac{4\Omega_\mu}{\delta}\Big)+2\sum_{n=1}^{\infty}J_{2n}\Big(\frac{4\Omega_\mu}{\delta}\Big)\cos(2n\delta t)\Big]\\ +2\hat{S}_z\sin(\delta t)\sum_{n=1}^{\infty}J_{2n-1}\Big(\frac{4\Omega_\mu}{\delta}\Big)\sin([2n-1]\delta t)\Big\}.\end{aligned} \tag{6.30}$$

The terms on the first and second lines have fast oscillations at δ and can be ignored. However, the term on the last line will produce stationary terms corresponding to $\hat{\sigma}_z$ ($\hat{S}_z$). If one is performing a $\hat{\sigma}_z\hat{\sigma}_z$ gate corresponding to the even resonances in Eq. 6.26, this term will commute with the gate interaction and can be treated as a static shift that can be echoed out. However, if one is performing a $\hat{\sigma}_y\hat{\sigma}_y$ gate corresponding to the odd resonances, this error term will no longer commute and will produce an error. This gate error will be small if $\Omega_g \gg \epsilon$. As $\Omega_g/2\pi$ ∼kHz, we would require ϵ to be much smaller than that. This requirement can be challenging to achieve experimentally as $\Omega_\mu/2\pi$ ∼MHz. Thus, both fields would need to be balanced at the 10^{-6} level; practically anything smaller than 10^{-3} would be difficult. We note that an additional dynamical decoupling field could be added to reduce sensitivity to this term, but that has its own challenges as discussed in Sec. 6.5.

6.2 Experimental implementation and calibration of $\hat{\sigma}_z\hat{\sigma}_z$ gates

We follow a similar implementation as described in Sec. 5.3. We perform a $\hat{\sigma}_z\hat{\sigma}_z$ gate corresponding to the J_2 resonance in Eq. 6.26. We use an out-of-phase radial mode[6] with frequency $\omega_r/2\pi \approx 6.9\,\mathrm{MHz}$. The frequency of our gradient is $\omega_g/2\pi = 5\,\mathrm{MHz}$. For the $\hat{\sigma}_z\hat{\sigma}_z$ gate, the detuning of the microwave fields is $\delta \approx (\omega_r - \omega_g)/2$, with $\delta/2\pi \approx 0.95\,\mathrm{MHz}$. For these gate experiments, we use currents of ≈1.2 A rms per electrode, producing a peak magnetic field gradient of ≈120 T/m at the ion. This corresponds to a gradient Rabi frequency of $\Omega_g/2\pi \approx 1.25\,\mathrm{kHz}$. In the next sections, we describe the calibration experiments performed and then discuss the results of our experiments.

As we use the out-of-phase (rocking) radial mode, the calibrations that require spin-motion

[6] We initially performed the gate on the center of mass mode, but the highest fidelity entanglement was obtained with the out-of-phase rocking mode. We discuss these other variations including two and four loop gates in Sec. 6.4.9.

coupling need to be done with two ions. Initially when the gate was performed on the center of mass mode, many of the gate dynamics could be investigated with a single ion. Because the two-ion lifetime is much shorter than the single-ion lifetime, we separate the calibrations into those that can be done with a single ion and those that require two.

For the single-ion calibrations, we perform the following steps:

- Calibrate the microwave π and $\pi/2$ pulses used in the gate as described in Sec. 4.4.4.
- Null the oscillating magnetic field as discussed in Sec. 5.5.
- Following the discussion in Sec. 6.1.1, we tune the Rabi frequency of the microwave fields to be at the intrinsic dynamical decoupling (IDD) point.
- Tune the bias voltage to maximize the gradient along the mode.
- Measure the ac Zeeman shift from the magnetic field orthogonal to the quantization axis oscillating at ω_g.

With two ions:

- We describe how we choose our motional frequencies to avoid resonances at ω_g.
- We calibrate the cooling of the motional mode using the radiofrequency gradient as described in Sec. 5.7, except we perform this cooling with **two** microwave fields instead of one.
- We calibrate the gate pulse sequence and the phase of the final $\pi/2$ pulse to take into account any asymmetries in our gate ramps.
- We calibrate the gate time and detuning to optimize the fidelity of our gate.

6.2.1 Calibrating microwave Rabi frequencies

We want to set the Rabi frequency of the microwave fields such that $J_0\left(\frac{4\Omega_\mu}{\delta}\right) = 0$. In this case, the detuning $\delta/2\pi \approx 0.95\,\mathrm{MHz}$, which requires $\Omega_\mu/2\pi = 0.571\,\mathrm{MHz}$. We perform a coarse

calibration by measuring this Rabi frequency on resonance for each of the microwave lines. A finer calibration is performed using an additional field on resonance. This additional field has a much weaker Rabi frequency $\Omega_c/2\pi \approx 4.2\,\mathrm{kHz}$. The Hamiltonian of these three fields is

$$\begin{aligned}
\hat{H}(t) =& 2\hbar(\Omega_\mu + \hbar\epsilon)\hat{S}_x \cos([\omega_0 + \delta + \Delta]t) && \text{blue-detuned field} \\
&+ 2\hbar\Omega_\mu \hat{S}_x \cos([\omega_0 - \delta + \Delta]t) && \text{red-detuned field} \\
&+ 2\hbar\Omega_c \hat{S}_x \cos([\omega_0 + \Delta]t). && \text{weaker carrier field}
\end{aligned}$$

We adjust the phase of the weaker carrier field to be the same as the beatnote of the blue and red detuned fields. We choose the pulse duration such that the weaker field drives a spin flip on resonance. We add a frequency offset Δ to all three fields. This offset can be seen as a qubit frequency error as described in Sec. 6.1.1. If the red and blue detuned microwave fields are balanced and at the IDD point, we should see a broadening of the resonance driven by the weaker field as shown in Fig. 6.4.

Following the discussion in Sec. 6.1.5, if the two fields have an imbalance ϵ, an additional term also weakly drives spin flips and we have an additional shift that is not removed by the IDD. This imbalance results in an asymmetry in the scan that we can use to calibrate the Rabi frequency more precisely. The data for this calibration is shown in Fig. 6.5.

6.2.1.1 Intrinsic dynamical decoupling

Our qubit is field-sensitive; therefor the qubit will have frequency fluctuations due to changing (nominally static) magnetic fields or changing ac Zeeman shifts from the various oscillating magnetic fields. In order to perform a high-fidelity gate, we need to suppress the effects of these fluctuations. We investigate the effect of intrinsic dynamical decoupling (IDD) on the qubit coherence by performing a spin-echo Ramsey experiment with and without IDD. The results are presented in Fig. 6.6. We find that the IDD extends our qubit coherence by more than order of magnitude, and for gate durations shorter than 1 ms, the effects of qubit decoherence are small.

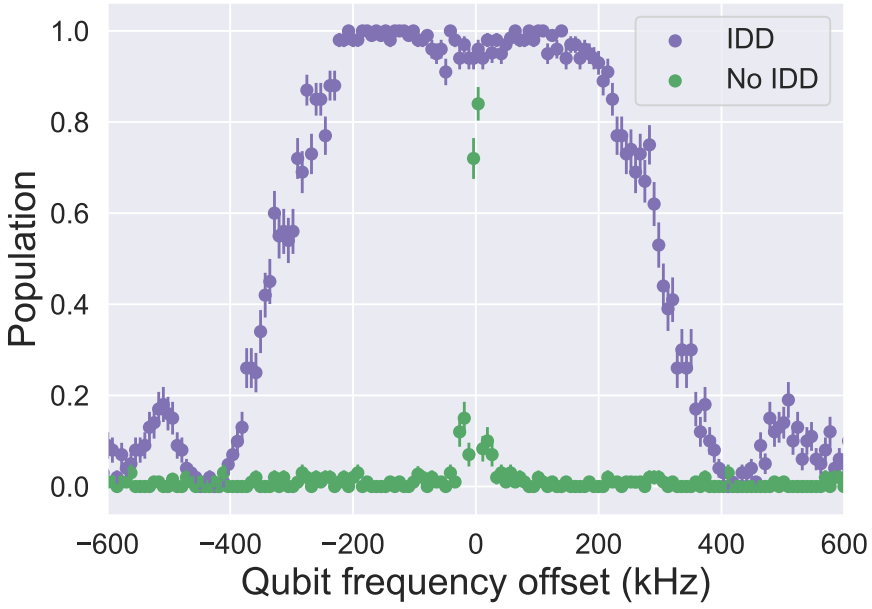

Figure 6.4: Rabi spectroscopy with and without intrinsic dynamical decoupling (IDD). With the bichromatic field off (no IDD), we have only one field with Rabi frequency $\Omega_c/2\pi \approx 4.2\,\text{kHz}$ which is pulsed for the duration of a π pulse that flips the ion spin from $|\downarrow\rangle \rightarrow |\uparrow\rangle$. As we sweep the frequency of this field, we see a narrow resonance shown by the points in green. With the IDD on the other hand (purple points), we see a broadening of this line as the IDD reduces the sensitivity to qubit frequency offsets.

6.2.2 Calibration of mode orientation

We tune the bias voltage on our RF electrodes as described in Sec. 3.6. As we change the bias, we change the orientation of the radial modes, and thus their overlap with the magnetic field gradient. As we maximize the overlap of the gradient with the mode, we maximize the gate speed using that mode. Increasing the gate speed typically increases the fidelity and reduces sensitivity to many different errors. As shown in [Warring et al., 2013a] using a similar trap geometry, this gradient is optimized at the maximum frequency of the low-frequency radial mode. We measure this frequency as a function of bias voltage and plot this variation in Fig. 6.7. We set the bias voltage to sit at the maximum frequency.

We note that it is experimentally challenging to verify that this mode orientation has the largest gradient. Verification would require careful calibrations of the gate times and detunings, and improvements in the gate speed would be small. For these experiments we simply set the bias as

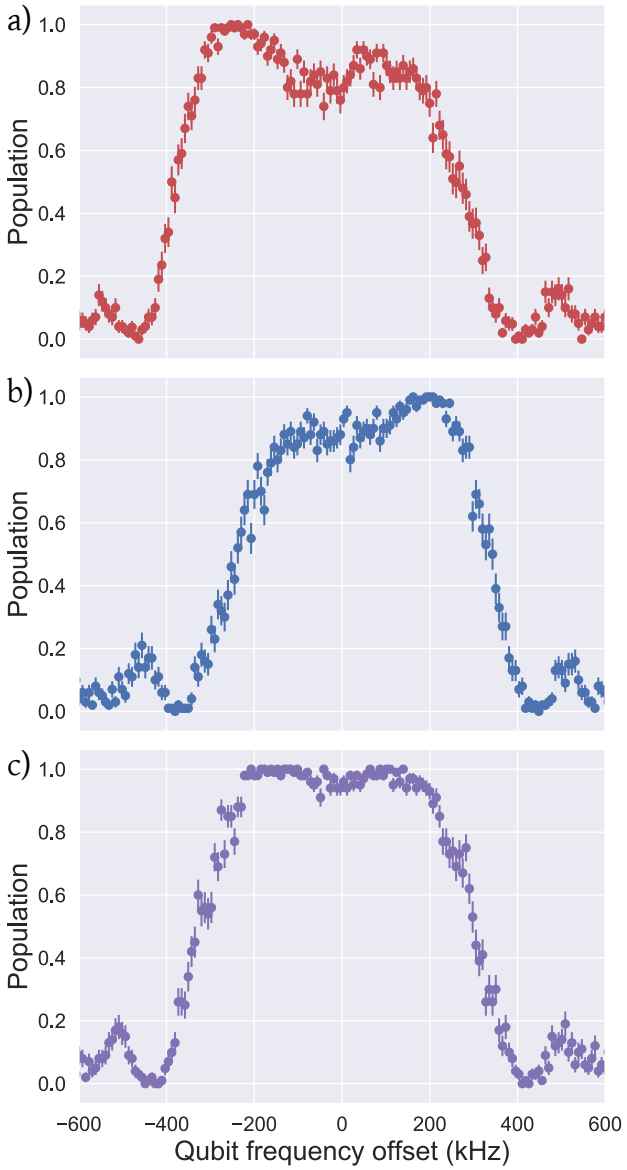

Figure 6.5: Plot of population in $|\uparrow\rangle$ versus qubit frequency offset for three cases of the bichromatic field Rabi frequences. For each of the three plots, the Rabi frequency of the blue-detuned microwave field is varied while the Rabi frequency of the red-detuned microwave field is kept constant at the ideal value of Ω_μ. An additional carrier pulse transfers $|\downarrow\rangle \rightarrow |\uparrow\rangle$ on resonance. For each qubit frequency offset, the frequency of all three fields is shifted by that amount. **a)** The blue detuned microwave has a Rabi frequency of 0.996 Ω_μ. **b)** The blue detuned microwave has a Rabi frequency of $\approx$1.006 Ω_μ. **c)** The blue detuned microwave has a Rabi frequency of Ω_μ. When the Rabi frequencies of the blue and red detuned fields are balanced, we see no asymmetry in the scan.

described and optimized the gate parameters there. Simulations could also be performed to verify the mode orientation.

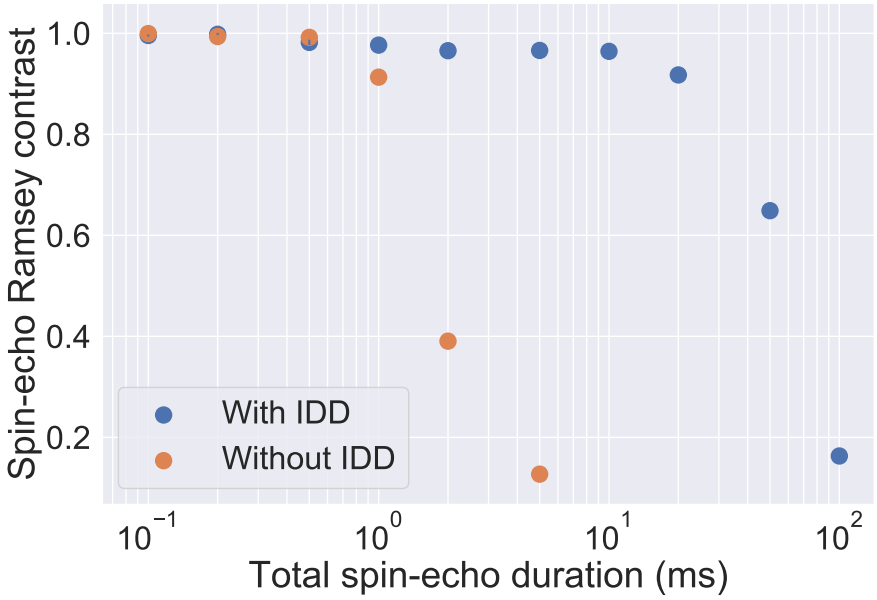

Figure 6.6: Qubit coherence with and without intrinsic dynamical decoupling (IDD). We perform a spin-echo Ramsey experiment with and without IDD and plot the contrast as a function of the interrogation time. For each point, we scan the phase of the second $\pi/2$ pulse in the spin-echo Ramsey sequence and measure the contrast of the resulting oscillation. We find that with IDD (blue points) we extend the qubit coherence by more than an order of magnitude compared to the bare qubit (orange points).

6.2.3 Measuring ac Zeeman shifts from magnetic field at ω_g

The qubit frequency experiences an ac Zeeman shift from the magnetic fields oscillating at ω_g. While we null the magnetic field at ω_g along the quantization axis, the orthogonal components of the field are not nulled and give rise to a significant ac Zeeman shift on the qubit frequency. We measure this for both the $|F=3, m_F=3\rangle \leftrightarrow |F=2, m_F=2\rangle$ and $|F=3, m_F=2\rangle \leftrightarrow |F=2, m_F=2\rangle$ transition. The former is the qubit transition for our gate and the shift is $\approx -400\,\mathrm{kHz}$. The latter corresponds to a additional transition required for our repump sequence for cooling while the gradient at ω_g is on and the shift is $\approx -240\,\mathrm{kHz}$.

6.2.4 Tuning motional mode frequencies

It is important to be aware of the frequencies of all six of the two-ion modes. Crucially, we want to avoid any mode frequencies, or the difference frequency of any of the modes at ω_g. An

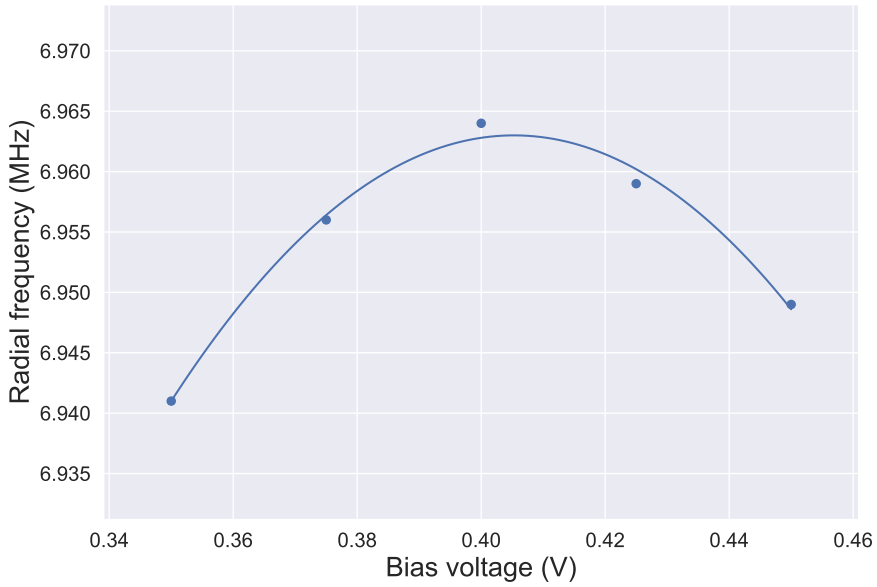

Figure 6.7: Plot of radial frequency versus bias voltage. This radial frequency is the lower radial frequency for a single ion. The higher radial frequency is at ≈7.4 MHz. As we change the bias voltage, we change the orientation of the radial modes and their overlap with the gradient. We set the bias to the maximum of the curve, corresponding to a bias voltage of 0.405 V, to maximize the overlap with the gradient.

electric field at ω_g would excite those modes as described in Sec. 5.11. Furthermore, there is also the oscillating magnetic field at ω_g to consider. If the magnetic field along the quantization axis is not nulled completely, the Hamiltonian for the residual magnetic field appears in the bichromatic interaction picture as

$$\begin{aligned}\hat{H}_{I,z} = \; & \tfrac{\hbar\Omega_z}{2}\cos(\omega_g t)\Big\{\hat{S}_z\Big[J_0\Big(\tfrac{4\Omega_\mu}{\delta}\Big) + 2\textstyle\sum_{n=1}^{\infty} J_{2n}\Big(\tfrac{4\Omega_\mu}{\delta}\Big)\cos(2n\delta t)\Big] \\ & -2\hat{S}_y \textstyle\sum_{n=1}^{\infty} J_{2n-1}\Big(\tfrac{4\Omega_\mu}{\delta}\Big)\sin([2n-1]\delta t)\Big\},\end{aligned} \tag{6.31}$$

where we follow a similar derivation as Sec. 6.1.1 and Ω_z is defined as in Sec. 5.5. If $n\delta \approx \omega_g$, some of the higher order terms in Eq. 6.31 will no longer be fast-oscillating and cannot be ignored. These terms could excite additional resonances that cause gate errors. These resonances can be avoided by choosing ω_r and ω_g such that $n\delta$ for a particular gate is far from resonance. Experimentally, ω_g is fixed for us due to hardware considerations and we adjust ω_r by adjusting the bias as described

in Sec. 3.6 or the scale for the axial confinement. The Raman beams are used to find the difference frequencies between our radial and axial modes as our microwave and rf gradients do not couple to the axial modes (see Sec. 3.1).

6.2.5 Cooling with a radiofrequency gradient and a bichromatic microwave field

We have shown in Sec. 5.7 that a motional mode can be cooled with a radiofrequency gradient and a single microwave field. Here, we extend this to two microwave fields, carefully tuning the blue sideband off resonance so it causes negligible heating. The reasons are two-fold. First, as we increase the Rabi frequency of the microwave fields, we increase the ac Zeeman shift. This limits the microwave Rabi frequencies that can be used as seen in Sec. 5.6.1. By including a second microwave field with the opposite sign for its detuning δ, we cancel the ac Zeeman shifts from each of the fields to first order. Second, we perform the cooling sequence before the gate. Thus, by turning on all the fields that are required for the gate during the cooling, we warm up all the relevant hardware and reduce duty cycle or thermal effects during the gate itself.

For a single microwave field, $\delta_{\text{red}} = -(\omega_r - \omega_g)$ to drive the red sideband, ignoring the effects of ac Zeeman shifts. To cool it with two fields, we have a second blue-detuned field at $\delta_{\text{blue}} = \omega_r - \omega_g + \Delta_{\text{offset}}$, where Δ_{offset} is an offset from resonance. Without Δ_{offset}, we would drive a spin-dependent force corresponding to the $\hat{\sigma}_y\hat{\sigma}_y$ interaction in Eq. 6.26. These values for δ are different from the detuning of the gate fields at $\delta = \pm\frac{\omega_r - \omega_g}{2}$. We keep the Rabi frequency of the microwave fields at the same values that are used for the gate sequence. The cooling sequence could be optimized further by adjusting this Rabi frequency to maximize the sideband interactions, but we eschew this step as this would be slow in our experiment.

Factoring in the ac Zeeman shifts, the detunings for both the fields are

$$\delta_{\text{red}} = -(\omega_r - \omega_g) + \Delta_{\text{ac}}, \tag{6.32}$$

$$\delta_{\text{blue}} = \omega_r - \omega_g + \Delta_{\text{ac}} + \Delta_{\text{offset}}, \tag{6.33}$$

where Δ_{ac} is the ac Zeeman shift from all three fields: the two microwave fields and the magnetic field at ω_g. With all three fields, $\Delta_{\mathrm{ac}}/2\pi \approx -390\,\mathrm{kHz}$ as opposed to -400 kHz without the microwave fields. This shift was measured with $\Delta_{\mathrm{offset}}/2\pi = 100\,\mathrm{kHz}$. We pick this value to be large compared to the sideband Rabi frequency, so it does not cause additional heating by driving motion-adding transitions.

For our cooling sequence, we use thirty 30 μs red sideband pulses interleaved with repump sequences to cool the two ion mode used for the gate close to ground state. If the gate operation is performed on the center-of-mass mode that is present with a single ion, the cooling sequence as well as the shifts can be calibrated with a single ion. For the two-ion out-of-phase mode, we perform these calibrations with both ions. Data showing cooling with the bichromatic field is shown in Fig. 6.8. We find that with cooling, Δ_{ac} is shifted slightly, most likely due to thermal effects from heat dissipation in the trap electrodes when all the fields are on for the cooling sequence.

We note that for the out-of-phase radial mode, we also cool the out-of-phase axial mode. The two modes have a significant coupling that can affect the coherence of the mode we use for the gate [Home et al., 2011]. As we do not have a magnetic field gradient along the axial mode, we perform cooling of this mode with our Raman beams before cooling the out-of-phase radial mode as described above.

6.2.6 Gate pulse sequence

The gate pulse sequence that we use corresponds to an 8-loop Walsh 7 sequence [Hayes et al., 2012] (see Sec. 2.5.2). We ramp the gradient and the bichromatic fields up and down 8 times. We turn the gradient at ω_g on first using a 5 μs Blackman envelope, and then we turn on the bichromatic fields also with a Blackman envelope over 5 μs. We ramp the gradient at ω_g first, as we also have an ac Zeeman shift from the magnetic fields at ω_g that shifts the qubit frequency. Our bichromatic fields are calibrated to this shifted value. This pulse sequence is shown in Fig. 6.9. Aside from the gradient and the bichromatic fields, we have an additional field on resonance with the qubit at ω_0 to perform the initial and final $\pi/2$ pulses as well as the π pulses during the gate sequence to provide

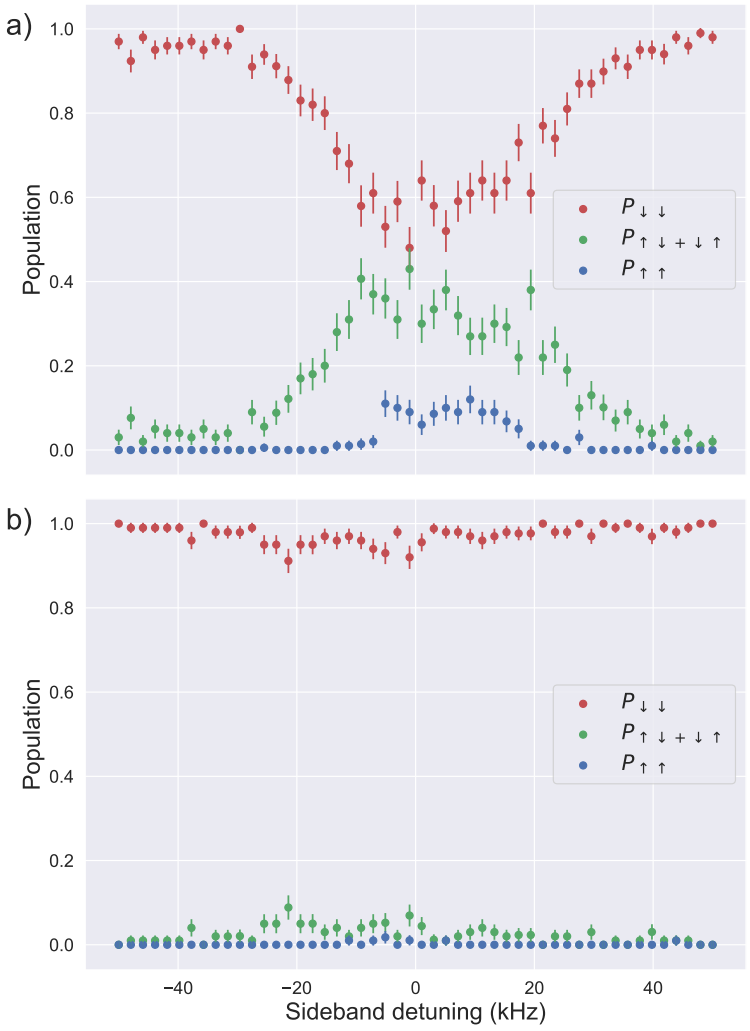

Figure 6.8: Red sideband transition with a bichromatic microwave field and radiofrequency magnetic field gradient. We scan the detuning from the red sideband transition on the out-of-phase rocking mode, with the two fields and the gradient pulsed for 30 μs. **a)** Without cooling, we see excitation of the ion populations from their initial internal states of $|\downarrow\downarrow\rangle$. **b)** After cooling, we see that the red sideband transition is significantly suppressed, indicating that the ions are cooled close to the ground state of this mode. We use a cooling sequence of thirty 30 μs red sideband pulses.

the Walsh 7 modulation. We alternate the phase of the π pulses to correct for any π pulse errors that cause under or over rotations [Levitt, 1996].

We shorten the ramp times compared to those in Sec. 5.8 to reduce the time taken just for the ramps during our gate sequence. During the ramps, the qubit is also unprotected and vulnerable to decoherence as the intrinsic dynamical decoupling only occurs when the bichromatic fields are on at

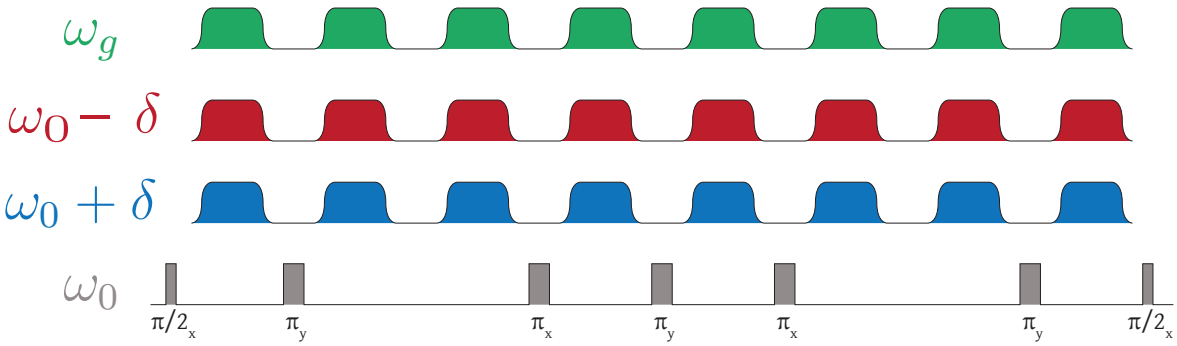

Figure 6.9: Gate pulse sequence for our Walsh 7 $\hat{\sigma}_z\hat{\sigma}_z$ gate. The field gradient at ω_g and the bichromatic microwave fields at $\omega_0 \pm \delta$, where $\delta \approx \omega_r - \omega_g$, are ramped up and down 8 times for our 8-loop gate, with ω_0 being the qubit frequency, and ω_r the motional mode frequency. We have an additional field on resonance with the qubit for our initial and final $\pi/2$ pulses and for the 5 π pulses during the gate sequence to produce the Walsh 7 modulation. The total gate duration including the $\pi/2$ pulses is 740 μs.

their calibrated amplitude.

6.2.7 Calibrating $\pi/2$ pulse phase

Our gate implementation is in theory robust to fluctuations in the qubit frequency. Aside from the intrinsic dynamical decoupling, qubit frequency fluctuations commute with the gate and are echoed out by the π pulses in the gate sequence. Thus, the initial and final $\pi/2$ pulses should have the same phase. In practice, however, we find that we have to make a small adjustment to the phase of the final $\pi/2$ pulse. We believe this adjustment is due to thermal effects that result in a time variation in the ac Zeeman shift from the magnetic field at ω_g. This time variation would result in the ac Zeeman shift during the first ramp not being identical to subsequent ramps. Our pulse sequence should remove up to quadratic variations of this shift, with the phase adjustment taking into account the higher-order variation. Having calibrated the gate time and detuning, we scan the phase of the second $\pi/2$ pulse and set the phase to be at the minimum of the one-ion bright population. This scan is shown in Fig. 6.10. We find the correction required to be on the order of $0.002\times2\pi$ radians or 0.8°.

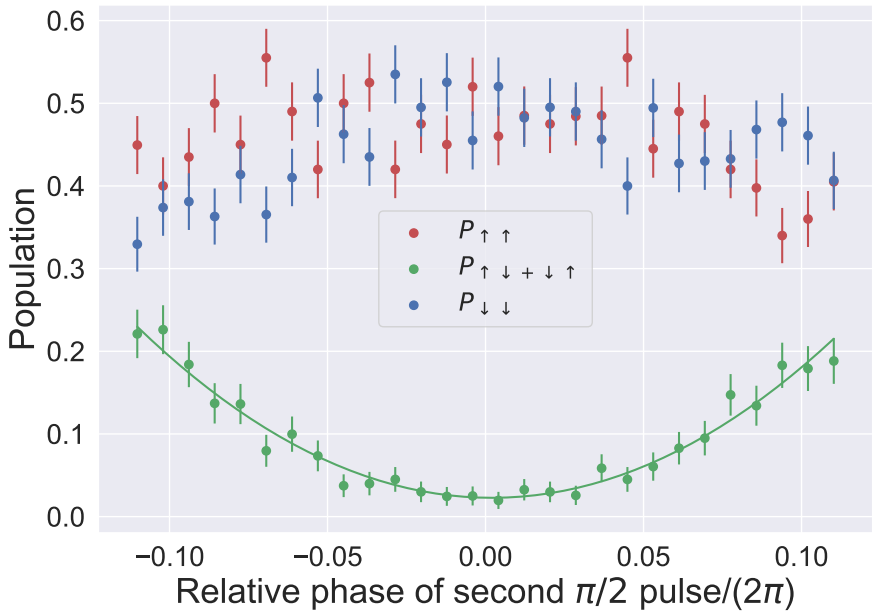

Figure 6.10: Scan of relative phase of the final $\pi/2$ pulse in the gate sequence to the first. We fit a quadratic to the one-ion bright data (green line) and determine the phase correction from the minimum of the fit. For this particular scan, the minimum was at a phase of $0.002\times 2\pi$ radians.

6.2.8 Gate duration and detuning

Finally, we discuss the gate duration and detuning calibrations. In principle, both these parameters are determined completely by the gate Rabi frequency. However, for our system, optimizing the gate determines our gate Rabi frequency. For a coarse calibration, we perform gate detuning scans at different gate durations and try to match the scans to numerical simulations performed using QuTiP [Johansson et al., 2013]. Simulations are shown in Fig. 6.11 with experimental data in Fig. 6.12. We perform detuning scans as opposed to duration scans to keep the duty cycle of gate fields and gradients constant and to minimize thermal effects.

A finer calibration is then performed by varying the gate duration and detuning in smaller steps and measuring the fidelity at each point. We then adjust both the gate detuning and duration to maximize the gate fidelity. We find the optimal gate duration to be 740 μs. Following Sec. 2.5.4, we are unable to resolve timing errors at the 5% level with the Walsh 7 seqeuence. We find that the optimal gate detuning has day-to-day variations at the 100 Hz level.

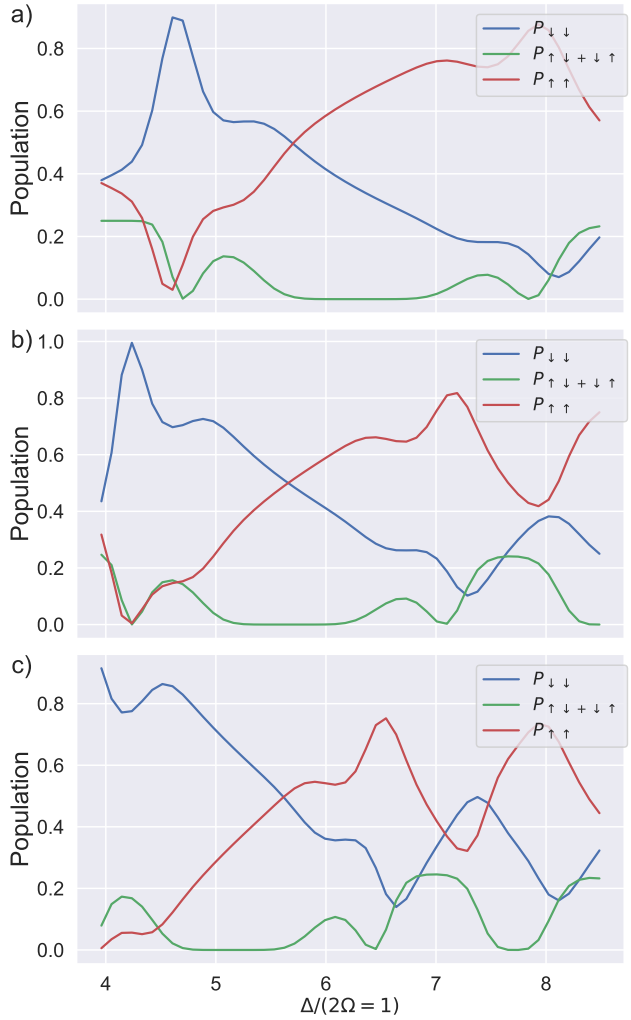

Figure 6.11: We perform simulations of gate detuning scans at three different durations: **a)** $t = 0.9t_g$, **b)** $t = t_g$ and **c)** $t = 1.1t_g$, where t_g is the duration required to generate the maximally entangled state $|\Phi\rangle = 1/\sqrt{2}\,(|\downarrow\downarrow\rangle + |\uparrow\uparrow\rangle)$ and Δ is the gate detuning (see Eq. 6.27). Depending on the duration of the interaction, the populations of $P_{\uparrow\uparrow}$ and $P_{\downarrow\downarrow}$ (red and blue lines) cross at different points above the null of the one ion bright population $P_{\uparrow\downarrow+\downarrow\uparrow}$ (green line). This feature can be used to calibrate the gate time close to its optimal value. Experimental data is shown in Fig. 6.12.

6.2.9 Stability of calibrations

The bulk of the data for the gate results was taken over a two month period from December 2019 to January 2020. During this time, the microwave parameters for the intrinsic dynamical decoupling (IDD), the phases for the nulling of the magnetic field at ω_g, the bichromatic cooling calibrations, and the gate duration were not adjusted from mid-December[7] onwards. However, we

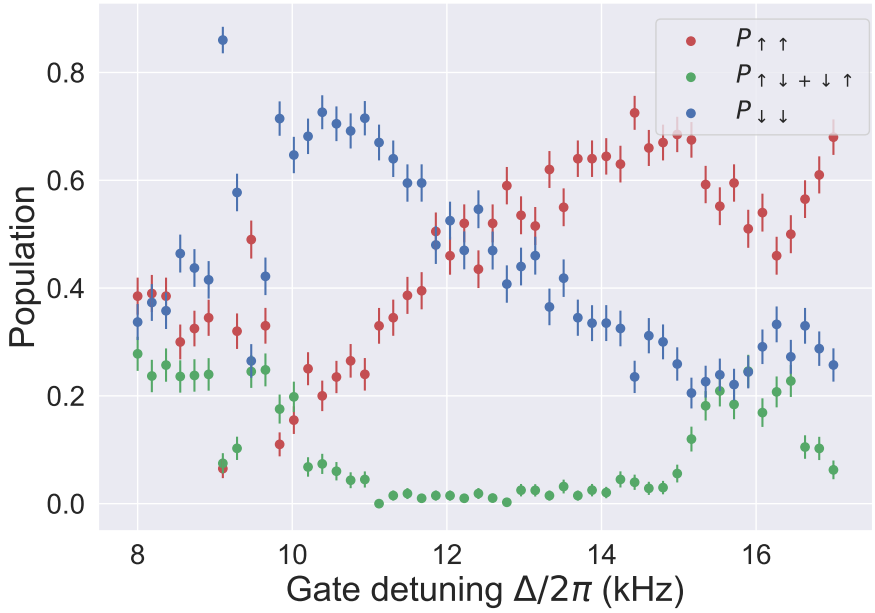

Figure 6.12: Gate detuning scan at total gate duration of 740 μs. We see similar features to the simulated data in Fig. 6.11. We use this scan as a coarse calibration of the gate time and detuning. For finer calibration of those parameters, we measure the gate fidelity at different values of the gate time and detuning.

typically calibrated the π and $\pi/2$ times used in the gate sequence daily. With each pair of ions that were loaded, we performed the micromotion compensation and adjusted the motional frequencies such that $\delta = (\omega_r - \omega_g)/2$ was close to the frequency where the IDD was calibrated. We also adjusted the gate detuning at the 100 Hz level to optimize the fidelity.

6.3 Gate data

While the fidelity analysis is detailed in Chapter. 8, we explain what raw data is collected. We measure the population and parity after a gate sequence. Raw data is shown in Fig. 6.13. In taking this data, we include 20 dummy points which are not used in the analysis at the start of the experiments in order for both the motional frequency tracking and thermal effects to stabilize. We then measure the populations after an additional parity $\pi/2$ pulse with a variable phase. For

[7] This included several power outages and large temperature swings ($>$ 5 K) in the lab. This stability offers the most compelling argument for laser-free gates; path length fluctuations are much easier to ignore with 60 m wavelengths (5 MHz gradient) as opposed to wavelengths $\sim$ 300 nm.

this measurement, we use a precalibrated phase offset to take more points at the peaks of the parity amplitude. In total, we measure the populations for 52 parity phases from 0 to 2π. In addition, within the same run we also measure the populations after the gate sequence without any parity pulse. We make 40 population measurements. Both the parity and population measurements are done with 200 repetitions each. These data were taken with interleaved measurements of the motional frequency in between every parity or population point as described in Sec. 4.7. More repetitions could be done per point, but that measurement would likely have to be interleaved with the motional frequency tracking before the end of all the repetitions. The drift tracking for these data is shown in Fig. 4.22. 200 repetitions were chosen for these data for simplicity and also ion-lifetime considerations.

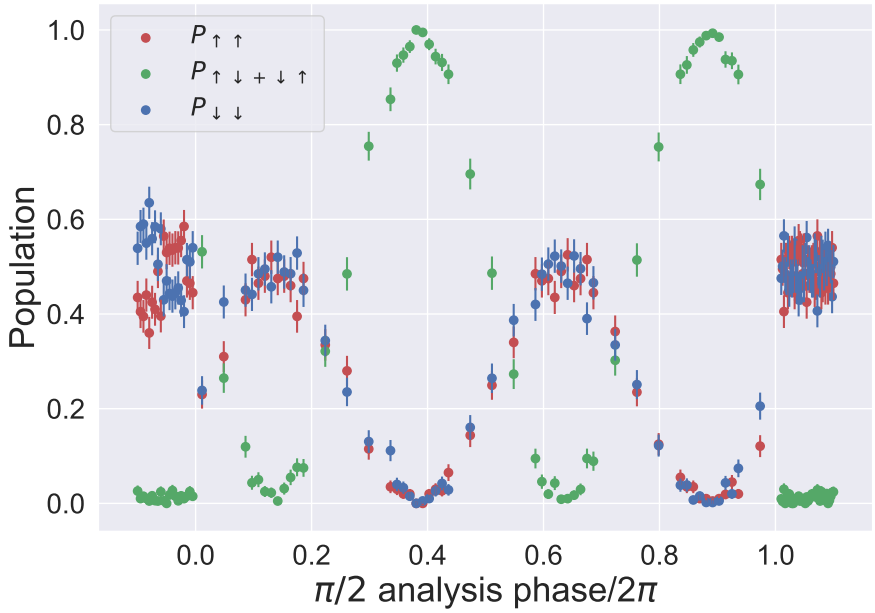

Figure 6.13: Raw population and parity data. We measure both the populations and parity within a single run of the experiment, where each point is averaged from 200 repetitions. For horizontal axis points below 0 or above 2π, there is no parity pulse and we simply measure the populations at the end of the gate sequence. The first twenty points of the experiment are "dummy" points that are not used for subsequent analysis. These data are used to generate the parity scan in Fig. 6.15.

In addition to the population and parity measurements, we also measure three different reference states to characterize our state preparation and measurement (SPAM). These states are

both ions bright, $|\downarrow\downarrow\rangle$, both ions dark $|\uparrow\uparrow\rangle$, following the application of a π pulse, and the ions in an equal superposition of $|\downarrow\downarrow\rangle$, $|\uparrow\uparrow\rangle$, $|\uparrow\downarrow\rangle$, $|\downarrow\uparrow\rangle$ after a $\pi/2$ pulse. The first measurement lets us characterize the two-ion bright state, the second the two-ion dark, and the third a measure of the one-ion bright state. Ideally, one would be able to prepare the one-ion bright state as well but that would require high-fidelity single-ion addressing. For the reference data, we take 500 repetitions per point, which corresponds to about 18,500 measurements per state. We use the exact same state preparation as we do for the gate sequence. Example data is shown in Fig. 6.14.

We note that each set of gate and reference data is taken with a single set of two ions. We perform the calibrations as described earlier, but want to take into account the changing conditions of the trap due to charging from our photoionization beams.

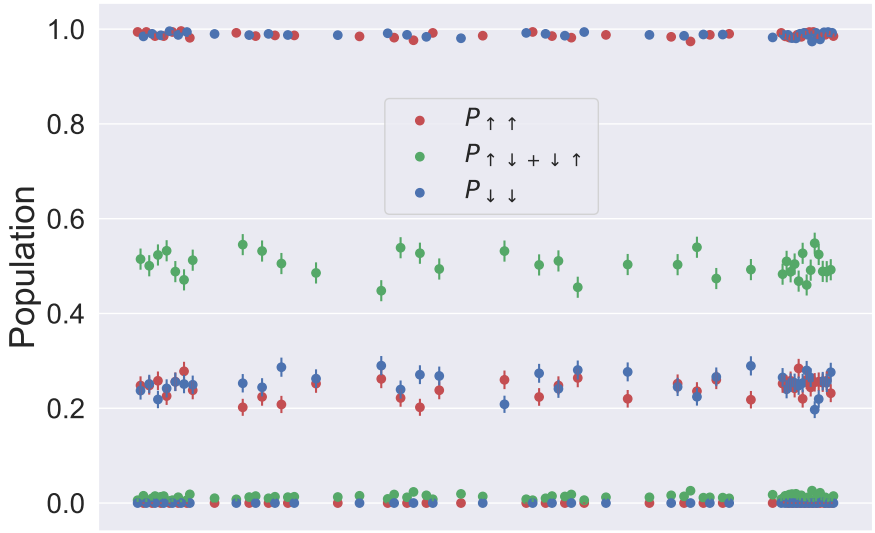

Figure 6.14: Raw reference data for fidelity analysis. From the initial state of $|\downarrow\downarrow\rangle$, we alternate between doing nothing, applying a π pulse, and applying a $\pi/2$ pulse and then measuring the ion populations. These measurements would correspond to $P_{\downarrow\downarrow} \approx 1$, $P_{\uparrow\uparrow} \approx 1$ and finally $P_{\downarrow\downarrow} = P_{\uparrow\uparrow} \approx 0.25$, $P_{\uparrow\downarrow+\downarrow\uparrow} \approx 0.5$. These measurements provide the reference data for the fidelity analysis as described in the text. Each point is an average of 500 measurements.

6.4 Results

Using our Walsh 7 $\hat{\sigma}_z\hat{\sigma}_z$ gate sequence, we obtain a Bell-state fidelity of 0.999(1). A scan of the parity of our entangled state is shown in Fig. 6.15. This result is the highest laser-free Bell-state

fidelity to date, and is competitive with the highest-fidelity two-qubit gates across any platform.

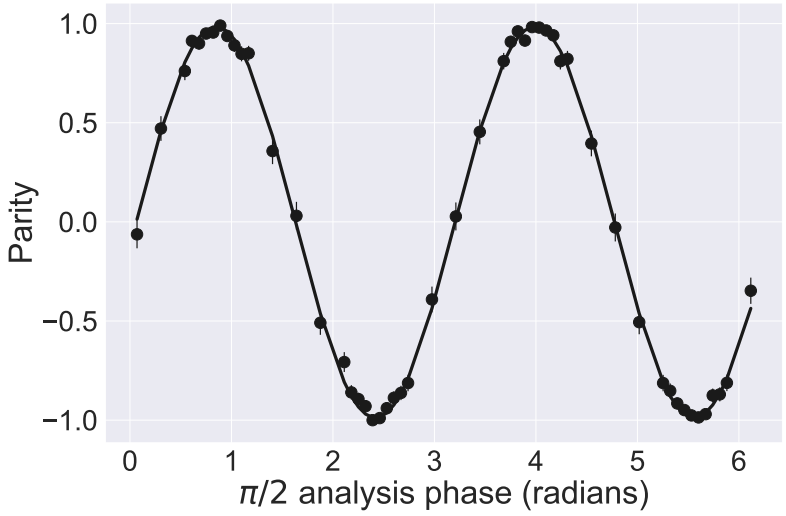

Figure 6.15: Parity scan of the entangled state produced at the end of the gate sequence. For these data, we perform the entangling operation and measure the ion populations after applying an additional $\pi/2$ pulse with a variable phase. The parity is $P = P_{\uparrow\uparrow} + P_{\downarrow\downarrow} - P_{\downarrow\uparrow+\uparrow\downarrow}$. The raw ion populations are shown in Fig. 6.13. These data are not corrected for SPAM errors.

6.4.1 Comparison to other laser-free gates

We compare our result to other laser-free trapped-ion entangling gates in table 6.1. Our result is the first gate using a radio-frequency magnetic field gradient, and we have managed to improve the Bell-state fidelity while simultaneously reducing the gate duration compared to other results with a similar fidelity. In comparison to schemes that use gradients close to the qubit at gigahertz frequencies, we also only require one field gradient. The entangling gate in [Weidt et al., 2016] required four microwave fields per ion, as opposed to two fields for our scheme. This reduction is due to our intrinsic dynamical decoupling scheme that does not require extra fields.

We note that our technique has also enabled generation of larger magnetic field gradients at the ion. However, this does not translate proportionately to a larger gate Rabi frequency as one must also take into account the factor of the J_2 function.

Gradient frequency	No. of field gradients	No. of microwave fields	Gate interaction	B-field gradient (T/m)	Gate Rabi frequency (kHz)	Gate duration (μs)	Bell-state infidelity (10^{-3})	Year	Ref.[8]
1.69 GHz	2	0	$\hat{\sigma}_x\hat{\sigma}_x$	35.3	0.9	400	240(30)	2011	NIST
Static	1	0	$\hat{\sigma}_z\hat{\sigma}_z$	19	0.02	8000	360(50)	2012	Siegen
3.2 GHz	2	1	$\hat{\sigma}_x\hat{\sigma}_x$	7	0.154	3250	3(1)	2016	Oxford
Static	1	8	$\hat{\sigma}_x\hat{\sigma}_x$	24	0.093	2700	15(12)	2016	Sussex
1.1 GHz	2	0	$\hat{\sigma}_x\hat{\sigma}_x$	19	0.59	808	18(12)	2019	PTB 1
1.1 GHz	2	0	$\hat{\sigma}_x\hat{\sigma}_x$	19	0.59	2938	3(1)	2019	PTB 2
5 MHz	1	2	$\hat{\sigma}_z\hat{\sigma}_z$	120	1.25	740	1(1)	2020	This work

Table 6.1: Comparison of laser-free entangling gates. Gate Rabi frequencies are listed following our convention where the single-loop gate duration is $t = 2\pi/(4\Omega_{\text{gate}})$ (see Eq. 2.35). Ramp times are included in the gate duration for this work but not factored into Rabi frequency estimate. We consider only the field gradients and fields required to generate the spin-spin interaction.

[8] NIST 2011 - [Ospelkaus et al., 2011], Siegen 2012 - [Khromova et al., 2012], Oxford 2016 - [Harty et al., 2016], Sussex 2016 - [Weidt et al., 2016], PTB 1 2019 - [Hahn et al., 2019] PTB 2- [Zarantonello et al., 2019]

6.4.2 Insensitivity to qubit frequency offsets

Our gate is insensitive to qubit frequency offsets in two ways. First, we employ the intrinsic dynamical decoupling described in Sec. 6.1.1. Second, qubit frequency offsets which are proportional commute with the $\hat{\sigma}_z\hat{\sigma}_z$ interaction that we generate, and thus can be echoed out. We investigate this experimentally and the data are shown in Fig. 6.16. For these data, we deliberately add a frequency offset to our blue and red detuned microwave fields for the gate operation. Explicitly, the detunings of the fields are

$$\begin{aligned} \delta_{\text{red}} &= -(\omega_r - \omega_g)/2 + \Delta_{\text{ac}} + \Delta_{\text{offset}}, \\ \delta_{\text{blue}} &= (\omega_r - \omega_g)/2 + \Delta_{\text{ac}} + \Delta_{\text{offset}}, \end{aligned} \tag{6.34}$$

where Δ_{ac} is the ac Zeeman shift from the field at ω_g and Δ_{offset} is an offset that we add. This offset mimics a qubit frequency miscalibration with the gradient and bichromatic microwave fields on. We note that the frequency of the carrier for the π and $\pi/2$ pulses was not modified, nor did we change any other gate parameters.

From the data, we can see that the gate fidelity is > 0.99 over a range of $\Delta_{\text{offset}}/2\pi$ from -200 to 200 kHz. This range is much larger than the gate Rabi frequency which is $\sim$kHz. For an $\hat{\sigma}_x\hat{\sigma}_x$, this error would not commute with the gate interaction and would severely impact the fidelity. We exploit this insensitivity to qubit frequency offsets to perform single-ion addressing in chapter 7.

6.4.3 Error analysis

We think our gate fidelity is primarily limited by motional errors. These errors come mainly from motional dephasing and motional frequency fluctuations as described in Sec. 2.5. We perform simulations in QuTiP with our gate parameters to estimate the errors in Table 6.2.

For the motional frequency error, we extract the errors from our motional frequency tracking data (see Sec. 4.7 and Fig. 4.23) and use that in our simulation.

The heating rate on our rocking mode is expected to be an order of magnitude lower than

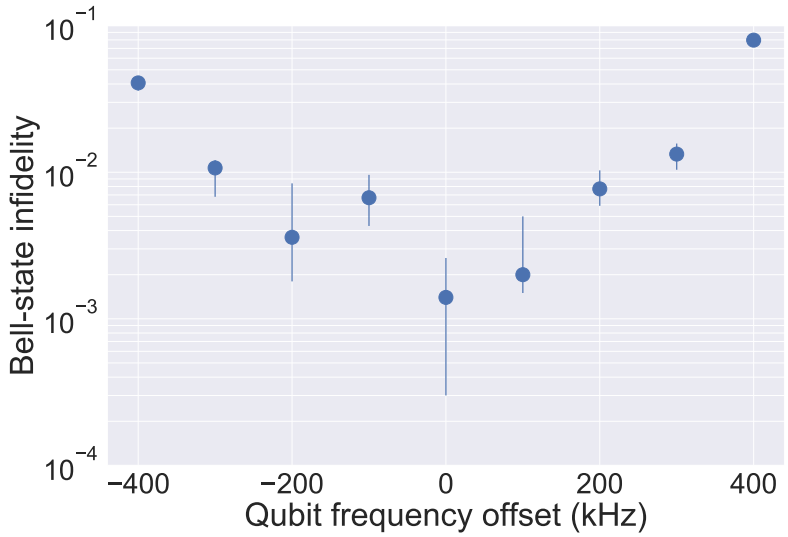

Figure 6.16: Plot of Bell-state fidelity versus qubit frequency offset during the gate. The qubit frequency offset is added to both the red- and blue-detuned microwave fields. For a region of $\pm 200\,\mathrm{kHz}$, the Bell-state fidelity is still > 0.99, demonstrating the robustness of this gate to such shifts. This region is much larger than the gate Rabi frequency $\Omega_g/2\pi \approx 1\,\mathrm{kHz}$. This robustness is a consequence of both the intrinsic dynamical decoupling as well as performing a $\hat{\sigma}_z\hat{\sigma}_z$ gate that commutes with frequency errors which are proportional to $\hat{\sigma}_z$.

the heating on the center-of-mass mode, which is about 40 quanta/s. A heating rate of a few quanta/s is challenging to measure, especially with our relatively short two-ion lifetimes. Based on measurements we have made, we place an upper bound on this heating rate at 4 quanta/s.

We believe motional dephasing is our leading error source. However, this is also a challenging measurement. From separate experiments using squeezed states [Burd, 2020], we estimate this dephasing rate to be 5-10/s, which corresponds to a motional coherence time of 100-200 ms.

Error mechanism	Error (10^{-4})
Motional dephasing	5-10
Motional frequency fluctuations	< 5
Heating	< 1
Total	5-10

Table 6.2: Estimated error budget.

6.4.4 Temperature insensitivity

While we believe that the infidelity of our highest-fidelity gate is dominated by motional errors, our gate implementation is relatively robust to the initial temperature of the gate mode. This dependence was examined using numerical simulations as shown in Fig. 6.17, following the model for gate errors discussed in Sec. 2.5. We assume a gate Rabi frequency $\Omega_g/2\pi = 1.25\,\mathrm{kHz}$, and calculate the error due to static detuning errors, motional dephasing, and motional heating at different thermal occupations $\bar{n}$ from 0 to 4. For a multi-loop sequence, the temperature dependence of these errors gets smaller and smaller, and for a Walsh 7 sequence, the only error that is significantly temperature dependent is from motional dephasing up to our Doppler temperature with $\bar{n} \approx 2$.

6.4.5 Gates at Doppler temperature

The highest fidelity gate was performed on the out-of-phase radial mode with ground state cooling on both that mode and the out-of-phase axial mode. Without ground-state cooling, we find that the increased temperature mainly makes us more sensitive to the motional dephasing error. If we could eliminate ground state cooling from the state preparation, that would increase the duty cycle of our experiments substantially. Ground state cooling typically takes several milliseconds, especially for multiple modes of motion.

We perform the gate with ions at the Doppler temperature with $\bar{n} \approx 2$. For this experiment, we perform the ground state cooling of the motional mode with the radiofrequency gradient and the microwaves as before but subsequently pulse the Doppler cooling laser to bring the ions back to their Doppler temperature. This step is done to keep the duty cycle of the high-power radiofrequency gradient roughly constant. We verify that the ions are at the Doppler temperature with $\bar{n} \approx 2$ in a separate experiment. Note that we perform this gate on the center of mass mode, as at the Doppler temperature, the out-of-phase radial mode has increased dephasing due to the out-of-phase axial stretch mode. We obtain a fidelity of 0.992(2) at the Doppler temperature.

The fidelity of laser gates would suffer more significantly at the Doppler temperature due

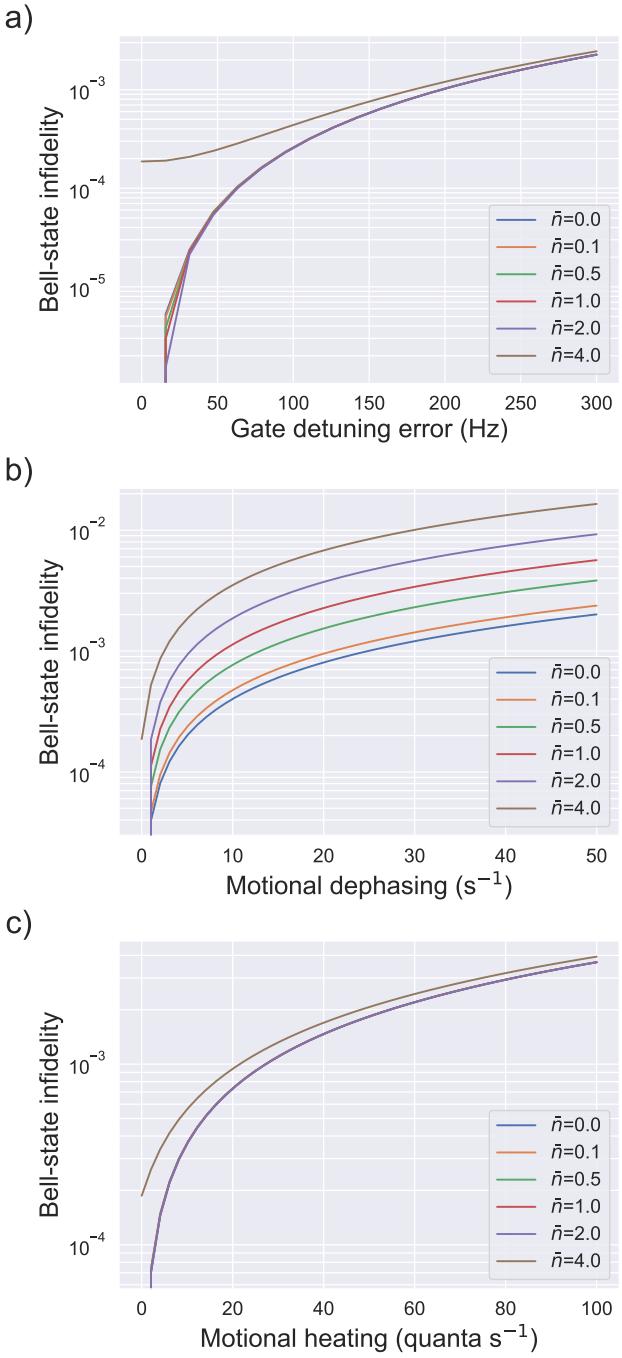

Figure 6.17: We analyze the temperature dependence of gate errors from three sources of motion-dependent error: **a)** static detuning errors, **b)** motional dephasing, and **c)** motional heating. With our multi-loop Walsh 7 sequence, the only error that exhibits significant temperature dependence is from motional dephasing, up to our Doppler temperature with $\bar{n} \approx 2$.

to the higher-order terms in $\hat{a}$ and $\hat{a}^\dagger$ present in the Hamiltonian from the Lamb-Dicke expansion.

These higher-order terms are negligible for our system as the second-order spatial derivatives of our magnetic field are relatively small.

6.4.6 Pulse shaping

We ramp our gradient and microwave fields on and off over $5\,\mu$s using a Blackman envelope. These ramps make up $160\,\mu$s of our $740\,\mu$s gate sequence, as we ramp the fields and gradient on and off eight times. Thus, there is a large incentive to keep these ramps as short as possible. However, we operate in a regime where our ramp times are not long compared to $2\pi/\delta$, which for our gate is $\approx 1\,\mu$s. Our short ramps result in qubit errors that are dependent on the gate detuning. For some detunings, we can operate with ramp times that are an integer multiple of $2\pi/\delta$ as discussed in Sec. 6.1.2. We investigate this effect with a single ion, performing the gate sequence and measuring how much population is lost. The data are shown in Fig. 6.18, where we see that the ion sometimes makes transitions to the bright state ($|\uparrow\rangle$) of the ion at specific gate detunings. These excitations will cause a gate error.

Ideally, we would not operate at those specific problematic gate detunings. However, our motional frequency ω_r changes as we run the gate experiments. This change is as much as a few kHz over the duration of the gate experiments, due to charging of the surface from our lasers as described in Sec. 4.7. We track this frequency and change $\delta \approx \omega_r - \omega_g$ accordingly to keep the gate detuning $\Delta = 2\delta - (\omega_r - \omega_g)$ constant. However, as δ changes, we suspect that we can sometimes hit one of these pulse shaping resonances. Keeping the gate duration and detuning constant and running multiple gate sequences one after another, we see variation in the gate fidelity at the 0.001–0.005 level as the motional frequency changes.

These effects could be mitigated by keeping δ constant, which can be achieved by either keeping ω_r fixed or changing ω_g instead. Changing ω_g might affect the magnitude of the fields and gradient at the ion as our diplexer has a fixed bandwidth. Phases and amplitudes for nulling might also be affected by changing ω_g. Keeping ω_r fixed would involve feeding back on the motional frequency instead of just tracking it. In the future, this problem can be mitigated by using a different

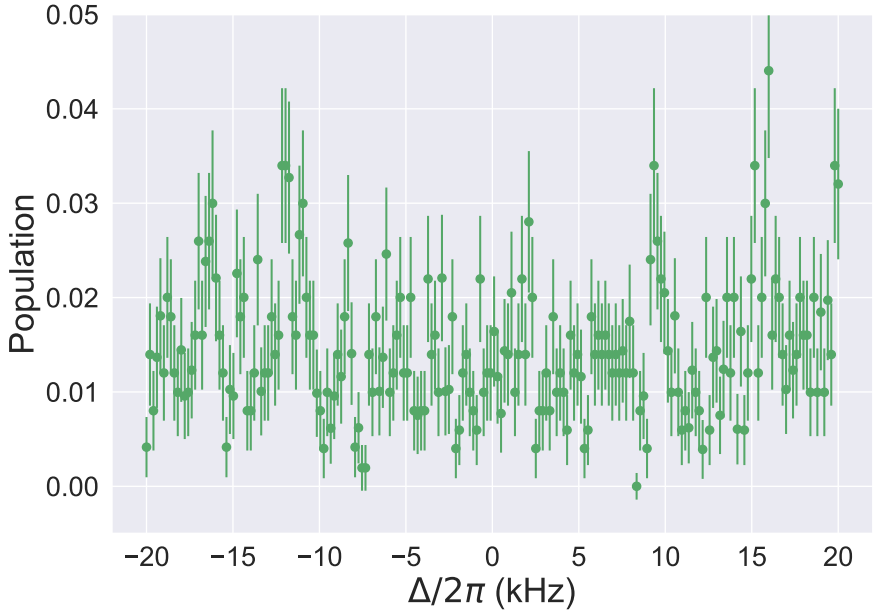

Figure 6.18: Effect of gate pulse shaping sequence on qubit. We perform the gate sequence on a single ion starting in $|\downarrow\rangle$ and measure its population in $|\uparrow\rangle$. Ideally, the ion should return to $|\downarrow\rangle$ after the gate sequence. However, we see excitations of the $|\uparrow\rangle$ state at specific gate detunings due to off-resonant carrier excitation from the fast microwave ramps.

ion with friendlier wavelengths, reducing charging.

6.4.7 Qubit decoherence

Our gate sequence should be robust to fluctuations in the qubit frequency; we have both spin-echo pulses as well as intrinsic dynamical decoupling. To measure the qubit decoherence due to such fluctuations, we perform the gate sequence with a single ion. With a single ion, the out-of-phase mode is absent and the nearest motional mode is $\approx 100\,\text{kHz}$ away from where the gate fields are calibrated, eliminating spin-motion coupling. Thus, we can isolate the effect of the gate sequence purely on the ion spin.

Starting in the $|\downarrow\rangle$ state, the ion's final population should be in the $|\uparrow\rangle$ state following the gate sequence. Any error due to decoherence would result in ion population in the $|\downarrow\rangle$ state. With a scan of 5×10^5 points, we measure a $|\downarrow\rangle$ population of 0.0069(4) with the gate fields. As a control, we make a measurement of 0.0076(4) with just a π pulse. The difference in populations between

between these two measurements is consistent with zero, showing that we see no effect from qubit decoherence within the statistics of the measurement.

6.4.8 Maximizing argument of J_2

As shown in Eq. 6.27, our gate Rabi frequency is $\Omega_g J_2\left(\frac{4\Omega_\mu}{\delta}\right)$. We tune $\frac{4\Omega_\mu}{\delta} = 2.4048$ to operate at the intrinsic dynamical decoupling (IDD) point such that $J_0\left(\frac{4\Omega_\mu}{\delta}\right) = 0$ and $J_2\left(\frac{4\Omega_\mu}{\delta}\right) \approx 0.432$ using $\Omega_\mu/2\pi = 0.571\,\text{MHz}$ for $\delta \approx 0.95\,\text{MHz}$.

We also attempted gates at $J_2\left(\frac{4\Omega_\mu}{\delta}\right) \approx 0.486$ by adjusting the microwave Rabi frequency Ω_μ. Here, $\frac{4\Omega_\mu}{\delta} = 3.0542$ with $\Omega_\mu/2\pi = 0.723\,\text{MHz}$. We reduced the gate duration from $740\,\mu$s to $650\,\mu$s, with a fidelity of $\approx$0.997(2). We believe the fidelity reduction is due to operating away from the IDD point, where slow qubit frequency fluctuations are still echoed out by our π pulses but we become more sensitive to faster fluctuations. At this Rabi frequency, $J_0\left(\frac{4\Omega_\mu}{\delta}\right) = -0.278$, which still reduces our sensitivity to qubit frequency fluctuations but not quite as much as with IDD.

6.4.9 Gates with fewer loops

Our highest fidelity gate used an eight-loop Walsh 7 sequence that has a duration of $740\,\mu$s. We also tried two-loop Walsh 1 and four-loop Walsh 3 sequences. The results are summarized in the table below. For the motional frequency fluctations, we assume a 100 Hz static shift. The heating on the centre-of-mass (COM) mode is 40 quanta/s, compared to <4 quanta/s on the out-of-phase (OOP) rocking mode. We assume a motional dephasing of 10/s (or motional coherence time of 100 ms).

While our errors are broadly consistent with the measured fidelities for the Walsh 7 sequence, both on the COM and OOP modes, they are not consistent with our Walsh 1 or Walsh 3 sequences. This inconsistency suggests that our Walsh 1 or Walsh 3 sequences were not as well-calibrated. There could be additional timing errors unaccounted for. In addition, we have assumed a static shift for our motional frequency fluctuations, but the motional frequency drifts might be time-varying during the gate sequence. This time variation would make the Walsh 7 sequence more robust

Walsh sequence	1	3	7	3	7
Loops	2	4	8	4	8
Mode	COM	COM	COM	OOP	OOP
Duration (μs)	≈ 300	≈ 500	≈ 800	≈ 500	740
Fidelity	0.987	0.993	0.997	0.993	0.999
Errors					
Motional dephasing	8×10^{-4}	5×10^{-4}	4×10^{-4}	5×10^{-4}	4×10^{-4}
Heating	2.9×10^{-3}	2×10^{-3}	1.4×10^{-3}	1×10^{-4}	1×10^{-5}
Motional frequency fluctuations	5×10^{-4}	2×10^{-4}	1×10^{-4}	2×10^{-4}	1×10^{-4}

Table 6.3: Comparison of estimated errors with different gate sequences.

compared to other sequences.

6.4.10 Comparison to laser-based gates

We also compare our gate to laser-based gates in table 6.4. While our gate is significantly slower, we achieve fidelities competitive with some of the highest fidelity laser-based gates. Our gates also not limited by photon scattering errors.

Duration (μs)	Bell-state infidelity (10^{-3})	Photon scattering error (10^{-4})	Year	Ref[9]
30	0.8(4)	5.7	2016	NIST
100	1(1)	4	2016	Oxford
1.6	2(1)	6	2018	Oxford
740	1(1)	0	2020	This work

Table 6.4: Comparison with laser-based gates.

6.5 Mølmer-Sørensen gates

When we first attempted entangling gates with a radiofrequency magnetic field gradient, we tried Mølmer-Sørensen (MS) type gates. In the discussion in the previous chapter, a single microwave field was used with the gradient to generate a sideband interaction. The natural extension of this was to add a second microwave field to produce an MS type interaction as described in Eq. 6.28,

[9] NIST 2016 [Gaebler et al., 2016], Oxford 1 2016 [Ballance et al., 2016], Oxford 2018 [Schäfer et al., 2018]

$$\hat{H}_{\mathrm{ms}} = i\hbar\Omega_g J_1 \left(\frac{4\Omega_\mu}{\delta}\right)(\hat{\sigma}_{y1} + \hat{\sigma}_{y2})\left\{-\hat{a}e^{i\Delta t} + \hat{a}^\dagger e^{i\Delta t}\right\}.$$

At the time, we were unaware of intrinsic dynamical decoupling and instead added an extra field as described in [Harty et al., 2016] to give us dynamical decoupling from qubit frequency shifts during the gate sequence. We obtained a fidelity of ≈ 0.95 with a gate time of about 1 ms. The parity scan from this gate sequence is shown in Fig. 6.19.

The main challenge for this gate is that since qubit frequency errors ($\propto \hat{\sigma}_z$) did not commute with the gate interaction ($\propto \hat{\sigma}_y$), we needed to calibrate qubit frequency shifts very precisely. We needed to calibrate these shifts to the level of our gate Rabi frequency ~ 1 kHz, even though the extra dynamical decoupling field afforded us some insensitivity to this. We were constantly challenged with keeping track of small changes in the magnetic field as well as calibrating ion crystal rotations so both ions saw the same ac Zeeman shift from the magnetic field at ω_g. All of these challenges were mitigated by performing the $\hat{\sigma}_z\hat{\sigma}_z$ gate instead. In addition, the extra dynamical decoupling field potentially added error terms to our interaction as discussed in the next section.

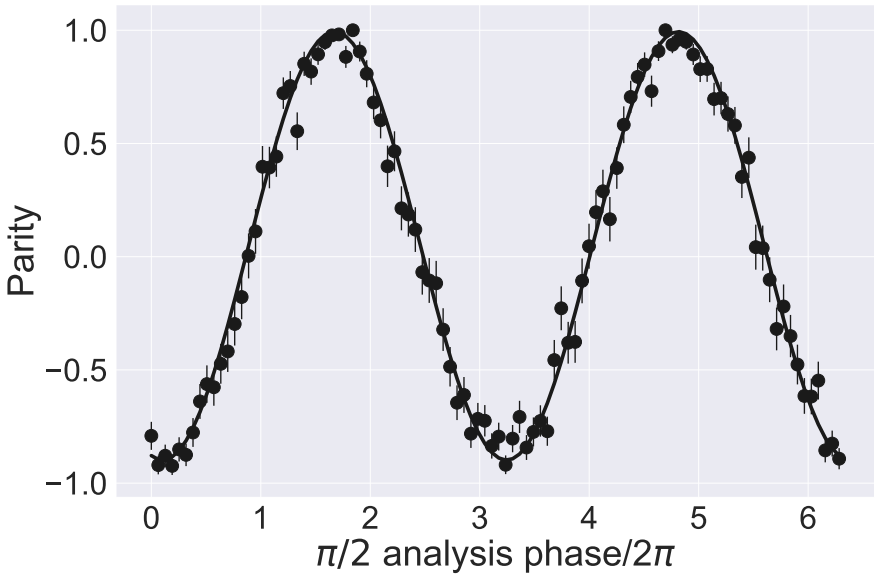

Figure 6.19: Parity scan from Mølmer-Sørensen gate with radiofrequency gate. The parity amplitude is ≈ 0.95.

6.5.1 Errors from dynamical decoupling field

The full Hamiltonian including the extra dynamical decoupling field is, similar to Eq. 6.25

$$\begin{aligned}\hat{H}(t) =& 2\hbar\Omega_\mu \cos(\delta t)\hat{S}_x + 2\hbar\Omega_g \cos(\omega_g t)\hat{S}_z\Big\{\hat{a}e^{-i\omega_r t} + \hat{a}^\dagger e^{i\omega_r t}\Big\} \\ &+ 2\hbar\Omega_{\mathrm{dd}}\hat{S}_y,\end{aligned} \tag{6.35}$$

where the last term corresponds to the extra field that we have added with Rabi frequency Ω_{dd}. Here, we have chosen this field to be proportional to $\hat{S}_y$, so it commutes with the MS interaction. However, in order for it to commute with the bichromatic microwave term which is proportional to $\hat{S}_x$. Thus, analyzing this term in the bichromatic interaction picture,

$$\begin{aligned}\hat{H}_{I,}(t) = \hbar\Omega_{\mathrm{dd}}\Big\{\hat{S}_y\Big[J_0\Big(\frac{4\Omega_\mu}{\delta}\Big) + 2\sum_{n=1}^{\infty} J_{2n}\Big(\frac{4\Omega_\mu}{\delta}\Big)\cos(2n\delta t)\Big] \\ +2\hat{S}_z\sum_{n=1}^{\infty} J_{2n-1}\Big(\frac{4\Omega_\mu}{\delta}\Big)\sin([2n-1]\delta t)\Big\}.\end{aligned} \tag{6.36}$$

First, the strength of our dynamical decoupling field is modified by a factor of $J_0\Big(\frac{4\Omega_\mu}{\delta}\Big)$, and we have additional error terms that might reduce the gate fidelity.

Just beat it, beat it

Beat it, beat it, beat it

Michael Jackson

7

Single-ion addressing with radiofrequency magnetic field gradient

In this chapter[1] , we demonstrate single-ion addressing using the magnetic field gradient oscillating at ω_g. If the two-ion crystal is twisted relative to the trap axis (and thus the currenty carrying electrodes), the two ions will see slightly different magnetic fields, and thus slightly different ac Zeeman shifts. The qubit transitions for the two ions become separated in frequency, and we use this frequency shift for individual addressing, either via a Ramsey sequence or Rabi spectroscopy. While using a spatially varying ac Zeeman shift for individual addressing has been shown in [Warring et al., 2013b], we integrate this single-ion addressing with our gate sequence in order to create antisymmetric Bell states. This integration is made possible by our gate's insensitivity to qubit frequency offsets as shown in Sec. 6.4.2, where we can create high-fidelity entangled states even though our two qubits have slightly different frequencies during the gate operation.

[1] Alternative chapter title from HMK - **Hot singlets in your area!**

7.1 Overview of laser-free single-ion addressing

Laser-based single-ion addressing typically involves focusing beams to spot sizes smaller than the ion separation. Single-ion addressing was first demonstrated using tightly focused lasers [Naégerl et al., 1999], which has more recently been extended to using ac Stark shifts to shift the frequency [Blatt and Roos, 2012]. The ions' position in the beam can also be adjusted such that each ion sees a different optical phase[2] [Rowe et al., 2001]. Such techniques are not possible with microwave radiation whose wavelength is typically much larger than the ion spacing.

Instead, laser-free individual addressing methods have been demonstrated using static magnetic field gradients. Using a static magnetic field gradient along the trap axis, for example [Johanning et al., 2009], ions in a string are naturally separated in frequency space and can be addressed individually. This technique has been extended to an eight-ion string to demonstrate single-ion microwave addressing with cross-talk errors at the 10^{-5} level [Piltz et al., 2014]. One challenge with a permanent static gradient, as in the experiments above, is that is that while all the ions are individually addressable, they are also at different frequencies. Each ion will require its own fields and phase tracking. For example, a two-qubit gate with dynamical decoupling required four fields per ion [Weidt et al., 2016]. This gradient can instead be generated from a dc current that can be turned on and off such as in [Wang et al., 2009] for addressing.

Spatial addressing can also be achieved using novel trap designs [Aude Craik et al., 2014]. Using a microfabricated surface trap with integrated microwave electrodes [Aude Craik et al., 2017], microwave fields that drive spin-flip transitions in one zone coherently cancel in other zones. For ions in zones 960 μm apart, the calculated crosstalk error was 1×10^{-6}.

An oscillating magnetic field gradient can also be used for single-ion addressing. In [Warring et al., 2013a], four methods were demonstrated using gigahertz magnetic fields and gradients: driving the qubits on resonance, using the micromotion sideband, and using differential ac Zeeman shifts with either Ramsey or Rabi spectroscopy. For each of these methods, the ions were switched between

[2] Also known as the "tricky-trick".

two spatial configurations over 80 μs such that one of the ions was along the RF and magnetic field null, while the other was displaced from the null. The same configuration does not work for both the gate operation and the individual addressing.

In our experiment, we use a similar method to that described in [Warring et al., 2013a]. However, since our gate is insensitive to qubit frequency shifts, we are able to keep the ion configuration constant between gate and individual addressing operations. Performing this single-ion addressing after a gate sequence, we are able to create an antisymmetric Bell state.

7.2 ac Zeeman shift from oscillating magnetic field on two ions

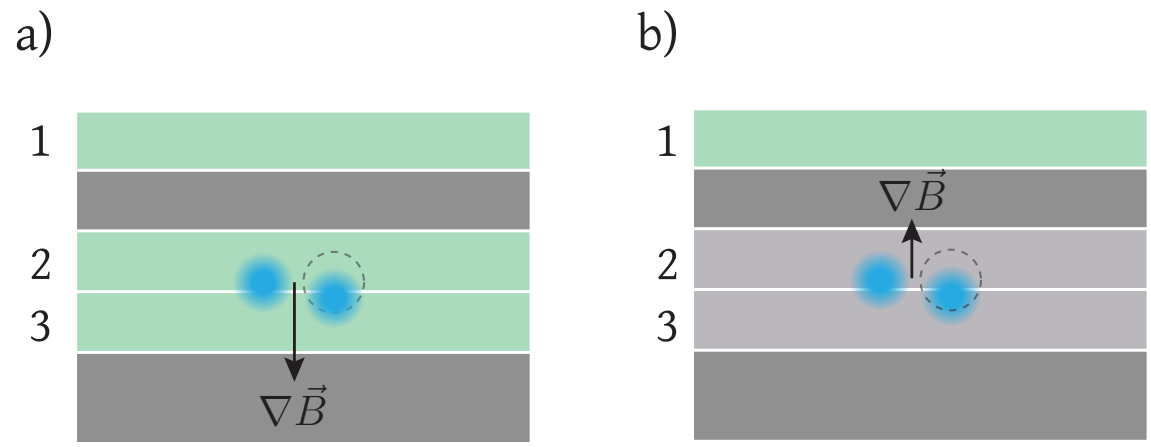

Figure 7.1: Ion crystal and electrode configuration for entangling gates and single-ion addressing. Our ion crystal is twisted relative to the current carrying electrodes, where the dotted line indicates the ion's original position along the axis. We use the same ion crystal configuration for both entangling gates and single-ion addressing. a) For entangling gates, we apply a current oscillating at ω_g to all three electrodes 1, 2, and 3. b) For single-ion addressing, a current is applied only to electrode 1.

If the two-ion crystal is not well-aligned to the electrode generating the magnetic field, the two ions will see a slightly different magnetic field and thus a different ac Zeeman shift (see Fig. 7.1). We first measure this shift using a spin-echo Ramsey sequence. The pulse sequence we use is

(1) $\pi/2$ pulse around ϕ axis.

(2) Turn on differential shift for some duration t (excluding ramp durations).

(3) π pulse around ϕ axis. This is our spin-echo pulse.

(4) Wait for duration t (excluding ramp durations) with no fields on.

(5) $\pi/2$ pulse around ϕ axis.

This pulse sequence is shown in Fig. 7.2. We explicitly label the phase ϕ. For just this spin-echo sequence, only the relative phase between the initial and final $\pi/2$ pulses is consequential. However, if the Ramsey sequence follows another sequence, for example an entangling gate, this phase will be important. This sequence is used for both measuring the differential shift as well as implementing an effective single-qubit rotation in Sec. 7.3.1. The results of this experiment are shown in Fig. 7.3. Measuring the fluorescence of the ions, we see the beating of two sinusoidal oscillations, with frequencies corresponding to the ac Zeeman shift for each ion. We see a slow envelope corresponding to the difference frequency between the two ions and faster oscillations corresponding to their mean frequency. From the data, we extract a difference frequency of $\approx 19.5\,\mathrm{kHz}$. For this experiment, the current at ω_g was applied only to electrode 1 (see Fig. 7.1) to generate the differential shift. We find that applying the current to only one electrode creates larger differential shifts, enabling faster single-ion addressing. We note that the same ion crystal configuration that was used for these experiments was also used for the highest-fidelity gates described in the previous chapter.

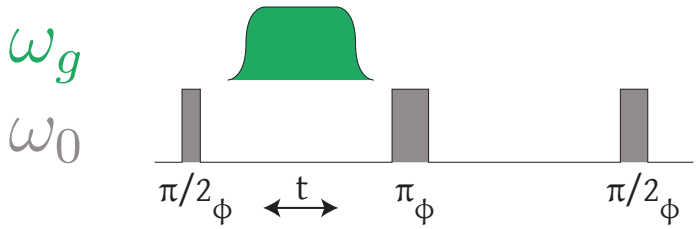

Figure 7.2: Pulse sequence for spin-echo Ramsey sequence. This pulse sequence is used to both measure the differential ac Zeeman shift, as well as to perform an effective single-qubit rotation. We apply a current at ω_g only to electrode 1 (see Fig. 7.1). A field on resonance at ω_0 is used for the π and $\pi/2$ pulses around the same axis ϕ. The single arm duration t does not include the duration of the ramps to turn on and off the current.

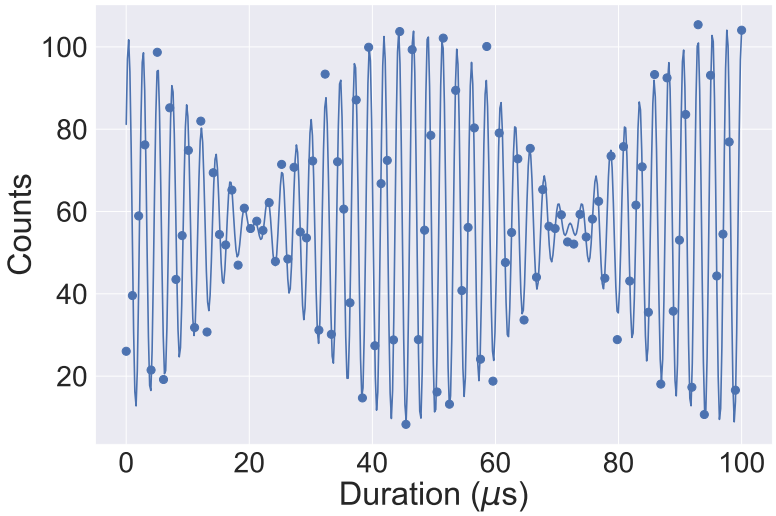

Figure 7.3: We perform a Ramsey experiment to measure the differential ac Zeeman shift between two ions from a magnetic field oscillating at ω_g. The solid line is a fit to the data assuming the sum of two sines. From the fit, the two ions have a difference frequency of $\approx$ 19.5 kHz. The absolute ac Zeeman shift of each ion is $\approx$2.5 MHz. This value is much larger than its fitted values of $\approx$ 400 kHz due to aliasing. However, the difference frequency is more important as it imparts a differential phase shift that we use for single-ion addressing.

7.3 Generating anti-symmetric Bell states

The four Bell states for a two-qubit system are

$$\begin{aligned}
|\Phi^+\rangle &= \frac{1}{\sqrt{2}}\left(|\uparrow\uparrow\rangle + |\downarrow\downarrow\rangle\right), \\
|\Phi^-\rangle &= \frac{1}{\sqrt{2}}\left(|\uparrow\uparrow\rangle - |\downarrow\downarrow\rangle\right), \\
|\Psi^+\rangle &= \frac{1}{\sqrt{2}}\left(|\downarrow\uparrow\rangle + |\uparrow\downarrow\rangle\right), \\
|\Psi^-\rangle &= \frac{1}{\sqrt{2}}\left(|\downarrow\uparrow\rangle - |\uparrow\downarrow\rangle\right).
\end{aligned} \tag{7.1}$$

Three of these states, $|\Phi^+\rangle$, $|\Phi^-\rangle$, and $|\Psi^+\rangle$ are symmetric under an exchange of qubits, while $|\Psi^-\rangle$ is antisymmetric. We can transform between the symmetric states using global rotations. However, in order to transform a symmetric Bell state to an antisymmetric one, such as $|\Phi^+\rangle \rightarrow |\Psi^-\rangle$, we need a non-global interaction. We generate this interaction via the differential ac Zeeman shift

described previously. We also discuss the use of Rabi spectroscopy for this purpose in Sec. 7.4.

7.3.1 Effective single-ion rotation with Ramsey sequence

We use the same sequence in the previous section to generate ion-dependent phase shifts that help us create an effective single-ion rotation. Analyzing the single ion case first, let us assume that there is a qubit frequency shift Δ_i from the magnetic field at ω_g which adds new terms to the Hamiltonian,

$$\hat{H}_{zi} = \frac{\hbar\Delta_i}{2}\hat{\sigma}_{zi}, \tag{7.2}$$

where i is the ion index. Its corresponding propagator is,

$$\begin{aligned}
\hat{U}_{zi}(t) &= \exp -\frac{i}{\hbar}\hat{H}_{zi}t \\
&= \exp\left(-i\frac{\Delta_i t}{2}\hat{\sigma}_{zi}\right), \\
&= \cos\frac{\Delta_i t}{2}\hat{I} - i\sin\frac{\Delta_i t}{2}\hat{\sigma}_z \\
&= \begin{pmatrix} \cos\frac{\Delta_i t}{2} - i\sin\frac{\Delta_i t}{2} & 0 \\ 0 & \cos\frac{\Delta_i t}{2} + i\sin\frac{\Delta_i t}{2} \end{pmatrix}.
\end{aligned} \tag{7.3}$$

We now evaluate the overall propagator on the single ion assuming a spin-echo sequence as shown in Fig. 7.2. Making use of the results in appendix B.1, the overall time evolution operator is

$$\begin{aligned}
\hat{U}_i &= \hat{U}_{\frac{\pi}{2}}\hat{U}_{\pi}\hat{U}_{zi}\hat{U}_{\frac{\pi}{2}} \\
&= \frac{1}{2}\begin{pmatrix} 1 & -ie^{-i\phi} \\ -ie^{i\phi} & 1 \end{pmatrix}\begin{pmatrix} 0 & -ie^{-i\phi} \\ -ie^{i\phi} & 0 \end{pmatrix}\begin{pmatrix} e^{-i\Delta_i t/2} & 0 \\ 0 & e^{i\Delta_i t/2} \end{pmatrix}\begin{pmatrix} 1 & -ie^{-i\phi} \\ -ie^{i\phi} & 1 \end{pmatrix} \\
&= \begin{pmatrix} -\cos\frac{\Delta_i t}{2} & e^{-i\phi}\sin\frac{\Delta_i t}{2} \\ -e^{i\phi}\sin\frac{\Delta_i t}{2} & -\cos\frac{\Delta_i t}{2} \end{pmatrix},
\end{aligned}$$

where we use the basis $|\downarrow\rangle = \begin{pmatrix} 0 \\ 1 \end{pmatrix}$ and $|\uparrow\rangle = \begin{pmatrix} 1 \\ 0 \end{pmatrix}$. The Bell-state we create in Chap. 6 is $|\Phi\rangle = \frac{1}{\sqrt{2}}(|\downarrow\downarrow\rangle + i\,|\uparrow\uparrow\rangle)$. For simplicity, we apply the propagator to the symmetric Bell state $|\Phi^+\rangle = \frac{1}{\sqrt{2}}(|\downarrow\downarrow\rangle + |\uparrow\uparrow\rangle)$,

$$\begin{aligned}\hat{U}_1\hat{U}_2\,|\Phi^+\rangle = \frac{1}{\sqrt{2}}\Bigg(&\left(\cos\frac{\Delta_1 t}{2}\cos\frac{\Delta_2 t}{2} + e^{-2i\phi}\sin\frac{\Delta_1 t}{2}\sin\frac{\Delta_2 t}{2}\right)|\uparrow\uparrow\rangle \\ &+\left(\cos\frac{\Delta_1 t}{2}\cos\frac{\Delta_2 t}{2} + e^{2i\phi}\sin\frac{\Delta_1 t}{2}\sin\frac{\Delta_2 t}{2}\right)|\downarrow\downarrow\rangle \\ &+\left(-e^{-i\phi}\sin\frac{\Delta_1 t}{2}\cos\frac{\Delta_2 t}{2} + e^{i\phi}\cos\frac{\Delta_1 t}{2}\sin\frac{\Delta_2 t}{2}\right)|\uparrow\downarrow\rangle \\ &+\left(-e^{-i\phi}\cos\frac{\Delta_1 t}{2}\sin\frac{\Delta_2 t}{2} + e^{i\phi}\sin\frac{\Delta_1 t}{2}\cos\frac{\Delta_2 t}{2}\right)|\downarrow\uparrow\rangle\Bigg).\end{aligned} \tag{7.4}$$

For the case of $\phi = 0$,

$$\begin{aligned}\hat{U}_1\hat{U}_2\,|\Phi^+\rangle = \frac{1}{\sqrt{2}}\Big(&\cos\frac{\Delta_1-\Delta_2}{2}t\,|\uparrow\uparrow\rangle + \cos\frac{\Delta_1-\Delta_2}{2}t\,|\downarrow\downarrow\rangle \\ &-\sin\frac{\Delta_1-\Delta_2}{2}t\,|\uparrow\downarrow\rangle + \sin\frac{\Delta_1-\Delta_2}{2}t\,|\downarrow\uparrow\rangle\Big).\end{aligned} \tag{7.5}$$

When $t = \pi/(\Delta_1 - \Delta_2)$,

$$\begin{aligned}\hat{U}_1\hat{U}_2\,|\Phi^+\rangle &= \frac{1}{\sqrt{2}}(|\downarrow\uparrow\rangle - |\uparrow\downarrow\rangle) \\ &= |\Psi^-\rangle\,,\end{aligned} \tag{7.6}$$

which gives us the singlet state. Note that we can also achieve the singlet state using $\phi = \pi$. An alternative, perhaps more intuitive way of analyzing this is to first look at the effect of a $\pi/2$ pulse on $|\Phi^+\rangle$. Following appendix B.2,

$$\hat{U}_{\frac{\pi}{2}1}\hat{U}_{\frac{\pi}{2}2}\,|\Phi^+\rangle = \frac{1}{2\sqrt{2}}\Big((1-e^{i2\phi})\,|\downarrow\downarrow\rangle - 2i\cos\phi(|\downarrow\uparrow\rangle + |\uparrow\downarrow\rangle) + (1-e^{-i2\phi}\,|\uparrow\uparrow\rangle).\Big) \tag{7.7}$$

When $\phi = 0$ or $\phi = \pi$,

$$\hat{U}_{\frac{\pi}{2}1}\hat{U}_{\frac{\pi}{2}2}\left|\Phi^{+}\right\rangle = \frac{-i}{\sqrt{2}}\left(\left|\downarrow\uparrow\right\rangle + \left|\uparrow\downarrow\right\rangle\right), \tag{7.8}$$

which is $\left|\Psi^{+}\right\rangle = \frac{1}{\sqrt{2}}(\left|\downarrow\uparrow\right\rangle + \left|\uparrow\downarrow\right\rangle)$ up to a global phase. At this point, if we apply the differential shift,

$$\begin{aligned}\hat{U}_{z1}\hat{U}_{z2}\left|\Psi^{+}\right\rangle &= \frac{1}{\sqrt{2}}\left(e^{-i(\Delta_1-\Delta_2)t/2}\left|\downarrow\uparrow\right\rangle + e^{i(\Delta_1-\Delta_2)t/2}\left|\uparrow\downarrow\right\rangle\right) \\ &= \frac{1}{\sqrt{2}}e^{-i(\Delta_1-\Delta_2)t/2}\left(\left|\downarrow\uparrow\right\rangle + e^{i(\Delta_1-\Delta_2)t/}\left|\uparrow\downarrow\right\rangle\right),\end{aligned} \tag{7.9}$$

which will result in the singlet state when $t = \pi/(\Delta_1 - \Delta_2)$. The larger the differential shift we can create, the faster we can implement this operation as well. The singlet state is invariant under global rotations and thus the additional π and $\pi/2$ pulses would leave it unaffected and could have been omitted entirely. However, we use them to cancel out any common shifts, and this sequence is more suited for general individual-qubit rotations rather than to only produce the singlet state. In order to generate the singlet state, we need to calibrate the phase ϕ relative to the phase of the entangled state we make, as well as the duration of the differential shift.

7.3.1.1 Calibration of Ramsey sequence duration and phase

Our calibration experiment for the duration and phase of the Ramsey sequence is

(1) Perform gate to generate symmetric entangled state.

(2) Spin-echo Ramsey sequence in Sec. 7.2 with phase ϕ.

(3) Additional $\pi/2$ pulse with phase $\neq \phi$ to analyze parity.

In order to calibrate the duration and phase of the Ramsey sequence, we first make our entangled state with our gate operation. We then apply the Ramsey sequence after the gate operation with some single-arm duration t and phase ϕ. For the calibration experiments, we apply an additional $\pi/2$ on both ions with a fixed phase at the end before measuring the population. This global $\pi/2$ pulse helps us distinguish between $\left|\Psi^{+}\right\rangle$ and $\left|\Psi^{-}\right\rangle$. $\left|\Psi^{+}\right\rangle$ will always be rotated to some

combination of $|\Phi^+\rangle$ and $|\Phi^-\rangle$ and will produce populations in $|\downarrow\downarrow\rangle$ and $|\uparrow\uparrow\rangle$. The antisymmetric singlet state $|\Psi^-\rangle$ on the other hand, will be invariant under the $\pi/2$ rotation and will only have populations in $|\downarrow\uparrow\rangle$ and $|\uparrow\downarrow\rangle$. We note that this final $\pi/2$ pulse cannot have the same phase as the spin-echo sequence in step two[3]; if it does, we will produce some combination of $|\Psi^+\rangle$ and $|\Psi^-\rangle$ which we cannot distinguish from measuring the ion populations.

First keeping the phase of the $\pi/2$ pulses in the Ramsey sequence fixed close to its optimal value, we scan the duration in each arm as shown in Fig. 7.4. The optimal duration is $t = \pi/(\Delta_1 - \Delta_2)$. For $(\Delta_1 - \Delta_2)/2\pi \approx 20\,\text{kHz}$, this is roughly $25\,\mu$s. Experimentally, we find this duration t is slightly lower than the measured value of the differential shift, due to the pulse shaping. We ramp the field up and down over $5\,\mu$s, giving us a shift in that duration which is not accounted for in the x-axis of the plot. Taking the ramps into account, assuming that on average the shift is only on for half the duration each $5\,\mu$s ramp, the total duration is roughly the $25\,\mu$s we expect.

We perform a numerical simulation in QuTiP to determine how precisely we need to calibrate this duration. This sensitivity is shown in Fig. 7.5. To keep the error below 1×10^{-3}, we need to calibrate the duration at the $\pm 500\,\text{ns}$ level. This sensitivity could be reduced by using a composite pulse sequence. We perform a similar calibration for the phase of the Ramsey sequence with respect to the entangled state we produce at the end of the gate operation. We keep the duration constant at close to its optimal value and instead scan the phase as shown in Fig. 7.6. Similarly, we perform an analysis of the sensitivity to this phase using a numerical simulation (see Fig. 7.7). To keep the error in the singlet state below 1×10^{-3}, we need to calibrate the phase to better than 0.03 radians[4]

.

7.3.2 Singlet data and results

Similar to Sec. 6.3, the fidelity analysis is detailed in Chapter 8. Here we describe the data that was collected. To measure the fidelity of the singlet state we produce, we measure both the

[3] Our pulse sequence will be $\hat{U}_{\frac{\pi}{2}}\hat{U}_{\frac{\pi}{2}}\hat{U}_{\pi}\hat{U}_{zi}\hat{U}_{\frac{\pi}{2}} = \hat{U}_{2\pi}\hat{U}_{zi}\hat{U}_{\frac{\pi}{2}}$. This sequence will leave us the state shown in Eq. 7.9 which is constantly alternating between $|\Psi^+\rangle$ and $|\Psi^-\rangle$.

[4] Or 0.005 of 2π.

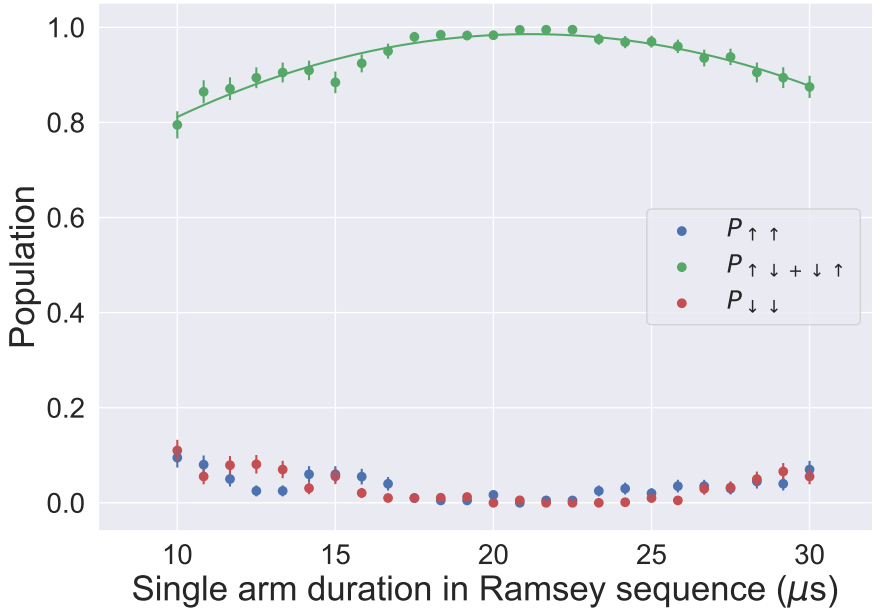

Figure 7.4: Calibration of single arm duration in Ramsey sequence for making a singlet state. The phase of the Ramsey sequence is close to its optimal value. As we scan the duration, we rotate between $|\Psi^+\rangle$ and $|\Psi^-\rangle$. The additional $\pi/2$ pulse turns $|\Psi^+\rangle$ into a combination of $|\downarrow\downarrow\rangle$ and $|\uparrow\uparrow\rangle$, $|\Psi^-\rangle$ is unchanged. We use a quadratic fit to the single-ion population (green line) to determine the optimal duration for the Ramsey sequence.

populations and parity after we produce the singlet state. To measure the population, we simply perform our entangling gate followed by the addressing sequence. To measure the parity, we add a $\pi/2$ pulse at the end with a variable phase. This pulse helps us distinguish between the singlet and any other Bell state, as the other Bell states will produce a parity oscillation, or in the case of $|\Psi^+\rangle$, will always be rotated to a superposition of $|\downarrow\downarrow\rangle$ and $|\uparrow\uparrow\rangle$. These rotations are shown in more detail in Appendix B.2.

Raw data are shown in Fig. 7.8. Similar to Sec. 8.1.1, we have 20 dummy points at the start that allow the motional frequency tracking and thermal effects to stabilize. We make measurements of the populations with and without an additional $\pi/2$ pulse with a variable phase. For this singlet state, we cycle through 6 different parity phases 7 times, each with 200 repetitions. We also make 40 population measurements without the additional $\pi/2$ pulse, also with 200 repetitions. In Fig. 7.9 we show the parity analysis of both the triplet and singlet states we produce. The triplet state

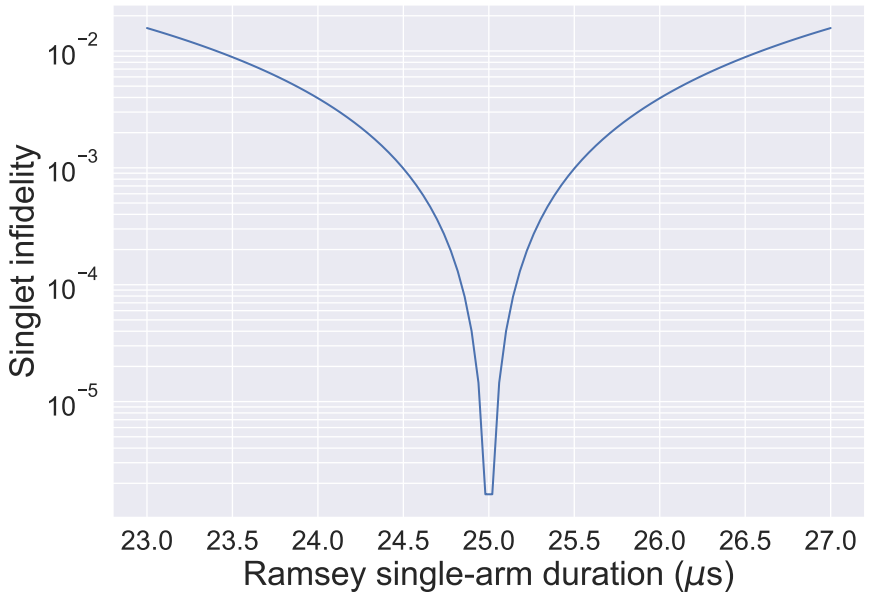

Figure 7.5: QuTiP simulation of the sensitivity of of the singlet fidelity to the Ramsey sequence duration. Starting with a perfect triplet state $|\Phi^+\rangle$, we plot the error in making a singlet state versus the duration of the Ramsey sequence. We assume the phase is calibrated at its optimal value and the two ion shifts are $\Delta_1/2\pi = 2500\,\text{kHz}$ and $\Delta_2/2\pi = 2520\,\text{kHz}$. The difference frequency $(\Delta_2 - \Delta_1)/2\pi = 20\,\text{kHz}$ which requires $25\,\mu\text{s}$ for the single-arm duration.

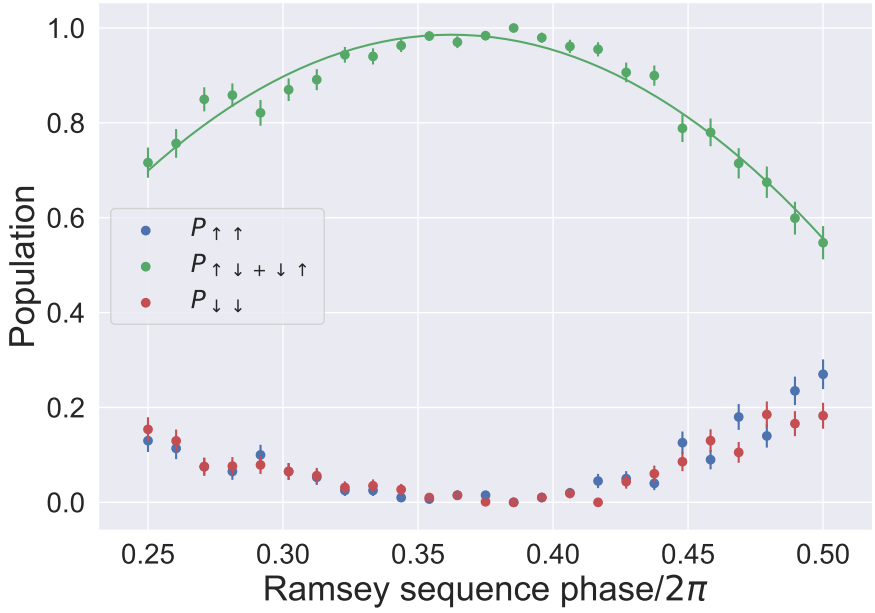

Figure 7.6: Calibration of phase in Ramsey sequence for making a singlet state. The time of the Ramsey sequence is close to its optimal value. At the optimal phase value, we should be producing $|\Psi^-\rangle$. We use a quadratic fit to the single-ion population (green line) to determine the optimal phase.

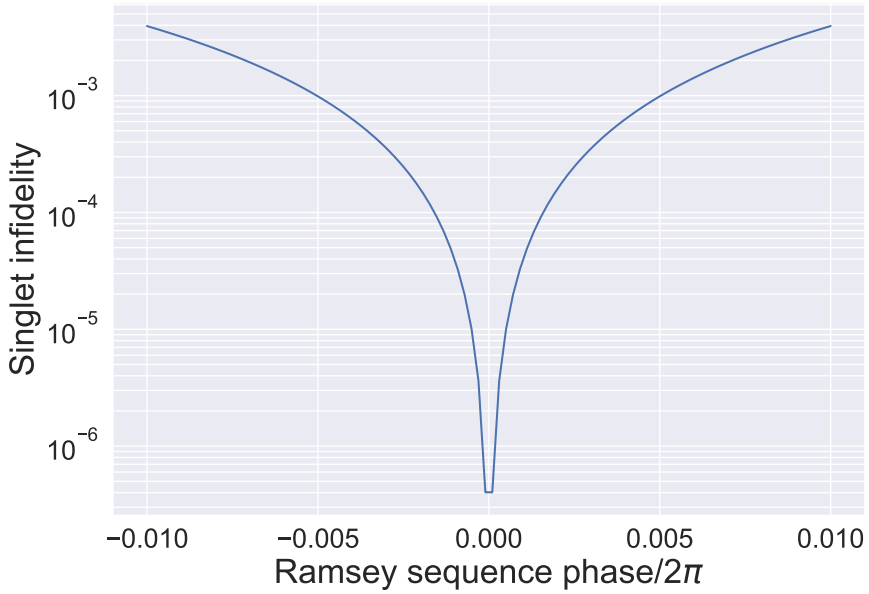

Figure 7.7: QuTiP simulation of the sensitivity of singlet fidelity to the Ramsey sequence phase.Starting with a perfect triplet state $|\Phi^+\rangle$, we plot the error in making a singlet state versus the phase of the Ramsey sequence. We assume the duration is calibrated at its optimal value and the two ion shifts are $\Delta_1/2\pi = 2500\,\text{kHz}$ and $\Delta_2/2\pi = 2520\,\text{kHz}$.

corresponding to $|\Phi\rangle$ exhibits a parity oscillation from +1 to -1, while the singlet state $|\Psi^-\rangle$ has a fixed parity of close to -1. Based on the fidelity analysis discussed in Chap. 8, we are able to produce singlets with fidelity 0.998(1), corrected for SPAM errors.

7.4 Rabi spectroscopy

Initially, the single-qubit rotations were implemented using Rabi spectroscopy. In this implementation, the differential ac Zeeman shift separated the ions' qubit frequencies, and they could be individually addressed using an additional microwave field that drives spin-flip transitions. When this field was tuned to a particular ion's qubit frequency, spin flips would be driven only on that ion.

To perform this rotation, we first turn on the gradient at ω_g, which also produces a magnetic field at ω_g. If the two ions are not aligned to the electrodes, they each see a different ac Zeeman shift from the magnetic field Δ_i. We then turn on an additional microwave field. The Hamiltonian

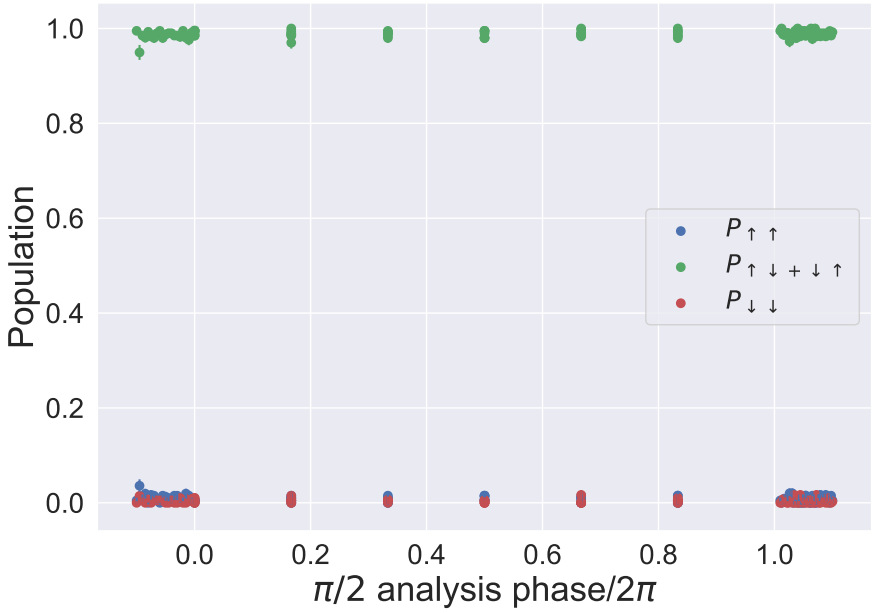

Figure 7.8: Raw data for preparing a singlet state. All points are averaged over 200 repetitions. For phases < 0 and $> 2\pi$, we only measure the populations without an additional $\pi/2$ pulse (x-axis irrelevant). To measure the parity, we have 7 measurements of 6 different $\pi/2$ pulse phases, each with 200 repetitions each. The points for phases < 0 are "dummy points" which are not used for further analysis.

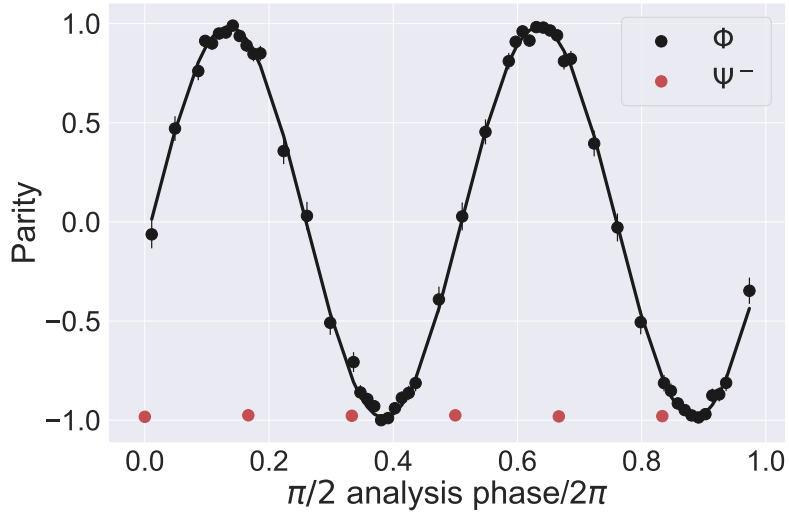

Figure 7.9: Parity analysis of both the triplet and singlet states we produce. The parity is $P = P_{\uparrow\uparrow} + P_{\downarrow\downarrow} - P_{\downarrow\uparrow+\uparrow\downarrow}$. The triplet state corresponding to $|\Phi\rangle = \frac{1}{\sqrt{2}}\left(|\downarrow\downarrow\rangle + e^{i\theta}|\uparrow\uparrow\rangle\right)$ exhibits a parity oscillation from +1 to -1. The singlet state $|\Psi^-\rangle = \frac{1}{\sqrt{2}}\left(|\downarrow\uparrow\rangle - |\uparrow\downarrow\rangle\right)$ on the other hand has a fixed parity of -1. These data are not corrected for SPAM errors.

for the two ions in the interaction picture is

$$\begin{aligned}\hat{H} =& \frac{\hbar\Delta_1}{2}\sigma_{z1} + \frac{\hbar\Delta_2}{2}\sigma_{z2} && \text{differential ac Zeeman shift} \\ &+\hbar\Omega_c\big((\hat{\sigma}_{+1}+\hat{\sigma}_{+2})e^{-i(\delta_c t+\phi)} + (\hat{\sigma}_{-1}+\hat{\sigma}_{-2})e^{i(\delta_c t+\phi)}\big), && \text{microwave field}\end{aligned} \tag{7.10}$$

where Ω_c and δ_c are the Rabi frequency and detuning of the additional field respectively. For these experiments, $\Omega_c/2\pi \approx 4\,\text{kHz}$. After applying the differential ac Zeeman shift, we pulse the additional microwave field long enough to perform a π pulse and scan its detuning δ_c as shown in Fig. 7.10. For $\delta_c = \Delta_i$, we ideally perform a π pulse on the resonant ion. The differential Rabi frequency $(\Delta_1 - \Delta_2)/2\pi \approx 20\,\text{kHz}$ is not large compared to the microwave Rabi frequency Ω_c. Thus, we see some off-resonant excitation of the second ion.

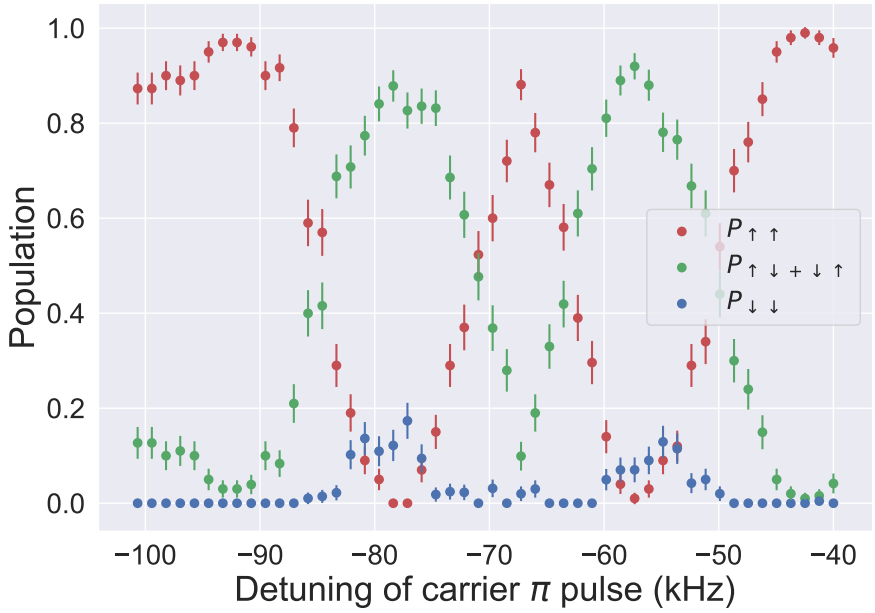

Figure 7.10: Rabi spectroscopy of two ions with a differential ac Zeeman shift from the magnetic field oscillating at ω_g. We scan the detuning of an additional microwave field in the presence of the differential shift. As the detuning of the field is equal to the shifted qubit frequencies of each of the ions, we see excitations of the one-ion-bright population (green points) from their initial $|\uparrow\uparrow\rangle$ state. As the differential shift is not large compared to the Rabi frequency of the microwave field, we see some off-resonant excitation of the second ion.

Setting the detuning of the microwave field to one of the resonances, we also scan the duration

as shown in Fig. 7.11. We see oscillations in the one-ion-bright population as we selectively excite only a single ion. Again, since our microwave Rabi frequency is not small compared to the ion frequency splitting, we see some off-resonant excitation of the other ion.

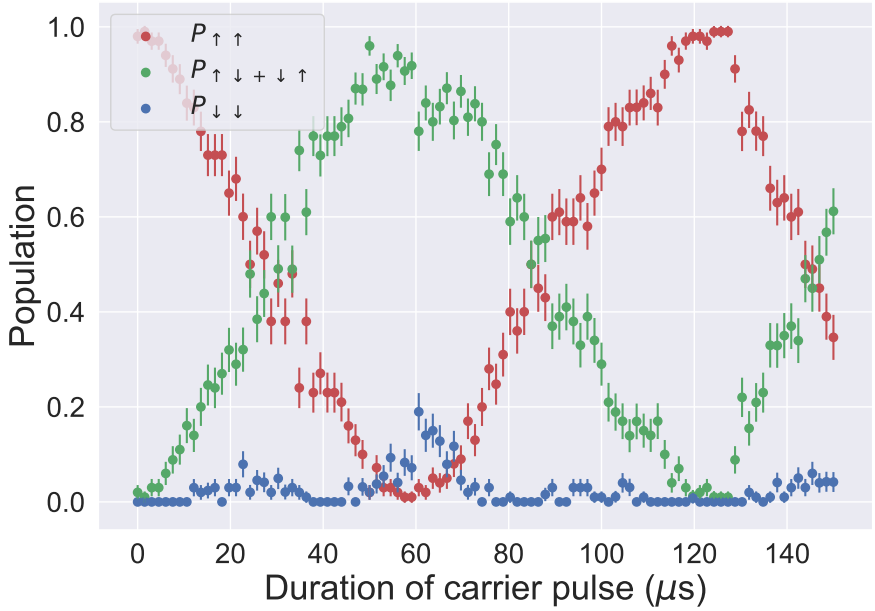

Figure 7.11: Duration scan of the single-ion addressing pulse. We fix the detuning of the microwave field to one of the resonances in Fig. 7.10 and scan the duration. Initializing the ions to $|\uparrow\uparrow\rangle$, we drive the $|\uparrow\uparrow\rangle \leftrightarrow |\uparrow\downarrow\rangle$ transition. As our microwave field Rabi frequency is not small compared to the frequency splitting of the two ions, we observe off-resonant excitation of the second ion, giving rise to some population in the $|\downarrow\downarrow\rangle$ state.

7.4.1 Generating singlet states

Similar to Sec. 7.3.1, we use this Rabi pulse to transform our entangled state after the gate sequence $|\Phi^+\rangle$, to the singlet state $|\Psi^-\rangle$. Ideally, we implement

$$\hat{U}_{\pi 1}\hat{I}_2 |\Phi^+\rangle = \frac{-i}{\sqrt{2}}\left(e^{i\phi}|\uparrow\downarrow\rangle + e^{-i\phi}|\downarrow\uparrow\rangle\right), \tag{7.11}$$

performing a spin flip on one ion and leaving the other unchanged. When $\phi = \pi/2$ or $3\pi/2$, we create the singlet state, and when $\phi = 0$ or π we create the triplet $|\Psi^+\rangle$ state.

To calibrate this phase, we perform our single-ion pulse after a gate operation that creates

the state $|\Phi^+\rangle$, and then add an additional $\pi/2$ pulse to distinguish between $|\Psi^+\rangle$ and $|\Psi^-\rangle$. The state $|\Psi^+\rangle$ will always be rotated to a state of even parity and $|\Psi^-\rangle$ will be unchanged as shown in appendix B.2. Figure 7.12 shows this behaviour as a function of the single-ion pulse phase.

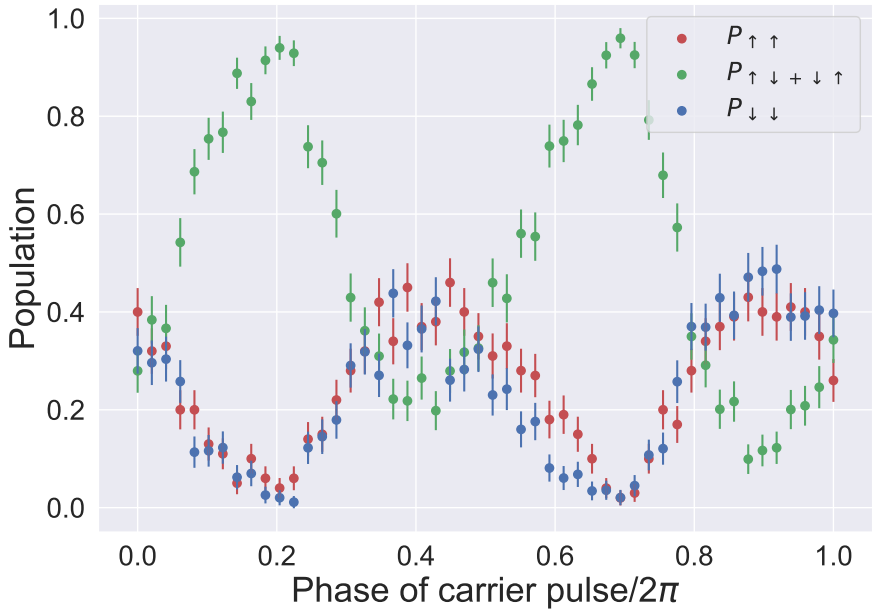

Figure 7.12: Scan of the phase of the single-ion pulse after a gate sequence. An additional $\pi/2$ pulse is used to distinguish between $|\Psi^+\rangle$ and $|\Psi^-\rangle$. The state $|\Psi^+\rangle$ corresponds to the minima of the one-ion population (green points) and $|\Psi^-\rangle$ to the peaks.

Finally, we use this calibrated phase to create the singlet state and analyze its fidelity following the same procedure described in Sec. 8.1.2. The raw data is shown in Fig. 7.13.

7.4.2 Comparison of Ramsey and Rabi individual addressing sequences

We have demonstrated single-ion addressing after a gate sequence to create a singlet state using both Ramsey and Rabi sequences. We achieve better singlet fidelity using the Ramsey sequence as shown in Fig. 7.8. We also prefer the Ramsey sequence as our addressing duration can be as fast as the inverse of the differential ac Zeeman shift, $2\pi/(\Delta_1 - \Delta_2)$, for the two ions. In contrast, the Rabi sequence requires the Rabi frequency for the additional pulse $\Omega_c \ll |\Delta_1 - \Delta_2|$, increasing the duration for the pulse in order to avoid off-resonant excitations. While we use a square pulse for this additional pulse, pulse-shaping could also be used to avoid off-resonant excitation of the

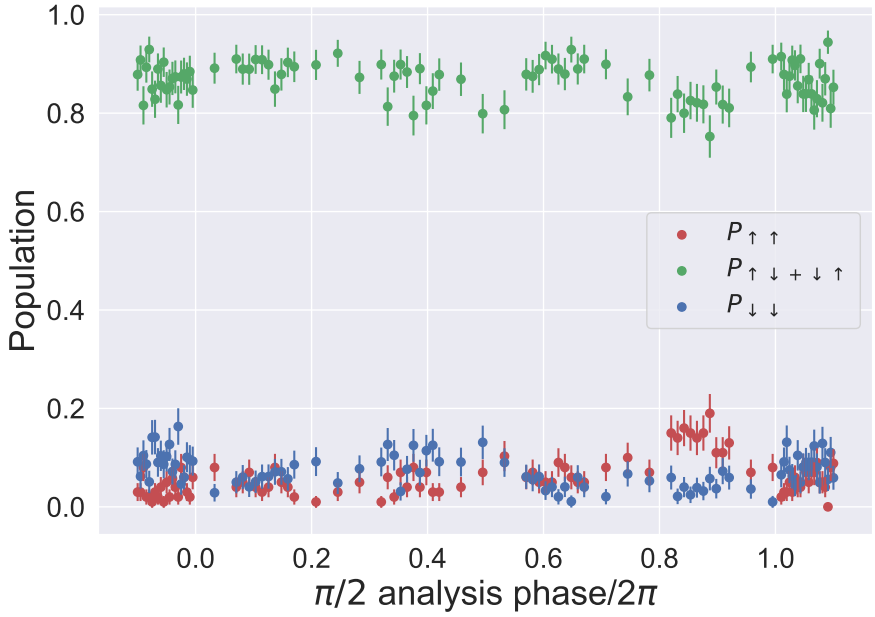

Figure 7.13: Raw data for generating singlet state with Rabi spectroscopy. For phases < 0 and $> 2\pi$, we only measure the population of the singlet state and omit the addtional $\pi/2$ pulse. For phases between 0 and 2π, we have an additional $\pi/2$ pulse with that phase. Ideally, the singlet state should produce a constant one-ion population of 1. However, we see that we have an imperfect singlet and have a slight oscillation in the ion populations.

non-resonant ion while minimizing the duration penalty.

In a larger string of ions however, the Rabi sequence might provide a more straightforward way of individual addressing. The two-ion case that we have provides a simple implementation of the Ramsey sequence, with more ions we would likely need a longer sequence as well as additional global rotations.

Why'd you have to go and make things so complicated?

Avril Lavigne

8

Fidelity analysis

We have described how we have created entangled states in the previous chapters, but how well can we make them? We now explain how we determine the fidelity of the entangled states we have created. We discuss how we correct for state preparation and measurement (SPAM) errors, including leakage out of the qubit manifold before laser-free operations. We validate our analysis with simulated data. We want to ensure that we are estimating our true fidelity accurately, and that if there is a bias it is towards a lower fidelity; we want a number we can trust.

Unless otherwise stated, all error bars in the figures in this chapter correspond to the standard error of the mean, $\sigma/\sqrt{n}$ where σ is the standard deviation and n is the number of measurements. In addition, for most of the simulated data, we try to replicate our experimental data as closely as possible, especially with regards to the number of measurements made as described in Sections 6.3, and 7.3.2. In some cases, we generate simulated data with more statistics than experimental data[1] . We describe this increase by a "data factor", where if the "data factor" is 10, we have 2000 repetitions per point rather than the 200 in the experiment.

[1] If only it were that easy to take that much more data in real life.

8.1 Measuring fidelity

We want to measure how well we can implement a two-qubit gate. One could use process tomography to measure the final state fidelities for all possible input states, but that requires preparing input states better than you can entangle them. This requires robust individual addressing, which is what we are trying to demonstrate in the first place.

More sophisticated methods such as randomized benchmarking [Emerson et al., 2005, Knill et al., 2008, Gaebler et al., 2012] involve doing multiple random sequences of single-qubit and two-qubit gates to extract an average error per gate. Randomized benchmarking of two-qubit gates requires the single-qubit gate error, including individual addressing, to be much smaller than the two-qubit gate error. Symmetric subspace benchmarking [Baldwin et al., 2020b] removes the requirement for individual addressing. However, our limited two-ion lifetime and possible duty cycle effects in our system could potentially make benchmarking challenging, i.e. not all gates in a longer sequence would be the same.

We have developed a new technique for entangling gates, and the fidelity of making the singlet state is our measure of the individual addressing error. Thus, we decided to keep our fidelity measurement as simple as possible and only measure the fidelity of producing a target Bell state from a specific starting state. We only perform one entangling gate. As pointed out in Ref. [Ballance, 2017], this is a "cheat". We assume all input states would have the same operation fidelity. We also have the challenge of extracting a two-qubit gate error lower than our SPAM error. This chapter explains how we address that challenge.

8.1.1 Triplet state

We measure the fidelity of producing a target Bell state. The target state of our gate sequence, starting from $|\downarrow\downarrow\rangle$, is

$$|\Phi\rangle = \frac{1}{\sqrt{2}}\left(|\downarrow\downarrow\rangle + e^{i\theta}\,|\uparrow\uparrow\rangle\right). \tag{8.1}$$

The fidelity F of producing that target state is

$$\begin{aligned} F = |\langle\psi|\Phi\rangle|^2 =& \frac{1}{2}\langle\psi|\left(|\downarrow\downarrow\rangle\langle\downarrow\downarrow| + |\uparrow\uparrow\rangle\langle\uparrow\uparrow|\right)|\psi\rangle && \text{Populations} \\ &+\frac{1}{2}\langle\psi|\left(e^{-i\theta}|\downarrow\downarrow\rangle\langle\uparrow\uparrow| + e^{i\theta}|\uparrow\uparrow\rangle\langle\downarrow\downarrow|\right)|\psi\rangle, && \text{Coherences} \end{aligned} \tag{8.2}$$

where $|\psi\rangle$ is the state that we produce at the end of our gate sequence. The first line in Eq. 8.2 corresponds to the populations, or the diagonal elements of our density matrix, and the second line corresponds to the coherences, the off-diagonal elements. We can measure the populations naturally by looking at the fluorescence of the ions. However, measuring the coherences is harder. Instead of a direct measurement, we use an additional $\pi/2$ pulse with a variable phase ϕ to map the off-diagonal elements to the populations [Sackett et al., 2000]. We define the parity as

$$P = P_{\uparrow\uparrow} + P_{\downarrow\downarrow} - P_{\downarrow\uparrow} - P_{\uparrow\downarrow}, \tag{8.3}$$

where $P_{\uparrow\uparrow}$ for example is the population in the $|\uparrow\uparrow\rangle$ state. Following Appendix B.2, the parity will be a function of the analysis phase ϕ such that

$$\mathcal{P}(\phi) = A\cos(2\phi), \tag{8.4}$$

where the magnitude of A is equal to the magnitude of the coherences in Eq. 8.2. Thus, our fidelity is

$$\begin{aligned} F = |\langle\psi|\Phi\rangle|^2 =& \frac{1}{2}(P_{\uparrow\uparrow} + P_{\downarrow\downarrow}) && \text{Populations} \\ &+\frac{1}{2}|A|. && \text{Coherences} \end{aligned} \tag{8.5}$$

We note that we need both population and parity measurements to distinguish our state from a mixed state, as well as to ensure that we produce an entangled state with a fixed phase θ.

8.1.2 Singlet state

Our measurement of the singlet state follows a similar procedure, where we measure its populations and its parity. The singlet state is

$$|\Psi^-\rangle = \frac{1}{\sqrt{2}}\left(|\downarrow\uparrow\rangle - |\uparrow\downarrow\rangle\right). \tag{8.6}$$

The parity of the singlet state as a function of the $\pi/2$ phase is

$$\mathcal{P}(\phi) = -1, \tag{8.7}$$

for the ideal singlet. For non-ideal singlets, we analyze a couple of cases. If our state is a combination of $|\Psi^-\rangle$ and $|\Psi^+\rangle$, the parity of the state would be less negative than -1 as the parity of $|\Psi^+\rangle$ after applying a $\pi/2$ pulse is +1. If our state contains any population in one of the other triplet states, we will have a parity signal that oscillates as $\cos\phi$. We could in theory fit this oscillation, however in practice it is difficult to fit a low amplitude sinusoid. We instead take the average value of our parity across all phases. For any residual triplet, the average value of this oscillation will be zero. We make a measurement of the parity with six different $\pi/2$ pulse phases equally spaced between 0 and 2π. These measurements also average to zero as

$$\begin{aligned}\sum_{n=0}^{n=5}\cos(\frac{2n\pi}{3}+\phi_0) &= \sum_{n=0}^{n=2}\left(\cos(\frac{2n\pi}{3}+\phi_0)+\cos(\frac{(2n+1)\pi}{3}+\phi_0)\right)\\ &= 2\cos(\frac{\pi}{3})\sum_{n=0}^{n=2}\cos\left(\frac{(4n+1)\pi}{3}+\phi_0\right)\\ &= 0.\end{aligned} \tag{8.8}$$

If there is any non-singlet population, the average parity measured is less negative. Overall, our singlet fidelity is

$$F = |\langle\psi|\Psi^-\rangle|^2 = \frac{1}{2}(P_{\downarrow\uparrow} + P_{\uparrow\downarrow}) \quad \text{Populations}$$
$$-\frac{1}{2}A, \quad \text{Coherences} \tag{8.9}$$

where A is the average parity measured across all $\pi/2$ phases. For the ideal singlet, $F = 1$. For $|\Psi^+\rangle$ for example, $A = 1$ and $F = 0$.

8.2 Leakage correction

The previous analysis assumes perfect SPAM. However, neither our state preparation nor measurement is perfect. We need to account for repumping, depumping, and leakage. Repumping occurs when a nominally dark ion is optically pumped by the detection beam to the fluorescing state, and starts to scatter photons. Depumping refers to a nominally bright state that is optically pumped to a dark state due to imperfect polarization of the detection beam. Leakage occurs when our ion population is outside the qubit manifold, for example due a scattering event before the gate sequence. When preparing the ion in the qubit state $|\downarrow\rangle$, there is a small probability that the ion is instead in an auxiliary state $|a\rangle$ that does not participate in the gate dynamics. There are several such states within the hyperfine manifold. This state is also a dark state that does not fluoresce. To be clear, these measurement and leakage errors do **not** occur during the gate sequence, only before (leakage) or after during measurement (repumping and depumping)[2] .

Our raw data includes both reference and gate data as described in Sections 6.3 and 7.3.2. From the reference data, we are able to extract depumping, repumping, leakage, as well as ion fluorescence rates. This process is discussed in more detail in Sec. 8.3.2. Using these extracted parameters, we are able to use maximum likelihood estimation to extract the ion populations from the count histograms[3] in the gate data, largely removing any measurement error. Our analysis leaves us only leakage to correct. The initial state of each ion $\rho_{0,1}$ is

[2] And at some level these are all caused by our lasers. Even with our laser-free gate there is no escape.
[3] Count histogram analysis mainly done by DHS.

$$\rho_{0,1} = (1-\epsilon)\rho_{\downarrow} + \epsilon\rho_a, \tag{8.10}$$

where ϵ is the probability of producing the leaked state, $\rho_{\downarrow} = |\downarrow\rangle\langle\downarrow|$, and $\rho_a = |a\rangle\langle a|$. For two ions, the initial state is thus,

$$\rho_{0,2} = (1-\epsilon)^2\rho_{\downarrow\downarrow} + \epsilon(1-\epsilon)(\rho_{\downarrow a} + \rho_{a\downarrow}) + \epsilon^2\rho_{aa}. \tag{8.11}$$

We now analyze the effect of this leaked state on both the triplet and singlet fidelity analysis. Specifically, we need to determine how our gate sequence and parity analysis affect populations with one leaked state ($\rho_{\downarrow a}$ and $\rho_{a\downarrow}$) or two leaked states (ρ_{aa}).

8.2.1 Triplet state fidelity

We assume the leaked state $|a\rangle$ and $|\uparrow\rangle$ are dark, while $|\downarrow\rangle$ is bright. Let the probabilities of two ions bright, one ion bright, and zero ions bright be P_2, P_1, and P_0 respectively[4]. These probabilities correspond to the different ion states $P(|\psi\rangle)$ as

$$\begin{aligned} P_2 &= P(|\downarrow\downarrow\rangle), \\ P_1 &= P(|\uparrow\downarrow\rangle) + P(|\downarrow\uparrow\rangle) + P(|a\downarrow\rangle) + P(|\downarrow a\rangle), \\ P_0 &= P(|\uparrow\uparrow\rangle) + P(|\uparrow a\rangle) + P(|a\uparrow\rangle) + P(|aa\rangle). \end{aligned} \tag{8.12}$$

For an entangling gate with fidelity F,

$$\rho_{\downarrow\downarrow} \to F\rho_{\downarrow\downarrow+\uparrow\uparrow} + \frac{(1-F)}{2}(\rho_{\downarrow\uparrow} + \rho_{\uparrow\downarrow}), \tag{8.13}$$

where $\rho_{\downarrow\downarrow+\uparrow\uparrow}$ is the density matrix corresponding to the triplet state[5] $\frac{1}{\sqrt{2}}(|\downarrow\downarrow\rangle + |\uparrow\uparrow\rangle$. We assume that any error in the entangling operation results in an incoherent mixture of $|\downarrow\uparrow\rangle$ and $|\uparrow\downarrow\rangle$. This

[4] These are P_{ff}, P_{1f}, and P_{dd} in Ref. [Ballance, 2017].

[5] Not the exact entangled state we create ($\frac{1}{\sqrt{2}}(|\downarrow\downarrow\rangle + i\,|\uparrow\uparrow\rangle)$), but we assume this for simplicity here.

assumption holds if the leading error is motional dephasing. If instead the leading error were coherent, such as a timing or detuning error, this would have to be modified.

8.2.1.1 Gate flips spin of single ion

We now analyze a couple of different cases depending on the effect of the gate sequence on a single-ion spin state. At the end of our entangling operation, our gate operation transforms the single-ion state $|\downarrow\rangle \rightarrow |\uparrow\rangle$ due to the sequence of $\pi/2$ and π pulses (see Fig. 6.9). Thus, our state ρ_g is

$$\rho_g = F(1-\epsilon)^2\rho_{\downarrow\downarrow+\uparrow\uparrow} + \frac{(1-F)}{2}(1-\epsilon)^2(\rho_{\downarrow\uparrow}+\rho_{\uparrow\downarrow}) + \epsilon(1-\epsilon)(\rho_{\uparrow a}+\rho_{a\uparrow}) + \epsilon^2\rho_{aa}. \tag{8.14}$$

Measuring the fluorescence of this state,

$$\begin{aligned} P_2 &= \frac{F(1-\epsilon)^2}{2}, \\ P_1 &= (1-F)(1-\epsilon)^2, \\ P_0 &= \frac{F(1-\epsilon)^2}{2} + 2(1-\epsilon)\epsilon + \epsilon^2. \end{aligned} \tag{8.15}$$

Analysing each component of the fidelity measurement, our population would be

$$\begin{aligned} 1-P_1 &= 1-(1-F)(1-\epsilon)^2 \\ &= F + (1-F)2\epsilon - \epsilon^2(1-F) \\ &\approx F, \end{aligned} \tag{8.16}$$

for $(1-F), \epsilon \ll 1$. For the parity measurement, our entangled state alternates between $|\psi_e\rangle = \frac{1}{\sqrt{2}}(|\downarrow\downarrow\rangle + |\uparrow\uparrow\rangle)$ and $|\psi_o\rangle = \frac{1}{\sqrt{2}}(|\uparrow\downarrow\rangle + |\downarrow\uparrow\rangle)$ depending on the parity phase, and is in general a superposition of the two even and odd states. The parity pulse also transforms the following states as

$$
\begin{aligned}
|{\downarrow\uparrow}\rangle &\rightarrow \frac{1}{2}(|{\downarrow}\rangle + |{\uparrow}\rangle)(|{\downarrow}\rangle - |{\uparrow}\rangle) \\
&= \frac{1}{2}(|{\downarrow\downarrow}\rangle + |{\uparrow\downarrow}\rangle - |{\downarrow\uparrow}\rangle - |{\uparrow\uparrow}\rangle), \\
|{\uparrow\downarrow}\rangle &\rightarrow \frac{1}{2}(|{\downarrow\downarrow}\rangle - |{\uparrow\downarrow}\rangle + |{\downarrow\uparrow}\rangle - |{\uparrow\uparrow}\rangle), \\
|{\uparrow}\, a\rangle &\rightarrow \frac{1}{\sqrt{2}}(|{\downarrow}\, a\rangle - |{\uparrow}\, a\rangle), \\
|a\, {\uparrow}\rangle &\rightarrow \frac{1}{\sqrt{2}}(|a\, {\downarrow}\rangle - |a\, {\uparrow}\rangle), \\
|aa\rangle &\rightarrow |aa\rangle
\end{aligned}
\tag{8.17}
$$

We assume a particular phase for these transformations, but as the error state is an incoherent mixture of $|{\downarrow\uparrow}\rangle$, $|{\uparrow\downarrow}\rangle$ and the leaked states, this phase is not consequential. When we produce the even parity state $|\psi_e\rangle$ with fidelity F, the two ion populations after a parity pulse are

$$
\begin{aligned}
P_2 &= \frac{F(1-\epsilon)^2}{2} + \frac{(1-F)(1-\epsilon)^2}{4}, \\
P_1 &= \frac{(1-F)(1-\epsilon)^2}{2} + (1-\epsilon)\epsilon, \\
P_0 &= \frac{F(1-\epsilon)^2}{2} + (1-\epsilon)\epsilon + \epsilon^2 + \frac{(1-F)(1-\epsilon)^2}{4}.
\end{aligned}
\tag{8.18}
$$

With this state, the parity $\mathcal{P}$ is

$$
\begin{aligned}
\mathcal{P} &= 1 - 2P_1 \\
&= 1 - \left((1-F)(1-2\epsilon+\epsilon^2) + 2\epsilon - 2\epsilon^2\right) \\
&\approx 1 - (1-F) - 2\epsilon \\
&= F - 2\epsilon,
\end{aligned}
\tag{8.19}
$$

assuming $(1-F) \ll 1$. When we produce the odd parity state $|\psi_o\rangle$, the two ion populations after a parity pulse are

$$
\begin{aligned}
P_2 &= \frac{(1-F)(1-\epsilon)^2}{4}, \\
P_1 &= F(1-\epsilon)^2 + \frac{(1-F)(1-\epsilon)^2}{2} + (1-\epsilon)\epsilon, \\
P_0 &= (1-\epsilon)\epsilon + \epsilon^2 + \frac{(1-F)(1-\epsilon)^2}{4}.
\end{aligned}
\tag{8.20}
$$

The parity is,

$$
\begin{aligned}
\mathcal{P} &= 1 - 2P_1 \\
&= 1 - \left(2F(1-2\epsilon+\epsilon^2) + (1-F)(1-2\epsilon+\epsilon^2) + 2\epsilon - 2\epsilon^2\right) \\
&\approx 1 - (2F - 4F\epsilon + (1-F) + 2\epsilon) \\
&\approx -(F - 2\epsilon).
\end{aligned}
\tag{8.21}
$$

Thus, the parity oscillation should have an amplitude of $F-2\epsilon$ and be symmetric about 0. Combining the parity measurement with our population, our measured fidelity F_m is

$$
\begin{aligned}
F_m &= \frac{1}{2}\left[1 - (1-F)(1-\epsilon)^2 + F(1-\epsilon)^2\right] \\
&= \frac{1}{2}\left[1 + (2F-1)(1-\epsilon)^2\right] \\
&= \frac{1}{2}\left[2F - 2\epsilon(2F-1) + \epsilon^2(2F-1)\right] \\
&= F - \epsilon(2F-1) + \epsilon^2(2F-1) \\
&\approx F - \epsilon,
\end{aligned}
\tag{8.22}
$$

Thus, to obtain the true fidelity F, we would need to add ϵ to our measured fidelity.

8.2.1.2 Gate does not flip spin of single ion

We now assume the gate operation leaves the single ion state unchanged such that $|\uparrow\rangle \rightarrow |\uparrow\rangle$. This is **not** the case for our experiment but we include it for completeness. Our density matrix ρ_g is

$$
\rho_g = F(1-\epsilon)^2\rho_{\downarrow\downarrow+\uparrow\uparrow} + \frac{(1-F)}{2}(1-\epsilon)^2(\rho_{\downarrow\uparrow} + \rho_{\uparrow\downarrow}) + \epsilon(1-\epsilon)(\rho_{\downarrow a} + \rho_{a\downarrow}) + \epsilon^2\rho_{aa}. \tag{8.23}
$$

Measuring the fluorescence of this state,

$$\begin{aligned} P_2 &= \frac{F(1-\epsilon)^2}{2}, \\ P_1 &= (1-F)(1-\epsilon)^2 + 2(1-\epsilon)\epsilon, \\ P_0 &= \frac{F(1-\epsilon)^2}{2} + \epsilon^2. \end{aligned} \tag{8.24}$$

Thus, for a fidelity measurement, our population, $(1-P_1)$ would be $\approx (F-2\epsilon)$, and the parity amplitude would be at most $1-2\epsilon+\epsilon^2$, giving a fidelity of approximately $F-2\epsilon$. The analysis of the parity is unchanged as in the previous section. Thus, 2ϵ would have to be added to the measured fidelity F_m instead of just ϵ in the previous case. While not applicable to our experiment, this analysis shows the importance of being aware of what the gate sequence does to a single spin, as it will affect the leakage correction. We note that an additional π pulse to half the population measurements would average[6] out this effect to $F-\epsilon$.

8.2.2 Singlet state fidelity

We now turn to the fidelity analysis of the singlet state. Following Eq. 8.14, the density matrix at the end of the gate sequence is

$$\rho_g = F(1-\epsilon)^2\rho_{\downarrow\downarrow+\uparrow\uparrow} + \frac{(1-F)}{2}(1-\epsilon)^2(\rho_{\downarrow\uparrow}+\rho_{\uparrow\downarrow}) + \epsilon(1-\epsilon)(\rho_{\uparrow a}+\rho_{a\uparrow}) + \epsilon^2\rho_{aa}.$$

With this state, we now perform a single-qubit rotation on only one of the ions, flipping its spin. We assume this addressing pulse is perfect for now, producing the singlet state from the triplet state. The state including gate errors and leakage is

$$\rho_s = F(1-\epsilon)^2\rho_{\downarrow\uparrow-\uparrow\downarrow} + \frac{(1-F)}{2}(1-\epsilon)^2(\rho_{\downarrow\downarrow}+\rho_{\uparrow\uparrow}) + \epsilon(1-\epsilon)(\rho_{\uparrow a}+\rho_{a\downarrow}) + \epsilon^2\rho_{aa}.$$

Measuring the populations at this point,

[6] Pointed out to us by our theory collaborator Alex Kwiatkowski. Unfortunately, too late to take more data.

$$
\begin{aligned}
P_2 &= \frac{(1-F)}{2}(1-\epsilon)^2 \\
P_1 &= F(1-\epsilon)^2 + \epsilon(1-\epsilon), \\
P_0 &= \frac{(1-F)}{2}(1-\epsilon)^2 + \epsilon(1-\epsilon) + \epsilon^2.
\end{aligned}
\tag{8.25}
$$

Thus, the single ion population would be $\approx (F-\epsilon)$ keeping terms first order in ϵ and assuming $1-F \ll 1$.

Including a parity pulse, the singlet state should be unchanged but the other spin states should be transformed into an equal superposition of $|\downarrow\rangle$ and $|\uparrow\rangle$. Now, the probability of measuring one ion bright is

$$
\begin{aligned}
P_1 &= F(1-\epsilon)^2 + \epsilon(1-\epsilon) + \frac{(1-F)}{2}(1-\epsilon)^2 \\
&= (F + \frac{1-F}{2})(1-\epsilon)^2 + \epsilon(1-\epsilon) \\
&= \frac{1+F}{2}(1-\epsilon)^2 + \epsilon(1-\epsilon) \\
&\approx \frac{1+F}{2} - \epsilon,
\end{aligned}
\tag{8.26}
$$

again assuming $(1-F), \epsilon << 1$. the parity $\mathcal{P}$

$$
\begin{aligned}
\mathcal{P} &= 1 - 2P_1 \\
&= 1 - (1+F)(1-\epsilon)^2 - 2\epsilon(1-\epsilon) \\
&\approx -F + 2\epsilon
\end{aligned}
\tag{8.27}
$$

Subtracting the parity from the one ion populations and then dividing by two for F_m,

$$
\begin{aligned}
F_m &= \frac{1}{2}\left(F(1-\epsilon)^2 + \epsilon(1-\epsilon) + (1+F)(1-\epsilon)^2 - 1 + 2\epsilon(1-\epsilon)\right) \\
&= \frac{1}{2}\left((1+2F)(1-\epsilon)^2 + 3\epsilon(1-\epsilon) - 1\right) \\
&= \frac{1}{2}\left((1+2F)(1-2\epsilon+\epsilon^2) + 3\epsilon(1-\epsilon) - 1\right) \\
&= \frac{1}{2}\left((1+2F) - 2\epsilon(1+2F) + (1+2F)\epsilon^2 + 3\epsilon(1-\epsilon) - 1\right) \\
&\approx \frac{1}{2}\left(2F + \epsilon - 4F\epsilon\right) \\
&= F(1-2\epsilon) + \frac{\epsilon}{2} \\
&\approx \frac{1}{2}\left(2F - 3\epsilon\right) \\
&= F - \frac{3}{2}\epsilon.
\end{aligned}
\tag{8.28}
$$

8.3 Simulating data

In order to validate our analysis, we create simulated data where we can simulate various gate errors as well as leakage errors. The goal is to have simulated data with controllable fidelities that we can test our analysis on. We create these data using QuTiP [Johansson et al., 2013]. Our simulated entangling gate does not contain the full Hamiltonian described in Eq. 6.1, only the interaction described by Eq. 6.27. Our simulation includes the π pulses required for the Walsh 7 modulation (Sec. 6.2.6) as well as errors such as heating and motional dephasing (Sec. 2.5). For generating singlet states, we have an additional sequence after the entangling gate that follows our experimental implementation in the previous chapter closely.

The free parameters in our simulation are the output state after the gate sequence, the leakage, depumping, and repumping rates. We also set the mean zero-ion, one-ion, and two-ion bright counts c_0, c_1 and c_2 respectively which we later use to sample from a Poisson distribution. Each set of simulated gate data has its own set of simulated reference data, in order to replicate our experimental data as closely as possible. To determine the fidelity of a set of gate data, we analyze the corresponding reference data to characterize our SPAM errors, including leakage. These values are subsequently used to determine the fidelity from the simulated gate data.

8.3.1 Mapping populations to counts

Our analysis will ultimately use the ion counts to extract a population. Our simulation first creates a density matrix corresponding to a particular state. To account for projection noise, we make a "measurement" for every repetition of the simulation. We generate a random number from 0 to 1, and based on the value, assign an outcome following the original density matrix. To simplify the "measurement", we group populations that are identical after swapping the two ions as our experiment cannot distinguish between the state of each ion. For example, $\rho_{\downarrow\uparrow}$ and $\rho_{\uparrow\downarrow}$ are grouped together. We then map the "measured" populations to two ions bright, one ion bright, and zero ions bright following Eq. 8.12.

To factor in depumping and repumping, we assign a probability that repumping and depumping occurs during detection. We generate a random number from 0 to 1 to determine if a repump or depump event occurs. If it does occur, a new random number between 0 and 1 is used to determine **when** it occurs and the counts are modified accordingly. As an example, let us assume the ions are initially in $|\uparrow\uparrow\rangle$, the dark state, and it stays in the dark state for a fraction f of the detection duration, before it is repumped to a bright state (instantaneously). The counts for this "measurement" would be the sum of a sample of two Poissonians with $\lambda = fc_0$ and $\lambda = (1-f)c_1$ respectively.

In our simulation, we make the following assumptions:

(1) There is only one depump or repump event during each "measurement".

   (a) The zero-ion-bright state only repumps once to the one-ion-bright state.

   (b) The one-ion-bright state only repumps or depumps once to the two-ion-bright and zero-ion-bright state respectively.

   (c) The two-ion-bright state only depumps once to the one-ion-bright state.

(2) The leaked state behaves identically to the dark state and has the same probability of repumping. Since the probability of having a leaked event **and** a repumping event is low,

we treat the leaked state identically to simplify the simulation.

8.3.2 State preparation and readout errors

An example of simulated and experimental data is shown in Fig. 8.1. The parameters for the simulated data are obtained from fitting the experimental data. We obtain repump and depump probabilities of 0.0192 and 0.0169 respectively. The ion counts c_0, c_1, and c_2 are 5, 56, and 107 respectively, and the leakage was $\epsilon = 0.0035$. We generate count histograms for three different ion states: the bright state corresponding to the starting state in Eq. 8.11 (Fig. 8.1c), the starting state after a $\pi/2$ pulse (Fig. 8.1b), and the dark state corresponding to the starting state after a π pulse (Fig. 8.1a). For each of those three states, we generate 200,000 measurements which are renormalized to the experimental data that has about 18,500 measurements per state (see Sec. 6.3), such that the total number of measurements plotted for both the simulated and experimental data is identical.

Figure 8.1 shows good agreement between our model (green lines) and the data (blue lines). For reference, we also plot the results from a purely Poissonian model (orange lines) where there is no repumping, or depumping, or leakage. This model works fairly well but fails to capture the behaviour of the tails that occur a couple of orders of magnitudes below the peaks.

8.3.3 Characterizing leakage

We vary the leakage in the simulation from 0 to 0.005 per qubit and check that our analysis is able to track this as shown in Fig. 8.2. We find good agreement between the simulated and inferred values, with larger uncertainties as the leakage increases. We then check that the leakage estimate improves as we increase the amount of data in the simulation. The estimated value converges to its set value of 0.0035 per qubit as shown in Fig. 8.3.

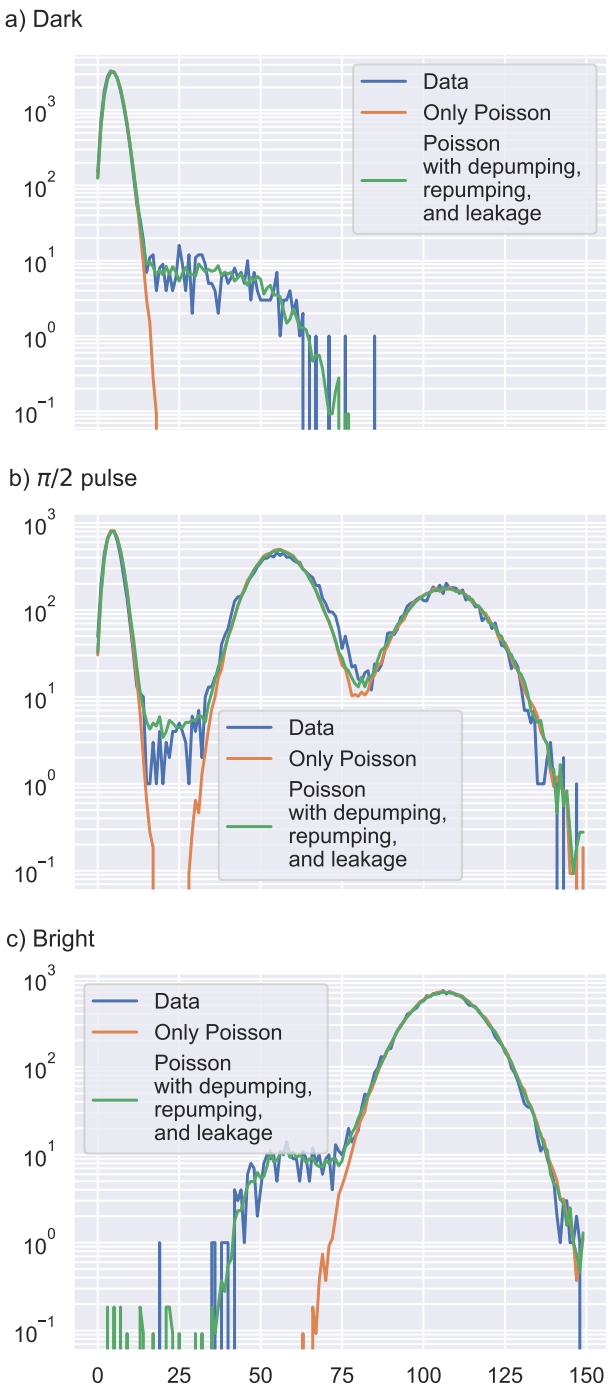

Figure 8.1: Comparison of count histograms between experimental and simulated data for three different states. a) Dark state after applying a π pulse to the initial state in Eq. 8.11. b) State after $\pi/2$ pulse to the initial state. c) The initial bright state. For the simulated data, we generate 200,000 "measurements" that are renormalised to the experimental value of about 18,500 measurements. This rescaling causes the counts can go below 1 for the simulated data. We see good agreement between the experimental data (blue) and our model that incorporates depumping, repumping, and leakage (green). For reference we also include data from a purely Poissonian model.

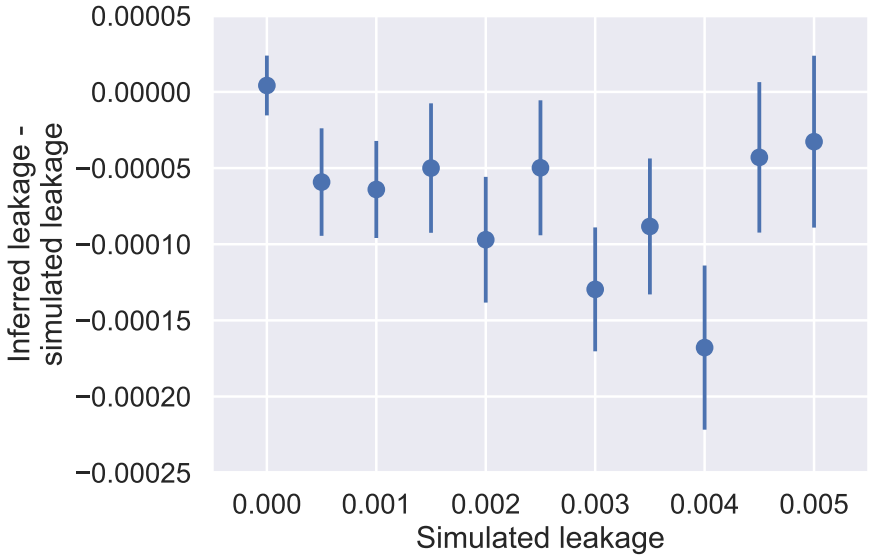

Figure 8.2: Analysis of leakage estimation with varying leakages. For each simulated leakage, we generate 100 sets of simulated data. We plot the mean of the inferred leakages minus the simulated leakage versus the simulated leakage.

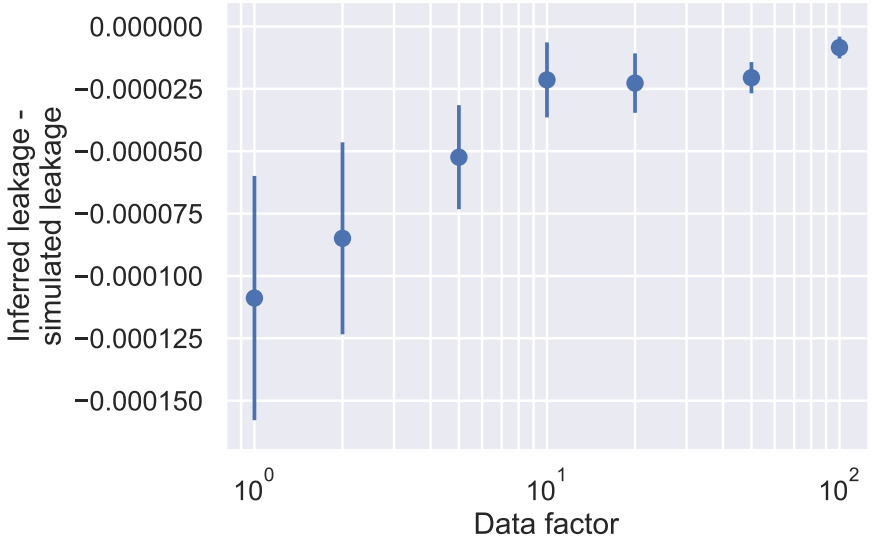

Figure 8.3: Analysis of leakage estimation with more data. For a fixed simulated leakage of $\epsilon = 0.0035$ per qubit, we generate 100 sets of simulated data. We plot the mean of the inferred leakages minus the simulated leakage. As we increase the amount of data in the simulation, we find that the our estimates get both more accurate and more precise.

8.3.4 Characterizing other parameters

We perform a similar analysis with the other parameters required to map a given population to counts: the repump rate, depump rate, zero ion, and one-ion-bright counts. The results are shown in Fig. 8.4. Similar to Fig. 8.3, the more data we provide the better we are able to extract the true value of the parameter from the count histograms. These data show our analysis and simulations are behaving consistently.

8.3.5 Asymmetry in ion counts

A slightly less significant effect we examine is an asymmetry in the ion counts. If the ions are unequally illuminated by the detection beam, they will have slightly different fluorescence rates and the one-ion-bright histogram would have a central peak that is the sum of two Poissonians with different means instead. For a fixed triplet and singlet fidelity of 0.999, we examine this effect and find that it is negligible for the estimated fidelity. Moreover, this effect only seems to bias us negatively, predicting a lower fidelity than the actual value. In our experimental data we see little count asymmetry. Thus, we do not factor in count asymmetry into our simulations.

8.4 Analyzing simulated data

Confident that our analysis is characterizing our simulated reference data and determining the leakage (and other parameters) appropriately, we now check our analysis with simulated gate data with varying fidelities. The goal is to establish if there are any systematic biases in our analysis and to sanity check the leakage correction. For the simulations in this section, the mean counts are set to 5, 57 and 109 for the zero-ion-bright, one-ion-bright and two-ion-bright histograms respectively[7]. There was no asymmetry between the the ion counts for these simulations. The repump and depump rates are 0.0192 and 0.0169 respectively. When simulating data with varying fidelities, we are fortunately able to measure the true fidelity of the underlying state with QuTiP, which is what we will refer to as simulated fidelity. This is in contrast to the fidelities we extracted from count

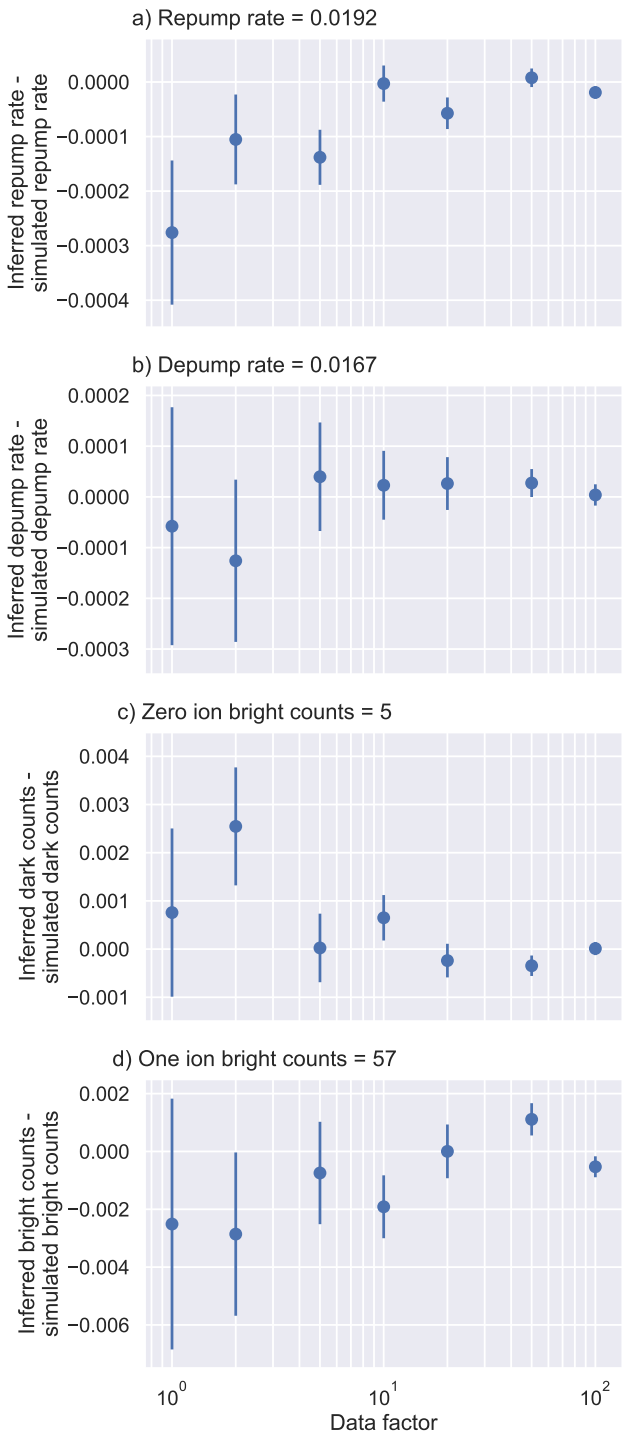

Figure 8.4: Estimation of other parameters in simulation as we increase the amount of data. The parameters are: a) Repump rate, b) Depump rate, c) Zero-ion-bright counts, and d) One-ion-bright-counts. For each data factor, we generate 100 sets of simulated data. Similar to the leakage in Fig. 8.3, the more data we have, the the more the analysis converges to the set simulation values.

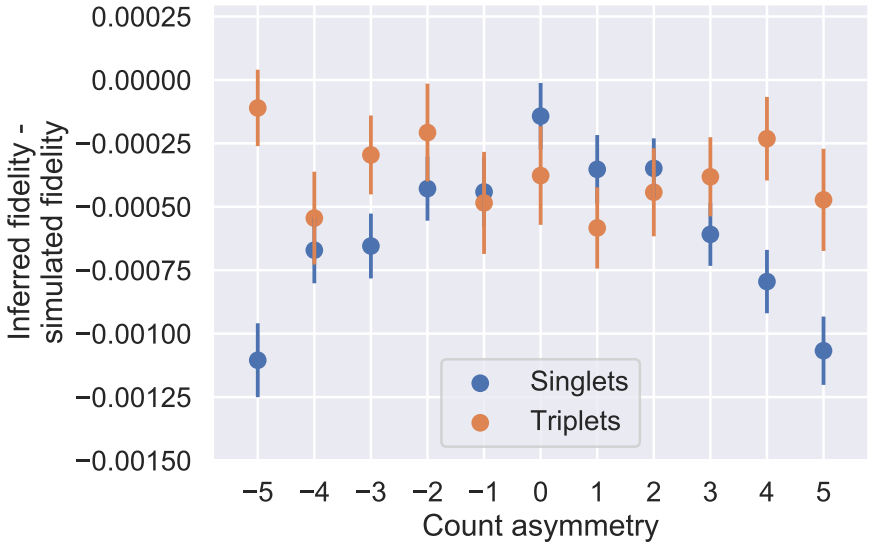

Figure 8.5: Effect of count asymmetry on triplet and singlet fidelity. For a simulated triplet and singlet fidelity of 0.999, we find that count asymmetry has little effect on the analysis, and if at all it biases the fidelity estimate negatively. The count asymmetry has a stronger effect on the singlet state. The singlet state more heavily involves measuring one-ion-bright counts which are more significantly affected by count asymmetry.

histograms, as is the case for the fidelity analysis on experimental data. Every set of simulated gate data also has its own simulated reference data.

8.4.1 Triplet state

We first characterize our analysis for the triplet state. Following Eq. 8.5, we need to determine both the parity and the populations. The parity A is determined from the parity oscillation with maximum likelihood estimation and the populations are extracted from the count histograms of the corresponding points. We first look at varying leakages and then different types of errors.

8.4.1.1 Leakage correction

We check our leakage correction by setting the triplet fidelity to 0.999 and varying the leakages from 0 to 0.005 per qubit. The results are plotted in Fig. 8.6. From the analysis, the leakage

[7] We spent a long time trying to debug our analysis when the two ion counts were at 107 instead of 109. It is **very** important that $c_2 = 2c_1 - c_0$ where c_0, c_1 and c_2 are the mean zero, one and two ion counts respectively.

correction seems to track with increasing leakages.

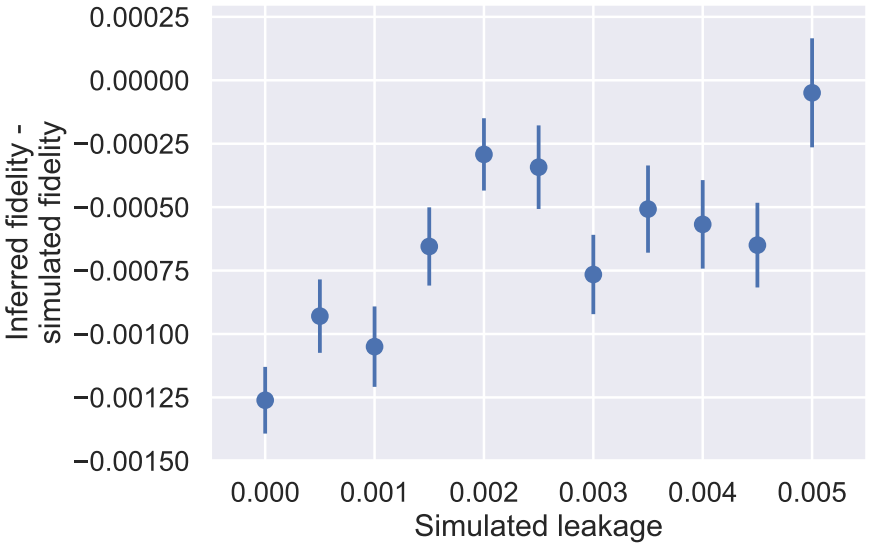

Figure 8.6: Analysis of triplet fidelity with varying leakage. For each simulated leakage, we generate 100 sets of simulated data with a fixed underlying fidelity of 0.999. We plot the mean of the inferred fidelities from the count histograms minus the simulated fidelity.

8.4.1.2 Motional dephasing

We analyze the effect of motional dephasing on the estimated fidelity for fidelities from 0.99 to 1, We add motional dephasing to our gate model until the required fidelity is reached, i.e. lower fidelities need more motional dephasing. We then make 1000 sets of simulated data per simulated fidelity, with each data set having the same statistics as the experiment described in Sec. 6.3.

This analysis is plotted in Fig. 8.7. We see that our analysis has a negative bias that infers a lower fidelity than the true fidelity. This bias gets worse as we get closer to a true underlying fidelity of 1. This bias is likely due to our populations and parity estimates being constrained in the region [0, 1]. As the fidelity gets closer to 1, we are closer to this boundary. We plot the histograms of the inferred fidelities for simulated fidelities of 0.998, 0.999 and 1 in Fig. 8.8. Note that our analysis method does allow fidelity estimates above 1, due to the leakage correction.

We verify that the bias in the fidelity estimation is reduced with increasing statistics in Fig. 8.9. Indeed, the more statistics we have, the closer the inferred fidelity is to the simulated

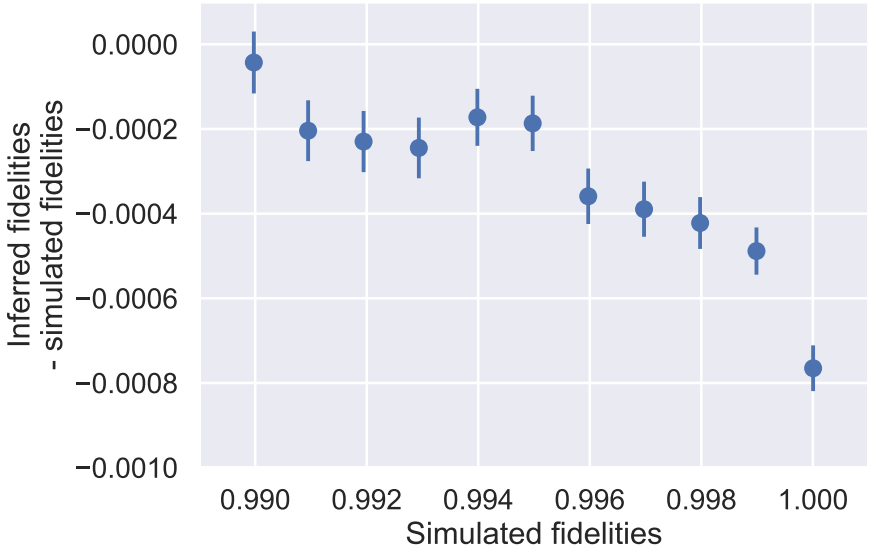

Figure 8.7: Analysis of simulated triplet data with varying fidelities. For each simulated fidelity, we generate 1000 sets of simulated data. We plot the mean of the inferred fidelities from the count histograms minus the simulated fidelities. We see a negative bias across all fidelities that gets more negative the closer we get to a fidelity of 1.

fidelity. We check that the spread in our fidelity estimates are also well-behaved in Fig. 8.10. As one would expect, the spread decreases as we have more data and the standard error of the mean follows $1/\sqrt{n}$ scaling where n is the number of measurements.

8.4.1.3 Detuning errors

Finally, aside from motional dephasing errors, we also check that our fidelity analysis works well with our next leading error. This error arises from miscalibrations of the motional frequency that will cause an error in the detuning of the gate. Figure 8.11 shows this analysis. We are able to estimate the true fidelity as a function of detuning well, usually with a negative bias close to the optimal detuning.

8.4.2 Singlet state

We perform a similar set of analyses for the singlet states, following equations 8.9 and 8.28 to estimate the fidelity. We determine the parity A and populations directly from the count histogram

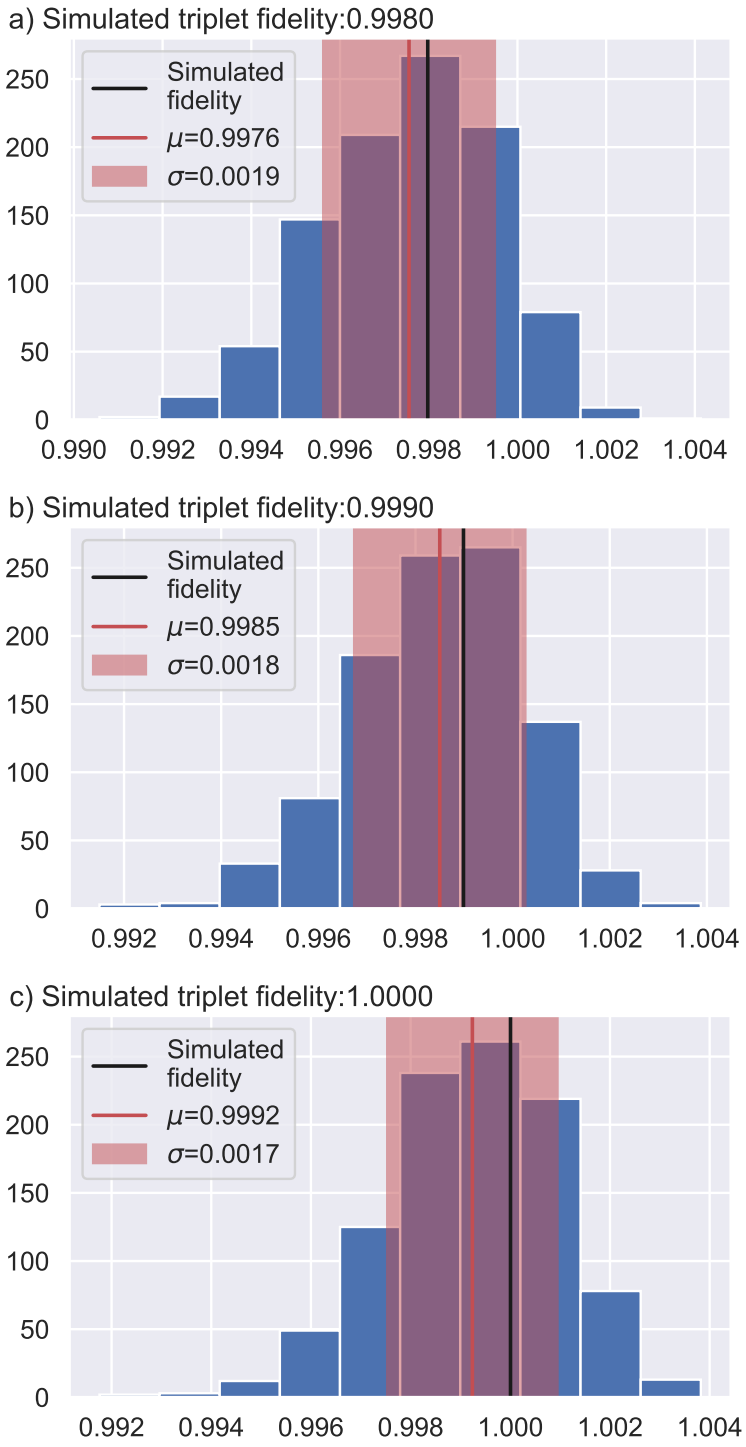

Figure 8.8: Histograms of inferred fidelities from analysis for underlying triplet fidelities of 0.998, 0.999, and 1. For each simulated fidelity, we generate 1000 sets of simulated data. The mean and standard deviation are indicated by the red line and red shaded region. As the fidelity approaches 1, we see a larger negative bias between the mean of the analysed fidelities and the simulated fidelity.

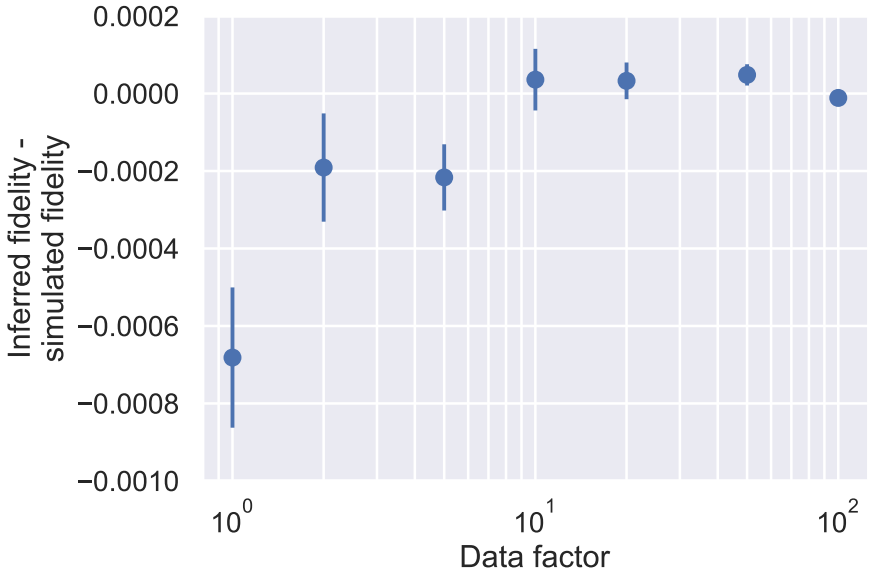

Figure 8.9: Analysis of simulated triplet data with more data compared to the experiment. For each data factor, we generate 100 sets of simulated data. We plot the mean of the inferred fidelities minus the simulated fidelities.

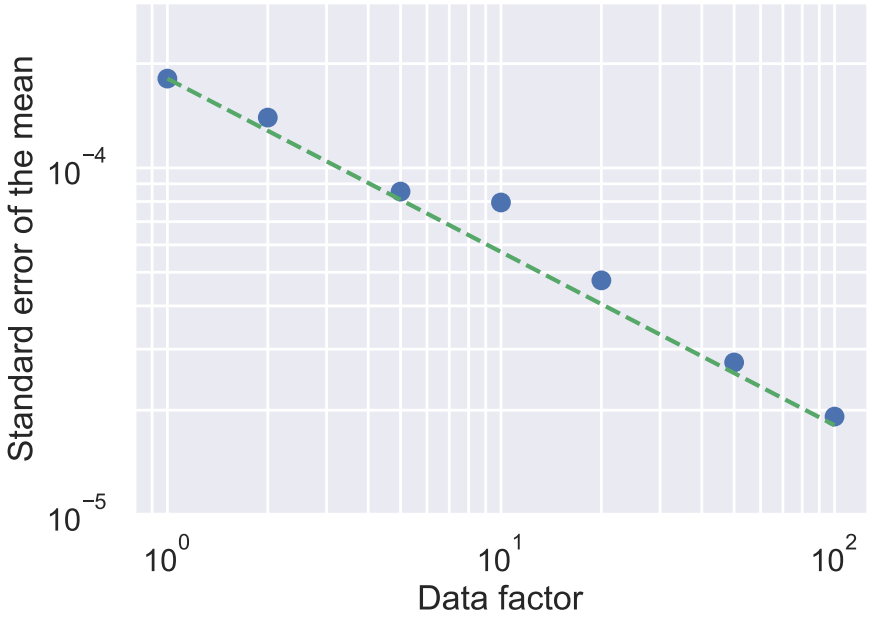

Figure 8.10: Analysis of standard deviation of simulated triplet data analysis with more data. As we generate more data, the standard deviation decreases linearly on a log-log scale as one would expect. The green dashed line corresponds to a $1/\sqrt{n}$ scaling where n is the number of measurements which will be proportional to the data factor.

measurements with and without the additional $\pi/2$ pulse respectively (see Sec. 7.3.2).

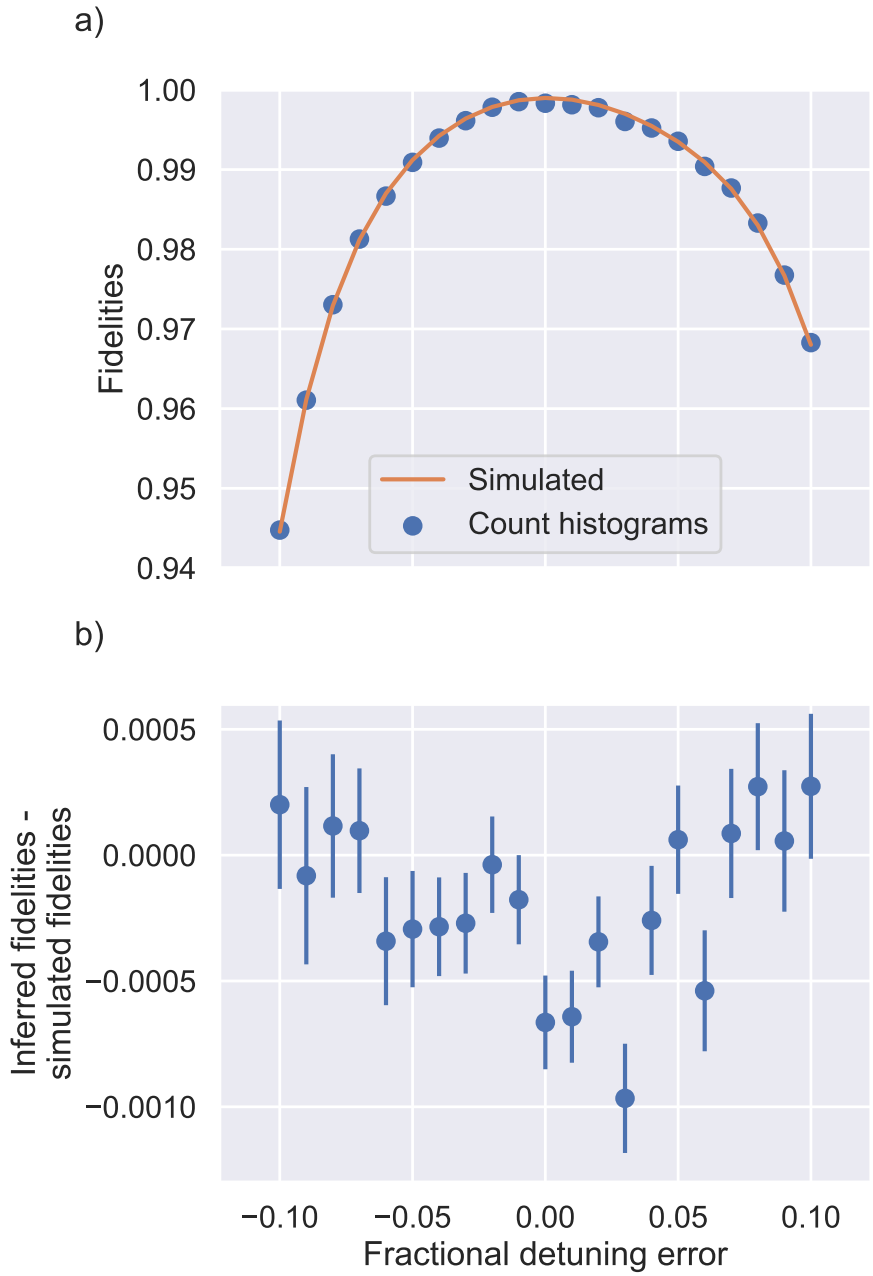

Figure 8.11: Simulated triplet data with detuning errors. a) We plot the fidelity as a function of the fractional detuning error. The insensitivity we see close to zero is due to the Walsh 7 sequence we employ (see sec. 6.2.6). b) We plot the mean of the inferred fidelities minus the simulated fidelity. We find that our estimated fidelity tracks the simulated fidelity well.

8.4.2.1 Leakage correction

We first verify our leakage correction. For a fixed fidelity of 0.999, we vary the leakage from 0 to 0.005 per qubit. The results are shown in Fig. 8.12.

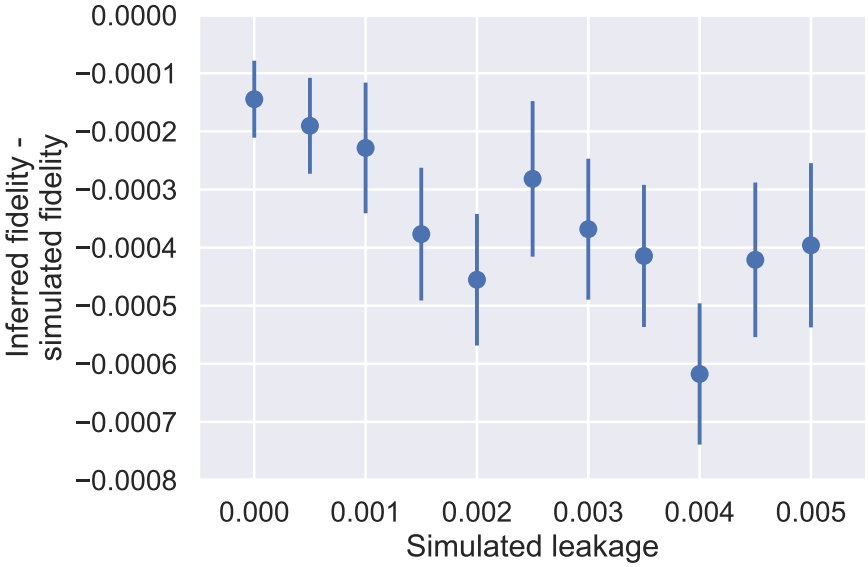

Figure 8.12: Analysis of singlet fidelity with varying leakage. For each simulated leakage, we generate 100 sets of simulated data with a fixed underlying fidelity of 0.999. We plot the mean of the inferred fidelities minus the simulated fidelity.

8.4.2.2 Entangling gate errors

We first look at singlet states with varying fidelities. Here, the error is only from motional dephasing during the entangling gate; the individual addressing is perfect. For the singlets, we also verify our fidelity estimations using the populations from the simulations before mapping them to counts[8]. The analysis is shown in Fig. 8.13. Similar to the triplets in Fig. 8.7, we see an overall negative bias that gets worse as we get closer to 1. For the fidelities extracted from the populations, the bias is fairly independent of the underlying fidelity. Histograms for simulated fidelities of 0.998, 0.999 and 1 are shown in Fig. 8.14.

To check if this bias is due to the limited statistics used in the experiment, we generated

[8] In principle we could have done this for the triplets as well. Unfortunately, at the time of writing, our code was only setup to do the analysis from the count histograms.

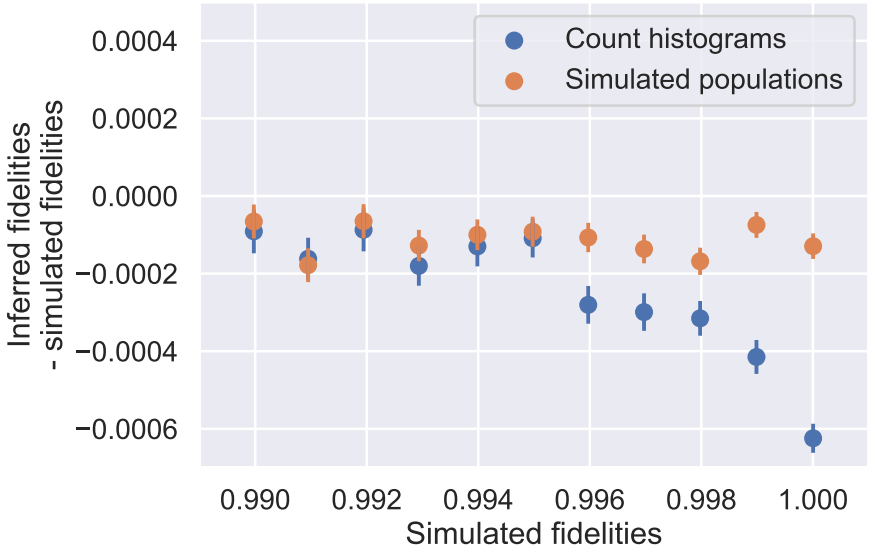

Figure 8.13: Analysis of simulated singlet data with varying fidelities. For each simulated fidelity, we generate 1000 sets of simulated data. We plot the mean of the inferred fidelities minus the simulated fidelities. We plot the fidelities from the count histograms as well as the simulated populations (which includes projection noise). Our measurements are negatively biased, with the bias from the simulated populations being fairly uniform across all fidelities. The fidelities from the count histograms have a worse bias the closer the true underlying fidelity is to 1.

simulated data with more statistics. The simulated fidelity was set to 0.999. Figure 8.15 shows that as we have more simulated data the bias decreases for fidelities derived from both the count histograms and the simulated populations.

8.4.2.3 Individual addressing errors

Next, we investigate the effect of individual addressing errors, from incorrectly calibrating either the phase or the duration of the Ramsey sequence discussed in Sec. 7.3.1.1. The results are plotted in Figures 8.17 and 8.18 respectively. For both cases, the estimated fidelity tracks the simulated fidelity closely. Near the optimal phase and duration, we have a negative bias.

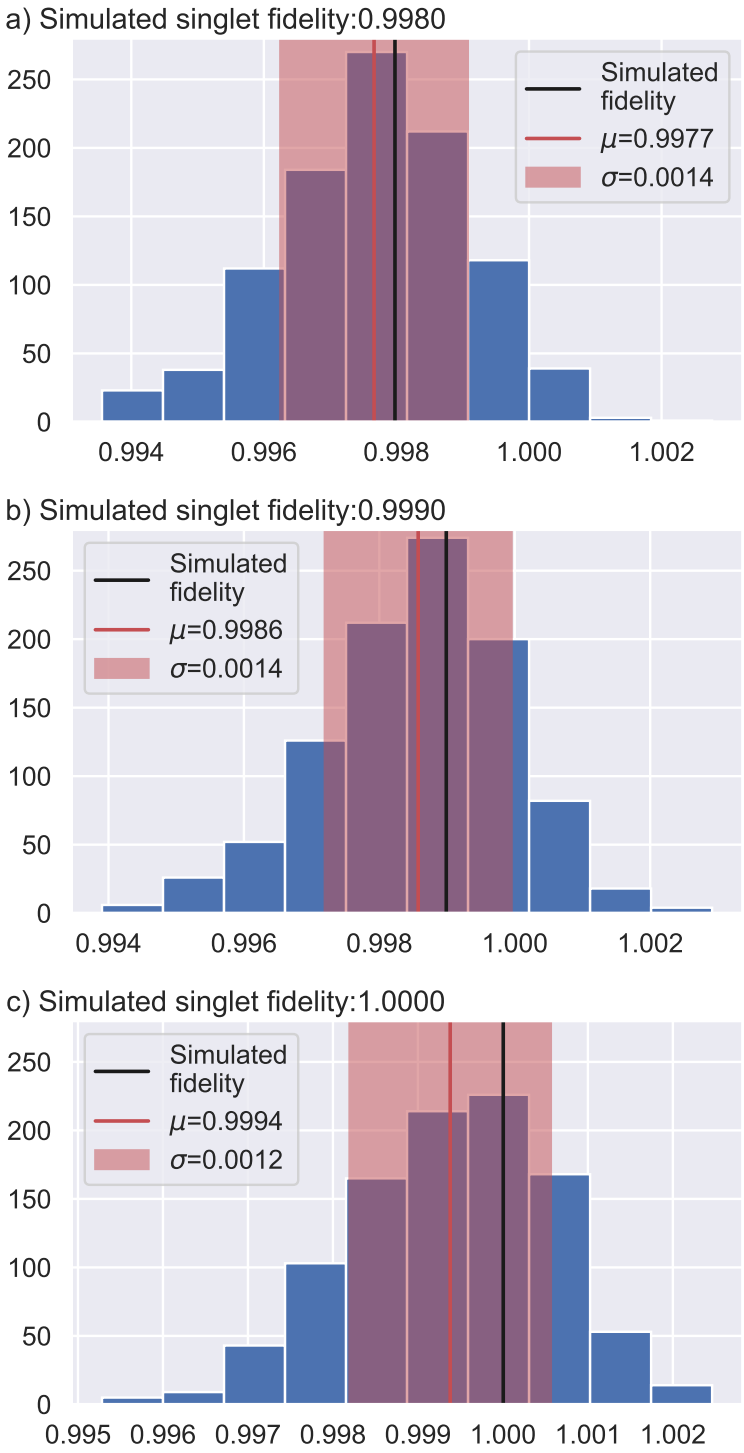

Figure 8.14: Histograms of inferred fidelities from analysing the count histograms for underlying singlet fidelities of 0.998, 0.999 and 1. For each simulated fidelity, we generate 1000 sets of simulated data. The mean and standard deviation are indicated by the red line and red shaded region. As the fidelity approaches 1, we see a larger negative bias between the mean of the analysed fidelities and the simulated fidelity.

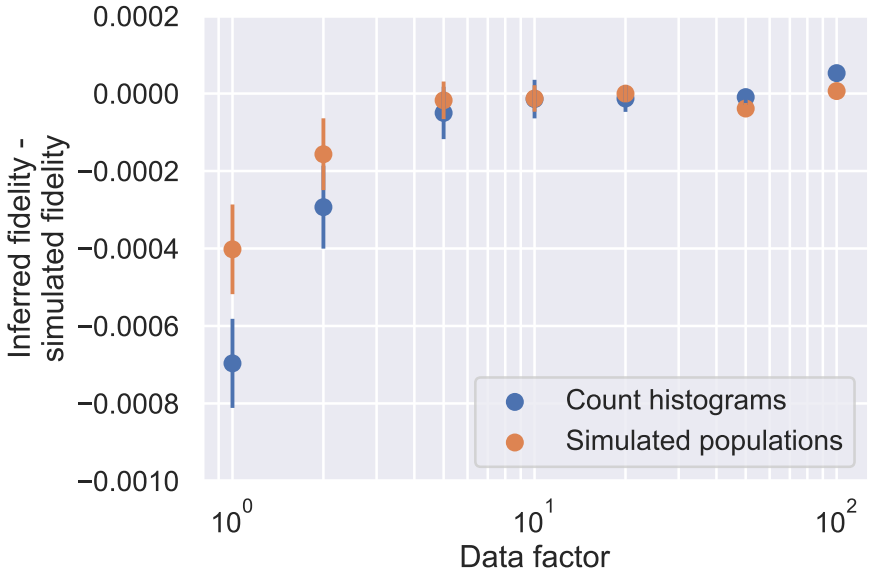

Figure 8.15: Analysis of simulated singlet data with more data compared to the experiment. We plot the mean of the inferred fidelities minus the simulated fidelities. As we increase the amount of data, our inferred fidelity is less biased for both the fidelities from the count histograms (blue) and simulated populations (orange).

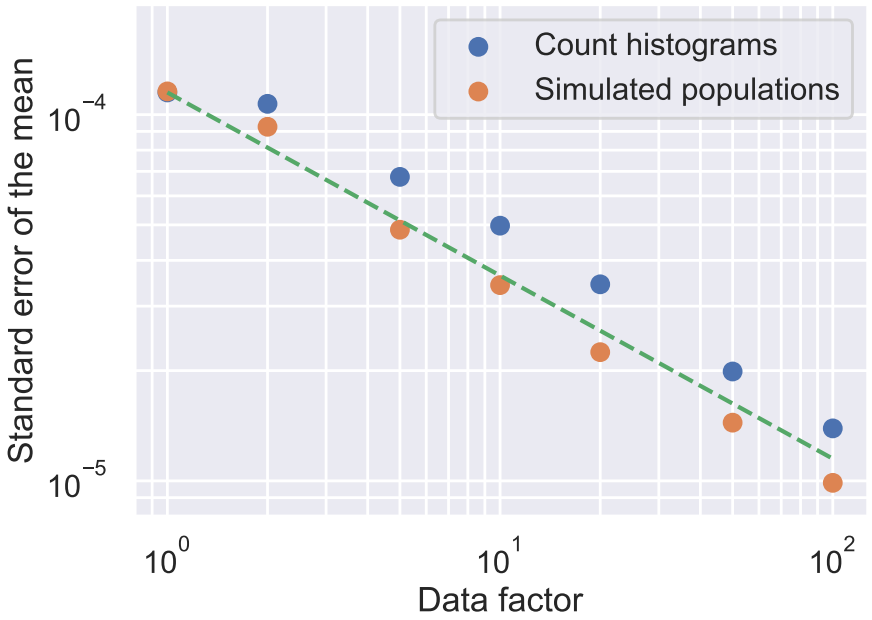

Figure 8.16: We plot the standard error of the mean as a function of the amount of simulated data for both the analysis from the count histograms (blue) and the simulated populations (orange). The green dashed line corresponds to $1/\sqrt{n}$ scaling where n is the number of measurements, which is proportional to the data factor.

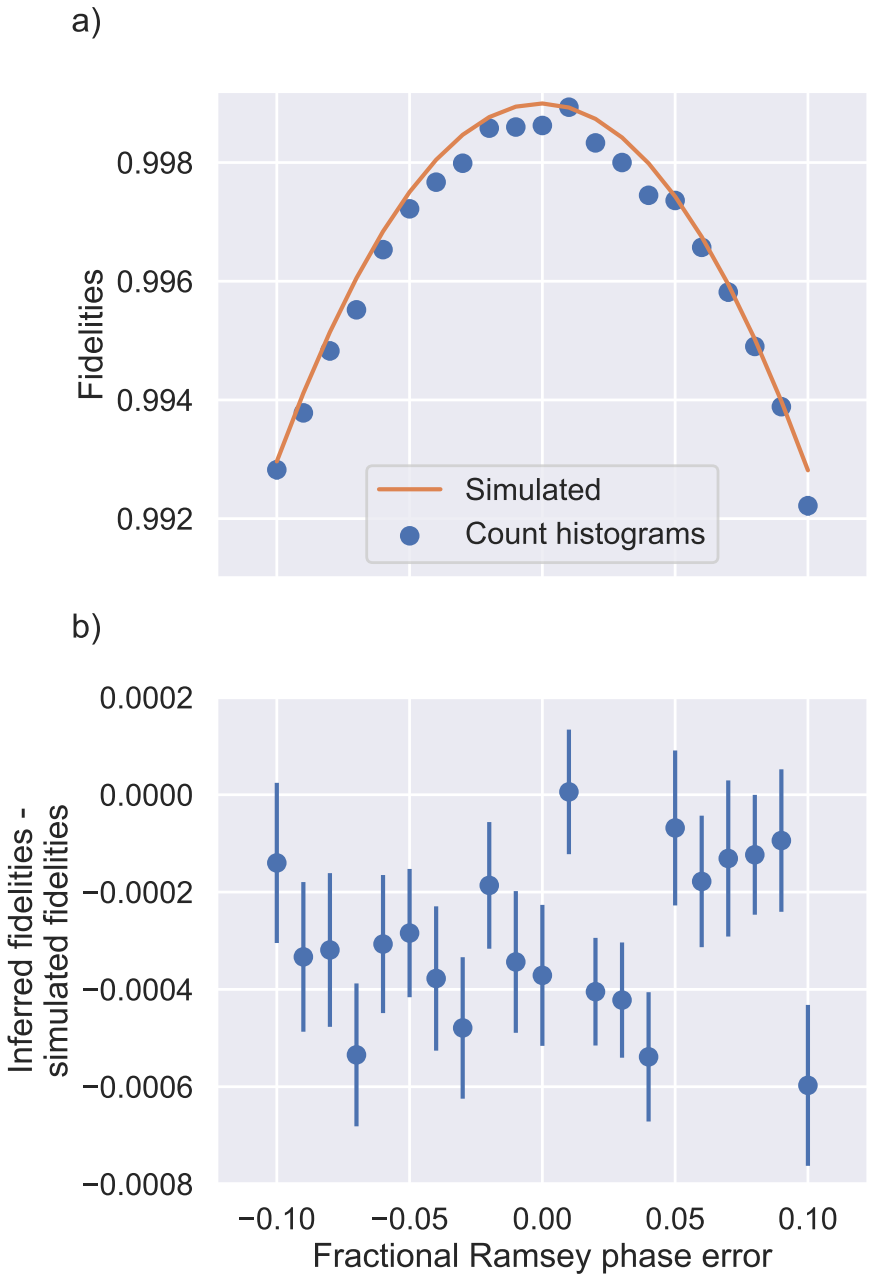

Figure 8.17: Analysis of simulated singlet data with an error in the phase of the Ramsey sequence. For each error value, we simulate 100 sets of data. a) We plot the fidelity as a function of the error, with the orange line indicating the simulated fidelities while the blue points are the fidelities extracted from the data points. b) We plot the difference between the inferred and simulated fidelities.

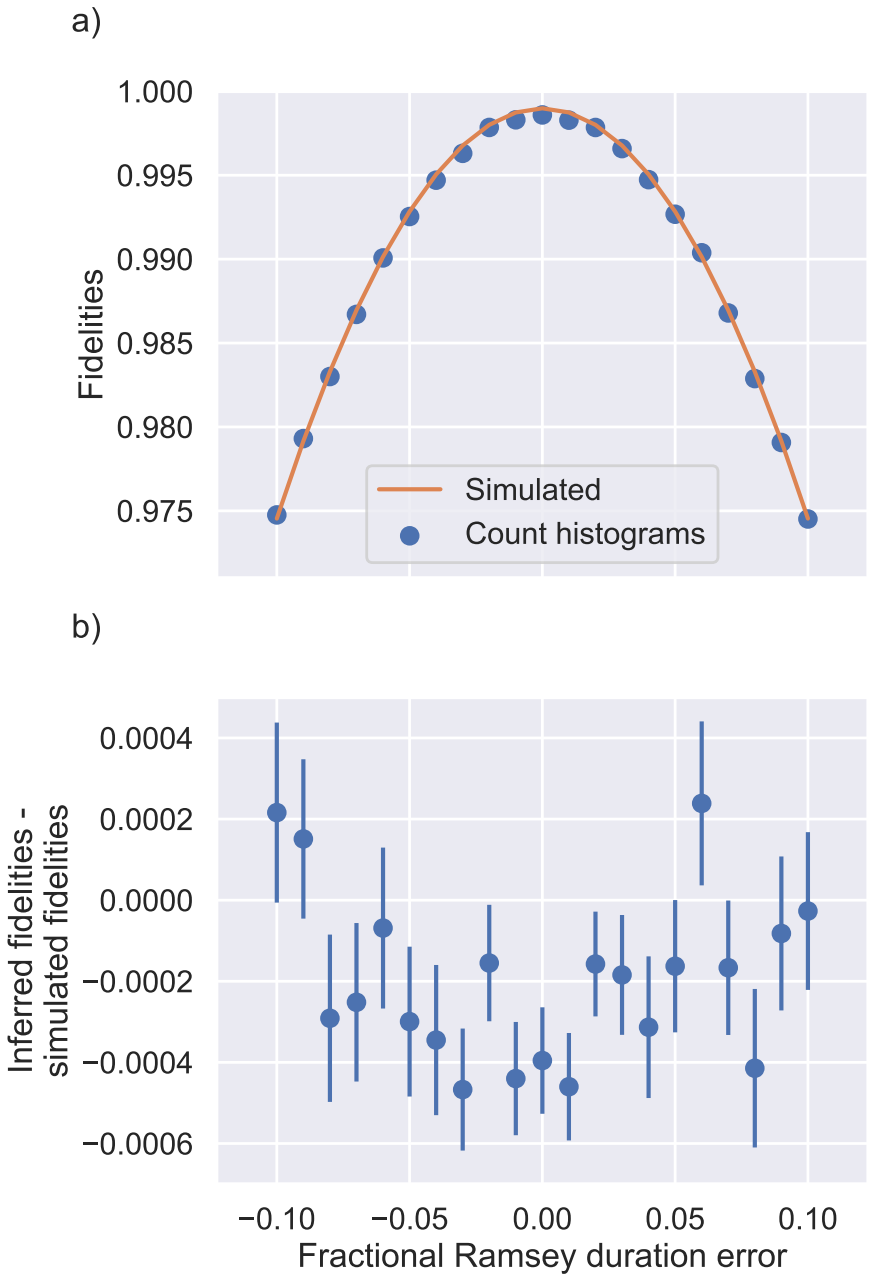

Figure 8.18: Analysis of simulated singlet data with an error in the duration of the Ramsey sequence. For each error value, we simulated 100 sets of data. a) We plot the fidelity as a function of the error, with the orange line indicating the simulated fidelities while the blue points correspond to fidelities extracted from the count histograms. b) We plot the difference between the inferred and simulated fidelities.

Every year is getting shorter never seem to find the time.

Plans that either come to naught or half a page of scribbled lines.

Hanging on in quiet desperation is the English way,

The time is gone, the song is over,

Thought I'd something more to say.

Pink Floyd

9

Conclusion

We have demonstrated a new technique for laser-free spin-motion coupling in trapped ions that uses a radiofrequency magnetic field gradient. We extended this technique to two-qubit entangling gates, generating symmetric and antisymmetric Bell states with fidelities of 0.999(1) and 0.998(1) respectively. The symmetric Bell-state fidelity is competitive with the highest fidelity across any platform. The antisymmetric Bell-state fidelity is as far as we know, the highest that has been demonstrated, integrating both high-fidelity entanglement and individual addressing, both without lasers. Where do we go from here?

9.1 Improvements to entangling gate

Our gate duration is currently 740 μs. Preliminary experiments have shown that we can reduce that duration to approximately 560 μs while maintaining a fidelity of ≈ 0.999 with current hardware. To reduce the duration further, we can increase the current used to generate the magnetic field gradient. We currently use about 1.2 A, but we estimate that our trap can handle close to 3 A safely. If we can reduce the gate duration without any other adverse effects, that should improve the fidelity as well. Motional errors decrease as the gate duration is decreased.

Aside from increasing the current, improvements could be made to the pulse shaping to reduce the ramp times for turning our radiofrequency gradient and microwave fields on and off. These ramps comprise a significant portion of the gate duration at 160 μs.

9.2 Randomized benchmarking

Aside from reducing the error in our gates, we want to characterize the error more carefully. For our entangling gate, we currently perform only one gate and measure the Bell-state fidelity from one input state. Furthermore, our analysis is complicated by the state preparation and measurement error that is larger than our gate error.

Randomized benchmarking [Knill et al., 2008] of our two-qubit operations, where a series of two-qubit and single-qubit operations are performed, would enable more sensitive characterization of our errors, assuming we do not have duty cycle related effects with longer sequences. The individual addressing we demonstrate makes benchmarking viable in our system. Benchmarking also provides a more practical demonstration for our gates; multiple gates are required for any useful computation. Currently, laser-free randomized benchmarking in trapped ions has only been performed for single-qubit operations [Harty et al., 2014, Piltz et al., 2014].

9.3 New trap geometries

The techniques described in this thesis could enable new trap geometries. The use of a current at megahertz instead of gigahertz frequencies vastly simplifies the current handling in surface electrode traps. Larger electrodes could be used for larger currents, and thus larger gradients at the ion for stronger spin-motion coupling. Instead of a single-layer trap that we use, a multi-layer trap with buried electrodes would enable larger currents while reducing the effect of the electric field.

9.4 Mixed-species entanglement

Finally, the new technique we have developed also simplifies mixed-species entangling gates. Using field-sensitive states on both Mg^+ and Ca^+, for which we have an oven in our system, would

enable a single gradient to couple the spins of both species to their shared motion. Compared to our current implementation, just two additional fields symmetrically detuned from the Ca^+ qubit would be required to entangle an Mg^+ and Ca^+ ions. To date, no mixed species entangling operations have been performed without lasers. Mixed-species entanglement would enable an "all-electronic" qubit, where the state preparation and logical operations could be performed on the Mg^+ qubit without lasers. Their internal states could then be mapped to the Ca^+ qubit for readout, which has lasers at longer wavelengths ($\approx$ 400 nm), that will hopefully cause less charging than lasers at 280 nm. High-fidelity entanglement and mixed species operations should enable a host of experiments to be carried out. We have built a versatile system and it will be exciting to see what else it is capable of!

Bibliography

[Abramowitz and Stegun, 1972] Abramowitz, M. and Stegun, I. A. (1972). Handbook of mathematical functions. New York: Dover.

[Allcock et al., 2013] Allcock, D. T. C., Harty, T. P., Ballance, C. J., Keitch, B. C., Linke, N. M., Stacey, D. N., and Lucas, D. M. (2013). A microfabricated ion trap with integrated microwave circuitry. Appl. Phys. Lett., 102(4):044103.

[Analog Devices, 2009] Analog Devices, . (2009). Fundamentals of direct digital synthesis (DDS). Analog Devices MT-085 Tutorial, see http://www. analog. com/static/imported-files/tutorials/MT-085. pdf.

[Anderson et al., 1995] Anderson, M. H., Ensher, J. R., Matthews, M. R., Wieman, C. E., and Cornell, E. A. (1995). Observation of Bose-Einstein condensation in a dilute atomic vapor. Science, 269(5221):198–201.

[Aspect et al., 1982] Aspect, A., Dalibard, J., and Roger, G. (1982). Experimental test of bell's inequalities using time-varying analyzers. Phys. Rev. Lett., 49(25):1804.

[Aude Craik et al., 2017] Aude Craik, D., Linke, N., Sepiol, M., Harty, T., Goodwin, J., Ballance, C., Stacey, D., Steane, A., Lucas, D., and Allcock, D. (2017). High-fidelity spatial and polarization addressing of Ca+ 43 qubits using near-field microwave control. Phys. Rev. A, 95(2):022337.

[Aude Craik et al., 2014] Aude Craik, D. P. L., Linke, N. M., Harty, T. P., Ballance, C. J., Lucas, D. M., Steane, A. M., and Allcock, D. T. C. (2014). Microwave control electrodes for scalable, parallel, single-qubit operations in a surface-electrode ion trap. Appl. Phys. B, 114(1-2):3–10.

[Baldwin et al., 2020a] Baldwin, C. H., Bjork, B. J., Foss-Feig, M., Gaebler, J. P., Hayes, D., Kokish, M. G., Langer, C., Sedlacek, J. A., Stack, D., and Vittorini, G. (2020a). A high fidelity light-shift gate for clock-state qubits. arXiv preprint arXiv:2003.01102.

[Baldwin et al., 2020b] Baldwin, C. H., Bjork, B. J., Gaebler, J. P., Hayes, D., and Stack, D. (2020b). Subspace benchmarking high-fidelity entangling operations with trapped ions. Physical Review Research, 2(1):013317.

[Ballance et al., 2015] Ballance, C., Schäfer, V., Home, J. P., Szwer, D., Webster, S. C., Allcock, D., Linke, N. M., Harty, T., Craik, D. A., Stacey, D. N., et al. (2015). Hybrid quantum logic and a test of bell's inequality using two different atomic isotopes. Nature, 528(7582):384–386.

[Ballance, 2017] Ballance, C. J. (2017). High-fidelity quantum logic in Ca+. Springer.

[Ballance et al., 2016] Ballance, C. J., Harty, T. P., Linke, N. M., Sepiol, M. A., and Lucas, D. M. (2016). High-Fidelity Quantum Logic Gates Using Trapped-Ion Hyperfine Qubits. Phys. Rev. Lett., 117:060504.

[Bell, 1964] Bell, J. S. (1964). On the einstein podolsky rosen paradox. Physics Physique Fizika, 1(3):195.

[Bell and Bell, 2004] Bell, J. S. and Bell, J. S. (2004). Speakable and unspeakable in quantum mechanics: Collected papers on quantum philosophy. Cambridge university press.

[Berkeland et al., 1998] Berkeland, D., Miller, J., Bergquist, J. C., Itano, W. M., and Wineland, D. J. (1998). Minimization of ion micromotion in a Paul trap. Journal of Applied Physics, 83(10):5025–5033.

[Biercuk et al., 2009] Biercuk, M. J., Uys, H., VanDevender, A. P., Shiga, N., Itano, W. M., and Bollinger, J. J. (2009). Experimental Uhrig dynamical decoupling using trapped ions. Phys. Rev. A, 79(6):062324.

[Blatt and Roos, 2012] Blatt, R. and Roos, C. F. (2012). Quantum simulations with trapped ions. Nature Phys., 8(4):277.

[Bollinger et al., 1991] Bollinger, J. J., Heizen, D. J., Itano, W. M., Gilbert, S. L., and Wineland, D. J. (1991). A 303-MHz frequency standard based on trapped Be^+ ions. IEEE Transactions on Instrumentation and Measurement, 40(2):126–128.

[Bourdeauducq et al., 2016] Bourdeauducq, S., whitequark, Jördens, R., enjoy digital, JBoulder, dhslichter, r srinivas, Smith, Z., Sionneau, Y., kemstevens, and Held, F. (2016). m-labs/artiq 2.0.

[Bowler et al., 2013] Bowler, R., Warring, U., Britton, J. W., Sawyer, B., and Amini, J. (2013). Arbitrary waveform generator for quantum information processing with trapped ions. Review of Scientific Instruments, 84(3):033108.

[Breit and Rabi, 1931] Breit, G. and Rabi, I. I. (1931). Measurement of Nuclear Spin. Phys. Rev., 38:2082–2083.

[Brewer et al., 2019] Brewer, S. M., Chen, J.-S., Hankin, A. M., Clements, E. R., Chou, C. W., Wineland, D. J., Hume, D. B., and Leibrandt, D. R. (2019). $^{27}Al^+$ Quantum-Logic Clock with a Systematic Uncertainty below 10^{-18}. Phys. Rev. Lett., 123:033201.

[Brown et al., 2011] Brown, K. R., Wilson, A. C., Colombe, Y., Ospelkaus, C., Meier, A. M., Knill, E., Leibfried, D., and Wineland, D. J. (2011). Single-qubit-gate error below 10- 4 in a trapped ion. Phys. Rev. A, 84(3):030303.

[Brownnutt et al., 2015] Brownnutt, M., Kumph, M., Rabl, P., and Blatt, R. (2015). Ion-trap measurements of electric-field noise near surfaces. Rev. Mod. Phys., 87:1419–1482.

[Bruzewicz et al., 2019] Bruzewicz, C. D., Chiaverini, J., McConnell, R., and Sage, J. M. (2019). Trapped-ion quantum computing: Progress and challenges. Applied Physics Reviews, 6(2):021314.

[Burd et al., 2019] Burd, S., Srinivas, R., Bollinger, J., Wilson, A., Wineland, D., Leibfried, D., Slichter, D., and Allcock, D. (2019). Quantum amplification of mechanical oscillator motion. Science, 364(6446):1163–1165.

[Burd, 2020] Burd, S. C. (2020). Squeezing and amplication of trapped-ion motion. PhD thesis, University of Colorado, Boulder.

[Burd et al., 2016] Burd, S. C., Allcock, D. T., Leinonen, T., Penttinen, J.-P., Slichter, D. H., Srinivas, R., Wilson, A. C., Jördens, R., Guina, M., Leibfried, D., et al. (2016). VECSEL systems for the generation and manipulation of trapped magnesium ions. Optica, 3(12):1294–1299.

[Chiaverini and Sage, 2014] Chiaverini, J. and Sage, J. M. (2014). Insensitivity of the rate of ion motional heating to trap-electrode material over a large temperature range. Phys. Rev. A, 89:012318.

[Cirac and Zoller, 1995] Cirac, J. I. and Zoller, P. (1995). Quantum computations with cold trapped ions. Phys. Rev. Lett., 74(20):4091.

[Colombe et al., 2014] Colombe, Y., Slichter, D. H., Wilson, A. C., Leibfried, D., and Wineland, D. J. (2014). Single-mode optical fiber for high-power, low-loss UV transmission. Optics Express, 22(16):19783–19793.

[Daniilidis et al., 2014] Daniilidis, N., Gerber, S., Bolloten, G., Ramm, M., Ransford, A., Ulin-Avila, E., Talukdar, I., and Häffner, H. (2014). Surface noise analysis using a single-ion sensor. Phys. Rev. B, 89:245435.

[Davis et al., 1995] Davis, K. B., Mewes, M. O., Andrews, M. R., van Druten, N. J., Durfee, D. S., Kurn, D. M., and Ketterle, W. (1995). Bose-Einstein Condensation in a Gas of Sodium Atoms. Phys. Rev. Lett., 75:3969–3973.

[Dehmelt, 1986] Dehmelt, H. (1986). Continuous Stern-Gerlach effect: principle and idealized apparatus. Proceedings of the National Academy of Sciences, 83(8):2291–2294.

[Deslauriers et al., 2006] Deslauriers, L., Olmschenk, S., Stick, D., Hensinger, W. K., Sterk, J., and Monroe, C. (2006). Scaling and suppression of anomalous heating in ion traps. Phys. Rev. Lett., 97:103007.

[Ding et al., 2014] Ding, S., Loh, H., Hablutzel, R., Gao, M., Maslennikov, G., and Matsukevich, D. (2014). Microwave control of trapped-ion motion assisted by a running optical lattice. Phys. Rev. Lett., 113:073002.

[Einstein et al., 1935] Einstein, A., Podolsky, B., and Rosen, N. (1935). Can Quantum-Mechanical Description of Physical Reality Be Considered Complete? Phys. Rev., 47:777–780.

[Emerson et al., 2005] Emerson, J., Alicki, R., and Życzkowski, K. (2005). Scalable noise estimation with random unitary operators. Journal of Optics B: Quantum and Semiclassical Optics, 7(10):S347.

[Fisk et al., 1995] Fisk, P. T., Sellars, M. J., Lawn, M. A., Coles, C., Mann, A. G., and Blair, D. G. (1995). Very high Q microwave spectroscopy on trapped/sup 171/Yb/sup+/ions: application as a frequency standard. IEEE transactions on instrumentation and measurement, 44(2):113–116.

[Flühmann et al., 2019] Flühmann, C., Nguyen, T. L., Marinelli, M., Negnevitsky, V., Mehta, K., and Home, J. P. (2019). Encoding a qubit in a trapped-ion mechanical oscillator. Nature, 566(7745):513–517.

[Foot, 2007] Foot, C. J. (2007). Atomic physics. Oxford master series in atomic, optical and laser physics. Oxford University Press, Oxford.

[Förster et al., 2009] Förster, L., Karski, M., Choi, J.-M., Steffen, A., Alt, W., Meschede, D., Widera, A., Montano, E., Lee, J. H., Rakreungdet, W., and Jessen, P. S. (2009). Microwave control of atomic motion in optical lattices. Phys. Rev. Lett., 103(23):233001.

[Freedman and Clauser, 1972] Freedman, S. J. and Clauser, J. F. (1972). Experimental test of local hidden-variable theories. Phys. Rev. Lett., 28(14):938.

[Friedrich and Herschbach, 2003] Friedrich, B. and Herschbach, D. (2003). Stern and gerlach: How a bad cigar helped reorient atomic physics. Physics Today, 56(12):53–59.

[Gaebler et al., 2012] Gaebler, J. P., Meier, A. M., Tan, T. R., Bowler, R., Lin, Y., Hanneke, D., Jost, J. D., Home, J., Knill, E., Leibfried, D., et al. (2012). Randomized benchmarking of multiqubit gates. Phys. Rev. Lett., 108(26):260503.

[Gaebler et al., 2016] Gaebler, J. P., Tan, T. R., Lin, Y., Wan, Y., Bowler, R., Keith, A. C., Glancy, S., Coakley, K., Knill, E., Leibfried, D., and Wineland, D. J. (2016). High-Fidelity Universal Gate Set for Be 9 + Ion Qubits. Phys. Rev. Lett., 117:060505.

[Gerlach and Stern, 1922] Gerlach, W. and Stern, O. (1922). Der experimentelle nachweis der richtungsquantelung im magnetfeld. Zeitschrift für Physik, 9(1):349–352.

[Giustina et al., 2015] Giustina, M., Versteegh, M. A. M., Wengerowsky, S., Handsteiner, J., Hochrainer, A., Phelan, K., Steinlechner, F., Kofler, J., Larsson, J.-A., Abellán, C., Amaya, W., Pruneri, V., Mitchell, M. W., Beyer, J., Gerrits, T., Lita, A. E., Shalm, L. K., Nam, S. W., Scheidl, T., Ursin, R., Wittmann, B., and Zeilinger, A. (2015). Significant-Loophole-Free Test of Bell's Theorem with Entangled Photons. Phys. Rev. Lett., 115:250401.

[Hahn et al., 2019] Hahn, H., Zarantonello, G., Schulte, M., Bautista-Salvador, A., Hammerer, K., and Ospelkaus, C. (2019). Integrated $^{9}Be^{+}$ multi-qubit gate device for the ion-trap quantum computer. New J. Phys. Quantum Information, 5:70.

[Harris, 1978] Harris, F. J. (1978). On the use of windows for harmonic analysis with the discrete fourier transform. Proc. IEEE, 66(1):51–83.

[Harty, 2013] Harty, T. P. (2013). High-fidelity microwave-driven quantum logic in intermediate-field 43Ca+. PhD thesis, Oxford University, UK.

[Harty et al., 2014] Harty, T. P., Allcock, D. T. C., Ballance, C. J., Guidoni, L., Janacek, H. A., Linke, N. M., Stacey, D. N., and Lucas, D. M. (2014). High-fidelity preparation, gates, memory, and readout of a trapped-ion quantum bit. Phys. Rev. Lett., 113(22):220501.

[Harty et al., 2016] Harty, T. P., Sepiol, M. A., Allcock, D. T. C., Ballance, C. J., Tarlton, J. E., and Lucas, D. M. (2016). High-Fidelity Trapped-Ion Quantum Logic Using Near-Field Microwaves. Phys. Rev. Lett., 117:140501.

[Hayes et al., 2012] Hayes, D., Clark, S. M., Debnath, S., Hucul, D., Inlek, I. V., Lee, K. W., Quraishi, Q., and Monroe, C. (2012). Coherent Error Suppression in Multiqubit Entangling Gates. Phys. Rev. Lett., 109:020503.

[Hensen et al., 2015] Hensen, B., Bernien, H., Dréau, A. E., Reiserer, A., Kalb, N., Blok, M. S., Ruitenberg, J., Vermeulen, R. F., Schouten, R. N., Abellán, C., et al. (2015). Loophole-free Bell inequality violation using electron spins separated by 1.3 kilometres. Nature, 526(7575):682–686.

[Hite et al., 2012] Hite, D. A., Colombe, Y., Wilson, A. C., Brown, K. R., Warring, U., Jördens, R., Jost, J. D., McKay, K., Pappas, D., Leibfried, D., et al. (2012). 100-fold reduction of electric-field noise in an ion trap cleaned with in situ argon-ion-beam bombardment. Phys. Rev. Lett., 109(10):103001.

[Home et al., 2011] Home, J. P., Hanneke, D., Jost, J. D., Leibfried, D., and Wineland, D. J. (2011). Normal modes of trapped ions in the presence of anharmonic trap potentials. New Journal of Physics, 13(7):073026.

[Hu et al., 2011] Hu, Y. M., Yang, W. L., Xu, Y. Y., Zhou, F., Chen, L., Gao, K. L., Feng, M., and Lee, C. (2011). Franck–Condon physics in a single trapped ion. New Journal of Physics, 13(5):053037.

[Hughes et al., 2020] Hughes, A., Schäfer, V., Thirumalai, K., Nadlinger, D., Woodrow, S., Lucas, D., and Ballance, C. (2020). Benchmarking of a high-fidelity mixed-species entangling gate. arXiv preprint arXiv:2004.08162.

[Itano and Wineland, 1981] Itano, W. M. and Wineland, D. (1981). Precision measurement of the ground-state hyperfine constant of mg+ 25. Physical Review A, 24(3):1364.

[Johanning et al., 2009] Johanning, M., Braun, A., Timoney, N., Elman, V., Neuhauser, W., and Wunderlich, C. (2009). Individual addressing of trapped ions and coupling of motional and spin states using rf radiation. Phys. Rev. Lett., 102(7):073004.

[Johansson et al., 2013] Johansson, J. R., Nation, P. D., and Nori, F. (2013). QuTiP 2: A Python framework for the dynamics of open quantum systems. Computer Physics Communications, 184(4):1234–1240.

[Khromova et al., 2012] Khromova, A., Piltz, C., Scharfenberger, B., Gloger, T. F., Johanning, M., Varón, A. F., and Wunderlich, C. (2012). Designer Spin Pseudomolecule Implemented with Trapped Ions in a Magnetic Gradient. Phys. Rev. Lett., 108:220502.

[Kienzler et al., 2015] Kienzler, D., Lo, H.-Y., Keitch, B., De Clercq, L., Leupold, F., Lindenfelser, F., Marinelli, M., Negnevitsky, V., and Home, J. (2015). Quantum harmonic oscillator state synthesis by reservoir engineering. Science, 347(6217):53–56.

[Knill et al., 2008] Knill, E., Leibfried, D., Reichle, R., Britton, J., Blakestad, R. B., Jost, J. D., Langer, C., Ozeri, R., Seidelin, S., and Wineland, D. J. (2008). Randomized benchmarking of quantum gates. Physical Review A, 77(1):012307.

[Lake et al., 2015] Lake, K., Weidt, S., Randall, J., Standing, E. D., Webster, S. C., and Hensinger, W. K. (2015). Generation of spin-motion entanglement in a trapped ion using long-wavelength radiation. Phys. Rev. A, 91:012319.

[Langer et al., 2005] Langer, C., Ozeri, R., Jost, J. D., Chiaverini, J., DeMarco, B., Ben-Kish, A., Blakestad, R., Britton, J., Hume, D., Itano, W. M., et al. (2005). Long-lived qubit memory using atomic ions. Phys. Rev. Lett., 95(6):060502.

[Langer, 2006] Langer, C. E. (2006). High fidelity quantum information processing with trapped ions. PhD thesis, University of Colorado at Boulder.

[Lee et al., 2005] Lee, P. J., Brickman, K.-A., Deslauriers, L., Haljan, P. C., Duan, L.-M., and Monroe, C. (2005). Phase control of trapped ion quantum gates. Journal of Optics B: Quantum and Semiclassical Optics, 7(10):S371.

[Leibfried et al., 2003] Leibfried, D., Blatt, R., Monroe, C., and Wineland, D. (2003). Quantum dynamics of single trapped ions. Reviews of Modern Physics, 75(1):281.

[Leibfried et al., 2002] Leibfried, D., DeMarco, B., Meyer, V., Rowe, M., Ben-Kish, A., Britton, J., Itano, W. M., Jelenković, B., Langer, C., Rosenband, T., et al. (2002). Trapped-ion quantum simulator: experimental application to nonlinear interferometers. Phys. Rev. Lett., 89(24):247901.

[Leibfried et al., 2007] Leibfried, D., Knill, E., Ospelkaus, C., and Wineland, D. J. (2007). Transport quantum logic gates for trapped ions. Phys. Rev. A, 76(3):032324.

[Leibrandt and Heidecker, 2015] Leibrandt, D. R. and Heidecker, J. (2015). An open source digital servo for atomic, molecular, and optical physics experiments. Review of Scientific Instruments, 86(12):123115.

[Levitt, 1996] Levitt, M. H. (1996). Composite pulses. Encyclopedia of nuclear magnetic resonance, 2:1396.

[Lin et al., 2020] Lin, Y., Leibrandt, D. R., Leibfried, D., and Chou, C.-w. (2020). Quantum entanglement between an atom and a molecule. Nature, 581(7808):273–277.

[Madsen et al., 2000] Madsen, D., Balslev, S., Drewsen, M., Kjærgaard, N., Videsen, Z., and Thomsen, J. (2000). Measurements on photo-ionization of 3s3p 1p1 magnesium atoms. Journal of Physics B: Atomic, Molecular and Optical Physics, 33(22):4981.

[McCormick et al., 2019] McCormick, K. C., Keller, J., Burd, S. C., Wineland, D. J., Wilson, A. C., and Leibfried, D. (2019). Quantum-enhanced sensing of a single-ion mechanical oscillator. Nature, 572(7767):86–90.

[Meekhof et al., 1996] Meekhof, D., Monroe, C., King, B., Itano, W. M., and Wineland, D. J. (1996). Generation of nonclassical motional states of a trapped atom. Phys. Rev. Lett., 76(11):1796.

[Meir et al., 2018] Meir, Z., Sikorsky, T., Ben-shlomi, R., Akerman, N., Pinkas, M., Dallal, Y., and Ozeri, R. (2018). Experimental apparatus for overlapping a ground-state cooled ion with ultracold atoms. J. Mod. Optics, 65(5-6):501–519.

[Merkel et al., 2019] Merkel, B., Thirumalai, K., Tarlton, J., Schäfer, V., Ballance, C., Harty, T., and Lucas, D. (2019). Magnetic field stabilization system for atomic physics experiments. Review of Scientific Instruments, 90(4):044702.

[Milburn et al., 2000] Milburn, G., Schneider, S., and James, D. (2000). Ion trap quantum computing with warm ions. Fortschritte der Physik: Progress of Physics, 48(9-11):801–810.

[Mintert and Wunderlich, 2001] Mintert, F. and Wunderlich, C. (2001). Ion-trap quantum logic using long-wavelength radiation. Phys. Rev. Lett., 87:257904.

[Mølmer and Sørensen, 1999] Mølmer, K. and Sørensen, A. (1999). Multiparticle entanglement of hot trapped ions. Phys. Rev. Lett., 82(9):1835.

[Monroe et al., 1995] Monroe, C., Meekhof, D. M., King, B. E., Itano, W. M., and Wineland, D. J. (1995). Demonstration of a fundamental quantum logic gate. Phys. Rev. Lett., 75(25):4714.

[Naégerl et al., 1999] Naégerl, H. C., Leibfried, D., Rohde, H., Thalhammer, G., Eschner, J., Schmidt-Kaler, F., and Blatt, R. (1999). Laser addressing of individual ions in a linear ion trap. Physical Review A, 60(1):145.

[Ospelkaus et al., 2008] Ospelkaus, C., Langer, C. E., Amini, J. M., Brown, K. R., Leibfried, D., and Wineland, D. J. (2008). Trapped-ion quantum logic gates based on oscillating magnetic fields. Phys. Rev. Lett., 101:090502.

[Ospelkaus et al., 2011] Ospelkaus, C., Warring, U., Colombe, Y., Brown, K., Amini, J. M., Leibfried, D., and Wineland, D. J. (2011). Microwave quantum logic gates for trapped ions. Nature (London), 476:181–184.

[Ozeri et al., 2007] Ozeri, R., Itano, W. M., Blakestad, R. B., Britton, J., Chiaverini, J., Jost, J. D., Langer, C., Leibfried, D., Reichle, R., Seidelin, S., Wesenberg, J. H., and Wineland, D. J. (2007). Errors in trapped-ion quantum gates due to spontaneous photon scattering. Phys. Rev. A, 75:042329.

[Piltz et al., 2014] Piltz, C., Sriarunothai, T., Varón, A., and Wunderlich, C. (2014). A trapped-ion-based quantum byte with 10- 5 next-neighbour cross-talk. Nature communications, 5(1):1–10.

[Pozar, 2009] Pozar, D. M. (2009). Microwave engineering. John Wiley & Sons.

[Pritchard, 1983] Pritchard, D. E. (1983). Cooling Neutral Atoms in a Magnetic Trap for Precision Spectroscopy. Phys. Rev. Lett., 51:1336–1339.

[Raab et al., 1987] Raab, E. L., Prentiss, M., Cable, A., Chu, S., and Pritchard, D. E. (1987). Trapping of Neutral Sodium Atoms with Radiation Pressure. Phys. Rev. Lett., 59:2631–2634.

[Reiher et al., 2017] Reiher, M., Wiebe, N., Svore, K. M., Wecker, D., and Troyer, M. (2017). Elucidating reaction mechanisms on quantum computers. Proceedings of the National Academy of Sciences, 114(29):7555–7560.

[Roos, 2008] Roos, C. F. (2008). Ion trap quantum gates with amplitude-modulated laser beams. New Journal of Physics, 10(1):013002.

[Rowe et al., 2001] Rowe, M. A., Kielpinski, D., Meyer, V., Sackett, C. A., Itano, W. M., Monroe, C., and Wineland, D. J. (2001). Experimental violation of a Bell's inequality with efficient detection. Nature, 409(6822):791–794.

[Sackett et al., 2000] Sackett, C. A., Kielpinski, D., King, B. E., Langer, C., Meyer, V., Myatt, C. J., Rowe, M., Turchette, Q., Itano, W. M., Wineland, D. J., et al. (2000). Experimental entanglement of four particles. Nature, 404(6775):256–259.

[Schäfer et al., 2018] Schäfer, V., Ballance, C., Thirumalai, K., Stephenson, L., Ballance, T., Steane, A., and Lucas, D. (2018). Fast quantum logic gates with trapped-ion qubits. Nature, 555(7694):75–78.

[Schmidt et al., 2005] Schmidt, P. O., Rosenband, T., Langer, C., Itano, W. M., Bergquist, J. C., and Wineland, D. J. (2005). Spectroscopy using quantum logic. Science, 309(5735):749–752.

[Schmidt-Kaler et al., 2003] Schmidt-Kaler, F., Häffner, H., Riebe, M., Gulde, S., Lancaster, G. P., Deuschle, T., Becher, C., Roos, C. F., Eschner, J., and Blatt, R. (2003). Realization of the Cirac–Zoller controlled-NOT quantum gate. Nature, 422(6930):408–411.

[Sedlacek et al., 2018] Sedlacek, J. A., Stuart, J., Slichter, D. H., Bruzewicz, C. D., McConnell, R., Sage, J. M., and Chiaverini, J. (2018). Evidence for multiple mechanisms underlying surface electric-field noise in ion traps. Phys. Rev. A, 98:063430.

[Sepiol, 2016] Sepiol, M. (2016). A high-fidelity microwave driven two-qubit quantum logic gate in 43Ca+. PhD thesis, University of Oxford.

[Shalm et al., 2015] Shalm, L. K., Meyer-Scott, E., Christensen, B. G., Bierhorst, P., Wayne, M. A., Stevens, M. J., Gerrits, T., Glancy, S., Hamel, D. R., Allman, M. S., Coakley, K. J., Dyer, S. D., Hodge, C., Lita, A. E., Verma, V. B., Lambrocco, C., Tortorici, E., Migdall, A. L., Zhang, Y., Kumor, D. R., Farr, W. H., Marsili, F., Shaw, M. D., Stern, J. A., Abellán, C., Amaya, W., Pruneri, V., Jennewein, T., Mitchell, M. W., Kwiat, P. G., Bienfang, J. C., Mirin, R. P., Knill, E., and Nam, S. W. (2015). Strong Loophole-Free Test of Local Realism. Phys. Rev. Lett., 115:250402.

[Shor, 1994] Shor, P. W. (1994). Algorithms for quantum computation: discrete logarithms and factoring. In Proceedings 35th annual symposium on foundations of computer science, pages 124–134. Ieee.

[Sørensen and Mølmer, 1999] Sørensen, A. and Mølmer, K. (1999). Quantum computation with ions in thermal motion. Phys. Rev. Lett., 82(9):1971.

[Sriarunothai et al., 2018] Sriarunothai, T., Giri, G. S., Wölk, S., and Wunderlich, C. (2018). Radio frequency sideband cooling and sympathetic cooling of trapped ions in a static magnetic field gradient. J. Mod. Optics, 65(5-6):560–567.

[Srinivas et al., 2019] Srinivas, R., Burd, S. C., Sutherland, R. T., Wilson, A. C., Wineland, D. J., Leibfried, D., Allcock, D. T. C., and Slichter, D. H. (2019). Trapped-ion spin-motion coupling with microwaves and a near-motional oscillating magnetic field gradient. Phys. Rev. Lett., 122:163201.

[Sutherland et al., 2019] Sutherland, R. T., Srinivas, R., Burd, S. C., Leibfried, D., Wilson, A. C., Wineland, D. J., Allcock, D. T. C., Slichter, D. H., and Libby, S. B. (2019). Versatile laser-free trapped-ion entangling gates. New Journal of Physics, 21(3):033033.

[Tan et al., 2013] Tan, T. R., Gaebler, J. P., Bowler, R., Lin, Y., Jost, J. D., Leibfried, D., and Wineland, D. J. (2013). Demonstration of a dressed-state phase gate for trapped ions. Phys. Rev. Lett., 110(26):263002.

[Timoney et al., 2011] Timoney, N., Baumgart, I., Johanning, M., Varón, A., Plenio, M. B., Retzker, A., and Wunderlich, C. (2011). Quantum gates and memory using microwave-dressed states. Nature, 476(7359):185.

[Uhrig, 2007] Uhrig, G. S. (2007). Keeping a Quantum Bit Alive by Optimized π-Pulse Sequences. Phys. Rev. Lett., 98(10):100504.

[Van Dyck et al., 1987] Van Dyck, R. S., Schwinberg, P. B., and Dehmelt, H. G. (1987). New high-precision comparison of electron and positron g factors. Phys. Rev. Lett., 59:26–29.

[Viola et al., 1999] Viola, L., Knill, E., and Lloyd, S. (1999). Dynamical decoupling of open quantum systems. Phys. Rev. Lett., 82(12).

[Viola and Lloyd, 1998] Viola, L. and Lloyd, S. (1998). Dynamical suppression of decoherence in two-state quantum systems. Phys. Rev. A, 58(4):2733.

[Wang et al., 2009] Wang, S. X., Labaziewicz, J., Ge, Y., Shewmon, R., and Chuang, I. L. (2009). Individual addressing of ions using magnetic field gradients in a surface-electrode ion trap. Applied Physics Letters, 94(9):094103.

[Wang et al., 2017] Wang, Y., Um, M., Zhang, J., An, S., Lyu, M., Zhang, J.-N., Duan, L.-M., Yum, D., and Kim, K. (2017). Single-qubit quantum memory exceeding ten-minute coherence time. Nature Photonics, 11(10):646–650.

[Warring et al., 2013a] Warring, U., Ospelkaus, C., Colombe, Y., Brown, K. R., Amini, J. M., Carsjens, M., Leibfried, D., and Wineland, D. J. (2013a). Techniques for microwave near-field quantum control of trapped ions. Phys. Rev. A, 87:013437.

[Warring et al., 2013b] Warring, U., Ospelkaus, C., Colombe, Y., Jördens, R., Leibfried, D., and Wineland, D. J. (2013b). Individual-ion addressing with microwave field gradients. Phys. Rev. Lett., 110(17):173002.

[Weidt et al., 2016] Weidt, S., Randall, J., Webster, S. C., Lake, K., Webb, A. E., Cohen, I., Navickas, T., Lekitsch, B., Retzker, A., and Hensinger, W. K. (2016). Trapped-Ion Quantum Logic with Global Radiation Fields. Phys. Rev. Lett., 117:220501.

[Weidt et al., 2015] Weidt, S., Randall, J., Webster, S. C., Standing, E. D., Rodriguez, A., Webb, A. E., Lekitsch, B., and Hensinger, W. K. (2015). Ground-State Cooling of a Trapped Ion Using Long-Wavelength Radiation. Phys. Rev. Lett., 115:013002.

[Welzel et al., 2019] Welzel, J., Stopp, F., and Schmidt-Kaler, F. (2019). Spin and motion dynamics with zigzag ion crystals in transverse magnetic gradients. J. Phys. B: At. Mol. Opt. Phys., 52:025301.

[Wilson et al., 2011] Wilson, A. C., Ospelkaus, C., VanDevender, A., Mlynek, J. A., Brown, K. R., Leibfried, D., and Wineland, D. J. (2011). A 750-mw, continuous-wave, solid-state laser source at 313 nm for cooling and manipulating trapped 9 be+ ions. Applied Physics B, 105(4):741–748.

[Wineland et al., 1998] Wineland, D. J., Monroe, C., Itano, W. M., Leibfried, D., King, B. E., and Meekhof, D. M. (1998). Experimental issues in coherent quantum-state manipulation of trapped atomic ions. J. Res. Natl. Inst. Stand. Technol., 103(3):259–328.

[Woodgate, 1970] Woodgate, G. K. (1970). Elementary atomic structure.

[Zarantonello et al., 2019] Zarantonello, G., Hahn, H., Morgner, J., Schulte, M., Bautista-Salvador, A., Werner, R., Hammerer, K., and Ospelkaus, C. (2019). Robust and resource-efficient microwave near-field entangling be+ 9 gate. Phys. Rev. Lett., 123(26):260503.

A

Baker-Campbell-Hausdorff Theorem

The Baker-Campbell-Hausdorff (BCH) theorem helps us evaluate expressions in the form of

$$e^{\hat{A}}\hat{B}e^{-\hat{A}} = \hat{B} + [\hat{A}, \hat{B}] + \frac{1}{2}[\hat{A}, [\hat{A}, \hat{B}]]... \tag{A.1}$$

where $\hat{A}$ and $\hat{B}$ are operators. One usually encounters this when trying to take some Hamiltonian into the interaction picture with another term. For example, taking a Hamiltonian $\hat{H}$ into the interaction picture with respect to $\hat{H}_0$, we first find the time evolution operator for $\hat{H}_0$, $\hat{U}_0(t)$

$$\hat{U}_0(t) = \exp\left(-\frac{i}{\hbar}\int_0^t \hat{H}_0 \mathrm{d}t\right). \tag{A.2}$$

To obtain the interaction picture Hamiltonian $\hat{H}_I(t)$,

$$\hat{H}_I(t) = \hat{U}_0^\dagger(t)\hat{H}\hat{U}_0(t), \tag{A.3}$$

which is in the form of eq. A.1, with $\hat{A} = \frac{i}{\hbar}\int_0^t \hat{H}_0 \mathrm{d}t$ and $\hat{B} = \hat{H}$.

If $[\hat{A}, \hat{B}] = s\hat{B}$ where s is some constant,

$$e^{\hat{A}}\hat{B}e^{-\hat{A}} = e^{s}\hat{B}. \tag{A.4}$$

A.1 Common interaction picture transformations

We now go through common interaction picture transformations that were encountered in the main text. We list them here to avoid repetition and to focus on the physics in the main text while having the details here.

A.1.1 Qubit

The qubit energy is usually described by

$$\hat{H}_{\text{qubit}} = \frac{\hbar\omega_0}{2}\hat{\sigma}_z, \tag{A.5}$$

where ω_0 is the qubit frequency. The propagator corresponding to this interaction is

$$U^{\dagger}_{\text{qubit}} = \exp(i\omega_0 t\sigma_z). \tag{A.6}$$

For another operator $\hat{B}$, going into the interaction picture with respect to $\hat{H}_{\text{qubit}}$ is

$$\hat{B}_I = \hat{U}^{\dagger}_{\text{qubit}} B \hat{U}_{\text{qubit}}. \tag{A.7}$$

If $\hat{B} \propto \hat{\sigma}_z$, $\hat{B}_I = \hat{B}$. If $\hat{B} \propto \hat{\sigma}_{x,y}$, we understand that

$$\begin{aligned} \hat{\sigma}_x &= \hat{\sigma}_+ + \hat{\sigma}_-, \\ \hat{\sigma}_y &= -i\hat{\sigma}_+ + i\hat{\sigma}_-, \\ [\hat{\sigma}_z, \hat{\sigma}_+] &= 2\hat{\sigma}_+, \\ [\hat{\sigma}_z, \hat{\sigma}_-] &= -2\hat{\sigma}_-. \end{aligned} \tag{A.8}$$

Thus, for the example of some field oscillating at ω that couples our two-level system such that

$$\hat{H} = 2\hbar\Omega \cos\omega t \hat{\sigma}_x, \tag{A.9}$$

Our interaction Hamiltonian $\hat{H}_I$ with respect to the qubit is

$$\begin{aligned}
\hat{H}_I &= 2\hbar\Omega \cos\omega t \hat{U}^\dagger_{\text{qubit}} \hat{\sigma}_x \hat{U}_{\text{qubit}} \\
&= 2\hbar\Omega \cos\omega t \left(\hat{\sigma}_+ e^{i\omega_0 t} + \hat{\sigma}_- e^{-i\omega_0 t}\right) \\
&= \hbar\Omega (e^{i\omega t} + e^{-i\omega t}) \left(\hat{\sigma}_+ e^{i\omega_0 t} + \hat{\sigma}_- e^{-i\omega_0 t}\right) \\
&= \hbar\Omega \left(\hat{\sigma}_+ e^{-i\delta t} + \hat{\sigma}_- e^{i\delta t}\right),
\end{aligned} \tag{A.10}$$

where $\delta = \omega - \omega_0$ and we have made the rotating wave approximation that $\omega, \omega_0 \gg |\omega - \omega_0|$.

A.1.2 Motion

The ions' motional energy is described by

$$\hat{H}_{\text{motion}} = \hbar\omega_r \hat{a}^\dagger \hat{a}, \tag{A.11}$$

where ω_r is the motional mode frequency. The propagator corresponding to this interaction is,

$$U^\dagger_{\text{motion}} = \exp(i\omega_r \hat{a}^\dagger \hat{a} t). \tag{A.12}$$

We usually transform the creation and annihilation operators $\hat{a}$ and $\hat{a}^\dagger$ with respect to this term. We use the commutator relations,

$$\begin{aligned}
[\hat{a}^\dagger \hat{a}, \hat{a}] &= [\hat{a}^\dagger, \hat{a}]\hat{a} = -\hat{a}, \\
[\hat{a}^\dagger \hat{a}, \hat{a}^\dagger] &= \hat{a}^\dagger [\hat{a}, \hat{a}^\dagger] = \hat{a}^\dagger,
\end{aligned} \tag{A.13}$$

where we understand that $[\hat{a}, \hat{a}^\dagger] = 1$ and $[\hat{A}\hat{B}, \hat{C}] = \hat{A}[\hat{B}, \hat{C}] + [\hat{A}, \hat{C}]\hat{B}$. Using these results, we obtain,

$$\begin{aligned} \hat{U}^\dagger_{\text{motion}} \hat{a} \hat{U}_{\text{motion}} &= \hat{a} e^{-i\omega_r t}, \\ \hat{U}^\dagger_{\text{motion}} \hat{a}^\dagger \hat{U}_{\text{motion}} &= \hat{a}^\dagger e^{i\omega_r t}. \end{aligned} \tag{A.14}$$

A.1.3 Modified BCH

Equation A.1 can be modified to

$$e^{\hat{A}\hat{C}} \hat{B} e^{-\hat{A}\hat{C}} = \hat{B} + [\hat{A}\hat{C}, \hat{B}] + \frac{1}{2}[\hat{A}\hat{C}, [\hat{A}\hat{C}, \hat{B}]]... \tag{A.15}$$

We assume that $[\hat{A}, \hat{C}] = 0, [\hat{C}, \hat{B}] = 0$, and $[\hat{A}, \hat{B}] = s\hat{B}$ where s is some constant.

$$\begin{aligned} [\hat{A}\hat{C}, \hat{B}] &= \hat{A}[\hat{C}, \hat{B}] + [\hat{A}, \hat{B}]\hat{C} \\ &= s\hat{B}\hat{C}, \end{aligned}$$

and

$$\begin{aligned} [\hat{A}\hat{C}, [\hat{A}\hat{C}, \hat{B}]] &= [\hat{A}\hat{C}, s\hat{B}\hat{C}] \\ &= [\hat{A}, s\hat{B}\hat{C}]\hat{C} \\ &= s^2 \hat{B}\hat{C}^2. \end{aligned}$$

Thus,

$$\begin{aligned} e^{\hat{A}\hat{C}} \hat{B} e^{-\hat{A}\hat{C}} &= \hat{B} + s\hat{B}\hat{C} + \frac{1}{2} s^2 \hat{B}\hat{C}^2... \\ &= \hat{B} e^{s\hat{C}}. \end{aligned} \tag{A.16}$$

B

Single qubit rotations

Here we describe some of the single-qubit operations presented in the main text in more detail.

B.1 Rotation matrices

First, looking at the Hamiltonian for a resonant field with a variable phase on a single spin,

$$\begin{aligned}\hat{H} &= \hbar\Omega(\hat{\sigma}_+ e^{-i\phi} + \hat{\sigma}_- e^{i\phi}) \\ &= \hbar\Omega(\hat{\sigma}_x \cos\phi + \hat{\sigma}_y \sin\phi).\end{aligned}$$

The time evolution operator is

$$\begin{aligned}\hat{U}(t) &= \exp -\frac{i}{\hbar}\hat{H}t \\ &= \exp\left(-i\Omega t(\hat{\sigma}_x\cos\phi + \hat{\sigma}_y\sin\phi)\right), \\ &= \cos\Omega t\hat{I} - i\sin\Omega t(\hat{\sigma}_x\cos\phi + \hat{\sigma}_y\sin\phi),\end{aligned}$$

where $\exp\left(-i\hat{A}\omega t\right) = \cos\left(\omega t\right)\hat{I} - i\hat{A}\sin\left(\omega t\right)$ for $\hat{A}^2 = \hat{I}$.

For a $\frac{\pi}{2}$ pulse,

$$\hat{U}_{\frac{\pi}{2}} = \hat{U}(t = \frac{\pi}{4\Omega}) = \frac{1}{\sqrt{2}}(\hat{I} - i\hat{\sigma}_x\cos\phi - i\hat{\sigma}_y\sin\phi)$$

For a π pulse,

$$\hat{U}_{\pi} = \hat{U}(t = \frac{\pi}{2\Omega}) = -i\hat{\sigma}_x\cos\phi - i\hat{\sigma}_y\sin\phi.$$

For qubit frequency shifts,

$$\hat{H} = \hbar\tfrac{\Delta}{2}\hat{\sigma}_z.$$

The corresponding time evolution operator is

$$\hat{U}_z(t) = \cos\frac{\Delta}{2}t\hat{I} - i\sin\frac{\Delta}{2}t\hat{\sigma}_z.$$

B.2 Parity flopping

Here we derive the effect of a parity $\pi/2$ pulse on two-qubit entangled states. First analysing the effect of the propagator $\hat{U}_1$ for a $\pi/2$ pulse on a single ion,

$$\begin{aligned}\hat{U}_1 |\downarrow\rangle &= \frac{1}{\sqrt{2}}(|\downarrow\rangle - ie^{-i\phi} |\uparrow\rangle),\\ \hat{U}_1 |\uparrow\rangle &= \frac{1}{\sqrt{2}}(-ie^{i\phi} |\downarrow\rangle + |\uparrow\rangle).\end{aligned}$$

Evaluating the propogators on the two-ion states,

$$\begin{aligned}\hat{U}_1\hat{U}_2 |\downarrow\downarrow\rangle &= \frac{1}{\sqrt{2}}(|\downarrow\rangle - ie^{-i\phi} |\uparrow\rangle) \otimes \frac{1}{\sqrt{2}}(|\downarrow\rangle - ie^{-i\phi} |\uparrow\rangle)\\ &= \frac{1}{2}(|\downarrow\downarrow\rangle - ie^{-i\phi}(|\uparrow\downarrow\rangle + |\downarrow\uparrow\rangle) - e^{-i2\phi} |\uparrow\uparrow\rangle),\end{aligned}$$

$$\begin{aligned}\hat{U}_1\hat{U}_2 |\downarrow\uparrow\rangle &= \frac{1}{\sqrt{2}}(|\downarrow\rangle - ie^{-i\phi} |\uparrow\rangle) \otimes \frac{1}{\sqrt{2}}(-ie^{i\phi} |\downarrow\rangle + |\uparrow\rangle)\\ &= \frac{1}{2}(-ie^{i\phi} |\downarrow\downarrow\rangle + |\downarrow\uparrow\rangle - |\uparrow\downarrow\rangle - ie^{-i\phi} |\uparrow\uparrow\rangle),\end{aligned}$$

$$\begin{aligned}\hat{U}_1\hat{U}_2 |\uparrow\downarrow\rangle &= \frac{1}{\sqrt{2}}(-ie^{i\phi} |\downarrow\rangle + |\uparrow\rangle) \otimes \frac{1}{\sqrt{2}}(|\downarrow\rangle - ie^{-i\phi} |\uparrow\rangle)\\ &= \frac{1}{2}(-ie^{i\phi} |\downarrow\downarrow\rangle - |\downarrow\uparrow\rangle + |\uparrow\downarrow\rangle - ie^{-i\phi} |\uparrow\uparrow\rangle),\end{aligned}$$

$$\begin{aligned}\hat{U}_1\hat{U}_2 |\uparrow\uparrow\rangle &= \frac{1}{\sqrt{2}}(-ie^{i\phi} |\downarrow\rangle + |\uparrow\rangle) \otimes \frac{1}{\sqrt{2}}(-ie^{i\phi} |\downarrow\rangle + |\uparrow\rangle)\\ &= \frac{1}{2}(-e^{i2\phi} |\downarrow\downarrow\rangle - ie^{i\phi}(|\downarrow\uparrow\rangle + |\uparrow\downarrow\rangle) + |\uparrow\uparrow\rangle).\end{aligned}$$

Applying the propagators to the Bell states,

$$\hat{U}_1\hat{U}_2(\frac{1}{\sqrt{2}}(|\downarrow\uparrow\rangle + |\uparrow\downarrow\rangle)) = \frac{-i}{\sqrt{2}}(e^{i\phi} |\downarrow\downarrow\rangle + e^{-i\phi} |\uparrow\uparrow\rangle).$$

And the parity, $P(\phi) := P_{\uparrow\uparrow} + P_{\downarrow\downarrow} - P_{\downarrow\uparrow+\uparrow\downarrow}$, is always 1 regardless of phase.

For the singlet state,

$$\begin{aligned}\hat{U}_1\hat{U}_2(\frac{1}{\sqrt{2}}(|\downarrow\uparrow\rangle - |\uparrow\downarrow\rangle)) &= \frac{1}{\sqrt{2}}(|\downarrow\uparrow\rangle - |\uparrow\downarrow\rangle),\\ P(\phi) &= -1.\end{aligned}$$

For the other triplet states,

$$\begin{aligned}\hat{U}_1\hat{U}_2(\frac{1}{\sqrt{2}}(|\downarrow\downarrow\rangle + |\uparrow\uparrow\rangle)) &= \frac{1}{2\sqrt{2}}\left((1-e^{i2\phi})\,|\downarrow\downarrow\rangle - 2i\cos\phi(|\downarrow\uparrow\rangle + |\uparrow\downarrow\rangle) + (1-e^{-i2\phi}\,|\uparrow\uparrow\rangle)\right)\\ P(\phi) &= \frac{1}{8}(2 - 2\cos 2\phi + 2 - 2\cos 2\phi - 8\cos^2\phi)\\ &= \frac{1}{8}(4 - 4\cos 2\phi - 4 - 4\cos 2\phi)\\ &= -\cos 2\phi,\end{aligned}$$

$$\begin{aligned}\hat{U}_1\hat{U}_2(\frac{1}{\sqrt{2}}(|\downarrow\downarrow\rangle - |\uparrow\uparrow\rangle)) &= \frac{1}{2\sqrt{2}}\left((1+e^{i2\phi})\,|\downarrow\downarrow\rangle - 2\sin\phi(|\downarrow\uparrow\rangle + |\uparrow\downarrow\rangle) - (1+e^{-i2\phi}\,|\uparrow\uparrow\rangle)\right)\\ P(\phi) &= \frac{1}{8}(2 + 2\cos 2\phi + 2 + 2\cos 2\phi - 8\sin^2\phi)\\ &= \frac{1}{8}(4 + 4\cos 2\phi - 4 + 4\cos 2\phi)\\ &= \cos 2\phi.\end{aligned}$$

These triplet states have parity oscillations that are π periodic in ϕ.

C

Displacements in phase space

This section outlines how we calculate displacements using static and oscillating gradients. The goal is derive the expressions for the displacements quantum mechanically and show that they agree with classical intuitions.

C.1 Rotating frame transformations

We first quickly recap the theory required to transfer into and out of different rotating frames. These are specifically for rotating frames at the ion's motion. We also equivalently call this moving into the interaction frame with respect to some Hamiltonian. For example, moving into the rotating frame with respect to the ion motion, the Hamiltonian describing its motion is $\hat{H}_m = \hbar\omega_r \hat{a}^\dagger \hat{a}$ where ω_r is the ion's motional frequency. The propagator for this Hamiltonian is

$$\hat{U}_{rot}^\dagger(t) = \exp\left(i\omega_r \hat{a}^\dagger \hat{a} t\right). \tag{C.1}$$

For a general operator $\hat{A}$, it transforms at $\hat{A} \rightarrow \hat{U}_{rot}^\dagger(t)\hat{A}\hat{U}_{rot}(t)$. For the creation and annihilation operators $\hat{a}$, $\hat{a}^\dagger$, we make use of the Baker-Campbell-Hausdorff (BCH) formula to

perform this transformation. For simpler commutation relations where $[\hat{A}, \hat{B}] = s\hat{B}$, $e^{\hat{A}}\hat{B}e^{-\hat{A}} = e^{s}\hat{B}$. Making use of the commutators $[\hat{a}^\dagger\hat{a}, \hat{a}] = -\hat{a}$ and $[\hat{a}^\dagger\hat{a}, \hat{a}^\dagger] = \hat{a}^\dagger$,

$$\begin{aligned} \hat{a} &\to e^{-i\omega_r t}\hat{a} \\ \hat{a}^\dagger &\to e^{i\omega_r t}\hat{a}^\dagger. \end{aligned} \tag{C.2}$$

C.1.1 Transformation of displacement operator

Making use of those transformations for $\hat{a}$ and $\hat{a}^\dagger$, we can evaluate the transformation on a displacement operator, which is what the propagators we are interested in will look like. The displacement operator $\hat{D}(\alpha)$ is

$$\hat{D}(\alpha) = \exp\left(\alpha\hat{a}^\dagger - \alpha^*\hat{a}\right), \tag{C.3}$$

where α is the displacement in phase space. Making use of BCH again, where $e^{\hat{A}}e^{\hat{B}} = e^{\hat{A}+\hat{B}+[\hat{A},\hat{B}]/2}$, we can rewrite $\hat{D}(\alpha)$ as

$$\begin{aligned} \hat{D}(\alpha) &= e^{(\alpha\hat{a}^\dagger - \alpha^*\hat{a})} \\ &= e^{(\alpha\hat{a}^\dagger - \alpha^*\hat{a})}e^{|\alpha|^2/2}e^{-|\alpha|^2/2} \\ &= e^{-|\alpha|^2/2}e^{\alpha\hat{a}^\dagger}e^{-\alpha^*\hat{a}}. \end{aligned} \tag{C.4}$$

Now if we want to transform this displacement operator out of a specific rotating frame, we can undo the previous transformation. In some rotating frame, the displacement is

$$\hat{D}(\alpha_{rot}) = \hat{U}_{rot}^\dagger\hat{D}(\alpha)\hat{U}_{rot}. \tag{C.5}$$

Transforming out of this rotating frame,

$$\begin{aligned}\hat{D}(\alpha) &= \hat{U}_{rot}\hat{D}(\alpha_{rot})\hat{U}_{rot}^{\dagger} \\ &= e^{-|\alpha_{rot}|^2/2}\hat{U}_{rot}e^{\alpha_{rot}\hat{a}^{\dagger}}e^{-\alpha_{rot}^{*}\hat{a}}\hat{U}_{rot}^{\dagger} \\ &= e^{-|\alpha_{rot}|^2/2}\hat{U}_{rot}e^{\alpha_{rot}\hat{a}^{\dagger}}\hat{U}_{rot}^{\dagger}\hat{U}_{rot}e^{-\alpha_{rot}^{*}\hat{a}}U_{rot}^{\dagger} \\ &= e^{-|\alpha_{rot}|^2/2}e^{\alpha_{rot}\hat{a}^{\dagger}e^{-i\omega_r t}}e^{-\alpha_{rot}^{*}\hat{a}e^{i\omega_r t}} \\ &= \hat{D}(\alpha e^{-i\omega_r t}),\end{aligned} \tag{C.6}$$

where we made use of $e^{\hat{A}}e^{\hat{B}}e^{-\hat{A}} = \hat{B}e^{s}$ for $[\hat{A},\hat{B}] = s\hat{B}$. So now we have an easy way of transforming displacement operators from one frame to another, which is useful in transforming the displacement operators that we've evaluated before in a frame rotating at the ion's motion.

C.2 Static gradient

Let us start first with the static gradient case. Our propagator for the gradient, which is a displacement operator, in the rotating frame of the ion is

$$\begin{aligned}\hat{U}_g^{\dagger}(t) &= \exp\frac{2\Omega_g}{\omega_r}\hat{\sigma}_z(-\hat{a}e^{-i\omega_r t} + \hat{a}^{\dagger}e^{i\omega_r t})^1 \\ &= \hat{D}\big(\hat{\sigma}_z\frac{2\Omega_g}{\omega_r}e^{i\omega_r t}\big) \\ &= \hat{D}(\hat{\sigma}_z\alpha_{rot}),\end{aligned} \tag{C.7}$$

where Ω_g is

$$\Omega_g = \frac{r_0 B_z'}{4\hbar}(\mu_{z\uparrow\uparrow} - \mu_{z\downarrow\downarrow}). \tag{C.8}$$

This is the term describing the gradient spin-motion coupling strength; this term is proportional to the ground state extent, the B field gradient, and the matrix element. The displacement in this rotating frame at the ion's motion is

$$\alpha_{rot} = \frac{2\Omega_g}{\omega_r}e^{i\omega_r t}. \tag{C.9}$$

We want to find the change in the position, $\hat{r} = r_0(\hat{a} + \hat{a}^\dagger)$, where r_0 is the ground state extent of the motional mode with frequency ω_r.

$$\begin{aligned}\hat{r}_{rot} &= \hat{D}(\alpha_{rot}) r_0(\hat{a} + \hat{a}^\dagger)\hat{D}^\dagger(\alpha_{rot}) \\ &= r_0(\hat{a} - \alpha_{rot} + \hat{a}^\dagger - \alpha^*_{rot}) \\ &= r_0(\hat{a} + \hat{a}^\dagger - 2\mathrm{Re}(\alpha_{rot})).\end{aligned} \tag{C.10}$$

To obtain the spin-dependent displacement Δx_{rot}, we need to multiply $2r_0\mathrm{Re}(\alpha_{rot})$ by a factor of 2 as $|\uparrow\rangle$ is displaced one direction, and $|\downarrow\rangle$ the other direction.

$$\begin{aligned}\Delta x_{rot} &= 4r_0\mathrm{Re}(\alpha_{rot}) \\ &= \frac{8r_0\Omega_g}{\omega_r}\cos\omega_r t \\ &= \frac{8r_0^2 B'_z}{4\hbar\omega_r}(\mu_{z\uparrow\uparrow} - \mu_{z\downarrow\downarrow})\cos\omega_r t \\ &= \frac{8\hbar}{2m\omega_r}\frac{B'_z}{4\hbar\omega_r}(\mu_{z\uparrow\uparrow} - \mu_{z\downarrow\downarrow})\cos\omega_r t \\ &= \frac{B'_z(\mu_{z\uparrow\uparrow} - \mu_{z\downarrow\downarrow})}{m\omega_r^2}\cos\omega_r t \\ &= \frac{F_B}{m\omega_r^2}\cos\omega_r t,\end{aligned} \tag{C.11}$$

where we define the magnetic force $F_B = B'_z(\mu_{z\uparrow\uparrow} - \mu_{z\downarrow\downarrow})$. Note that this is in the rotating frame of the ion's motion and we have a displacement that is oscillating at the motional frequency. Moving to the lab frame, we make use of Eq. C.6 to obtain the displacement

$$\begin{aligned}\alpha &= \alpha_{rot}e^{-i\omega_r t} \\ &= \frac{2\Omega_g}{\omega_r}.\end{aligned} \tag{C.12}$$

And following a similar process as before we obtain the displacement in the lab frame,

[1] I've dropped the constant terms from $a(e^{-i\omega_r t} - 1)$ as that comes about from the pulse shaping. See that section for more details.

$$\Delta x = \frac{F_B}{m\omega_r^2}. \tag{C.13}$$

This displacement is in complete agreement with a classical harmonic oscillator that is displaced by a constant force (which is turned on adiabatically).

C.3 Oscillating gradient

We now determine the displacement of an oscillating gradient. Again, our starting point is the displacement operator that we obtain having gone into the rotating frame of the ion.

$$\begin{aligned}\hat{U}_g^\dagger(t) = \exp\Big[&\frac{\Omega_g}{\omega_r-\omega_g}\hat{\sigma}_z(-\hat{a}e^{-i(\omega_r-\omega_g)t} + \hat{a}^\dagger e^{i(\omega_r-\omega_g)t}) + \\ &\frac{\Omega_g}{\omega_r+\omega_g}\hat{\sigma}_z(-\hat{a}e^{-i(\omega_r+\omega_g)t} + \hat{a}^\dagger e^{i(\omega_r+\omega_g)t})\Big] \\ &= \hat{D}\Big(\hat{\sigma}_z\Big[\frac{\Omega_g}{\omega_r-\omega_g}e^{i(\omega_r-\omega_g)t} + \frac{\Omega_g}{\omega_r+\omega_g}e^{i(\omega_r+\omega_g)t}\Big]\Big) \\ &= \hat{D}(\hat{\sigma}_z\alpha_{rot}),\end{aligned} \tag{C.14}$$

where the displacement in the rotating frame is

$$\alpha_{rot} = \frac{\Omega_g}{\omega_r-\omega_g}e^{i(\omega_r-\omega_g)t} + \frac{\Omega_g}{\omega_r+\omega_g}e^{i(\omega_r+\omega_g)t}. \tag{C.15}$$

Moving to the lab frame,

$$\alpha = \alpha_{rot}e^{-i\omega_r t} = \frac{\Omega_g}{\omega_r-\omega_g}e^{-i\omega_g t} + \frac{\Omega_g}{\omega_r+\omega_g}e^{i\omega_g t}. \tag{C.16}$$

Now calculating the displacement Δx,

$$\begin{aligned}
\Delta x &= 4r_0 \mathrm{Re}(\alpha) \\
&= 4r_0 \Big(\frac{\Omega_g}{\omega_r - \omega_g} + \frac{\Omega_g}{\omega_r + \omega_g} \Big) \cos \omega_g t \\
&= 4r_0 \frac{2\Omega_g \omega_r}{\omega_r^2 - \omega_g^2} \cos \omega_g t \\
&= \frac{8 r_0^2 B_z' (\mu_{z\uparrow\uparrow} - \mu_{z\downarrow\downarrow})}{4\hbar} \frac{\omega_r}{\omega_r^2 - \omega_g^2} \cos \omega_g t \\
&= \frac{8F_B}{4\hbar} \frac{\hbar}{2m\omega_r} \frac{\omega_r}{\omega_r^2 - \omega_g^2} \cos \omega_g t \\
&= \frac{F_B}{m(\omega_r^2 - \omega_g^2)} \cos \omega_g t
\end{aligned} \tag{C.17}$$

In the lab frame, we have a displacement that's oscillating at ω_g. The amplitude of this displacement also increases as $\omega_g \to \omega_r$. This displacement is in agreement with a classical harmonic oscillator driven non-resonantly.

C.3.1 Rotating frame at ω_g

We finally analyze the displacement in the rotating frame at ω_g. We follow a similar procedure to transform the displacement into this frame. We first look at the displacement in phase space,

$$\begin{aligned}
\alpha_{\omega_g} &= \alpha e^{i\omega_g t} \\
&= \Big[\frac{\Omega_g}{\omega_r - \omega_g} e^{-i\omega_g t} + \frac{\Omega_g}{\omega_r + \omega_g} e^{i\omega_g t} \Big] e^{i\omega_g t} \\
&= \frac{\Omega_g}{\omega_r - \omega_g} + \frac{\Omega_g}{\omega_r + \omega_g} e^{i2\omega_g t}
\end{aligned} \tag{C.18}$$

Now to calculate the displacement of the spins,

$$\begin{aligned}\Delta x_{\omega_g} &= 4r_0 \mathrm{Re}(\alpha_{\omega_g}) \\ &= 4r_0\big[\frac{\Omega_g}{\omega_r-\omega_g}+\frac{\Omega_g}{\omega_r+\omega_g}\cos 2\omega_g t\big] \\ &= \frac{4r_0^2F_B}{4\hbar}\big[\frac{1}{\omega_r-\omega_g}+\frac{1}{\omega_r+\omega_g}\cos 2\omega_g t\big] \\ &= \frac{F_B}{2m\omega_r}\big[\frac{1}{\omega_r-\omega_g}+\frac{1}{\omega_r+\omega_g}\cos 2\omega_g t\big] \\ &\approx \frac{F_B}{2m\omega_r(\omega_r-\omega_g)},\end{aligned} \tag{C.19}$$

where in the last line we have dropped the fast oscillating displacement. Comparing this displacement in the rotating frame at ω_g to amplitude of the displacement in the lab frame,

$$\begin{aligned}\frac{\Delta x_{\omega_g}}{\Delta x} &\approx \frac{F_B}{2m\omega_r(\omega_r-\omega_g)}\Big/\frac{F_B}{m(\omega_r^2-\omega_g^2)} \\ &= \frac{\omega_r+\omega_g}{2\omega_r},\end{aligned} \tag{C.20}$$

Which is a number that is close to but slightly smaller than 1. Thus, as far as the figure is concerned, the displacement in this frame should be roughly the same amplitude as the displacement in the lab frame.

C.4 Summary of displacements

The displacements we need for the figure are summarised below.

	Static gradient	**Oscillating gradient**	
Rotating frame	Lab	Lab	ω_g
Displacement Δx	$\frac{F_B}{m\omega_r^2}$	$\frac{F_B}{m(\omega_r^2-\omega_g^2)}\cos\omega_g t$	$\frac{F_B}{2m\omega_r(\omega_r-\omega_g)}$

C.5 Pulse shaping

We finally look at the effect of pulse shaping on the gradient propagator. For simplicity, we just do this for the static gradient case. From the previous set of notes, the propagator associated

with this gradient is,

$$\begin{aligned}\hat{U}_g^\dagger(t) &= i2\Omega_g\hat{\sigma}_z\int_0^t(\hat{a}e^{-i\omega_r t_1}+\hat{a}^\dagger e^{i\omega_r t_1})dt_1\\ &= \frac{2\Omega_g}{\omega_r}\hat{\sigma}_z\left[-\hat{a}e^{-i\omega_r t_1}+\hat{a}^\dagger e^{i\omega_r t_1}\right]_0^t\\ &= \frac{2\Omega_g}{\omega_r}\hat{\sigma}_z(-\hat{a}(e^{-i\omega_r t}-1)+\hat{a}^\dagger(e^{i\omega_r t}-1)).\end{aligned} \tag{C.21}$$

There is an extra term that corresponds to the force suddenly being turned on at $t = 0$. Now let us assume that the force is instead ramped on slowly over time τ with the amplitude function $F(t)$, where $F(0) = 0$, $F(\tau) = F(t) = 1$. Evaluating the propagator here,

$$\begin{aligned}\hat{U}_g^\dagger(t) &= i2\Omega_g\hat{\sigma}_z\int_0^t F(t_1)(\hat{a}e^{-i\omega_r t_1}+\hat{a}^\dagger e^{i\omega_r t_1})dt_1\\ &= i2\Omega_g\hat{\sigma}_z\int_\tau^t F(t_1)(\hat{a}e^{-i\omega_r t_1}+\hat{a}^\dagger e^{i\omega_r t_1})dt_1\\ &+ i2\Omega_g\hat{\sigma}_z\int_0^\tau F(t_1)(\hat{a}e^{-i\omega_r t_1}+\hat{a}^\dagger e^{i\omega_r t_1})dt_1\\ &= \frac{2\Omega_g}{\omega_r}\hat{\sigma}_z\left[F(t_1)(-\hat{a}e^{-i\omega_r t_1}+\hat{a}^\dagger e^{i\omega_r t_1})\right]_\tau^t\\ &+ \frac{2\Omega_g}{\omega_r}\hat{\sigma}_z\left[F(t_1)(-\hat{a}e^{-i\omega_r t_1}+\hat{a}^\dagger e^{i\omega_r t_1})\right]_0^\tau\\ &- \frac{2\Omega_g}{\omega_r}\int_0^\tau F'(t_1)(-\hat{a}e^{-i\omega_r t_1}+\hat{a}^\dagger e^{i\omega_r t_1})dt_1\\ &= \frac{2\Omega_g}{\omega_r}\hat{\sigma}_z\left[F(t)(-\hat{a}e^{-i\omega_r t}+\hat{a}^\dagger e^{i\omega_r t})\right]\\ &- \frac{2\Omega_g}{\omega_r}\int_0^\tau F'(t_1)(-\hat{a}e^{-i\omega_r t_1}+\hat{a}^\dagger e^{i\omega_r t_1})dt_1,\end{aligned} \tag{C.22}$$

where we have made use of the boundary conditions and that the fact that $F'(t) = 0$ for $t > \tau$. If we assume a linear ramp for $F(t)$, so $F'(t) = 1/\tau$ for $\tau \geq t \geq 0$, the last term would scale as $(1/\omega_r)/\tau$. Thus, if we ramp the force on slowly compared to $1/\omega_r$, the last term can be ignored.

This would be analogous to a classical harmonic oscillator with a static force. If harmonic oscillator is initially at no displacement and the force is turned on adiabatically, it will eventually have a fixed but static displacement depending on the magnitude of the force. If instead the force was turned on suddenly, it would be oscillating at its natural frequency with amplitude corresponding

to that force.

D

Derivations of Hamiltonians

Here we collate the lengthier derivations for equations in the main text.

D.1 Magnus Expansion

We use the Magnus expansion to evalute the time evolution operator for Hamiltonians that do not commute with itself at different times. Let $\hat{A}(t) = -\frac{i}{\hbar}\hat{H}_g(t)$. The time-evolution operator corresponding to $\hat{H}_g$ is,

$$\hat{U}_e(t) = \exp \sum_{k=1}^{\infty} \hat{\Omega}_k(t),$$

where,

$$\begin{aligned}
\hat{\Omega}_1(t) &= \int_0^t \hat{A}(t_1)dt_1 \\
\hat{\Omega}_2(t) &= \frac{1}{2}\int_0^t dt_1 \int_0^{t_1} dt_2[\hat{A}(t_1), \hat{A}(t_2)] \\
\hat{\Omega}_3(t) &= \frac{1}{6}\int_0^t dt_1 \int_0^{t_1} dt_2 \int_0^{t_2} dt_3 \left\{[\hat{A}(t_1), [\hat{A}(t_2), \hat{A}(t_3)]] + [[\hat{A}(t_3), [\hat{A}(t_2), \hat{A}(t_1)]]\right\}.
\end{aligned}$$

D.2 Geometric phase gates

We derive the propogator of the gate interaction (Eq. 2.31)

$$\hat{H}_g = \hbar\Omega_g \left(\hat{\sigma}_{i1} \pm \hat{\sigma}_{i2}\right) \left\{\hat{a}e^{i\Delta t} + \hat{a}^\dagger e^{-i\Delta t}\right\},$$

We determine the Magnus expansion with

$$\hat{A} = -i\Omega_g \left(\hat{\sigma}_{i1} \pm \hat{\sigma}_{i2}\right) \left\{\hat{a}e^{i\Delta t} + \hat{a}^\dagger e^{-i\Delta t}\right\}. \tag{D.1}$$

The first term is

$$\begin{aligned}
\hat{\Omega}_1(t) &= -i\Omega_g \left(\hat{\sigma}_{i1} \pm \hat{\sigma}_{i2}\right) \int_0^t dt_1 \left\{\hat{a}e^{i\Delta t_1} + \hat{a}^\dagger e^{-i\Delta t_1}\right\} \\
&= -i\Omega_g \left(\hat{\sigma}_{i1} \pm \hat{\sigma}_{i2}\right) \left[\frac{\hat{a}e^{i\Delta t_1}}{i\Delta} + \frac{\hat{a}^\dagger e^{-i\Delta t_1}}{-i\Delta}\right]_0^t \\
&= \frac{\Omega_g}{\Delta} \left(\hat{\sigma}_{i1} \pm \hat{\sigma}_{i2}\right) \left\{-\hat{a}(e^{i\Delta t} - 1) + \hat{a}^\dagger(e^{-i\Delta t} - 1)\right\} \\
&= \hat{D}\left(\frac{\Omega_g}{\Delta} \left(\hat{\sigma}_{i1} \pm \hat{\sigma}_{i2}\right) (e^{-i\Delta t} - 1)\right).
\end{aligned} \tag{D.2}$$

The second term is

$$\begin{aligned}
\hat{\Omega}_2(t) &= -\frac{1}{2}\Omega_g^2 \left(\hat{\sigma}_{i1} \pm \hat{\sigma}_{i2}\right)^2 \int_0^t \int_0^{t_1} dt_1 dt_2 \left[\hat{a}e^{i\Delta t_1} + \hat{a}^\dagger e^{-i\Delta t_1}, \hat{a}e^{i\Delta t_2} + \hat{a}^\dagger e^{-i\Delta t_2}\right] \\
&= -\frac{1}{2}\Omega_g^2 \left(\hat{\sigma}_{i1} \pm \hat{\sigma}_{i2}\right)^2 \int_0^t \int_0^{t_1} dt_1 dt_2 (e^{i\Delta(t_1 - t_2)} - e^{-i\Delta(t_1 - t_2)}) \\
&= -i\Omega_g^2 \left(\hat{\sigma}_{i1} \pm \hat{\sigma}_{i2}\right)^2 \int_0^t \int_0^{t_1} dt_1 dt_2 \sin\Delta(t_1 - t_2) \\
&= -i\frac{\Omega_g^2}{\Delta} \left(\hat{\sigma}_{i1} \pm \hat{\sigma}_{i2}\right)^2 \int_0^t dt_1 [\cos\Delta(t_1 - t_2)]_0^{t_1} \\
&= -i\frac{\Omega_g^2}{\Delta} \left(\hat{\sigma}_{i1} \pm \hat{\sigma}_{i2}\right)^2 \int_0^t dt_1 (1 - \cos(\Delta t_1)) \\
&= -i\frac{\Omega_g^2}{\Delta^2} \left(\hat{\sigma}_{i1} \pm \hat{\sigma}_{i2}\right)^2 [\Delta t_1 - \sin(\Delta t_1)]_0^t \\
&= -i\frac{\Omega_g^2}{\Delta^2} \left(\hat{\sigma}_{i1} \pm \hat{\sigma}_{i2}\right)^2 (\Delta t - \sin(\Delta t)).
\end{aligned} \tag{D.3}$$

Further terms vanish. The first term corresponds to a spin-dependent displacement, the second to a spin-dependent phase.

D.3 Static gradient with detuned microwaves

First, looking at the case with just a static gradient with detuned microwaves, the interaction Hamiltonian,

$$\begin{aligned}\hat{H}_I(t) &= \hat{H}_g(t) + \hat{H}_\mu(t),\\ \hat{H}_g(t) &= 2\hbar\Omega_g\hat{\sigma}_z(\hat{a}e^{-i\omega_r t} + \hat{a}^\dagger e^{i\omega_r t}),\\ \hat{H}_\mu(t) &= \hbar\Omega_\mu(\hat{\sigma}_+ e^{-i\delta t} + \hat{\sigma}_- e^{i\delta t}),\end{aligned} \tag{D.4}$$

where Ω_g describes the gradient term,

$$\Omega_g = \frac{b_r r_0 B'_z}{4\hbar}(\mu_{z\uparrow\uparrow} - \mu_{z\downarrow\downarrow}).$$

$\mu_{z\uparrow\uparrow} = \langle\uparrow|\,\mu_z\,|\uparrow\rangle$ and $\mu_{z\downarrow\downarrow} = \langle\downarrow|\,\mu_z\,|\downarrow\rangle$ describe the matrix elements of the ion's magnetic moment along the quantization axis, z. B'_z is the gradient of the B field along the quantization axis in the direction of the motional mode. This term is Ω_z^z in Ref. [Ospelkaus et al., 2008]. The Rabi frequency of the microwave field on resonance is described by Ω_μ. The frequency of the motional mode of interest is ω_r. The detuning of the microwave field from the qubit frequency is δ.

We want to go into the interaction picture with respect to the gradient term $\hat{H}_g(t)$. However, once you include the $\hat{a}$ and $\hat{a}^\dagger$ terms, the commutator at different times is no longer 0. Fortunately, it's a relatively straightforward application of the Magnus expansion in Appendix D.1.

$\hat{\Omega}_3$ and higher vanish and $\hat{A}(t) = -i2\Omega_g\hat{\sigma}_z(\hat{a}e^{-i\omega_r t} + \hat{a}^\dagger e^{i\omega_r t})$. So now evaluating the non-vanishing terms,

$$\begin{aligned}\hat{\Omega}_1(t) &= \int_0^t \hat{A}(t_1)dt_1 \\ &= -i2\Omega_g\hat{\sigma}_z \int_0^t (\hat{a}e^{-i\omega_r t_1} + \hat{a}^\dagger e^{i\omega_r t_1})dt_1 \\ &= \frac{2\Omega_g}{\omega_r}\hat{\sigma}_z \left[\hat{a}e^{-i\omega_r t_1} - \hat{a}^\dagger e^{i\omega_r t_1}\right]_0^t \\ &= \frac{2\Omega_g}{\omega_r}\hat{\sigma}_z(\hat{a}(e^{-i\omega_r t} - 1) - \hat{a}^\dagger(e^{i\omega_r t} - 1)).\end{aligned}$$

To evaluate $\hat{\Omega}_2(t)$, we first need to look at the commutator $[\hat{A}(t_1), \hat{A}(t_2)]$,

$$\begin{aligned}[\hat{A}(t_1), \hat{A}(t_2)] &= -4\Omega_g^2[\hat{a}e^{-i\omega_r t_1} + \hat{a}^\dagger e^{i\omega_r t_1}, \hat{a}e^{-i\omega_r t_2} + \hat{a}^\dagger e^{i\omega_r t_2}] \\ &= -4\Omega_g^2(e^{-i\omega_r(t_1-t_2)} - e^{i\omega_r(t_1-t_2)}) \\ &= -8i\Omega_g^2 \sin(\omega_r(t_1 - t_2)).\end{aligned}$$

This term is independent of the spin/motional state, so would commute with all the terms and can be ignored. Higher order commutators ($\hat{\Omega}_3$ onwards would also vanish as this term would commute with $\hat{A}(t)$. Thus,

$$\hat{U}_e^\dagger(t) = \exp\frac{2\Omega_g}{\omega_r}\hat{\sigma}_z(-\hat{a}(e^{-i\omega_r t} - 1) + \hat{a}^\dagger(e^{i\omega_r t} - 1)) \tag{D.5}$$

Now to get the new interaction Hamiltonian $\hat{H}_I'$,

$$\hat{H}_I'(t) = \hat{U}_e(t)^\dagger \hbar\Omega_\mu(\hat{\sigma}_+ e^{-i\delta t} + \hat{\sigma}_- e^{i\delta t})\hat{U}_e(t).$$

We make use of BCH here,

$$e^{\hat{A}}\hat{B}e^{-\hat{A}} = \hat{B} + [\hat{A}, \hat{B}] + \frac{1}{2}[\hat{A}, [\hat{A}, \hat{B}]]...$$

where $\hat{A} = \frac{2\Omega_g}{\omega_r}\hat{\sigma}_z(-\hat{a}(e^{-i\omega_r t}-1)+\hat{a}^\dagger(e^{i\omega_r t}-1))$ and $\hat{B} = \hbar\Omega_\mu(\hat{\sigma}_+ e^{-i\delta t}+\hat{\sigma}_- e^{i\delta t})$.

The relevant commutators are,

$$[\hat{\sigma}_z, \hat{\sigma}_+] = 2\hat{\sigma}_+$$
$$[\hat{\sigma}_z, \hat{\sigma}_-] = -2\hat{\sigma}_-.$$

Thus,

$$[\hat{A}, \hat{B}] = \frac{4\hbar\Omega_g\Omega_\mu}{\omega_r}(\hat{\sigma}_+ e^{-i\delta t} - \hat{\sigma}_- e^{i\delta t})(-\hat{a}(e^{-i\omega_r t}-1)+\hat{a}^\dagger(e^{i\omega_r t}-1)).$$

The higher order terms will go as $(\frac{\Omega_g'}{\omega_r})^n$ so we can probably ignore them. This gives us the interaction Hamiltonian $\hat{H}_I'$,

$$\begin{aligned}\hat{H}_I'(t) =& \hbar\Omega_\mu(\hat{\sigma}_+ e^{-i\delta t}+\hat{\sigma}_- e^{i\delta t})+ \\ & \frac{4\hbar\Omega_g\Omega_\mu}{\omega_r}(\hat{\sigma}_+ e^{-i\delta t} - \hat{\sigma}_- e^{i\delta t})(-\hat{a}(e^{-i\omega_r t}-1)+\hat{a}^\dagger(e^{i\omega_r t}-1)).\end{aligned} \tag{D.6}$$

When $\delta = \omega_r$ we get the BSB interaction,

$$\hat{H}_{bsb} = \frac{4\hbar\Omega_g\Omega_\mu}{\omega_r}(\hat{\sigma}_+\hat{a}^\dagger + \hat{\sigma}_-\hat{a}),$$

dropping the fast rotating terms. Similarly when $\delta = -\omega_r$ we get the RSB interaction which gives us,

$$\hat{H}_{rsb} = -\frac{4\hbar\Omega_g\Omega_\mu}{\omega_r}(\hat{\sigma}_+\hat{a} + \hat{\sigma}_-\hat{a}^\dagger).$$

D.4 Oscillating gradient with carrier microwaves

We now derive this for the oscillating gradient case, following a similar procedure as before.

$$\begin{aligned}
\hat{H}_I(t) =& 2\hbar\Omega_g\hat{\sigma}_z\cos\omega_g t(\hat{a}e^{-i\omega_r t}+\hat{a}^\dagger e^{i\omega_r t}) \\
&+\hbar\Omega_\mu(\hat{\sigma}_+e^{-i\delta t}+\hat{\sigma}_-e^{i\delta t}) \\
=&\hbar\Omega_g\hat{\sigma}_z(e^{i\omega_g t}+e^{-i\omega_g t})(\hat{a}e^{-i\omega_r t}+\hat{a}^\dagger e^{i\omega_r t}) \\
&+\hbar\Omega_\mu(\hat{\sigma}_+e^{-i\delta t}+\hat{\sigma}_-e^{i\delta t}) \\
=&\hbar\Omega_g\hat{\sigma}_z(\hat{a}e^{-i(\omega_r-\omega_g)t}+\hat{a}^\dagger e^{i(\omega_r-\omega_g)t}) \quad \text{negative frequency component} \\
&+\hbar\Omega_g\hat{\sigma}_z(\hat{a}e^{-i(\omega_r+\omega_g)t}+\hat{a}^\dagger e^{i(\omega_r+\omega_g)t}) \quad \text{positive frequency component} \\
&+\hbar\Omega_\mu(\hat{\sigma}_+e^{-i\delta t}+\hat{\sigma}_-e^{i\delta t}).
\end{aligned}$$

Here, the negative and positive frequency components of the oscillating gradient have explicitly been separated. We can now going through the same process as before to obtain the propagator,

$$\begin{aligned}
U_e^\dagger(t) = \exp\Big[&\frac{\Omega_g}{\omega_r-\omega_g}\hat{\sigma}_z(-\hat{a}(e^{-i(\omega_r-\omega_g)t}-1)+\hat{a}^\dagger(e^{i(\omega_r-\omega_g)t}-1))+ \\
&\frac{\Omega_g}{\omega_r+\omega_g}\hat{\sigma}_z(-\hat{a}(e^{-i(\omega_r+\omega_g)t}-1)+\hat{a}^\dagger(e^{i(\omega_r+\omega_g)t}-1))\Big].
\end{aligned} \tag{D.7}$$

This propagator corresponds to two displacements with different magnitudes oscillating at different frequencies. This is elaborated on more in section D.5. Now to obtain the interaction Hamiltonian,

$$\begin{aligned}
\hat{H}_I'(t) =&\hbar\Omega_\mu(\hat{\sigma}_+e^{-i\delta t}+\hat{\sigma}_-e^{i\delta t})+ \\
&\frac{2\hbar\Omega_g\Omega_\mu}{\omega_r-\omega_g}(\hat{\sigma}_+e^{-i\delta t}-\hat{\sigma}_-e^{i\delta t})(\hat{a}^\dagger(e^{i(\omega_r-\omega_g)t}-1)-\hat{a}(e^{-i(\omega_r-\omega_g)t}-1))+ \\
&\frac{2\hbar\Omega_g\Omega_\mu}{\omega_r+\omega_g}(\hat{\sigma}_+e^{-i\delta t}-\hat{\sigma}_-e^{i\delta t})(\hat{a}^\dagger(e^{i(\omega_r+\omega_g)t}-1)-\hat{a}(e^{-i(\omega_r+\omega_g)t}-1)).
\end{aligned} \tag{D.8}$$

Which more or less gives us the dynamics as before. The only differences are that $\omega_r \to \omega_r \pm \omega_g$, and that we lose a factor of two in the gradient term. That could be understood by the fact that

with the oscillating gradient, the sideband gets split into two frequency components. However, you can probably more than make up for that by making $\omega_r - \omega_g$ smaller in the denominator.

The BSB is now at $\delta = \omega_r \pm \omega_g$ and the RSB with $\delta = -(\omega_r \pm \omega_g)$. In practice, you would probably always want to use the $\omega_r - \omega_g$ sideband as that will be much stronger. Of course, one is also closer to the carrier so would have to employ pulse shaping to get rid of off-resonant effects.

D.5 Comparison of displacements between static and oscillating gradients

We want to look at the expressions we've derived in terms of displacements. Looking at the propagator for the static gradient,

$$\hat{U}_{\text{static}} = \exp \frac{2\Omega_g}{\omega_r} \hat{\sigma}_z(-\hat{a}^\dagger(e^{i\omega_r t} - 1) + \hat{a}(e^{-i\omega_r t} - 1)).$$

We can rewrite this as a displacement operator $\hat{D}(\alpha)$,

$$\hat{D}(\hat{\sigma}_z \alpha) = \exp\left(\hat{\sigma}_z(\alpha \hat{a}^\dagger - \alpha^* \hat{a})\right),$$

where for the static gradient,

$$\alpha_{\text{static}} = -\frac{2\Omega_g}{\omega_r}(e^{i\omega_r t} - 1) \tag{D.9}$$

Essentially, we get a spin-dependent displacement on the ion, and this displacement is oscillating in time. For the oscillating gradient case, the two displacements α_-, α_+ corresponding to negative or positive frequency components are,

$$\alpha_- = -\frac{\Omega_g}{\omega_r - \omega_g}(e^{i(\omega_r - \omega_g)t} - 1) \tag{D.10}$$

$$\alpha_+ = -\frac{\Omega_g}{\omega_r + \omega_g}(e^{i(\omega_r + \omega_g)t} - 1). \tag{D.11}$$

Summarising,

	Static gradient	**Oscillating gradient**	
Rotating frame	ω_r	$\omega_r - \omega_g$	$\omega_r + \omega_g$
Displacement proportional to	$2\Omega_g/\omega_r$	$\Omega_g/(\omega_r - \omega_g)$	$\Omega_g/(\omega_r + \omega_g)$

D.6 Derivation of spin-flip Rabi frequency from electric field sideband

We are using the magnetic field gradient to measure the E field from the oscillating field at $\omega_g/2\pi$ =5 MHz. This procedure follows Ref. [Warring et al., 2013a]. Let's first start with the Hamiltonian from this E field.

$$\begin{aligned}\hat{H}_e(t) &= 2\hbar\Omega_e \cos\omega_g t(\hat{a}^\dagger e^{i\omega_r t} + \hat{a}e^{-i\omega_r t}) \\ &= \hbar\Omega_e(e^{i\omega_g t} + e^{-i\omega_g t})(\hat{a}^\dagger e^{i\omega_r t} + \hat{a}e^{-i\omega_r t}) \\ &= \hbar\Omega_e\left((\hat{a}^\dagger e^{i\delta_- t} + \hat{a}e^{-i\delta_- t}) + (\hat{a}^\dagger e^{i\delta_+ t} + \hat{a}e^{-i\delta_+ t})\right),\end{aligned}$$

where ω_g is the angular frequency of this electric field, ω_r is the frequency of the motional mode, $\delta_\pm = \omega_r \pm \omega_g$, and Ω_e is the Rabi frequency associated with this E field. This expression is after going into the interaction picture with respect to the ion's motion ($\hbar\omega_r a^\dagger a$) and thus the creation and annihilation operators pick up the time-dependent terms.

$$\Omega_e = \frac{qEr_0}{2\hbar}.$$

q is the charge of the ion, E is the peak amplitude of the electric field at the ion and r_0 the ground state extent of the ion along that particular mode of motion.

We are using the oscillating gradient close to a GHz to measure this. The Hamiltonian of the microwave gradient is,

$$\hat{H}_{\mu w} = \hbar\Omega_{sb}(\hat{\sigma}_+ e^{-i\delta t} + \hat{\sigma}_- e^{i\delta t})(\hat{a}^\dagger e^{i\omega_r t} + \hat{a}e^{-i\omega_r t}),$$

where Ω_{sb} is the ground state sideband Rabi frequency, and δ is the detuning of the microwave gradient from the qubit. Again, this is after going into the interaction picture with respect to the qubit ($\frac{\hbar\omega_0}{2}\hat{\sigma}_z$) and the motion $\hbar\omega_r(a^\dagger a)$.

Now, we want to go into the interaction picture with respect to the E field term. We have to evaluate the time evolution operator from this Hamiltonian, $\hat{H}_e$. However, what's a little tricky is that the commutator at different times for this Hamiltonian is not 0. One solution is to use the Magnus expansion as described in Appendix D.1.

For this case $\hat{\Omega}_3$ onwards vanishes. Now evaluating these quantities for the expression we have,

$$\begin{aligned}
\hat{\Omega}_1(t) &= -i\int_0^t dt_1\Omega_e\left((\hat{a}^\dagger e^{i\delta_- t_1} + \hat{a}e^{-i\delta_- t_1}) + (\hat{a}^\dagger e^{i\delta_+ t_1} + \hat{a}e^{-i\delta_+ t_1})\right) \\
&= -i\Omega_e\left[\frac{\hat{a}^\dagger e^{i\delta_- t_1} - \hat{a}e^{-i\delta_- t_1}}{i\delta_-} + \frac{\hat{a}^\dagger e^{i\delta_+ t_1} - \hat{a}e^{-i\delta_+ t_1}}{i\delta_+}\right]_0^t \\
&= \Omega_e\left(\frac{-\hat{a}^\dagger(e^{i\delta_- t} - 1) + \hat{a}(e^{-i\delta_- t} - 1)}{\delta_-} + \frac{-\hat{a}^\dagger(e^{i\delta_+ t} - 1) + \hat{a}(e^{-i\delta_+ t} - 1)}{\delta_+}\right).
\end{aligned}$$

Now for $\hat{\Omega}_2$, let's first evaluate the commutator,

$$\begin{aligned}
[\hat{A}(t_1), \hat{A}(t_2)] = -\Omega_e^2[&(\hat{a}^\dagger e^{i\delta_- t_1} + \hat{a}e^{-i\delta_- t_1}) + (\hat{a}^\dagger e^{i\delta_+ t_1} + \hat{a}e^{-i\delta_+ t_1}), \\
&(\hat{a}^\dagger e^{i\delta_- t_2} + \hat{a}e^{-i\delta_- t_2}) + (\hat{a}^\dagger e^{i\delta_+ t_2} + \hat{a}e^{-i\delta_+ t_2})] \\
= -\Omega_e^2(&-e^{i\delta_-(t_1-t_2)} + e^{-i\delta_-(t_1-t_2)} - e^{i(\delta_- t_1 - \delta_+ t_2)} + e^{-i(\delta_- t_1 - \delta_+ t_2)} \\
&- e^{i\delta_+(t_1-t_2)} + e^{-i\delta_+(t_1-t_2)} - e^{i(\delta_+ t_1 - \delta_- t_2)} + e^{-i(\delta_+ t_1 - \delta_- t_2)}),
\end{aligned}$$

using $[\hat{a}, \hat{a}^\dagger] = 1$. One can see that all the operators have been removed from this expression and we are left with scalar, time-dependent terms. Since this is spin/motion independent, it would just contribute a global phase that we can just ignore.

Thus, back to our original problem of the propagator of the electric field

$$\begin{aligned}\hat{U}_e(t) &= \exp\hat{\Omega}_1(t) \\ &= \exp\left(\Omega_e\left[\frac{-\hat{a}^\dagger(e^{i\delta_- t}-1)+\hat{a}(e^{-i\delta_- t}-1)}{\delta_-}+\frac{-\hat{a}^\dagger(e^{i\delta_+ t}-1)+\hat{a}(e^{-i\delta_+ t}-1)}{\delta_+}\right]\right),\end{aligned}$$

and

$$\hat{U}_e^\dagger(t) = \exp\left(\Omega_e\left[\frac{\hat{a}^\dagger(e^{i\delta_- t}-1)-\hat{a}(e^{-i\delta_- t}-1)}{\delta_-}+\frac{\hat{a}^\dagger(e^{i\delta_+ t}-1)-\hat{a}(e^{-i\delta_+ t}-1)}{\delta_+}\right]\right).$$

Now we wish to evaluate the interaction Hamiltonian $\hat{H}_I(t) = \hat{U}_e^\dagger(t)\hat{H}_{\mu w}\hat{U}_e(t)$. We can make use of BCH,

$$\begin{aligned}[\hat{\Omega_1}(t)^\dagger, H_{\mu w}] = &\left[\left(\Omega_e\left[\frac{\hat{a}^\dagger(e^{i\delta_- t}-1)-\hat{a}(e^{-i\delta_- t}-1)}{\delta_-}+\frac{\hat{a}^\dagger(e^{i\delta_+ t}-1)-\hat{a}(e^{-i\delta_+ t}-1)}{\delta_+}\right]\right),\right. \\ &\left.\hbar\Omega_{sb}(\hat{\sigma}_+e^{-i\delta t}+\hat{\sigma}_-e^{i\delta t})(\hat{a}^\dagger e^{i\omega_r t}+\hat{a}e^{-i\omega_r t})\right] \\ =&\hbar\Omega_{sb}\Omega_e(\hat{\sigma}_+e^{-i\delta t}+\hat{\sigma}_-e^{i\delta t}) \\ &\times\left[\frac{-e^{-i\omega_r t}(e^{i\delta_- t}-1)-e^{i\omega_r t}(e^{-i\delta_- t}-1)}{\delta_-}+\frac{-e^{-i\omega_r t}(e^{i\delta_+ t}-1)-e^{i\omega_r t}(e^{-i\delta_+ t}-1)}{\delta_+}\right] \\ =&\hbar\Omega_{sb}\Omega_e(\hat{\sigma}_+e^{-i\delta t}+\hat{\sigma}_-e^{i\delta t})\left(-e^{-i\omega_g t}+e^{-i\omega_r t}-e^{i\omega_g t}+e^{i\omega_r t}\right) \\ &\times(\frac{1}{\omega_r-\omega_g}+\frac{1}{\omega_r+\omega_g}) \\ =&\hbar\Omega_{sb}\Omega_e(\hat{\sigma}_+e^{-i\delta t}+\hat{\sigma}_-e^{i\delta t})\left(-e^{-i\omega_g t}+e^{-i\omega_r t}-e^{i\omega_g t}+e^{i\omega_r t}\right)(\frac{2\omega_r}{\omega_r^2-\omega_g^2}) \\ =&\frac{2\hbar\Omega_{sb}\Omega_e\omega_r}{(\omega_r^2-\omega_g^2)}(\hat{\sigma}_+e^{-i\delta t}+\hat{\sigma}_-e^{i\delta t})\left(-e^{-i\omega_g t}+e^{-i\omega_r t}-e^{i\omega_g t}+e^{i\omega_r t}\right).\end{aligned}$$

When $\delta = \omega_g$, we thus get spin flips whose Rabi frequency is,

$$\Omega_{\text{spin-flip}} = \frac{2\Omega_{sb}\Omega_e\omega_r}{(\omega_r^2-\omega_g^2)}. \tag{D.12}$$

From that we should be able to evaluate the magnitude of the E field.

D.6.1 Comparison to classical derivation

From Ref. [Ospelkaus et al., 2008],

$$\Omega_{sb} = \frac{B' r_0}{2\hbar}\mu_B,$$

where B' is the gradient of the magnetic field and μ_B the magnetic moment. $r_0 = \sqrt{\frac{\hbar}{2m\omega_r}}$. Plugging those values in,

$$\begin{aligned}
\Omega_{\text{spin-flip}} &= \frac{B' r_0}{2\hbar}\mu_B \frac{qEr_0}{2\hbar}\frac{2\omega_r}{\omega_r^2 - \omega_g^2} \\
&= \frac{B'\mu_B}{2\hbar}\frac{qE}{\hbar}\frac{\omega_r}{\omega_r^2 - \omega_g^2}\frac{\hbar}{2m\omega_r} \\
&= \frac{B'}{2}\frac{\mu_B}{2\hbar}\frac{qE}{m}\frac{1}{\omega_r^2 - \omega_g^2} \\
&= \frac{B'}{2}\frac{\mu_B}{2\hbar} r_e,
\end{aligned} \tag{D.13}$$

where r_e is the displacement of the ion by the E field. For a classical harmonic oscillator with frequency ω_0 that's driven at some non-resonant frequency ω without damping, the amplitude of the displacement is $\frac{F/m}{\omega_0^2 - \omega^2}$. For our case, $F = qE$ and now this agrees with equation 4 in Ulrich's paper exactly now.

Note: We are not considering other modes of motion which might come in to play, but to a smaller extent.